

1. Report No. FHWA/TX-10/0-5798-2		2. Government Accession No.		3. Recipient's Catalog No.	
4. Title and Subtitle DEVELOPMENT, CALIBRATION, AND VALIDATION OF PERFORMANCE PREDICTION MODELS FOR THE TEXAS M-E FLEXIBLE PAVEMENT DESIGN SYSTEM				5. Report Date January 2010 Resubmitted: April 2010 Published: August 2010	
				6. Performing Organization Code	
7. Author(s) Fujie Zhou, Emmanuel Fernando, and Tom Scullion				8. Performing Organization Report No. Report 0-5798-2	
9. Performing Organization Name and Address Texas Transportation Institute The Texas A&M University System College Station, Texas 77843-3135				10. Work Unit No. (TRAIS)	
				11. Contract or Grant No. Project 0-5798	
12. Sponsoring Agency Name and Address Texas Department of Transportation Research and Technology Implementation Office P. O. Box 5080 Austin, Texas 78763-5080				13. Type of Report and Period Covered Technical Report: September 2008-August 2009	
				14. Sponsoring Agency Code	
15. Supplementary Notes Project performed in cooperation with the Texas Department of Transportation and the Federal Highway Administration. Project Title: Develop Test Procedures to Characterize Material Response Behavior and Transfer Functions for TxDOT M-E Design URL: http://tti.tamu.edu/documents/0-5798-2.pdf					
16. Abstract This study was intended to recommend future directions for the development of TxDOT's Mechanistic-Empirical (TexME) design system. For stress predictions, a multi-layer linear elastic system was evaluated and its validity was verified by comparing the measured tensile strains under accelerated pavement (ALF) loading with the computed values. After reviewing all existing pavement performance models, the VESYS model was recommended for predicting flexible pavement layer rutting and an Overlay Tester-based fatigue cracking model was proposed, which includes both crack initiation and propagation models. For hot-mix asphalt (HMA) rutting predictions, the dynamic modulus test and repeated load test are proposed to provide material properties. The proposed HMA rutting model was calibrated using the rutting data from the NCAT test track and the Texas LTPP-SPS 5 test sections. The proposed fatigue cracking models were calibrated with performance data from NCAT. Resilient modulus and permanent deformation testing is recommended for base and subgrade materials and future research efforts are required to improve the repeatability of the permanent deformation test. For stabilized bases the traditional fatigue models are recommended and calibration factors were proposed based on existing accelerated pavement test data. A field experiment was conducted to evaluate the adequacy of the <i>LoadGage</i> program to compute allowable axle load limits for thin pavements. On sections trafficked to failure, very good results were obtained when moisture correction factors were applied to the laboratory measured engineering properties. Implementation should proceed by incorporating the proposed models and default material properties into a design software package, upgrading the available repeated load equipment, performing additional calibration, and developing additional default values for a wider range of Texas materials.					
17. Key Words Flexible Pavement Design, Overlay Test, Repeated Load Test, Rutting, Fatigue Cracking, TexME			18. Distribution Statement No restrictions. This document is available to the public through NTIS: National Technical Information Service Springfield, Virginia 22161 http://www.ntis.gov		
19. Security Classif.(of this report) Unclassified		20. Security Classif.(of this page) Unclassified		21. No. of Pages 216	22. Price

**DEVELOPMENT, CALIBRATION, AND VALIDATION OF
PERFORMANCE PREDICTION MODELS FOR THE TEXAS M-E
FLEXIBLE PAVEMENT DESIGN SYSTEM**

by

Fujie Zhou, P.E.
Associate Research Engineer
Texas Transportation Institute

Emmanuel Fernando, P.E.
Research Engineer
Texas Transportation Institute

and

Tom Scullion, P.E.
Senior Research Engineer
Texas Transportation Institute

Report 0-5798-2
Project 0-5798

Project Title: Develop Test Procedures to Characterize Material Response Behavior
and Transfer Functions for TxDOT M-E Design

Performed in cooperation with the
Texas Department of Transportation
and the
Federal Highway Administration

January 2010
Resubmitted: April 2010
Published: August 2010

TEXAS TRANSPORTATION INSTITUTE
The Texas A&M University System
College Station, Texas 77843-3135

DISCLAIMER

The contents of this report reflect the views of the authors, who are responsible for the facts and the accuracy of the data presented herein. The contents do not necessarily reflect the official views or policies of the Texas Department of Transportation or the Federal Highway Administration. This report does not constitute a standard, specification, or regulation. The engineer in charge was Tom Scullion, P.E. (Texas, #62683).

ACKNOWLEDGMENTS

This project was made possible by the Texas Department of Transportation (TxDOT) in cooperation with the Federal Highway Administration. In particular, the guidance and technical assistance provided by the project director Joe Leidy, P.E., of TxDOT and the program coordinator Darrin Grenfell, P.E., proved invaluable. The following project advisors also provided valuable input throughout the course of the project, and their technical assistance is acknowledged: Mark McDaniel, P.E., Construction Division, Dr. German Claros, P.E. Research Implementation; Billy Pigg, P.E., Waco District; and Ricky Boles, P.E., Lufkin District.

TABLE OF CONTENTS

	Page
List of Figures	ix
List of Tables	xiii
Chapter 1. Introduction	1
Chapter 2. HMA Modulus and Pavement Response Model Validation	3
2.1 Introduction	3
2.2 Rest Period and HMA Resilient Modulus	4
2.3 Proposed M_r Estimation Approach	9
2.4 Necessity of Both Square and Haversine Loading Waveforms	26
2.5 Proposed Loading Time Estimation Equations for Square and Haversine Loading Waveforms	32
2.6 Verification of the M_r Approach for Pavement Response Calculation Based on FHWA-ALF Field Data	36
2.7 Conclusions and Recommendations	42
Chapter 3. Development, Calibration, and Validation of M-E HMA Rutting Model	45
3.1 Introduction	45
3.2 Rutting Model Review and Recommendation	47
3.3 Development of HMA Rutting Model	52
3.4 Calibration of the Developed HMA Rutting Model	56
3.5 Validation of the Calibrated HMA Rutting Model	65
3.6 Summary and Conclusions	68
Chapter 4. Development, Calibration, and Validation of HMA Fatigue Cracking Model	69
4.1 Introduction	69
4.2 Fatigue Cracking Model Review and Recommendation	69
4.3 Further Development of the Proposed Fatigue Cracking Model	78
4.4 Calibration of the Developed Fatigue Cracking Model	102
4.5 Validation of the Calibrated Fatigue Cracking Model	108
4.6 Summary and Conclusions	110
Chapter 5. Development, Calibration, and Validation of CTB Fatigue Cracking Model	113
5.1 Definition of Chemically Stabilized Materials	113

5.2 Fatigue Cracking Models for Chemically Stabilized Materials	114
5.3 Model Input Requirements and Associated Laboratory Testing	116
5.4 Methods of Determining Input Values for Typical Materials	117
5.5 Summary and Conclusions	121
Chapter 6. Validation of LoadGage Program for Low-Volume Roads	123
6.1 Introduction.....	123
6.2 Description of Test Sections	124
6.3 Nondestructive Testing of As-Built Sections	126
6.4 LoadGage Verification	140
Chapter 7. Conclusions and Recommendations.....	149
7.1 Conclusions.....	149
7.2 Recommendations.....	150
References	155
Appendix A. SIF Regression Equations	165
Appendix B. Granular Base Testing	169
Appendix C. Overview of the Pavement Design Software (PCA-PAVE) for Pavements Containing Stabilized Layers.....	193

LIST OF FIGURES

Figure	Page
2.1. Difference between E^* and M_r Test.....	7
2.2. Aggregate Gradations of Five HMA Mixes	15
2.3. Specimen 1A: $ E^* $ and E' Master Curves.....	22
2.4. Specimen 1A: Shift Factors for $ E^* $ and E'	23
2.5. Specimen 1A: D' Master Curve.....	23
2.6. Specimen 1A: Stress-Strain Response Simulation (0.1 s loading+0.9 s rest)	24
2.7. Comparison between the Measured and the Estimated M_r	25
2.8. A Three-Layer HMA Pavement Structure.....	27
2.9. Vertical Stress Distributions at Different Depths of HMA Layer	27
2.10. Specimen 1A: $ E^* $ and M_r Results	30
2.11. $ E^* $ Haversine Loading and M_r Square Loading.....	30
2.12. Specimen 1A: Comparison between $ E^* $ under Haversine Loading and Shifted M_r under Square Loading	31
2.13. Normalized Compressive Stress Pulse at Different Depths beneath the Pavement Surface with Varied Modulus Ratio.....	33
2.14. Normalized Compressive Stress Pulse at Different Depths beneath the Pavement Surface with a Modulus Ratio of 50.....	34
2.15. Illustration of Loading Time Calculation	35
2.16. Layout of the 12 As-Built Pavement Lanes (Qi et al. 2004)	37
2.17. Pavement Temperature Predicted from EICM	39
2.18. Lane 2: Final Vertical Stress Distributions at Different Depths of HMA Layer.....	41
3.1. Trench Profiles for Sections 161 (Top) and 162 (Bottom) on US281	46
3.2. Trench Wire Lines for Overlay Sections 508 (Top) and 507 (Bottom) on US175	46
3.3. $\log K_{r1}$ Coefficient vs. Voids Filled with Asphalt (%) (Schwartz 2006)	49
3.4. Plot of Regression Constants “a” and “b” from Log Permanent Strain – Log Number of Loading Cycles.....	54
3.5. 2006 Experimental Sections of the NCAT Test Track.....	57
3.6. Accumulated Traffic Loads in ESALs at the NCAT Test Track.....	57
3.7. Measured Rut Depths of Test Track Sections	58

3.8.	Examples of Prepared Specimens for Dynamic Modulus Test and Repeated Load Test	59
3.9.	Dynamic Modulus Master Curves of the HMA Mixes Used for Calibration.....	59
3.10.	Comparisons between the Measured and Predicted Rut Development	61
3.11.	Annual Traffic Loading on US175 near Dallas, Texas	63
3.12.	Dynamic Modulus and Repeated Load Test Results	64
3.13.	Rut Depths Comparison of SPS5 Sections: Measured vs. Predicted.....	65
3.14.	Dynamic Modulus Master Curves of Sections N02, N12, and N13	66
3.15.	Comparisons between the Predicted and Measured Rutting Development of Sections N02, N12, and N13	67
4.1.	Predicted $\log k_I$ vs. Measured $\log k_I$	75
4.2.	Validation of k_I - k_2 Relationship Using Texas Mixes	79
4.3.	Finite Elements Meshing around Crack Tip	80
4.4.	SIF Comparison between SA- <i>CrackPro</i> and ANSYS-3D	81
4.5.	Pavement Structures and Associated Odemark's Transformation	83
4.6.	Verification of the MET Approach for Multi-Base Pavement Structures	84
4.7.	Two-HMA Pavement Structure and Associated Odemark's Transformation	85
4.8.	Verification of the MET Approach for Multi-HMA Pavement Structures	85
4.9.	Tandem Traffic Loading (Huang 1993).....	86
4.10.	K_I and K_{II} Comparison: Tridem vs. Single Axle Load	87
4.11.	Three-Layered Pavement Structures Used for Developing SIF Equations	89
4.12.	SIF Values Predicted by Regression Equation vs. SIF Calculated by SA- <i>CrackPro</i> Program.....	91
4.13.	OT Concept.....	92
4.14.	OT Specimen Preparation from SGC Molded Sample	93
4.15.	Sample End Plates and Glue Gig	94
4.16.	Connecting Plates	95
4.17.	External LVDTs and Overview of LVDT Mounted Specimen	96
4.18.	Normalized Maximum Load vs. Crack Length	98
4.19.	Calculated SIF vs. Crack Length	99
4.20.	Determination of Fracture Properties: A and n	101
4.21.	2006 Experimental Sections of the NCAT Test Track	102

4.22.	Sections with Fatigue Cracking: N6, N7, and S11	103
4.23.	Sections without Fatigue Cracking: N3, N4, N9, and N10.....	104
4.24.	Pavement Structural Information of NCAT Sections Used for Fatigue Cracking Model Calibration	105
4.25.	Dynamic Modulus Master Curves for the HMA Mixes Used for Fatigue Cracking Calibration.....	105
4.26.	Two-Step OT Test for HMA Fracture Properties: A and n	106
4.27.	Comparisons of the Measured and Predicted Fatigue Cracking Development	107
4.28.	Observed Fatigue Cracking at Section N1 (NCAT 2005).....	108
4.29.	Evidence of Bottom-Up Fatigue Cracking	109
4.30.	Pavement Structural Information of NCAT 2003 Sections N1 and N2.....	109
4.31.	Dynamic Modulus Master Curves of HMA Mixes Used for Sections N1 and N2	109
4.32.	Comparisons of the Measured and Predicted Fatigue Cracking Development	110
5.1.	Calibration for Cement Treated Base	115
5.2.	Calibration for Fine-Grained Soil Cement.....	115
5.3.	Seismic Modulus Test Being Conducted.....	118
5.4.	Modulus of Rupture Test Set-Up.....	120
6.1.	Schematic Layout of Test Sections Placed at the Riverside Campus.....	124
6.2.	Sequence of Test Track Construction (Elevation View Looking North)	125
6.3.	Picture of Test Track after Construction.....	126
6.4.	Air-Coupled GPR System Mounted on TTI Van	127
6.5.	Illustration of GPR Data Collected on Annex Sections.....	127
6.6.	Thickness Profiles Determined from GPR Data on West Wheel Path	128
6.7.	Thickness Profiles Determined from GPR Data on East Wheel Path	129
6.8.	Correspondence between Surface Thickness Profile and Annex Test Sections.....	129
6.9.	Comparison of FWD Sensor 1 Deflections on Both Wheel Paths.....	130
6.10.	DCP Test Data on Chip Seal LTS Section	132
6.11.	DCP Test Data on 2-inch HMAC LTS Section	133
6.12.	DCP Test Data on 4-inch HMAC LTS Section.....	133
6.13.	DCP Test Data on 4-inch HMAC Section without LTS.....	134
6.14.	DCP Test Data on 2-inch HMAC Section without LTS.....	134
6.15.	DCP Test Data on Chip Seal Section without LTS	135

6.16.	FWD Deflection Basins Measured at Five Stations along West Wheel Path of 2-inch HMA LTS Section	136
6.17.	SCIs Computed from Sensors 1 and 2 Deflections along West Wheel Path	136
6.18.	SCIs Computed from Sensors 1 and 2 Deflections along East Wheel Path	137
6.19.	Comparison of Fitted Deflection Basins to Measured Deflections at Station 37 on West Wheel Path of 2-inch HMA LTS Section	137
6.20.	Comparison of Fitted Deflection Basins to Measured Deflections at Station 43 on West Wheel Path of 2-inch HMA LTS Section	138
6.21.	Comparison of Fitted Deflection Basins to Measured Deflections at Station 48 on West Wheel Path of 2-inch HMA LTS Section	138
6.22.	Comparison of Fitted Deflection Basins to Measured Deflections at Station 53 on West Wheel Path of 2-inch HMA LTS Section	139
6.23.	Comparison of Fitted Deflection Basins to Measured Deflections at Station 60 on West Wheel Path of 2-inch HMA LTS Section	139
6.24.	Soil-Water Characteristic Curve for Clay Material at Test Site	142
6.25.	Comparison of Measured Rut Depths with <i>LoadGage</i> Predicted Allowable Loads on Sections Tested	145
6.26.	Relationship between Measured Rut Depths and <i>LoadGage</i> Predicted Allowable Loads	145
6.27.	Relationship between Measured Rut Depths and Tex-117E Predicted Allowable Loads	146
7.1.	Outline for the Proposed TexME Design System Site	151
7.2.	Material Testing to Support TexME	152
7.3.	New Generation of HMA Testing Equipment with Automated Sensors	153

LIST OF TABLES

Table	Page
2- 1. HMA Stiffness Testing Procedures	5
2-2. Simply Estimated Rest Periods.....	6
2-3. Proposed Loading Waveform for HMA M_r Test.....	11
2-4. Four HMA Mixes Used in This Study.....	15
2-5. Specimen 1/2A: E^* and M_r Test Results	18
2-6. Specimen 1A: E^* and M_r Test Results	19
2-7. Specimen FC1A: E^* and M_r Test Results.....	20
2-8. Specimen Trap1: E^* and M_r Test Results.....	21
2-9. Specimens 1A: Prony Series' Constants.....	24
2-10. Estimated M_r Values under Square Loading	29
2-11. The Measured vs. the Predicted Loading Times at the Virginia Smart Road	36
2-12. Measured and Predicted Maximum Strain.....	38
2-13. $ E^* $ and M_r Values at Different Frequency.....	40
2-14. HMA Modulus and Loading Frequency.....	42
3- 1. Fine Aggregate Angularity Index Used to Adjust F_{index}	49
3-2. Coarse Aggregate Angularity Index Used to Adjust C_{index}	49
3-3. Repeated Load Test Temperature and Load Levels	53
3-4. μ and α Values of Selected Sections Determined from the Repeated Load Test	60
3-5. Basic Information of the SPS5 Test Sections	63
3-6. Rutting Parameters at 40 °C.....	64
3-7. Permanent Deformation Properties of Sections N02, N12, and N13 at 100 °F.....	66
4-1. Comparison of Fatigue Cracking Modeling Approaches	77
4-2. Structural and Material Properties Used in the Analysis.....	82
4-3. Statistic Analysis Results.....	82
4-4. Four Single Axle Loads Recommended for SIF Analysis.....	89
4-5. Measured HMA Fracture Properties.....	106

5-1.	Minimum Values of 7 Days Unconfined Compressive Strength for Chemically Stabilized Materials in the MEPDG	113
5-2.	TEX-117-E UCS Results	118
5-3.	Seismic Modulus Results	119
5-4.	Modulus of Rupture Results	119
5-5.	Summary of All Results	120
6-1.	Matrix of Test Sections	125
6-2.	DCP Layer Stiffness Estimates	132
6-3.	Summary of FWD Backculations along West Wheel Path	140
6-4.	Summary of FWD Backculations along East Wheel Path	141
6-5.	Predicted Allowable Loads	142
6-6.	Moisture-Corrected Strength Properties of Clay Subgrade	143
6-7.	Measured Rut Depths after Repetitive Loading of Testing Sections	144

LIST OF ABBREVIATIONS

AASHTO	American Association of State Highway and Transportation Officials
AI	Asphalt Institute
ALF	Accelerated Loading Facility
CalME	California Mechanistic-Empirical Pavement Design Program
CTB	Cement-Treated Base
DIC	Digital Image Correlation
EICM	Enhanced Integrated Climatic Model
ESAL	Equivalent Single Axle Load
FPS	Flexible Pavement System
FHWA	Federal Highway Administration
FWD	Falling Weight Deflectometer
GPR	Ground Penetration Radar
HMA	Hot-Mix Asphalt
LTPP	Long-Term Pavement Performance
LVDT	Linear Variable Differential Transformer
MEPDG	Mechanistic-Empirical Pavement Design Guide
MOD	Maximum Opening Displacement
NCAT	National Center of Asphalt Technology
NCHRP	National Cooperative Highway Research Program
OT	Overlay Test
PCA	Portland Cement Association
RD	Rut Depth
RSST-CH	Repeated Simple Shear Test at Constant Height
SA-CrackPro	Semi-Analytical FE Method-Based Crack Propagation Program
SGC	Superpave Gyratory Compactor
SIF	Stress Intensity Factor
SPS	Specific Pavement Studies
SWCC	Soil-Water Characteristic Curve
TexME	Texas Mechanistic-Empirical Pavement Design System
TTI	Texas Transportation Institute
TxDOT	Texas Department of Transportation
UCS	Unconfined Compressive Strength

CHAPTER 1

INTRODUCTION

The objective of TxDOT Project 0-5798 was to develop the framework for the development and implementation of the next level of MEPDG (Mechanistic-Empirical Pavement Design guide) for TxDOT (TexME). As specified in the project statement this study focused on the following areas:

1. Identification and evaluation of test procedures that characterize material properties needed to predict pavement response;
2. Assembling existing performance prediction models (transfer functions) and evaluate their feasibility of being implemented in Texas. Key considerations will be the models' performance in basic sensitivity analysis, the practicality of the data input requirements and their performance at simulating results from accelerated pavements tests (APT); and
3. Calibration of the selected transfer functions with available performance data from the Long-Term Pavement Performance (LTPP) data bases, various test track studies, and whatever performance data are available from the databases being assembled in Texas.

In the first two years of this study a comprehensive review was made of the available models for predicting the major distresses in flexible pavements and of the laboratory test procedures used to measure the required materials properties. This information has been included in the two earlier reports in this study 0-5798-P1 and 0-5798-P2. In this final report a complete summary of all of the findings of this study including the recommendations for implementation are presented.

In [Chapter 2](#), a review is made of the adequacy of models to predict pavement response in flexible pavements. Response data were collected from various test tracks and a comparison was made of the measured versus computed responses.

In [Chapter 3](#), recommendations are proposed on test methods and models for the prediction of pavement rutting. Efforts were made to calibrate the proposed model, this included obtaining samples of pavement materials from test tracks and characterizing them in the Texas Transportation Institute (TTI) laboratory. Efforts to perform both calibration and verification are described in detail in this chapter.

In [Chapter 4](#), details are provided on the model requirements to adequately predict hot-mix asphalt (HMA) fatigue cracking. It was determined that none of the available models adequately model both crack initiation and crack propagation. A new model was proposed, and its development and eventual calibration and validation are described in detail in this chapter. The upgraded overlay tester is proposed as the method of providing both dynamic modulus and fracture properties to the new model.

In [Chapter 5](#), recommendations are proposed on the design of pavement containing stabilized bases. The fatigue models proposed in the existing MEPDG were judged to be reasonable. Recent studies to develop calibration factors for these models from available APT data are described in this chapter.

In [Chapter 6](#), the field experiments to evaluate the *LoadGage* program are described. Full scale testing of instrumented test pavements was conducted at TTI's Riverside campus.

In [Chapter 7](#), a summary of the recommendations of this study are proposed together with recommendations for the future development of the TexME system.

Three appendices are provided to this study. [Appendix A](#) includes details of the regression equations developed to compute the Stress Intensity Factors (SIF) proposed for use in the crack propagation model. [Appendix B](#) provides details of the granular base testing conducted in this study. It presents test repeatability for both resilient modulus and permanent deformation testing. It also compares the results from the traditional Texas-sized base samples (6 by 8 inches high) against the typically recommended 6 inch by 12 inch high samples. [Appendix C](#) presents an overview of the new structural design system recently developed by the Portland Cement Association (PCA) for thickness design of pavements containing cement stabilized layers.

CHAPTER 2

HMA MODULUS AND PAVEMENT RESPONSE MODEL VALIDATION

2.1 INTRODUCTION

Development of mechanistic–empirical ($M-E$) methods for pavement structural design and analysis have been pursued since the early 1960s. The most recent and significant effort in this area has been the development of the Mechanistic-Empirical Pavement Design Guide (NCHRP 1-37A 2004). The key assumption of these $M-E$ design methods including the MEPDG is that load-induced pavement structural responses (e.g., stress, strain, and deflection) determined by mechanistic analysis can be used to predict the development of pavement distresses such as fatigue cracking and rutting, through empirical distress models (or transfer functions). In terms of the current $M-E$ pavement design procedures, multi-layer elastic analysis is the primary method for defining the pavement response to traffic loading and environmental changes. Within the framework of multi-layer elastic analysis, the two well known material properties required are the elastic modulus and the Poisson’s ratio. While both these material properties are important, previous experience and the available literature have demonstrated that the elastic modulus has a much more significant impact on the $M-E$ analysis and the predicted distresses. Consequently, the Poisson’s ratio is often just assumed while greater attention is paid to the selection/determination of appropriate elastic moduli for pavement layers because of their greater sensitivity/contribution to the predicted results.

In the current MEPDG program, the dynamic modulus ($|E^*|$) is utilized to represent the elastic modulus of the HMA materials. Since the NCHRP Project 1-37A released the MEPDG and its companion software Version 0.7 in June 2004, several concerns about the HMA dynamic modulus have been raised. For example, Brown et al. (2006) noted in the NCHRP Research Results Digest 307 that *“in its present form, the Guide procedure for estimating complex modulus in the HMA layers results in unrealistic values, particularly for thick layers, showing a decrease in predicted modulus with depth in hot weather that is counterintuitive. This quandary results from the loading time/frequency effect overriding the temperature effect.”* By virtue of it being a visco-elastic material, HMA dynamic modulus is both temperature and loading time dependent. Therefore, both the temperature and the loading time must be known in order to select a reasonably appropriate dynamic modulus for the HMA materials. In the MEPDG, the pavement temperature is well modeled by the enhanced integrated climatic model (EICM). Thus, all the issues on HMA modulus are related to the loading time, which has been a topic discussed nationwide in the last several years (Dongré et al. 2005; Al-Qadi et al. 2008). How to select a reasonable loading time (or loading frequency) for a specific pavement structure is still not well established. Additionally, there are two other important aspects that are still missing in the current discussions, as listed below:

- Rest period: As noted previously, HMA response behavior is loading time dependent; consequently it is equally significantly influenced by the rest periods that occur between field traffic loads. The standard $|E^*|$ test protocol does not include the rest period within a given loading time (or frequency). It is apparent that the standard $|E^*|$ without

considering the rest period is an inaccurate characterization of the HMA modulus and associated performance prediction;

- Loading waveforms: Haversine loading waveform is used in the current $|E^*|$ test, but the haversine loading may not always be the best for representing the pavement vertical stress distributions at different depths within the pavement structure. For instance, [McLean \(1974\)](#) proposed to use the square loading waveform for characterizing HMA mixes in 1974.

Therefore, the main objectives of this chapter are to address these three issues (rest period, loading waveform, and loading time) and to recommend an appropriate HMA modulus for pavement structural design and analysis. To achieve these objectives, the methodology used includes the following steps:

1. Discussion of rest period and HMA resilient modulus (M_r);
2. Approach to estimation of M_r ;
3. Characterization of HMA using both square-loading and haversine wave forms for pavement design and analysis;
4. Development of loading time estimation equations; and
5. Field verification of the M_r approach for pavement response calculation.

A discussion of the results is subsequently presented followed by a summary of findings and recommendations to sum up this chapter.

2.2 REST PERIOD AND HMA RESILIENT MODULUS

The HMA modulus/stiffness is required to define the performance of an HMA mixture for a specific pavement structure since it is used to determine the pavement response (stress, strain, and deflection) and subsequently is used to predict pavement distresses due to loading and environmental effects. In pavement structures, HMA stiffness also influences the stresses and deformations of the other component layers (base, subbase, and subgrade), which in turn, influence the performance of the HMA concrete layer. The stiffness characteristic is, for any pavement structural design and performance prediction, a critical parameter.

Due to its visco-elastic nature, the HMA stiffness is dependent on both the time of loading and temperature and is typically represented by the following equation:

$$S_{mix}(t, T) = \frac{\sigma}{\varepsilon} \quad (2-1)$$

where $S_{mix}(t, T)$ is the mixture stiffness at a particular time of loading, t and temperature, T ; and σ and ε are the applied stress and resultant strain, respectively.

This model approach was first presented by [Van der Poel \(1954\)](#). Since then, different approaches have been proposed to measure the HMA stiffness as seen in [Table 2-1](#).

Table 2-1. HMA Stiffness Testing Procedures.

Mode of loading	Form of load application	Stiffness measure	Reference Number
Axial (normal stress): compression	Creep	Compliance, creep modulus	Witczak et al. (2000)
	Dynamic	Complex (dynamic) modulus	
	Repeated load	Resilient modulus	
Axial (normal stress): tension	Creep	Compliance, creep modulus	Chehab et al. (2000)
	Dynamic	Complex (dynamic) modulus	
	Repeated load	Resilient modulus	
Shear (shear stress)	Creep	Compliance, creep modulus	AASHTO T320-03 (2003)
	Dynamic	Complex (dynamic) modulus	
	Repeated load	Resilient modulus	
Diametral (indirect tensile stress)	Creep	Compliance, creep modulus	Kim et al. (2003)
	Dynamic	Complex (dynamic) modulus	
	Repeated load	Resilient modulus	
Flexure	Dynamic	Complex (dynamic) modulus	Deacon (1965)
	Repeated load	Resilient modulus	
Hollow cylinder	Dynamic	Complex (dynamic) modulus	Buttler et al. (2004)

Two of these approaches have significant impact on the pavement structural design and analysis: resilient modulus (M_r) and dynamic modulus ($|E^*|$). The resilient modulus concept was incorporated in the 1993 AASHTO Guide (AASHTO 1993) and the dynamic modulus concept was recently used in the MEPDG. With the release of the MEPDG and the publication of AASHTO TP62-03, *Standard Test Method for Determining the Dynamic Modulus of Hot-Mix Asphalt Concrete Mixtures* (AASHTO TP62-03), it appears that the uniaxial compression dynamic modulus test is becoming the standard test for measuring the HMA stiffness for pavement structural design. However, the concerns raised previously in the introductory section have made the authors re-think whether or not the dynamic modulus is the appropriate parameter to characterize the HMA stiffness for pavement design. These researchers suggest that the resilient modulus instead of the dynamic modulus should be considered for use in pavement structural designs and analyses. This suggestion is based on the following arguments:

- 1) Existence of rest periods: It is well known that traffic loading is not continuously applied to a pavement structure in the field. Instead, there are at least three kinds of rest periods between the loads applied by the vehicles:
 - a. the rest period that occurs between different vehicles traveling at different speeds;
 - b. the rest period that occurs between vehicles traveling at the same speed; and
 - c. the rest period that even occurs between axle groups, such as the tandem drive axle group and the tandem semi-trailer axle group on a single 3S2 truck.

In the literature (Lytton et al. 1993), the rest period ($t_{rest}=86400/N$) between

applications of traffic loads has been simply estimated by the number of seconds in a day (=86400 s) divided by daily traffic ESALs (N). In this way, the rest periods on different volume roads are simply estimated and tabulated, as shown in [Table 2-2](#).

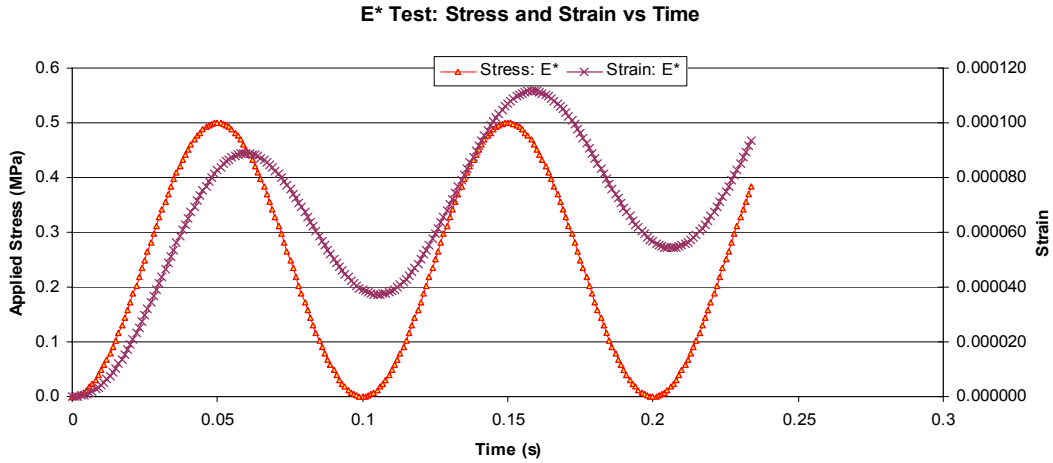
Table 2-2. Simply Estimated Rest Periods.

20-year design ESALs (million)	0.3	3.0	10.0	30.0	100.0
N , daily traffic (ESALs)	41	411	1370	4110	13,699
t_{rest} , rest periods (s)	2102.4	210.2	63.1	21.0	6.3

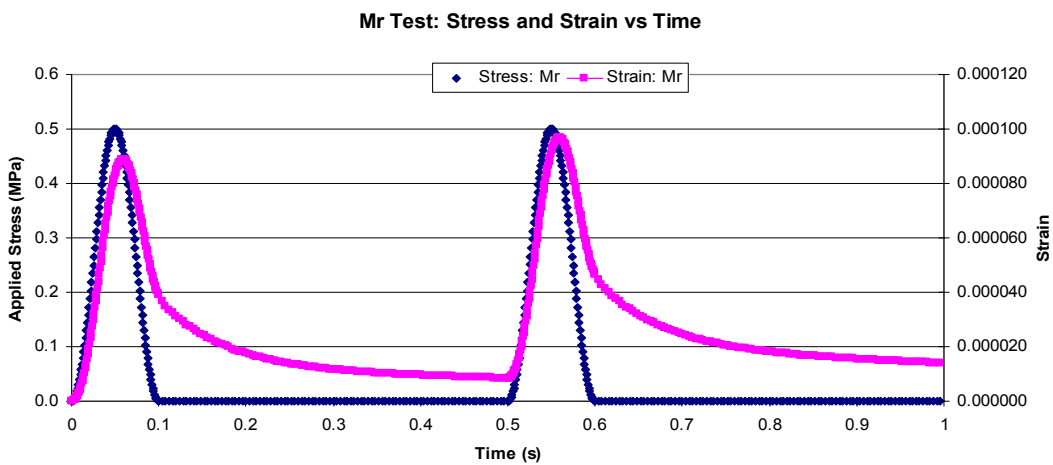
Compared to the loading time of less (or far less) than 0.1 s in the field ([Brown et al. 2006](#); [Barksdale 1971](#); [Huang 1993](#)), the rest periods shown in [Table 2-2](#) should not be neglected. Instead, these rest periods must be taken into account because of the visco-elastic nature of HMA materials. By contrast, the current dynamic modulus test protocol does not account for the rest periods for each specific frequency, which is an under-simulation of field conditions.

- 2) Influence of the rest periods on HMA stiffness: First, one of the major differences between dynamic modulus and resilient modulus tests is the rest period. Within a given loading frequency (i.e., 10 Hz), the load is applied continuously to the specimen under the dynamic modulus test, but a rest period exists between loading cycles in the resilient modulus test. For pure elastic material, the rest period has no effect on the stress-strain relationship (or stiffness/modulus). However, for visco-elastic materials like HMA mixes, this rest period has a significant influence on the HMA stress-strain relationship (or stiffness/modulus characteristics), because visco-elastic materials such as HMA mixes have good “memory” of the loading history. For example, their stress-strain response is loading-time dependent. [Figure 2-1](#) shows the stress loading and strain response histories of a linear visco-elastic HMA mix under two different loading modes. [Figure 2-1a](#) presents the load form of a dynamic modulus test in which there is no rest period; [Figure 2-1b](#) shows that of a resilient modulus test that has the same loading wave but with a 0.4 s rest period. For a more clear comparison, [Figure 2-1c](#) combines [Figures 2-1a](#) and [2-1b](#). It is apparent that the peak strains in the first cycle are completely the same for both dynamic and resilient modulus tests. However, the “peak” strain (= the second peak strain – the previous valley strain) of the dynamic modulus test is smaller than that of the resilient modulus test in the second cycle. A similar phenomenon would be observed in subsequent cycles. Therefore, the dynamic modulus would generally be larger than the resilient modulus, which will be verified by laboratory testing to be shown later.

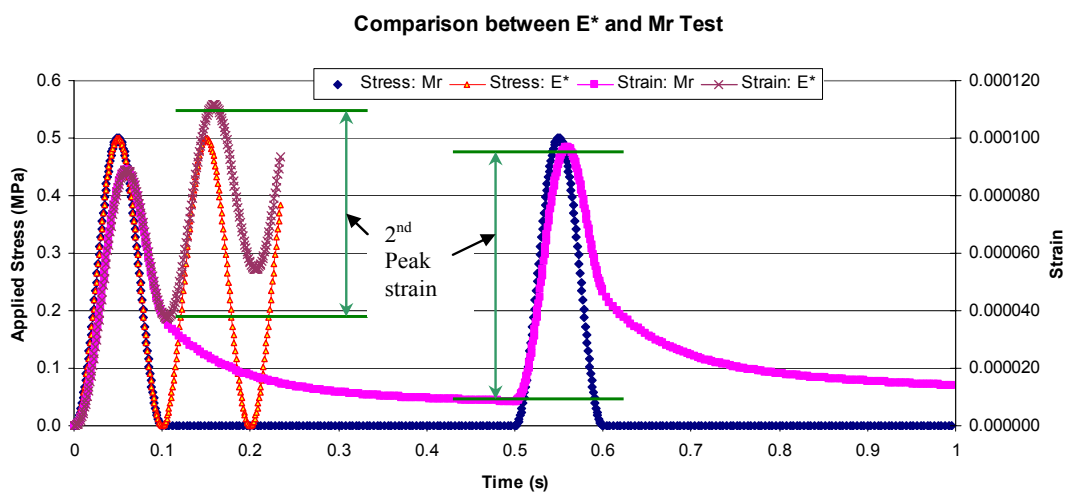
As clearly shown in [Figure 2-1](#), the rest period does have a significant influence on the stress-strain relationships of HMA mixes, which will further affect the prediction of pavement distresses, discussed subsequently in this report. Therefore, the resilient modulus test is preferred in order to better simulate field loading conditions.



(a) E^* Test: Stress and Strain vs. Time (10 Hz)



(b) M_r Test: Stress and Strain vs. Time (0.1 s loading + 0.4 s rest)



(c) Comparison between E^* and M_r Test

Figure 2-1. Difference between E^* and M_r Test.

- 3) M_r and HMA performance models: HMA stiffness is also closely related to pavement performance models. Equation 2-2 shows the calibrated HMA permanent deformation model used in the MEPDG (NCHRP 1-37A 2004). It seems that HMA stiffness is not included in this equation. However, the resilient strain (ε_r) in Equation 2-2 is directly related to resilient modulus M_r ($\varepsilon_r = \frac{\sigma}{M_r}$). Apparently, compared to $|E^*|$, M_r is the better choice for the HMA permanent deformation model.

$$\frac{\varepsilon_p}{\varepsilon_r} = k_1 \times 10^{-3.15552} T^{1.734} N^{0.39937} \quad (2-2)$$

where ε_p is the accumulated permanent strain; ε_r is the resilient strain; k_1 is a field calibration factor; N is the number of load repetitions; and T is the mix temperature (°F).

Another important distress model in the MEPDG is the calibrated fatigue cracking model presented in Equation 2-3. In this equation, dynamic modulus is one of the input parameters. It is apparent that the dynamic modulus is the best choice. However, it is well known that the most critical variable in the fatigue cracking model is tensile strain (ε_t). As noted previously, dynamic modulus (without rest period) often overestimates the “true” modulus of the HMA material. Accordingly, the tensile strain estimated based on the dynamic modulus will be smaller than the actual tensile strain. Hence the underestimated tensile strain will over-predict fatigue life of an asphalt pavement. Furthermore, if the fatigue endurance limit concept is used to design a perpetual pavement (Brown et al. 2006), this underestimated tensile strain caused by using dynamic modulus may make the designed pavement non-perpetual.

$$N_f = 0.00432 * k_1 * 10^{\left[4.84 \left(\frac{V_b}{V_b + V_a} - 0.69\right)\right]} \left(\frac{1}{\varepsilon_t}\right)^{3.9492} \left(\frac{1}{|E^*|}\right)^{1.281} \quad (2-3)$$

where N_f is the number of cycles to failure; k_1 is a calibration factor; ε_t is the tensile strain; $|E^*|$ is the dynamic modulus; V_b is the effective asphalt content, volume percent; and V_a is the air void content, volume percent.

In summary, there are rest periods between load applications among vehicles traveling at different speeds, same speed, and even a single vehicle traveling at a given speed. These rest periods do significantly influence the HMA stiffness and the subsequent stress-strain responses. In order to better represent field traffic loading conditions, the resilient modulus (M_r), with a simulation of the rest period regimes instead of the dynamic modulus is suggested. Furthermore, the HMA permanent deformation model in the MEPDG utilizes the resilient modulus (M_r) to estimate resilient strain. Additionally, if dynamic modulus is used, the tensile strain at the bottom of an asphalt bound layer will be underestimated, because the dynamic modulus itself is over-estimated compared to the “true” stiffness of the HMA material. Consequently, the fatigue life of an asphalt pavement may be overestimated. Therefore, it is suggested that the resilient modulus instead of dynamic modulus be utilized for HMA pavement structural design and analysis. With this suggestion, the next section discusses how to determine HMA M_r values for pavement structural design and analysis.

2.3 PROPOSED M_r ESTIMATION APPROACH

In general, there are two ways to determine HMA resilient modulus: either by using a laboratory testing approach or by using an alternative estimation approach from a known HMA property such as the dynamic modulus. Detailed discussion on these two approaches is presented below.

2.3.1 Laboratory Testing Approach for M_r

HMA M_r laboratory testing has been conducted for a long time. The existing test procedures for HMA M_r are listed as follows:

- ASTM D 4123-82: *Standard Test Method for Indirect Tension Test for Resilient Modulus of Bituminous Mixtures* (ASTM D 4132-82 1982);
- AASHTO TP31-94: *Standard Test Method for Determination of the Resilient Modulus of Bituminous Mixtures by Indirect Tension* (AASHTO TP31-94 1994);
- NCHRP 1-28 (October 1996): *Proposed Test Protocol for Determination of the Resilient Modulus of Bituminous Mixtures by Indirect Tension* (Barksdale 1996); and
- NCHRP 1-28A (May 2003): *Recommended Standard Test Method for Determination of the Resilient Modulus of Bituminous Mixtures by Indirect Tension* (Witzack 2003).

The common feature of these test procedures is to use the indirect tension test, which is often conducted at 3 temperatures (41 °F/5 °C, 77 °F/25 °C, and 104 °F/40 °C) with 0.1 s loading and 0.9 s rest period. This indirect tension-based M_r test, compared to dynamic modulus test (AASHTO TP62-03 2003), has one major limitation: there is insufficient test data to develop an M_r master curve for the tested specimen, even if M_r can be accurately measured by the indirect tension test. This limitation makes it difficult to employ current indirect tension test procedures as a standard M_r test for the MEPDG, which requires a master curve of the HMA stiffness. Therefore, a new M_r test protocol that allows development of the M_r master curve is needed.

As noted previously, the main difference between M_r and $|E^*|$ tests is the rest period. Therefore, the simplest way to determine resilient modulus is to slightly modify the current dynamic modulus test by including the rest period between loading waves within a given frequency. Then, the next question becomes what is the appropriate rest period for a given loading frequency?

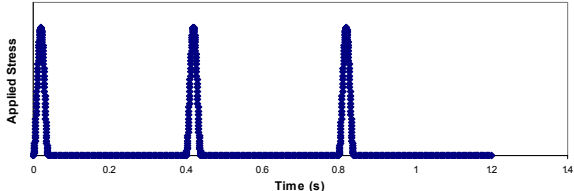
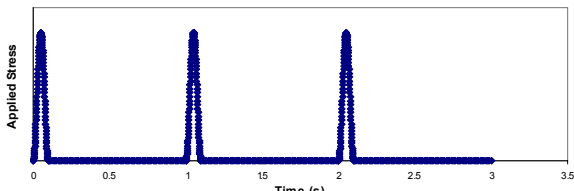
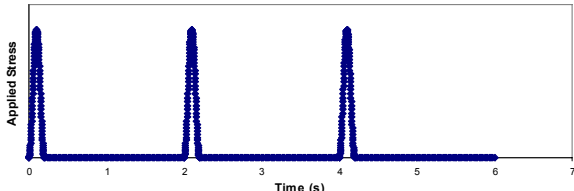
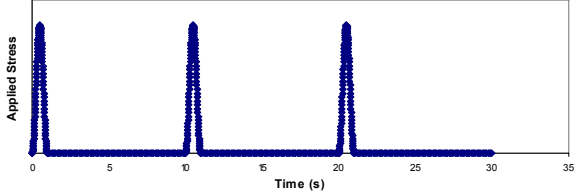
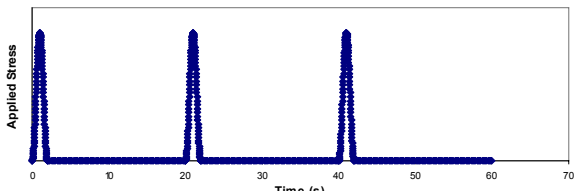
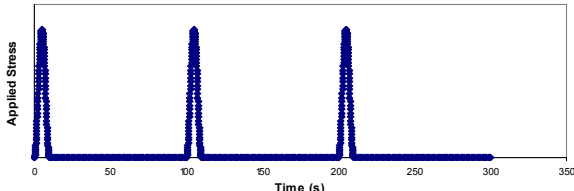
First, the calculated average rest period in the field shown in Table 2-2 is far larger than the loading pulse time, as discussed previously. Therefore, the ratio of rest period to loading pulse time should be as large as possible. Second, Monismith (1989) indicated that the beneficial effect of a longer rest period is not noticeable once the ratio of the rest period to loading time exceeds 8. Additionally, the most recent work done by Barksdale under NCHRP 1-28 (Barksdale 1996) showed that “*there was little effect on resilient modulus when the ratio of rest period to loading pulse increased from 4 to 24.*” Therefore, with consideration of past work and the most commonly used loading waveform, 0.1 s loading and 0.9 s rest period, the ratio of the rest period to the loading time that is finally recommended for the HMA M_r test is 9.

In summary, the proposed test protocol (specimen, test temperature, test machine, instrumentation, preconditioning, number of cycles for each loading frequency, etc.) for resilient modulus is exactly the same as that of the dynamic modulus except to add a rest period between the loading waveforms within a given loading frequency. Note that the ratio of the rest period to the loading time is 9. [Table 2-3](#) presents an example of the proposed haversine loading waveform for HMA M_r testing. With all these laboratory test results, it becomes possible to generate a M_r master curve through the time-temperature superposition principle. The main advantage of the laboratory M_r testing approach is to directly measure the M_r values of HMA specimens. However, it is worth noting that the laboratory M_r testing approach has at least two disadvantages:

1. Long testing time: Since a rest period is added between the loading waveforms within a given loading frequency, the HMA M_r testing is 9 times longer than that of $|E^*|$ testing, which means that if running an $|E^*|$ test (at 6 frequencies) at a given temperature takes 20 min., it will take more than 3 hours to finish the M_r test. Such a long testing time makes the M_r test impractical.
2. Loading waveform: The M_r loading waveform shown in [Table 2-3](#) is the same haversine loading waveforms as those of $|E^*|$ testing except the rest periods. However, the haversine loading waveforms may not always be the best to represent the stress conditions in HMA pavement. Other loading waveforms such as square loading ([Brown et al. 2006](#)) have been proposed in the literature. [Barksdale \(1996\)](#) clearly showed that the loading waveforms have significant influence on the strain response and consequently on M_r ; the M_r values under square loading are much smaller than those under haversine loading. Therefore, a comprehensive laboratory M_r testing approach becomes time-consuming, tedious, and sometimes difficult (i.e., square loading), because the M_r testing has to be conducted under both haversine and square waveforms of loading.

Noting the above disadvantages of M_r laboratory testing, an alternative M_r estimation approach is proposed and discussed in the following section.

Table 2-3. Proposed Loading Waveform for HMA M_r Test.

Loading time	Rest period	Loading wave form
$0.04s$ $(= \frac{1}{25Hz})$	0.36s	
$0.1s$ $(= \frac{1}{10Hz})$	0.9s	
$0.2s$ $(= \frac{1}{5Hz})$	1.8s	
$1.0s$ $(= \frac{1}{1Hz})$	9.0s	
$2.0s$ $(= \frac{1}{0.5Hz})$	18s	
$10.0s$ $(= \frac{1}{0.1Hz})$	90s	

2.3.2 Alternative M_r Estimation Approach

The alternative M_r estimation approach is established based on the assumption that HMA mixes under small strain conditions are linear visco-elastic materials. With this assumption, the conversion between linear visco-elastic material functions (dynamic modulus and phase angle, creep compliance, and relaxation modulus, etc.) has a basis in the theory of linear differential and integral equations that can be applied to HMA mixes. For example, HMA creep compliance and/or relaxation modulus can be mathematically determined, if the HMA dynamic modulus and phase angle are known over a wide enough range of (reduced) frequency. Furthermore, with the known creep compliance, the HMA stress-strain relationship under any waveform of loading can be predicted and the associated M_r can then be determined. In short, the alternative M_r estimation approach includes the following five steps:

- Step 1: Run dynamic modulus test (AASHTO TP62-07). In addition to the dynamic modulus value ($|E^*|$), the phase angle (θ) at each given frequency and temperature should also be recorded and reported. The total data will be 30 dynamic modulus and 30 phase angle values (i.e., 6 frequencies times 5 temperatures).
- Step 2: Develop $|E^*|$ and E' ($=|E^*|\cos\theta$) master curves with reduced angular frequency ω_r . Note that $\omega_r = 2\pi f = 2\pi/T$, where f is the frequency and T is the time period. The master curve formula is given in Equation 2-4:

$$\log|E^*| \text{ or } E' = \delta + \frac{\alpha}{1 + e^{\beta + \gamma \log \omega_r}} \quad (2-4)$$

where δ , α , β , and γ are material parameters; $\omega_r = \omega \times a_T$ is the reduced angular frequency; and a_T is the shift factor as a function of temperature T (Equation 2-5) in which a , b , and c are regression coefficients.

$$\log a_T = aT^2 + bT + c \quad (2-5)$$

- Step 3: Convert the complex (dynamic) modulus E^* in frequency domain to $D(t)$ in time domain through the storage compliance, $D'(\omega)$, in frequency domain.

The basis of this conversion lies in the following exact relationship for linear visco-elastic materials between complex modulus (E^*) and complex compliance (D^*):

$$E^*(\omega)D^*(\omega) = 1 \quad (2-6)$$

where E^* and D^* are defined below.

$$E^*(\omega) = E'(\omega) + iE''(\omega) \quad (2-7)$$

$$D^*(\omega) = D'(\omega) - iD''(\omega) \quad (2-8)$$

Note that the real and imaginary parts in the above equations are denoted with primes and double primes, respectively. Also, the minus sign is used in Equation 2-8 so that D'' will be positive.

Using Equations 2-6, 2-7, and 2-8, the real part (or storage compliance), D' , can then be derived and expressed through the following equation:

$$D'(\omega) = \frac{E'(\omega)}{[E'(\omega)]^2 + [E''(\omega)]^2} = \frac{E'(\omega)}{|E^*(\omega)|^2} \quad (2-9)$$

It is clear that the storage compliance in the frequency domain can be computed through Equation 2-9, if the dynamic modulus and phase angle are known.

In addition, the creep compliance can also be characterized more easily using the generalized Voigt model (or Kelvin model), which consists of a spring and m Voigt elements connected in series, and given by the following equation:

$$D(t) = D_0 + \sum_{i=1}^m D_i \left(1 - e^{-\frac{t}{\tau_i}} \right) \quad (2-10)$$

where D_0 (the glassy compliance), D_i (retardation strengths), and τ_i (retardation time) are all positive constants. The series expression in Equation 2-10 is often referred to as a Prony series. As demonstrated later, using the Prony series expression can significantly simplify the visco-elastic calculation. Similarly, the storage compliance in the frequency domain (Equation 2-9) can also be represented using the Prony series (Park and Schapery 1999) and is given by

$$D'(\omega) = D_0 + \sum_{i=1}^m \frac{D_i}{\omega^2 \tau_i^2 + 1} \quad (2-11)$$

Up to now, it has become clear that with known dynamic modulus $|E^*|$ and E' master curves, $D'(\omega)$ in a very wide range of (reduced) angular frequency (ω) can be determined through Equation 2-9. Then, the Prony series' constants (D_0 , D_i , and τ_i) can be simultaneously determined through Equation 2-11 using the Levenberg-Marquardt non-linear least squares algorithm (Press et al. 1992), and accordingly, the creep compliance in time-domain (Equation 2-10) is known.

- Step 4: Assume the applied stress with specific loading time, loading waveform (such as square, haversine), and rest period (noting that the ratio of the rest period to the loading time is 9), and then predict the corresponding strain response based on the Boltzmann superposition principle using the following equation.

$$\varepsilon(t) = \int_0^t D(t-\tau) \frac{\partial \sigma}{\partial \tau} d\tau \quad (2-12)$$

If a direct integration of the convolution function represented in Equation 2-12 is performed, the entire history of strains has to be stored. To avoid the need of storing the strain histories, the convolution representation was transformed into a two-step recurrence formula that involves internal variables. Detailed theoretical background can be found in the literature (Simo and Hughes 2000). The formula used in this research for computing strain response is given below:

$$\varepsilon(t) = D_0\sigma(t) + \sum_{i=1}^m D_i h^i(t) \quad (2-13)$$

where $h^i(t)$ is an internal variable for the specific Voigt element, i , at time t , and its definition is given below.

$$h^i(t) = \sigma(t) - e^{-\frac{\Delta t}{\tau_i}} \times \sigma(t - \Delta t) + e^{-\frac{\Delta t}{\tau_i}} \times h^i(t - \Delta t) - e^{-\frac{\Delta t}{2\tau_i}} \times (\sigma(t) - \sigma(t - \Delta t)) \quad (2-14)$$

- Step 5: Determine the corresponding M_r based on the results from Step 4.

Compared to the direct laboratory M_r testing approach, this alternative M_r estimation approach has some advantages. For example, the $|E^*|$ test required by the alternative approach is becoming a standard test (AASHTO TP62-07: *Standard Test Method for Determining Dynamic Modulus of Hot Mix Asphalt*) with a much shorter testing time. More comparison between these two approaches is presented later. For the purpose of verifying the alternative M_r estimation approach, a series of laboratory testing was conducted with results presented in the following section.

2.3.3 Laboratory Verification of the Alternative M_r Estimation Approach

Four HMA mixes including dense-graded and Superpave mixes were used for verification of the alternative M_r estimation approach proposed above. Both M_r and $|E^*|$ tests were conducted and the measured M_r values were compared with the M_r estimated from the $|E^*|$ test results using the alternative approach in this section. Detailed information including materials, laboratory testing and associated results, and data analyses are presented below.

2.3.3.1 HMA Materials and Specimens

Table 2-4 presents the four HMA mixes that were used. Two mix types (Superpave and dense-graded), three asphalt binders (PG64-22, PG70-22, and PG76-22), and three aggregate types (crushed river gravel, limestone, basalt) are covered in these four HMA mixes. Figure 2-2 shows the aggregate gradation for each mix. Note that these four HMA mixes are from different field projects in Texas and subjected to different traffic and environmental conditions.

Table 2-4. Four HMA Mixes Used in This Study.

Label	Mix type	Binder type	Aggregate	Binder content	Air voids	Highway
1/2A	12.5 mm Superpave	70-22	Crushed gravel	6.0%	6.20%	IH 35
1A	25 mm Superpave	76-22	Crushed gravel +Basalt	4.9%	4.90%	IH 35
FC1	Dense-graded Type B	64-22	Limestone	4.5%	5.81%	SH 114
Trap1	19 mm Superpave	76-22	Basalt	5.6 %	4.20%	IH 35

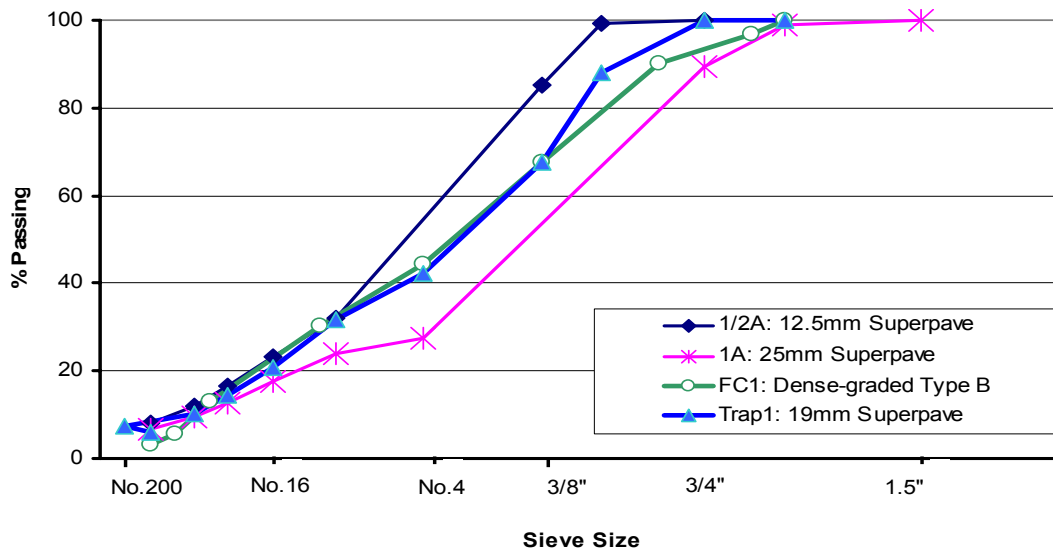


Figure 2-2. Aggregate Gradations of Five HMA Mixes.

For this trial M_r experiment one specimen of each mix was used for laboratory testing, with a total of four specimens, representing four different mixes. It is worth noting that the two specimens labeled FC1 and Trap1 in Table 2-4 are extracted from field cores with two intact lifts of exactly the same mix, and the other two labeled 1/2A and 1A are lab-molded. The test specimens were standard cylindrical-shaped with dimensions of 4-inch diameter by 6 inches in height. Note that Table 2-4 indicates the measured air void contents of these four specimens.

2.3.3.2 M_r and $|E^*|$ Tests

For each specimen and at each test temperature, the M_r test was conducted first and followed by the $|E^*|$ test. The M_r is considered a non-destructive test due to small strain input load and a longer rest period, and so, the same specimens were subjected to the $|E^*|$ test after conducting the M_r test. While the loading configurations were different, the test conditions such as the temperatures and loading frequencies ($=1/\text{loading time}$) were the same for both the M_r and $|E^*|$ tests.

The standard AASHTO TP62-03 test protocol was used for conducting $|E^*|$ test including the loading configuration. Based on this test protocol, the target testing conditions were five test temperatures of 14, 40, 70, 100, and 130 °F (-10, 4.4, 20, 38, and 54.4 °C) and six loading frequencies of 25, 10, 5, 1, 0.5, and 0.1 Hz for each test temperature, respectively. For the M_r test, the test loading configuration was as described in Table 2-3. During both M_r and $|E^*|$ testing, the temperature was monitored and recorded via a thermocouple probe inserted inside a dummy HMA specimen that was also placed in the same environmental temperature chamber as the test specimens. It is worth noting the following three issues encountered during laboratory testing:

- Lowest test temperature: The testing machine could not reach the required lowest testing temperature of 14 °F (-10 °C). The lowest temperature attained was 28 °F (-2.2 °C).
- Highest test temperature: During the M_r testing, some of the glued LVDT studs had dropped off from the specimen at the highest temperature of 130 °F (54.4 °C). This was deemed to have affected the captured test data, so the highest test temperature data were excluded in the analysis, for both the M_r and $|E^*|$.
- Variable testing temperature between specimens: Despite targeting for the set temperatures, the actual testing temperature varied between specimens because of opening and closing the door of the temperature chamber. In order to consider this variable testing temperature between specimens, the actual temperature for each specimen measured by the thermocouple probe was used in the later analyses. So each specimen had its own set of measured test temperatures for subsequent analysis.

2.3.3.3 M_r and $|E^*|$ Test Results and Comparison

The $|E^*|$, phase angle (θ), and M_r for the four HMA specimens are presented in Tables 2-5, 2-6, 2-7, and 2-8, respectively. Additionally, the ratio of the measured $|E^*|$ to M_r is also listed in each table. It is apparent that M_r , as expected, is always smaller than $|E^*|$. In the tables, the shaded numbers in column 7 represent cases where the $|E^*|/M_r$ ratio was significantly larger than unity by at least 17 percent.

Another interesting observation is that the ratio of $|E^*|$ to M_r varies with temperature and frequency, depending on the visco-elastic properties of the HMA mixes. Generally, at low temperatures, the elastic component of strain response may become dominant, and accordingly $|E^*|$ is only about 10 percent larger than M_r . On the other hand, in the case of high testing temperature plus low frequency, in which the strain response may be dominated by the visco-plastic component, $|E^*|$ is again close to M_r . However, in the middle of these two extremes

where the visco-elastic property of the HMA mixes is the main component of strain response, $|E^*|$ is 30 percent (or more) larger than the M_r values; see the shaded numbers in column 7 of each table. The largest ratio of $|E^*|$ to M_r observed in this study was around 2, which will have a significant influence on the pavement response and consequently, performance prediction. With these laboratory test results, it becomes possible to verify the alternative M_r estimation approach, which is presented in the subsequent text.

Table 2-5. Specimen 1/2A: E^* and M_r Test Results.

Temp. °F	Freq. Hz	E^* Test		M_{r-meas} from lab, psi	M_{r-esti} from E^* , psi	Ratios	
		$ E^* $, psi	Phase angle			$ E^* /M_{r-meas}$	M_{r-esti}/M_{r-meas}
34.6	25	2509579	6.41	2335041	2133700	1.07	0.91
34.6	10	2253120	8.47	2110271	1949814	1.07	0.92
34.6	5	2079390	10.76	1898035	1791546	1.10	0.94
34.6	1	1645283	14.00	1512312	1403340	1.09	0.93
34.6	0.5	1471263	15.24	1348587	1253715	1.09	0.93
34.6	0.1	1112772	18.79	937442	924841	1.19	0.99
39.8	25	2115820	7.22	1958122	1904940	1.08	0.97
39.8	10	1860377	9.88	1776997	1680396	1.05	0.95
39.8	5	1657475	12.37	1559978	1506595	1.06	0.97
39.8	1	1314078	16.37	1192000	1135551	1.10	0.95
39.8	0.5	1170972	18.12	1032392	975237	1.13	0.94
39.8	0.1	837446	22.06	691844	696130	1.21	1.01
59	25	1229463	16.41	953243	979713	1.29	1.03
59	10	982293	19.03	774981	782995	1.27	1.01
59	5	833672	22.28	619276	651309	1.35	1.05
59	1	553991	27.58	439688	392354	1.26	0.89
59	0.5	453411	30.58	352463	316332	1.29	0.90
59	0.1	261393	33.35	195805	188245	1.33	0.96
98	25	238171	25.59	117598	135836	2.03	1.16
98	10	148476	27.69	88695	94183	1.67	1.06
98	5	103483	27.48	64359	70774	1.61	1.10
98	1	56604	29.85	44363	38485	1.28	0.87
98	0.5	42525	29.89	36036	29695	1.18	0.82
98	0.1	25980	24.03	23287	18245	1.12	0.78

Table 2-6. Specimen 1A: E^* and M_r Test Results.

Temp. °F	Freq. Hz	E^* Test		M_{r-meas} from lab, psi	M_{r-esti} from E^* , psi	Ratios	
		$ E^* $, psi	Phase angle			$ E^* /M_{r-meas}$	M_{r-esti}/M_{r-meas}
30.2	25	4244267	3.42	3690107	3816832	1.15	1.03
30.2	10	3923948	6.01	3585916	3571728	1.09	1.00
30.2	5	3712192	7.66	3402008	3343909	1.09	0.98
30.2	1	3223657	9.90	2909357	2850632	1.11	0.98
30.2	0.5	2993904	10.59	2695410	2623409	1.11	0.97
30.2	0.1	2468215	12.85	2182281	2137352	1.13	0.98
39.4	25	3520755	5.65	3085605	3275988	1.14	1.06
39.4	10	3193033	8.95	2875756	2990414	1.11	1.04
39.4	5	2924673	10.68	2649199	2776413	1.10	1.05
39.4	1	2431640	13.45	2150336	2196654	1.13	1.02
39.4	0.5	2220900	15.41	1932415	1986348	1.15	1.03
39.4	0.1	1729753	18.05	1442665	1508312	1.20	1.05
59.5	25	2428302	11.93	2004175	2014647	1.21	1.01
59.5	10	2043396	14.16	1742868	1720190	1.17	0.99
59.5	5	1780261	17.91	1479584	1481622	1.20	1.00
59.5	1	1308708	21.35	1085858	1044877	1.21	0.96
59.5	0.5	1124238	23.39	917872	881940	1.22	0.96
59.5	0.1	745138	25.82	595822	606632	1.25	1.02
98	25	603048	21.14	327531	421279	1.84	1.29
98	10	422061	25.07	272514	313217	1.55	1.15
98	5	338026	27.78	211699	255245	1.60	1.21
98	1	206241	26.58	158707	154366	1.30	0.97
98	0.5	161248	27.75	134542	126193	1.20	0.94
98	0.1	106822	24.99	93634	82950	1.14	0.89

Table 2-7. Specimen FC1: E^* and M_r Test Results.

Temp. °F	Freq. Hz	E^* Test		M_{r-meas} from lab, psi	M_{r-esti} from E^* , psi	Ratios	
		$ E^* $, psi	Phase angle			$ E^* /M_{r-meas}$	M_{r-esti}/M_{r-meas}
37.3	25	2867925	2.96	2647375	2654475	1.08	1.00
37.3	10	2684761	6.03	2444665	2472109	1.10	1.01
37.3	5	2511901	6.87	2287386	2318174	1.10	1.01
37.3	1	2181567	9.12	1989060	2018684	1.10	1.01
37.3	0.5	2026415	9.96	1842366	1864574	1.10	1.01
37.3	0.1	1705951	12.39	1513728	1542609	1.13	1.02
41.5	25	2677068	3.86	2481282	2463706	1.08	0.99
41.5	10	2485486	6.83	2285257	2264425	1.09	0.99
41.5	5	2329028	7.99	2136698	2137589	1.09	1.00
41.5	1	1991872	10.09	1828156	1791349	1.09	0.98
41.5	0.5	1864151	11.38	1667923	1627855	1.12	0.98
41.5	0.1	1506096	14.45	1325432	1355884	1.14	1.02
59.8	25	1867489	9.23	1540553	1615999	1.21	1.05
59.8	10	1610305	11.91	1376187	1427128	1.17	1.04
59.8	5	1453556	15.22	1204435	1286749	1.21	1.07
59.8	1	1125544	18.49	924235	925865	1.22	1.00
59.8	0.5	989405	20.75	801865	811814	1.23	1.01
59.8	0.1	707112	24.71	541366	566002	1.31	1.05
98.5	25	518287	22.97	331944	354807	1.56	1.07
98.5	10	366038	25.77	248012	262135	1.48	1.06
98.5	5	288970	29.94	187202	199982	1.54	1.07
98.5	1	161684	32.71	136147	110463	1.19	0.81
98.5	0.5	123512	34.29	107318	83633	1.15	0.78
98.5	0.1	67925	31.28	65720	47108	1.03	0.72

Table 2-8. Specimen Trap1: E^* and M_r Test Results.

Temp. °F	Freq. Hz	E^* Test		M_{r-meas} from lab, psi	M_{r-esti} from E^* , psi	Ratios	
		$ E^* $, psi	Phase angle			$ E^* /M_{r-meas}$	M_{r-esti}/M_{r-meas}
28.3	25	2280116	2.74	2025648	1997938	1.13	0.99
28.3	10	2016255	5.84	1784430	1845298	1.13	1.03
28.3	5	1878374	6.24	1653878	1714180	1.14	1.04
28.3	1	1620029	8.08	1508639	1419062	1.07	0.94
28.3	0.5	1464006	8.59	1398528	1294866	1.05	0.93
28.3	0.1	1242816	9.97	1166302	1040403	1.07	0.89
37.4	25	2036139	3.86	1687989	1829904	1.21	1.08
37.4	10	1803628	6.35	1569948	1652853	1.15	1.05
37.4	5	1661103	7.20	1431309	1522348	1.16	1.06
37.4	1	1386067	9.54	1268801	1226839	1.09	0.97
37.4	0.5	1229608	10.28	1109476	1100958	1.11	0.99
37.4	0.1	1014514	11.22	918290	861052	1.10	0.94
58.5	25	1635269	7.73	1135982	1377268	1.44	1.21
58.5	10	1402758	9.53	1082487	1199373	1.30	1.11
58.5	5	1257184	12.30	964067	1070648	1.30	1.11
58.5	1	971698	15.18	807288	804991	1.20	1.00
58.5	0.5	849492	16.78	709455	699505	1.20	0.99
58.5	0.1	628882	18.23	486690	513040	1.29	1.05
99.0	25	733527	15.26	460410	544704	1.59	1.18
99.0	10	546734	17.11	392344	433024	1.39	1.10
99.0	5	458200	23.58	329845	362683	1.39	1.10
99.0	1	304935	24.72	243649	236067	1.25	0.97
99.0	0.5	241219	25.79	196027	195092	1.23	1.00
99.0	0.1	165893	24.45	137791	129598	1.20	0.94

2.3.3.4 Verification of the Alternative M_r Estimation Approach

Following the five steps of M_r estimation approach proposed previously, the M_r can be estimated from the $|E^*|$ test results. For purposes of demonstration, Specimen 1A is taken as an example to show the detailed five steps of estimating M_r from the $|E^*|$ test:

- Step 1: Run the dynamic modulus test. The $|E^*|$ test results for Specimen 1A were presented previously in Table 2-6.
- Step 2: Develop the $|E^*|$ and E' ($=|E^*|\cos\theta$) master curves.

$|E^*|$ and E' master curves shown in Figure 2-3 were developed using the Levenberg-Marquardt non-linear least squares algorithm (Press et al. 1992), and the 7 parameters: δ , α , β , γ , a , b , and c (Equations 2-4 and 2-5) that were simultaneously determined during generation of the master curves are also listed in Figure 2-3. The associated shift factors are presented in Figure 2-4.

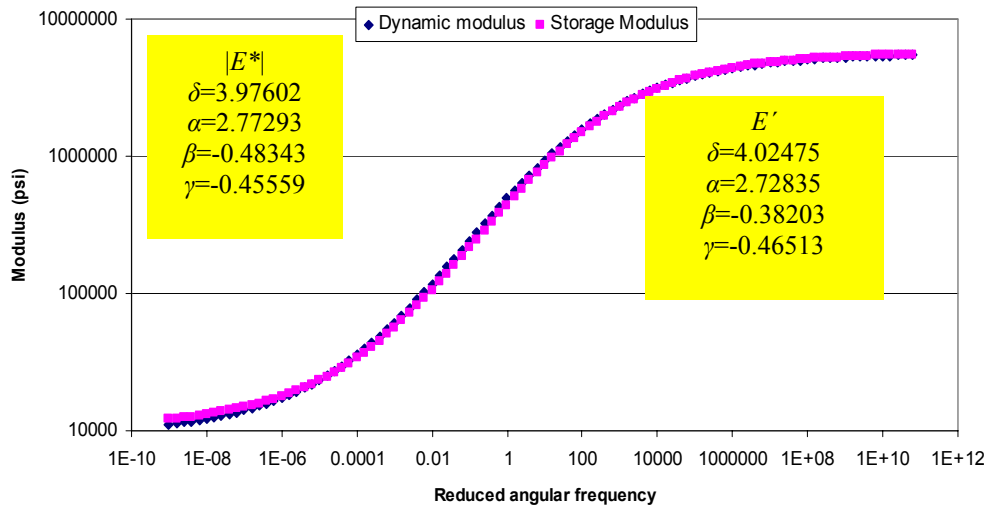


Figure 2-3. Specimen 1A: $|E^*|$ and E' Master Curves.

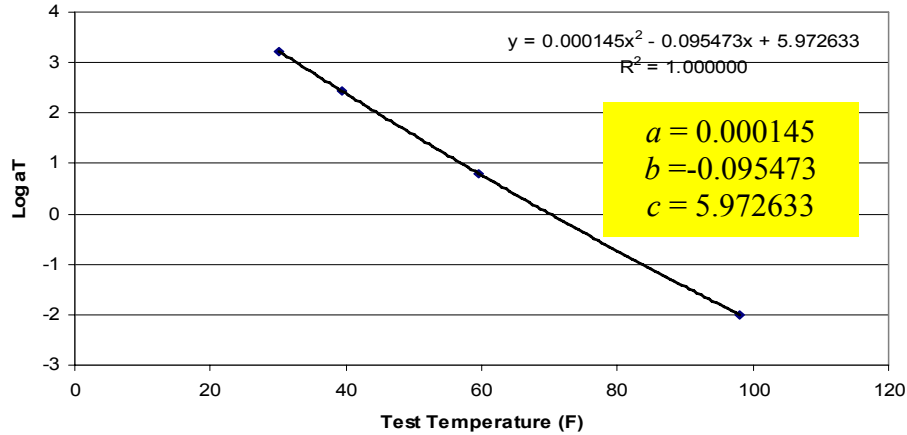


Figure 2-4. Specimen 1A: Shift Factors for $|E^*|$ and E' .

- Step 3: Convert the complex (dynamic) modulus E^* in frequency domain to the creep compliance, $D(t)$.

With known $|E^*|$ and E' master curves, $D'(\omega)$ master curve can be determined, as shown in Figure 2-5. Then, the Levenberg-Marquardt non-linear least squares algorithm (Press et al. 1992) was used again to simultaneously determine the number of terms and Prony series' constants given in Table 2-9, which are the Prony series' constants of creep compliance (Equation 2-15) for Specimen 1A.

$$D(t) = D_0 + \sum_{i=1}^{17} D_i \left(1 - e^{-\frac{t}{\tau_i}} \right) \quad (2-15)$$

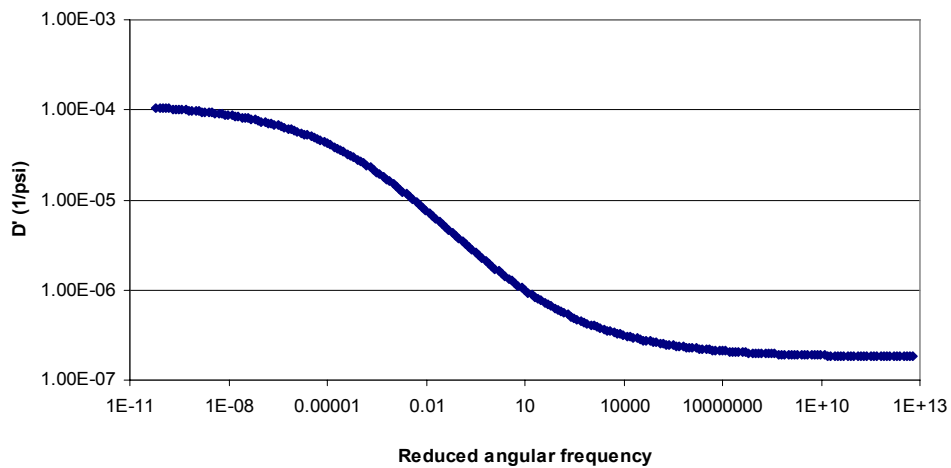


Figure 2-5. Specimen 1A: D' Master Curve.

Table 2-9. Specimen 1A: Prony Series' Constants.

i	D_i (1/psi)	τ_i	i	D_i (1/psi)	τ_i
0	1.78258E-07		9	2.89993E-07	8.75491E-03
1	2.25093E-05	1.27114E+08	10	1.31822E-07	5.23547E-04
2	2.48178E-05	2.27303E+06	11	6.39281E-08	2.89211E-05
3	2.17799E-05	8.75392E+04	12	3.26212E-08	1.49487E-06
4	1.51276E-05	4.95346E+03	13	1.72313E-08	7.29208E-08
5	8.42691E-06	3.41232E+02	14	9.29720E-09	3.34906E-09
6	3.93516E-06	2.54503E+01	15	5.07609E-09	1.41982E-10
7	1.65617E-06	1.89722E+00	16	4.66355E-09	8.24219E-14
8	6.80461E-07	1.34173E-01	17	2.78785E-09	5.29222E-12

- Step 4: Simulate the strain response under specific loading.

The assumed stress waveforms shown in [Table 2-3](#) are applied, and the corresponding strain response can be simulated for each waveform at each temperature following the approach ([Equations 2-13](#), [2-14](#), and [2-15](#)) recommended previously. As an example, [Figure 2-6](#) shows the stress-strain simulation at a reference temperature of 70 °F.

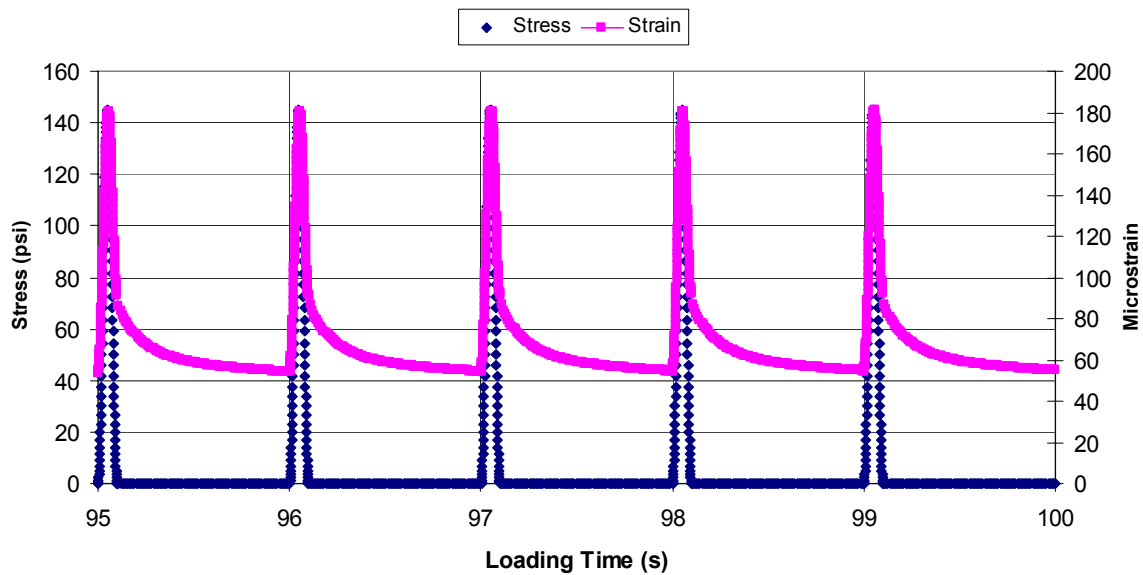


Figure 2-6. Specimen 1A: Stress-Strain Response Simulation (0.1 s loading+0.9 s rest).

- Step 5: Determine the corresponding M_r .

For each loading time, the same number of cycles of applied load as that of E^* test and associated strain response are simulated in Step 4. However, only the last five cycles, similar to $|E^*|$ calculation, were used to calculate the M_r values. The calculated M_r values of Specimen 1A are presented in [Table 2-6](#) as well.

The same steps demonstrated above were used to estimate the M_r values for other specimens and the results for Specimens 1/2A, FC1, and Trap1 are listed in [Tables 2-5, 2-7, and 2-8](#), respectively. Specifically, it is worth noting that for a given loading time T_l and a rest period T_r , the corresponding loading frequency (f) is still equal to $1/T_l$ rather than $1/(T_l+T_r)$. This is so because the influence of the rest period on M_r has been fully taken into account through using resilient strain when computing the M_r value, and consequently, the loading time T_l becomes the key factor for controlling the M_r value when the testing temperature is kept constant. Therefore, the M_r values tabulated in [Tables 2-5, 2-6, 2-7, and 2-8](#) used the same frequency as that of $|E^*|$.

2.3.4 Recommendation on M_r Estimation Approach

Two M_r determination approaches have been demonstrated above (laboratory- and estimation-based); the results from these two approaches and associated comparison for each specimen were presented in [Tables 2-5, 2-6, 2-7, 2-8, and 2-9](#). [Figure 2-7](#) shows the overall comparison between the measured and the estimated M_r . It is clear that the M_r values determined from the alternative approach are almost the same as those measured from the proposed M_r test with a coefficient of correlation of almost one (i.e., $R^2 = 0.99$).

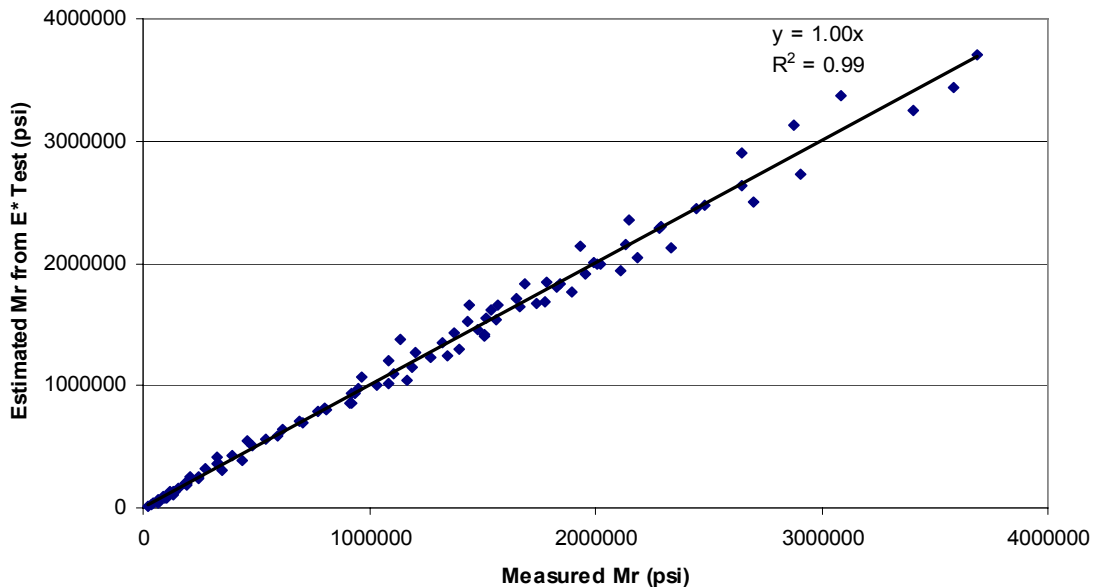


Figure 2-7. Comparison between the Measured and the Estimated M_r .

Compared to the direct laboratory testing approach, the proposed alternative M_r approach is recommended for the following reasons:

1. Accuracy of the results: both approaches provide almost the same M_r values with a coefficient of correlation of almost one (i.e., $R^2 = 0.99$).
2. Test popularity and the required time: the proposed M_r test has not been seen in the literature. In contrast, the $|E^*|$ test required by the alternative approach is becoming the standard test for characterizing HMA stiffness. Furthermore, the proposed M_r test will take 9 times longer compared to the testing time required by the $|E^*|$ test, and this longer testing time makes the M_r test impractical.
3. Flexibility: even if the $|E^*|$ test can not be conducted, M_r can still be estimated by the alternative approach, because $|E^*|$ and phase angle prediction formulas (such as the Witczak equation [Andrei et al.1999] and Hirsch models [Christensen et al. 2003]) are available in the literature.
4. Scope of application: the M_r determined from laboratory testing under a specific load waveform (i.e., haversine) may not be used for other load waveforms such as square loading. Sometimes it is very difficult to apply some types of load waveforms (such as square loading) at high frequency using the hydraulic system. However, the alternative M_r estimation approach is much more flexible than the direct laboratory testing approach, because HMA M_r values under any load waveform, loading time, and rest period, can be estimated with known $|E^*|$ test results. This is further demonstrated in next section of this report.

2.4 NECESSITY OF BOTH SQUARE AND HAVERSINE LOADING WAVEFORMS

Traffic moving over a pavement structure results in a large number of rapidly applied stress pulses to the material comprising each layer. Typically, these stress pulses last for only a short period of time. The type, magnitude, and duration of the pulse vary with the type of vehicle and its speed, the type and geometry of the pavement structure, and the position of the element of material under consideration.

In the literature, both haversine and sinusoidal loading waveforms have been used for characterizing HMA modulus. In the current MEPDG program, the loading waveform is assumed to be haversine. The haversine pulse is assumed to replicate what actually occurs on the pavement in the field. When a truck tire is at a considerable distance away from a point of interest in the pavement, the stress at that point is zero; when the tire is exactly at that point of interest, the stress is maximum. Meanwhile, as noted previously, the square loading waveform has also been proposed by McLean (McLean 1974). Actually, both the square and haversine loading waveforms are needed to better model the asphalt pavement response using a multi-layer linear elastic system.

To further justify the necessity of both the square and haversine loading waveforms, a three-layered HMA pavement structure consisting of an HMA surface layer, base layer, and subgrade was analyzed. Figure 2-8 shows the pavement structure and the associated material

properties. The assumed load is a standard 18 kip single axle (dual-tire) load with a contact pressure of 100 psi. The vertical stress distributions at different depths are shown in Figure 2-9. Note that each specific depth in Figure 2-9 is chosen based on the MEPDG asphalt layer sub-layer system (NCHRP 1-37A 2004). It is apparent that the haversine loading can not be used for all depths. For this case, the square loading has a much better representation of the vertical stress distribution in the top 1.0 inch HMA than the haversine loading. For the rest of the HMA layer, the haversine loading can be used. Similar observation can also be found in other pavement structures. Therefore, it is clear that both square and haversine loading waveforms and associated M_r values are necessary for asphalt pavement response analysis.

As shown previously, the HMA M_r values under the haversine loading waveforms can be accurately estimated using the proposed M_r alternative approach. The only question left is to determine HMA M_r values under a square loading waveform, to be discussed next.

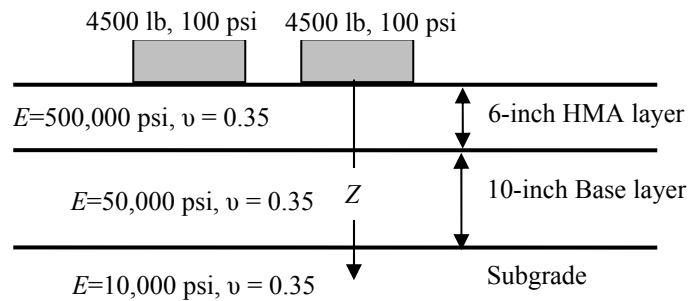


Figure 2-8. A Three-Layer HMA Pavement Structure.

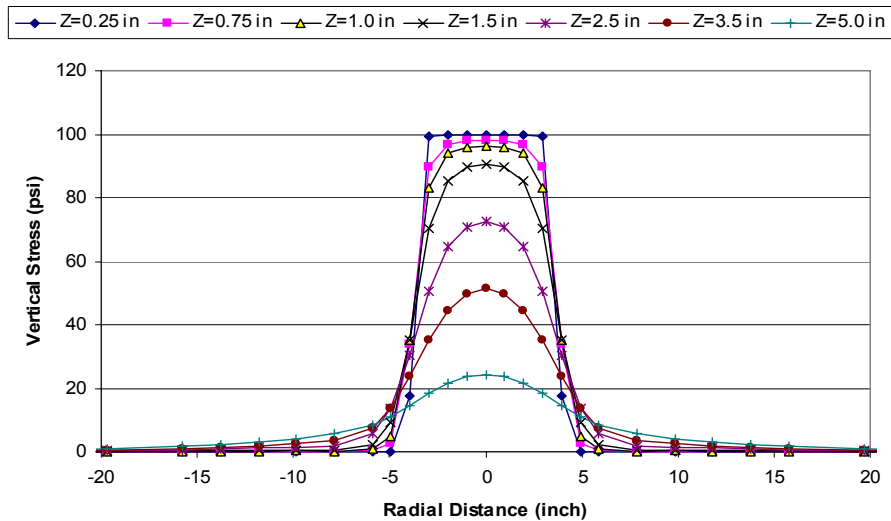


Figure 2-9. Vertical Stress Distributions at Different Depths of HMA Layer.

2.4.1 Estimation of HMA M_r under the Square Loading Waveform

Since the proposed M_r alternative estimation approach is a universal approach, it can be used to estimate HMA M_r values under any type of loading waveform, including the square loading waveform. Following the same five steps used for estimating the M_r values of specimens 1/2A, 1A, FC1, and Trap1 under the haversine loading, the M_r values for these four specimens under square loading were determined by replacing the haversine loading with square loading. The estimated M_r results are presented in [Table 2-10](#).

2.4.2 Comparison between $|E^*|$ and M_r under Square Loading

For the purpose of comparison, [Figure 2-10](#) presents the $|E^*|$ results under haversine loading and M_r results under square loading for Specimen 1A at four testing temperatures. Note that the loading frequency for $|E^*|$ is defined as $1/T$ (T —the period, see [Figure 2-11](#)) and the frequency used for M_r as $1/T_l$ (T_l —loading time, see [Figure 2-11](#)). It is apparent that the $|E^*|$ under haversine loading is much higher than the M_r under square loading at the same frequency and temperature. Similar observation can be seen for other specimens from [Tables 2-5](#), [2-6](#), [2-7](#), [2-8](#), and [2-10](#). Actually, these observations address the concerns raised by [Brown et al. \(2006\)](#) in the introductory section, because for the top HMA sub-layers (i.e., 1 inch), as clearly shown in [Figure 2-9](#), the M_r values under square loading waveform rather than haversine loading should be used as inputs for pavement design (i.e., MEPDG). In this way, “*a decrease in predicted modulus with depth in hot weather* ([Brown et al. 2006](#))” will not happen, because HMA modulus under square loading is much smaller than that under haversine loading.

Table 2-10. Estimated M_r Values under Square Loading.

Freq. Hz	1/2A		1A		FC1		Trap1	
	Temp. °F	M_r -square psi	Temp. °F	M_r -square psi	Temp. °F	M_r -square psi	Temp. °F	M_r -square psi
25	34.6	1647245	30.2	3416958	37.3	2222582	28.3	1759110
10	34.6	1619823	30.2	3103324	37.3	2169992	28.3	1575411
5	34.6	1399477	30.2	2905445	37.3	2016891	28.3	1415881
1	34.6	1095390	30.2	2347598	37.3	1675506	28.3	1161572
0.5	34.6	944338	30.2	2134286	37.3	1533406	28.3	1047128
0.1	34.6	732011	30.2	1814304	37.3	1343570	28.3	866726
25	39.8	1565522	39.4	2848073	41.5	2028303	37.4	1417808
10	39.8	1353139	39.4	2538655	41.5	1921208	37.4	1329451
5	39.8	1149494	39.4	2192402	41.5	1793079	37.4	1274694
1	39.8	837262	39.4	1781927	41.5	1468142	37.4	983039
0.5	39.8	725534	39.4	1562642	41.5	1369895	37.4	885152
0.1	39.8	511958	39.4	1212861	41.5	1102185	37.4	691501
25	59.0	715265	59.5	1585852	59.8	1342646	58.5	977294
10	59.0	551491	59.5	1286589	59.8	1142273	58.5	898600
5	59.0	438821	59.5	1111319	59.8	931508	58.5	851760
1	59.0	257968	59.5	745901	59.8	703444	58.5	606877
0.5	59.0	203824	59.5	624935	59.8	600561	58.5	535278
0.1	59.0	135643	59.5	464003	59.8	422110	58.5	395944
25	98.0	61303	98.0	224912	98.5	171903	99.0	321452
10	98.0	50665	98.0	218195	98.5	141923	99.0	282727
5	98.0	45565	98.0	162726	98.5	118219	99.0	244917
1	98.0	24723	98.0	107659	98.5	66289	99.0	164755
0.5	98.0	20047	98.0	90488	98.5	51218	99.0	138691
0.1	98.0	13203	98.0	62444	98.5	32374	99.0	97395

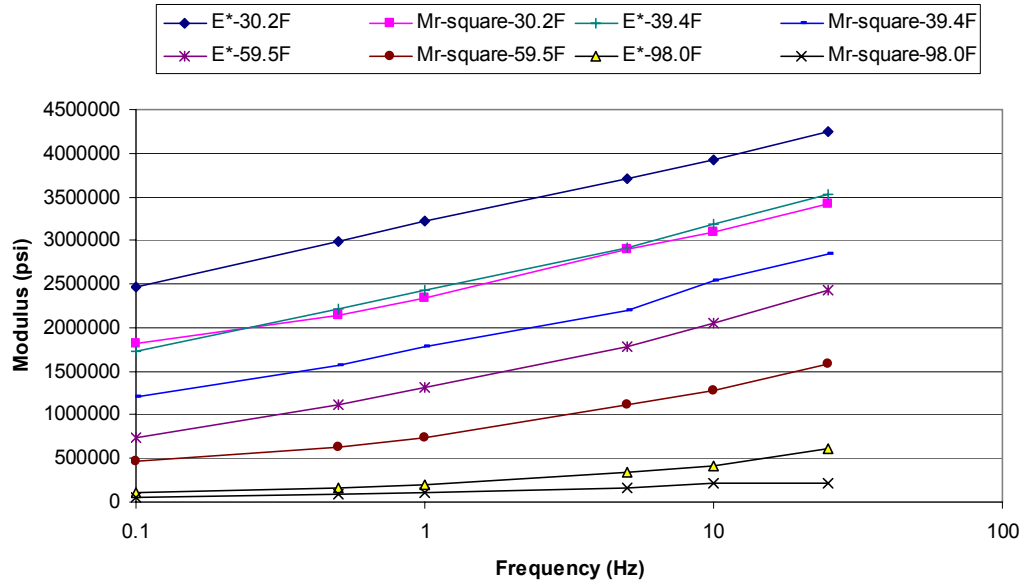


Figure 2-10. Specimen 1A: $|E^*|$ and M_r Results.

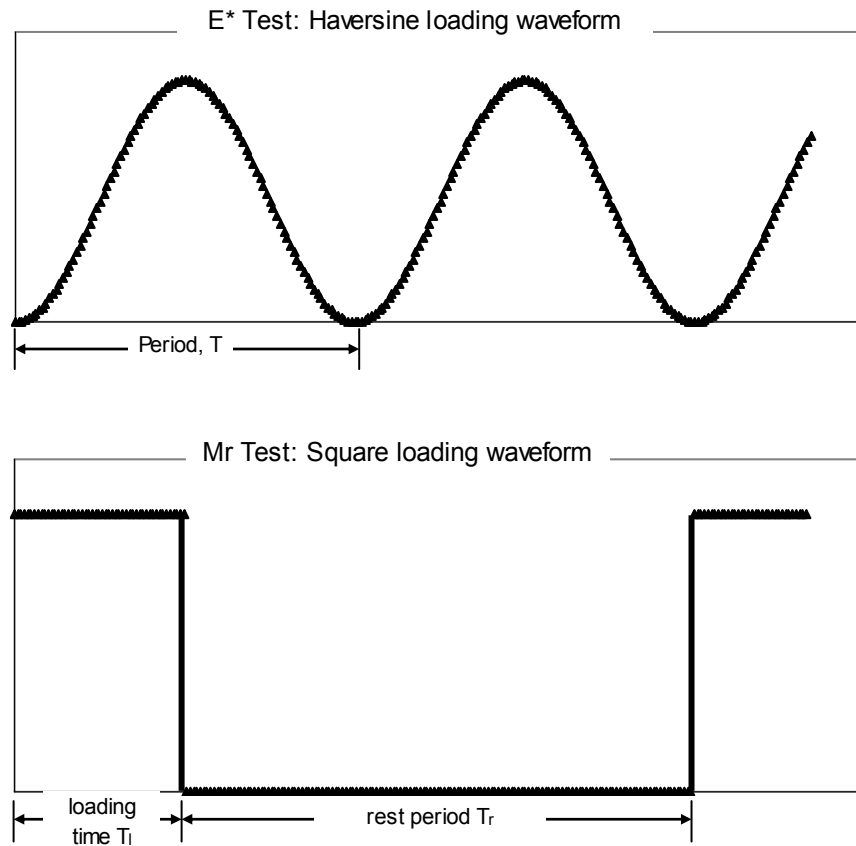


Figure 2-11. $|E^*|$ Haversine Loading and M_r Square Loading.

Another interesting observation is that for each specimen, the curves in Figure 2-10 are almost parallel at each temperature, which indicates that there may be some interchangeable relationship between the $|E^*|$ under haversine loading and the M_r under square loading. Carefully checking the M_r square loading waveform shown in Figure 2-11, it can be seen that if there is no rest period, it is actually a creep test. In the literature, the approximate relationship between dynamic modulus and creep stiffness ($=\varepsilon(t)/\sigma$) has been extensively discussed, and the proposed relationships have been well documented by Rongre et al. (2005). After matching the $|E^*|$ and M_r results tabulated in Tables 2-5, 2-6, 2-7, 2-8, and 2-10, it was found that the following relationship (Equation 2-16) provides the best approximation, which was proposed by Schapery, as noted by Rongre et al. (2005). Figure 2-12 shows the comparison between $|E^*|$ and the shifted M_r based on Equation 2-16 for Specimen 1A. However, it should be noted that this relationship is not applicable to the M_r under haversine loading but only the M_r under square loading.

$$f_{M_r\text{-square}} = \frac{1}{T_L} = 0.1 f_{|E^*|} = \frac{0.1}{T} \quad (2-16)$$

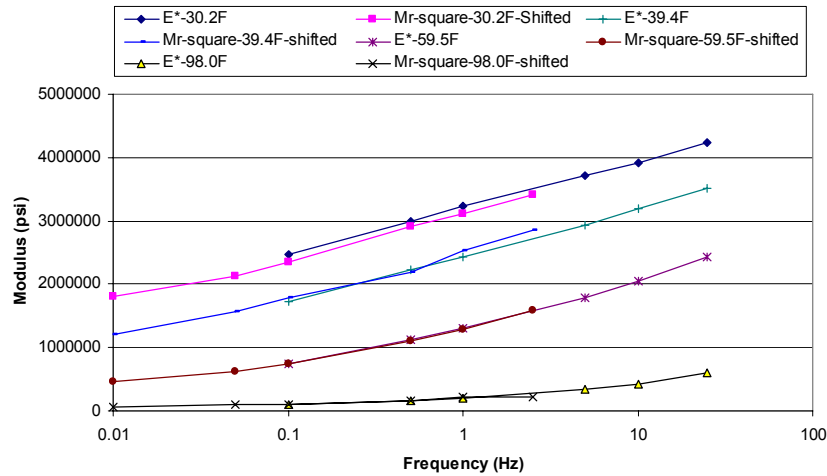


Figure 2-12. Specimen 1A: Comparison between $|E^*|$ under Haversine Loading and Shifted M_r under Square Loading.

In fact, the above finding (Equation 2-16) clearly addresses the concern raised by Rongre et al. (2005). Those approximate relationships widely used in the general field of rheology are validated when comparing the dynamic modulus under haversine or sinusoidal loading with the modulus (or stiffness) under square (or creep) loading.

2.5 PROPOSED LOADING TIME ESTIMATION EQUATIONS FOR SQUARE AND HAVERSINE LOADING WAVEFORMS

The following sections discuss the development of the loading time estimation equations first, following by the validation of the developed equations.

2.5.1 Development of Loading Time Estimation Equations for Square and Haversine Loading Waveforms

The type and duration of loading waveforms used for determining HMA modulus should simulate that actually occurring in the field. As discussed previously, it is reasonable to assume the stress pulse to be a square loading in the pavement surface and a haversine loading at the lower part of HMA layers. In the literature ([Barksdale 1970](#); [Brown 1973](#); [McLean 1974](#); [NCHRP 1-37A 2004](#)), it has been established that the durations of loading pulses depend on the vehicle speed and the depth of the point below the pavement surface. Additionally, based on the testing performed at the Virginia Smart Road project, [Loulizi et al. \(2002\)](#) made several important findings on the loading time issue:

- Either a haversine or a normalized bell-shaped equation represented the measured normalized vertical compressive stress pulse for a moving vehicle reasonably well, although the latter was slightly better.
- Testing time or pavement temperature did not significantly affect the measured normalized vertical compressive stress pulse at any speed between 6 mph and 45 mph.
- Mix types did not significantly affect the measured normalized vertical compressive stress pulse at any speed between 6 mph and 45 mph if the total thickness of asphalt layers remains constant.
- Measured response (vertical stress) waveform can be accurately represented by the linear elastic model, comparing the calculated vertical compressive stress pulse through linear elastic layered theory with the measured data at several depths below the pavement surface under different vehicle speeds.
- The loading times recommended by Barksdale are similar to the ones obtained from the Virginia Smart Road project for 40 mm and 190 mm depths beneath the pavement surface. However, at greater depths, Barksdale's recommendations are almost half those obtained from the Virginia Smart Road project in magnitude.

Based on the above sources, the following characteristics can be inferred about the loading time and the loading waveforms:

- 1) The vehicle speed and depth beneath the pavement surface are thought to be the most important factors influencing the loading time and the loading wave shape.
- 2) Linear elastic layered theory can be used to calculate the vertical compressive stress pulse.
- 3) The asphalt layer modulus variation due to mix type or temperature variations did not significantly affect the loading wave shape and the loading time, respectively.
- 4) The square and haversine (or a normalized bell-shape) loading waveforms should be used as the approximate simulative loading waveforms of the vertical compressive stress pulses.

Although there were numerous significant viewpoints resulting from the literature, at least the following two factual deficiencies, however, exist:

- 1) The modulus ratio (R) of the asphalt layer to the base layer was neglected. R values may vary from less than 1.0, i.e., asphalt layer over cement treated base, to more than 50.0, i.e., asphalt concrete layer with a weak granular base layer. Such wide ratio ranges can result in obvious different loading times, especially at the bottom of the asphalt layer, even if the vehicle speed and the depth beneath the pavement surface are the same, as shown in Figure 2-13.

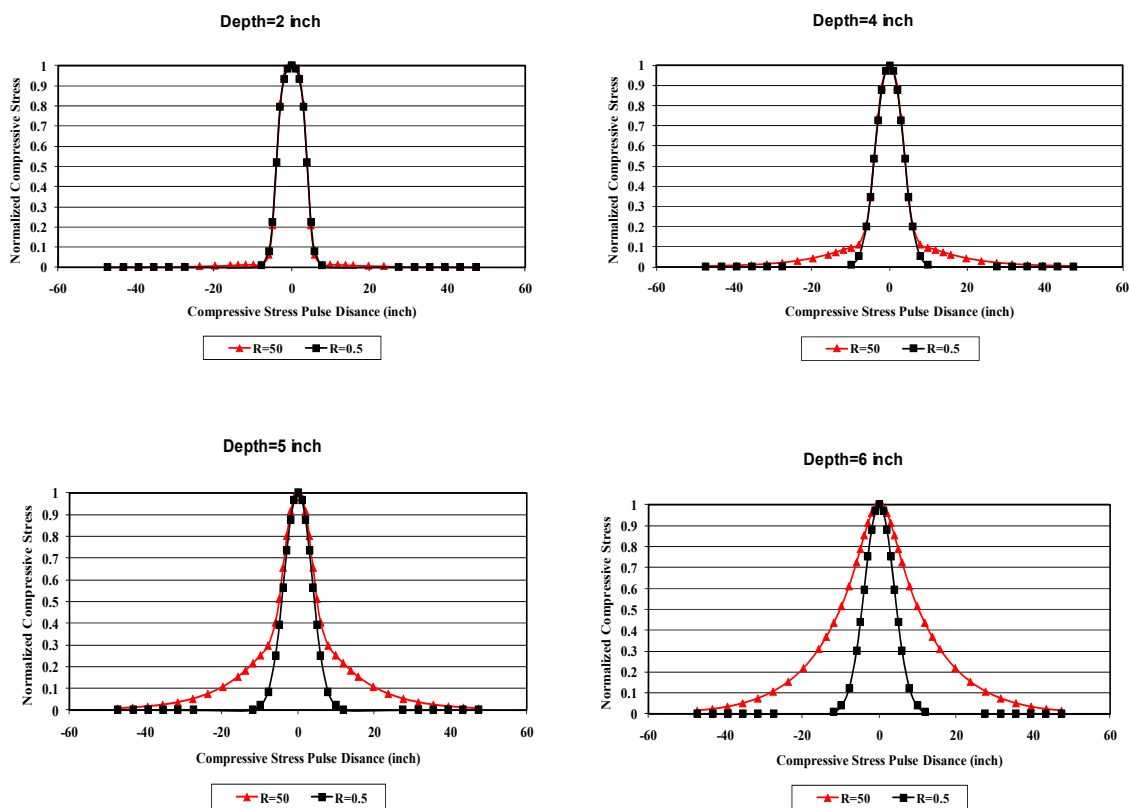


Figure 2-13. Normalized Compressive Stress Pulse at Different Depths beneath the Pavement Surface with Varied Modulus Ratio.

- 2) With increasing depth beneath the pavement surface, the loading waveforms change from square to haversine, as shown in Figure 2-14. In the reviewed literature, this rule of shifting waveforms was not found.

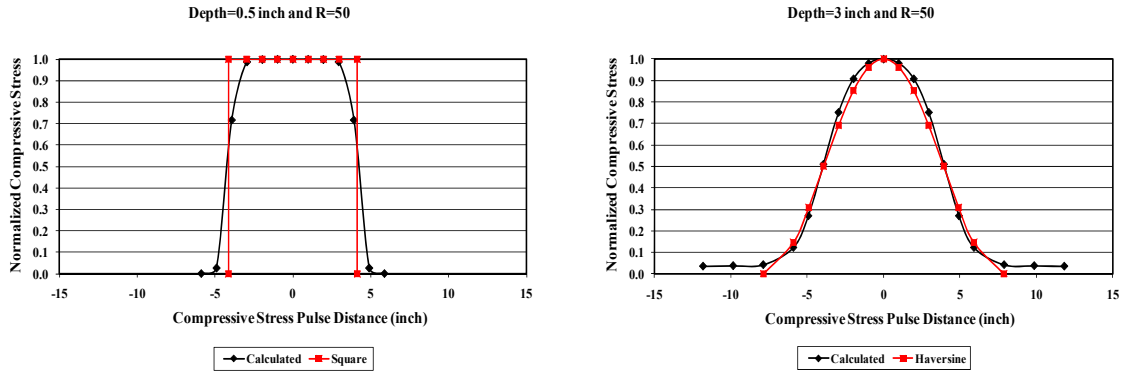


Figure 2-14. Normalized Compressive Stress Pulse at Different Depths beneath the Pavement Surface with a Modulus Ratio of 50.

In order to overcome the two deficiencies listed above, numerous pavement structures with variable R values were analyzed using a multi-layer elastic program. The equivalent single axle load (ESAL) of 18 kips was assumed during the analyses. After carefully reviewing all the pavement response analysis results, new loading time equations and simple rules for changing the loading waveform from square to haversine were developed and are presented below:

- Within top 1-inch of HMA:
 - square loading waveform, and
 - the corresponding loading time is defined as:

$$t = \frac{D}{v} \quad (2-17)$$

where t is loading time; D is the loading tire footprint diameter ($D=7.57$ inch [0.19 m] for the standard ESAL load); and v is the vehicle travel speed.

- Below top 1-inch HMA:
 - haversine loading waveform, and
 - the corresponding loading time is given by:

$$\text{for } 1 < h_i < H_2, t = \frac{(h_i - H_1)D_2 + (H_2 - h_i)D_1}{v(H_2 - H_1)} \quad (2-18)$$

$$\text{for } H_2 < h_i < H, t = \frac{(h_i - H_2)D_3 + (H - h_i)D_2}{v(H - H_2)} \quad (2-19)$$

where t is loading time; v is the vehicle travel speed; H_1 is a constant of 1 inch (see Figure 2-15); H is the total thickness of layers including the computing layer and all above layers (see Figure 2-15); h_i is depth of computing point for the loading time (see Figure 2-16); D_1 is a constant of 0.4; and D_2 , D_3 , and H_2 are defined as follows:

$$H_2 = 0.8553 * H - 0.0082 \quad (2-20)$$

$$D_2 = 1.8189 * H^2 + 0.3507 * H + 0.3929 \quad (2-21)$$

$$D_3 = 0.3304 * (R * H)^{0.5445} + 0.9551^R + 1.6151 * H - 0.8115$$

Note that in cases where the calculated $D_3 < 0.4$, let $D_3 = 0.4$.

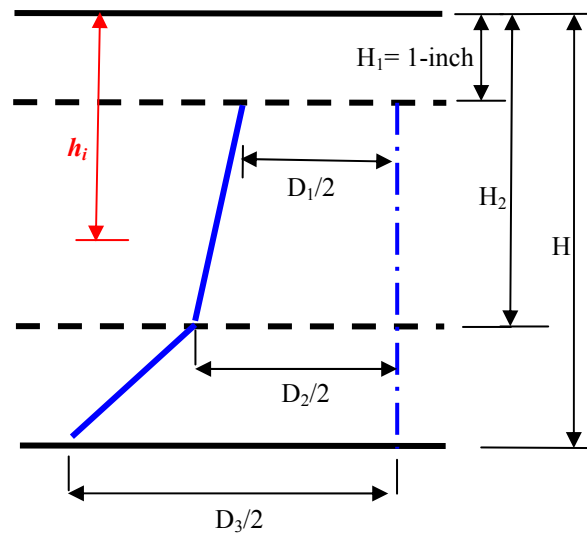


Figure 2-15. Illustration of Loading Time Calculation.

The validation of the developed loading time estimation equations is presented next.

2.5.2 Validation of the Developed Loading Time Estimation Equations

The following validation focused only on the developed loading time estimation equation for the haversine loading waveform, since there is no measured vertical compressive stress data within the top 1-inch of pavement surface available. The data used for the validation in this study were from the Virginia Smart Road project (Al-Qadi et al. 2004; Al-Qadi et al. 2005). The basic asphalt pavement structures consisted of a 1.5-inch wearing-surface mix and a 6-inch HMA layer, followed by a 3-inch open-graded drainage layer (OGDL) stabilized with asphalt cement; a 6-inch cement-treated base (CTB) layer; and then, a 7-inch thick unbound aggregate subbase layer was placed above the subgrade. Based on the falling weight deflectometer (FWD) measurements followed by back-calculation analysis, the moduli of the OGDL, the CTB, the unbound aggregate subbase layer, and the subgrade were determined as 282 ksi,

1597 ksi, 45 ksi, and 38 ksi, respectively. The moduli of the wearing-surface mixes and the HMA layer were almost the same: 1400 ksi at a vehicle speed of 45 mph and 750 ksi at a vehicle speed of 15 mph. [Table 2-11](#) presents the measured loading times at different depths within the pavement structure.

Based on the pavement layer thickness and moduli listed above, the loading times at different depths of the pavement structure were estimated using the developed equations; the loading times are presented in [Table 2-11](#) as well. It is apparent that the estimated loading times match reasonably well to the measured values in the field.

Table 2-11. The Measured vs. the Predicted Loading Times at the Virginia Smart Road.

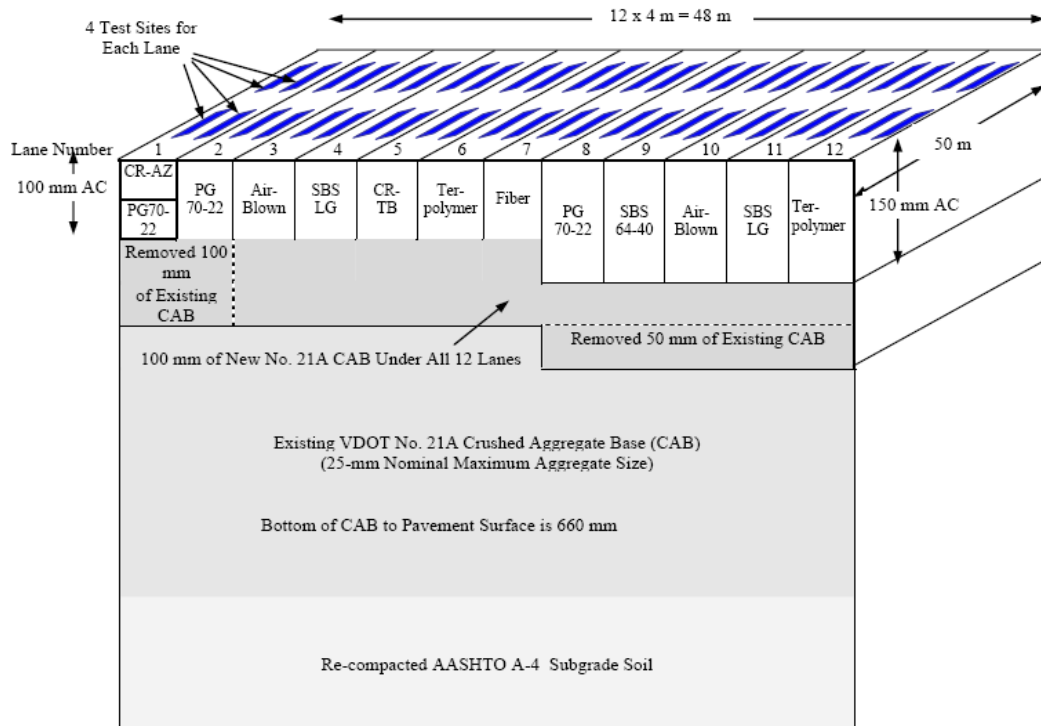
Truck speed	Depth (mm)	R value	Measured loading time from Smart Road	Loading time predicted from this study
45 mph	40	1	0.019	0.015
	190	2.66	0.031	0.036
	267	0.17	0.054	0.046
	419	36	0.113	0.121
	597	1.18	0.142	0.144
15 mph	40	1	0.06	0.046
	190	2.66	0.09	0.119
	267	0.17	0.14	0.120
	419	36	0.33	0.335
	597	1.18	0.42	0.402

2.6 VERIFICATION OF THE M_r APPROACH FOR PAVEMENT RESPONSE CALCULATION BASED ON FHWA-ALF FIELD DATA

After the developments presented above, this section focuses on the validation of the linear elastic pavement response model. The tensile stress data used here were measured at FHWA-ALF field sections, and detailed information is presented below.

2.6.1 Background of FHWA-ALF Response Measurement

Twelve full-scale pavement lanes with various modified asphalts were constructed at the FHWA-ALF test site in McLean, Virginia, in the summer of 2002 ([Qi et al. 2004](#)). The layout of the 12 as-built pavement lanes and associated pavement structure are presented in [Figure 2-16](#). Lanes 1 through 7 were constructed with a 4-inch thick layer of HMA in two lifts, while lanes 8 through 12 were constructed with 6 inch of HMA in two lifts as well. The asphalt binders used are also listed in [Figure 2-16](#).



- PG 70-22 = Unmodified Asphalt Binder Control
- CR-AZ = Crumb Rubber Asphalt Binder, Arizona DOT Wet Process
- CR-TB = Crumb Rubber Asphalt Binder, Terminal Blend
- Terpolymer = Ethylene Terpolymer Modified Asphalt Binder
- SBS LG = Styrene-Butadiene-Styrene Modified Asphalt Binder with Linear Grafting
- SBS 64-40 = Styrene-Butadiene-Styrene Modified Asphalt Binder Graded PG 64-40
- Air-Blown = Air-Blown Asphalt Binder
- Fiber = Unmodified PG 70-22 Asphalt Binder with 0.2 Percent Polyester Fiber by Mass of the Aggregate.

Figure 2-16. Layout of the 12 As-Built Pavement Lanes (Qi et al. 2004).

In order to evaluate the critical tensile strain response, five strain gauges (three in longitudinal direction and two in transverse direction) were installed at the bottom of the HMA layer in each of the 12 sections during the pavement construction. The strain responses were measured in all 12 test sections under various ALF loadings in early 2003. Detailed measured data for each lane are listed in Table 2-12. A 100 psi tire pressure and 14 kip super-single wheel load were used for all measurements. For this verification, only the longitudinal strain responses from 4-inch HMA thick sections measured at a testing temperature of 66.2 °F (19 °C) under a speed of 11.2 mph (18 km/h) were used. The measured maximum longitudinal tensile strains in Lanes 2, 3, 4, 5, and 6 are all presented in Table 2-12 as well. Note that Lanes 1 and 7 were excluded from this analysis, because dynamic modulus test results (Al-Khateeb et al. 2006) were not available for these two lane HMA materials.

Additionally, FWD tests were conducted before the strain response measurements. Since granular base and subgrade soil are not so sensitive to loading time and temperature as HMA mixes, the backcalculated moduli from the FWD data for granular base and subgrade soil (Zhou et al. 2007), as presented in Table 2-12, were directly used without adjustment to calculate the tensile strains at the bottom of HMA layer.

Table 2-12. Measured and Predicted Maximum Strain.

Lanes	Testing date	Layer modulus Psi		Measured maximum longitudinal tensile strain (microstrain)				Predicted (microstrain)	
		Base	Subgrade	TG1	TG3	TG5	Average	M_r approach	MEPDG approach
2	3/31/2003	8999	6967	414	409	367	397	389	345
3	4/11/2003	7402	5370	473	523	429	475	450	396
4	4/21/2003	8128	5951	689	-	559	624	604	519
5	3/28/2003	6386	4935	890	-	773	832	876	752
6	4/21/2003	6676	5660	-	-	806	806	763	645

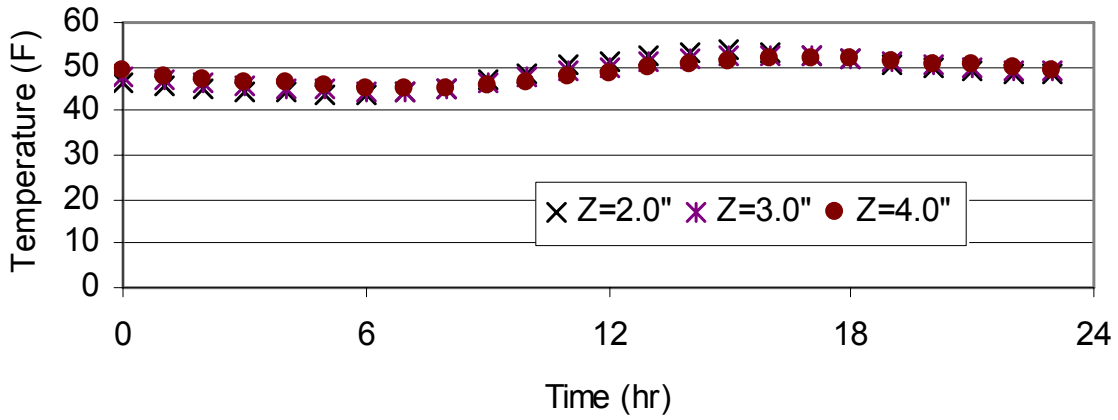
Note: - no data was measured, because of strain gauge damage.

2.6.2 Verification of the Proposed M_r Approach

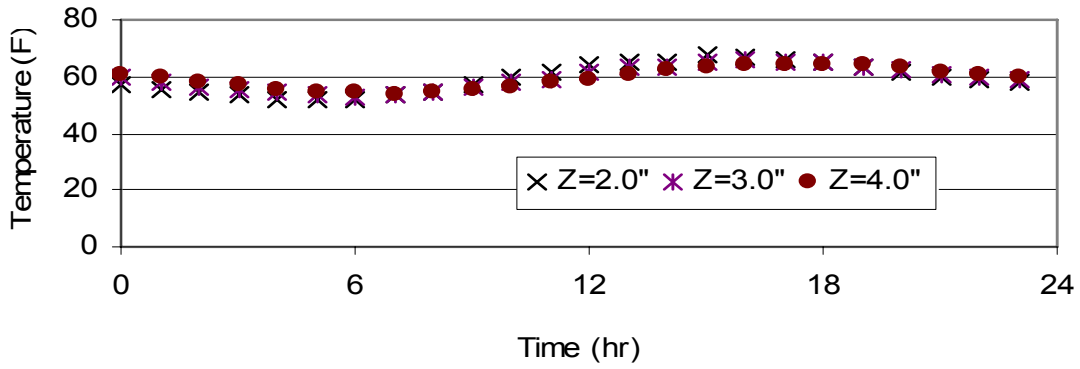
As presented above, the moduli for the base layer and subgrade were determined via FWD testing. If the HMA layer modulus is known, the strain response can then be calculated by a multi-layer elastic program. In order to determine the HMA layer modulus, it is necessary to know the pavement temperature and loading frequency in advance.

The testing temperature of 66.2 °F (19 °C) for strain measurements was the temperature at a depth of 20 mm from the pavement surface rather than the whole HMA layer. This temperature was controlled by radiant heaters. Since the testing time for the strain response measurements was very short, and considering that these tests were conducted at cold temperatures, it is reasonable to believe that the bottom 2-inch HMA lift had a different temperature from the top 2-inch HMA layer. To determine the representative temperatures for these two HMA lifts, it was assumed that the heat generated from the radiant heater of the ALF machine only transferred to the top 2 inches, and the temperature of bottom 2-inch HMA was not affected by the radiant heater. Accordingly, the target test temperature of 66.2 °F (19 °C) was used as the representative temperature for the top 2-inch HMA lift in this study; the pavement temperature of the bottom 2-inch HMA lift can be predicted by the EICM (NCHRP 1-37A 2004). The pavement temperatures of each lane at different depths for each specific testing date are shown in Figure 2-17. It is apparent that the temperatures at the depths of 2, 3, and 4 inches are very close. Therefore, the pavement temperature at the depth of 3 inches was chosen as the representative temperature for each test lane. Since the strain responses, except Lane 6, were measured in the late morning of each specific date, the pavement temperature at 11:00 a.m. was used for each lane for the strain analyses. Note that Lane 6 was tested on the same day as Lane 4, but the testing time was mid afternoon, so that the pavement temperature at 3:00 p.m. was selected for analysis. The final pavement temperatures used are given in Table 2-13. Additionally, Table 2-13 also presents the measured HMA $|E^*|$ (Al-Khateeb et al. 2006) and M_r under both square and haversine loading waveforms for each lane. Note that M_r under both square and haversine loading waveforms were determined using the proposed alternative M_r estimation approach.

Lane 3: Pavement Temperatures on April 11 2003



Lanes 4/6: Pavement Temperatures on April 21 2003



Lane 5: Pavement Temperatures on April 28 2003

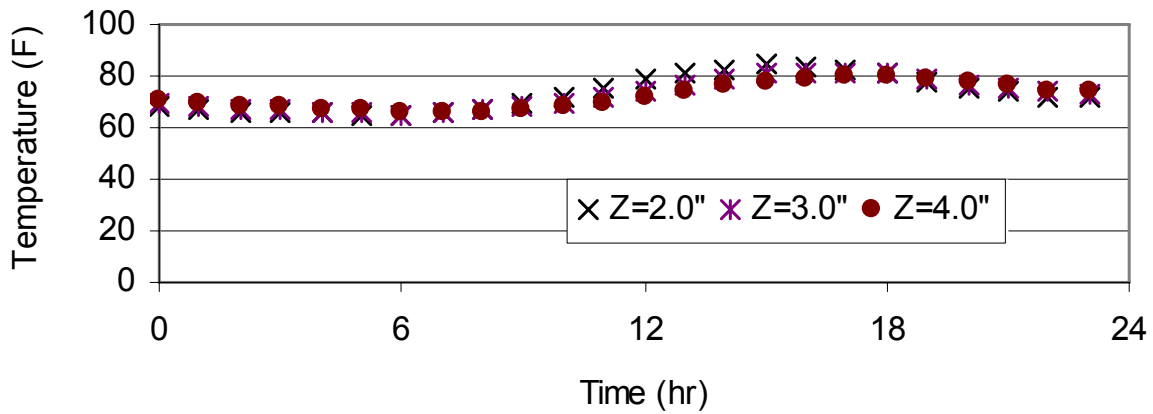


Figure 2-17. Pavement Temperatures Predicted from EICM.

Table 2-13. $|E^*|$ and M_r Values at Different Frequency.

Lanes	Temp.	Modulus	Frequency, Hz					
	°F	psi	20	10	5	1	0.5	0.1
2	66.2	$ E^* $	1146251	947847	813885	507837	408370	225399
		$M_{r-haversine}$	898164	768731	643930	390696	303234	155619
		$M_{r-square}$	644386	529509	425427	235189	176357	85737
	46.0	$ E^* $	1596206	1499308	1392597	1112951	983533	684146
		$M_{r-haversine}$	1457728	1347473	1228809	932062	802026	520364
		$M_{r-square}$	1220254	1096649	969189	675622	558392	329009
3	66.2	$ E^* $	1029366	880745	742767	486502	403967	248041
		$M_{r-haversine}$	834115	711359	599880	386473	313879	185859
		$M_{r-square}$	606716	507481	419793	259154	206961	118525
	49.0	$ E^* $	1600784	1439128	1281913	943179	812107	549739
		$M_{r-haversine}$	1383747	1228021	1079038	767268	650449	424248
		$M_{r-square}$	1081051	942045	812362	552342	459271	286836
4	66.2	$ E^* $	826899	691679	578133	360039	288824	159076
		$M_{r-haversine}$	657302	556181	461605	277875	216672	115090
		$M_{r-square}$	466098	379602	303251	168330	127615	65165
	59.0	$ E^* $	980126	873901	766471	526793	433954	256574
		$M_{r-haversine}$	834843	728417	624262	405249	325743	183098
		$M_{r-square}$	629549	529831	437296	259930	201696	106247
5	66.2	$ E^* $	757668	644630	548718	364248	304765	185390
		$M_{r-haversine}$	642850	545367	457475	291582	236088	139775
		$M_{r-square}$	445484	370315	304661	186682	149111	86417
	72	$ E^* $	649201	551588	463443	296589	240584	143043
		$M_{r-haversine}$	527092	441159	365166	226116	181081	105046
		$M_{r-square}$	356495	292704	238008	142468	112897	64648
6	66.2	$ E^* $	761732	619449	498404	286502	223996	115433
		$M_{r-haversine}$	578771	477584	385184	214373	161007	78302
		$M_{r-square}$	390316	309839	240801	124888	91961	44172
	63.0	$ E^* $	809693	698301	589657	364759	285389	148794
		$M_{r-haversine}$	656834	550906	451833	261114	198883	98898
		$M_{r-square}$	455806	367654	290166	155044	115164	55706

Note: frequency used for M_r is defined by $1/T_l$ (T_l –loading time, see [Figure 2-12](#) and [Table 2-3](#)).

The next step was to determine the reasonable loading waveform and to estimate the loading frequency ($=1/\text{loading time}$). Since the tensile strains presented in [Table 2-12](#) were measured under FHWA-ALF super-single tire loading rather than 18 kip ESAL, the developed loading time estimation equations are not applicable to this special case. Therefore, the FHWA-ALF test sections under super single-tire loading were particularly analyzed. As an example, [Figure 2-18](#) shows the final vertical stress distribution of Lane 2 at different depths of the HMA layer. It can be seen that the vertical stress in the top 3 inches of HMA should be represented by a square load waveform, and the associated wavelength was equal to the diameter of the loading area. Meanwhile, the haversine loading waveform is much better for the bottom 1-inch of HMA.

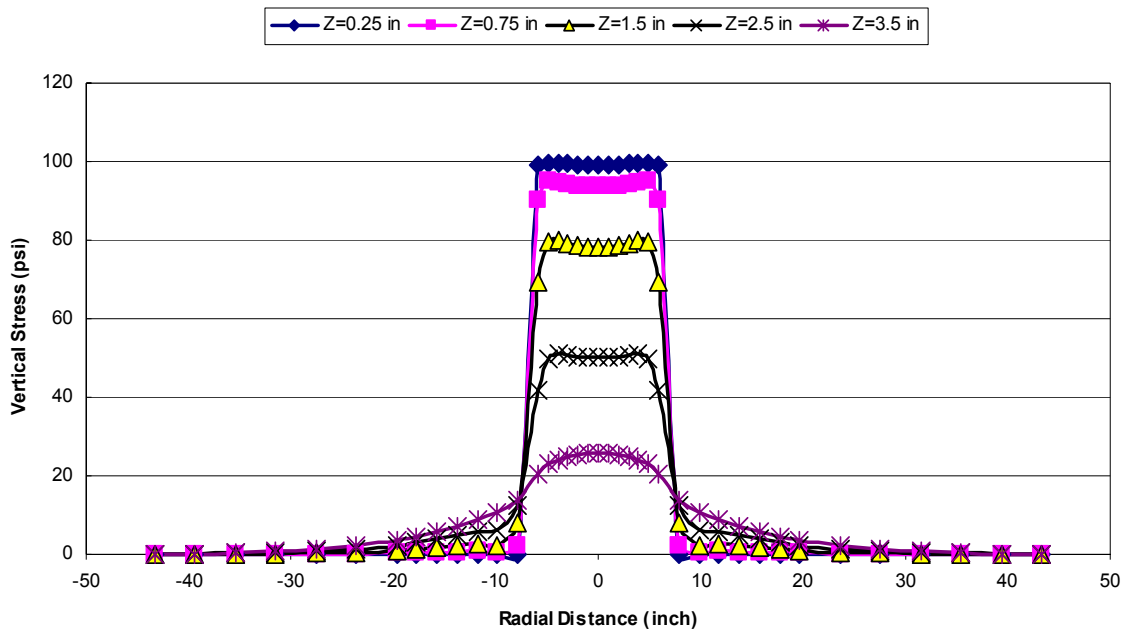


Figure 2-18. Lane 2: Final Vertical Stress Distributions at Different Depths of HMA Layer.

A similar observation is true for other lanes. Note that the applied load for strain response measurements was a super-single wheel load of 14 kips (62 kN), and consequently the chosen loading waveform for the top 3 inches of HMA had to be square loading. The loading frequency determined for each lane at each specific pavement depth is presented in [Table 2-14](#) and was used in the final analysis. The calculated tensile strain at the bottom of the composite HMA layer for each lane is presented in [Table 2-12](#). The calculated tensile strain matches the measured strain very well. Therefore, the M_r approach is well verified. However, further field validation under other loading regimes and speeds is still needed.

Additionally, the HMA dynamic modulus and associated strain responses were also calculated using the MEPDG approach in which the loading frequency was determined based on Odemark's equivalent thickness concept and effective length concept ([NCHRP 1-37A 2004](#)). The determined loading frequency for each lane for each specific pavement depth is presented in [Table 2-14](#) as well. It can be seen that although all the loading frequencies determined by the

MEPDG approach are smaller than the frequencies determined by the M_r approach, the corresponding $|E^*|$ modulus for each sub-layer is still larger than the M_r value, which clearly demonstrates the importance of the M_r approach. As expected, the MEPDG $|E^*|$ approach under-estimated the tensile strains at the bottom of the HMA layer, as was shown in Table 2-12.

Table 2-14. HMA Modulus and Loading Frequency.

Lane	Sublayer: 0-0.5"		Sublayer: 0.5-1"		Sublayer: 1-2"		Sublayer: 2-3"		Sublayer: 3-4"	
	$ E^* $, psi	f , Hz	$ E^* $, psi	f , Hz	$ E^* $, psi	f , Hz	$ E^* $, psi	f , Hz	$ E^* $, psi	f , Hz
2	994194	11.4	920174	8.6	870827	6.4	1378810	4.7	1313498	3.6
3	902758	11.3	849057	8.5	791001	6.2	1248186	4.5	1175617	3.5
4	711176	11.5	667634	8.8	624093	6.6	761974	4.9	718433	3.9
5	664731	11.4	624093	8.7	587808	6.4	457184	4.8	428157	3.9
6	638607	11.5	597968	8.9	551524	6.7	595065	5.0	551524	4.0
	$M_{r-square}$	f , Hz	$M_{r-square}$	f , Hz	$M_{r-square}$	f , Hz	$M_{r-haversine}$	f , Hz	$M_{r-haversine}$	f , Hz
2	571843	13.6	571843	13.6	571843	13.6	1146589	13.6	1217707	4.7
3	544267	13.6	544267	13.6	544267	13.6	998549	13.6	1065312	4.7
4	409289	13.6	409289	13.6	409289	13.6	567489	13.6	616836	4.9
5	400581	13.6	400581	13.6	400581	13.6	316401	13.6	365747	5.0
6	339623	13.6	339623	13.6	339623	13.6	400581	13.6	447025	4.9

2.7 CONCLUSIONS AND RECOMMENDATIONS

Based on the research presented in this chapter, the following conclusions and recommendations are made:

- A rest period is not considered for a given loading frequency in the $|E^*|$ test, and consequently, the HMA modulus is over-estimated using the $|E^*|$ approach. By contrast, the M_r approach fully takes into account the influence of the rest periods, thus better representing the field loading conditions. On this basis, the M_r approach should be considered for pavement design and analysis so as to better simulate the visco-elastic behavior of HMA under non-continuous field loading conditions.
- Two M_r determination approaches were proposed in this chapter. As seen from laboratory testing, the results from both approaches were comparable. However, the alternative M_r estimation approach based on the $|E^*|$ test is preferred on account of

- the reasons given in the report, including the M_r inherent longer test period, the potential for standardization, and popularity of the $|E^*|$ test, etc.
- As shown in the chapter, both square and haversine loading waveforms should be used when modeling HMA behavior for pavement design and analysis in order to better represent the vertical stress distribution along the pavement depth. Furthermore, using the square loading for the top portion of the HMA riding surface can eliminate the controversy surrounding the output from the MEPDG: *a decrease in predicted modulus with depth in hot weather* (Brown et al. 2006).
 - After numerous analyses on a variety of pavement structures with variable layer moduli using a multi-layer elastic program, a simple rule for changing the loading waveform from square to haversine was established, and new loading time estimation equations were developed for square and haversine loading waveforms. Additionally, the accuracy of the developed loading time estimation equation for the haversine loading waveform was validated using the measured loading time data from the Virginia Smart Road test sections.
 - The M_r approach was successfully verified based on the FHWA-ALF field response measurements. After consideration of the temperature gradient in the HMA layers, the calculated tensile strain for each lane was very comparable to the measured values.
 - It is highly recommended that the M_r approach be considered for pavement design and analysis. Meanwhile, further field validation is still needed, specifically the loading waveforms and associated frequency.

CHAPTER 3

DEVELOPMENT, CALIBRATION, AND VALIDATION OF M-E HMA RUTTING MODEL

3.1 INTRODUCTION

Rutting is another potential major distress and concern for HMA pavements for at least two reasons: 1) if the surface is impervious, the ruts trap water, and at depths of about 0.2 inch, hydroplaning (particularly for passenger cars) is a definite threat; and 2) as the ruts progress in depth, steering becomes increasingly difficult, leading to added safety concerns. Therefore, it is important to make efforts to minimize rutting, and at the same time it is necessary to develop a model to predict the potential rutting development when designing an HMA pavement.

Rutting occurs in flexible pavements because of the accumulation of small permanent deformations in any or all of the pavement layers or the subgrade. Such deformations may be caused by too much repeated stress applied to the pavement layers or by an HMA mix that is too low in shear strength. In the first case, the rutting is considered more of a structural or construction problem. It is generally the result of an underdesigned or undercompacted pavement section or of an unbound base or subgrade that has been weakened by the intrusion of moisture. In the second case, the rutting is normally a mixture design or placement-related problem. When an asphalt pavement layer has inadequate shear strength, a small but permanent shear deformation occurs each time a heavy truck applies a load. A perceptible rut will then appear with enough load applications. National rutting survey and trench studies ([Brown and Cross 1992](#); [Harvey and Popescu 2000](#); [Gokhale et al. 2005](#)) clearly indicated that, at least for typical pavement structures with stiff supporting materials, most pavement rutting is confined to the HMA layers. Furthermore, rutting or permanent deformation, in most cases, is limited to the upper 4–6 inches of HMA layers. Also, several field trench studies on Texas highways, including US 281 and US 175, clearly showed that the rutting was coming primarily from the top 2–4 inches of HMA layers, as shown in [Figures 3-1](#) and [3-2](#). Thus, the rutting for thick HMA pavements or pavements with stiff base layers is mainly from HMA layers, which is the focus of this chapter.

Regarding HMA rutting, it is commonly accepted that rutting (permanent deformation) is a manifestation of two different mechanisms, a combination of densification (volume change) and repetitive shear deformation (plastic flow with no volume change). It is difficult to determine the relative amounts of rutting occurring in each HMA layer, and the relative proportions of rut depth that can be attributed to densification and shear, because many factors, such as binder type, binder content, mix type, load level, temperature, initial compacted density, etc., have an influence on rutting. To adequately consider all these influential factors, it is necessary to develop an M-E rutting model. Based on this background, the main objective of this chapter was to develop an M-E rutting model for HMA pavement design and analysis.



Figure 3-1. Trench Profiles for Sections 161 (Top) and 162 (Bottom) on US281.



Figure 3-2. Trench Wire Lines for Overlay Sections 508 (Top) and 507 (Bottom) on US175.

The research approach utilized to achieve the above objective includes four steps:

- 1) Rutting model review and recommendation;
- 2) Development of an HMA rutting model;
- 3) Calibration of the developed HMA rutting model; and
- 4) Validation of the calibrated HMA rutting model.

It is worth noting that HMA rutting development, regardless of it occurring at new flexible pavements or HMA overlays, follows the same mechanisms discussed previously so that the same M-E framework and the same principles are applicable both types of pavements. Hence, the rutting model developed for HMA overlays under Project 0-5123 is applicable to HMA layers of new flexible pavements. But for HMA overlays, it is often assumed that rutting occurs in HMA overlays only; for new flexible pavements, other pavement structural layers and subgrade, except the HMA layers, may also contribute to the surface overall rutting. Actually, the HMA layer rutting model for new flexible pavements under Project 0-5798 and HMA overlays under Project 0-5123 (Zhou et al. 2009b) was developed by the same researchers, following the same principles and the same framework. A review of work accomplished under both Projects 0-5123 and 0-5798 is provided below for purpose of comprehensiveness in this study.

3.2 RUTTING MODEL REVIEW AND RECOMMENDATION

Rutting prediction and modeling have been studied for a long time. Various models have been developed to predict rutting (or permanent deformation). In general, these models can be categorized as 1) layer strain rutting model and 2) shear strain rutting model. A detailed review of each model type is presented below.

3.2.1 Category 1: Layer Strain Rutting Model

The most often used approach for predicting rutting is based on the use of elastic theory and the results of plastic strains determined by repeated load tests on pavement materials. The approach was initially introduced by Heukelom and Klomp (1967). Since then, research has been conducted by others such as Romain (1969), Monismith (1971), Barksdale (1972), Morris and Hass (1972), and McLean (1974) for soils, granular materials, and asphalt concrete. The fundamental concept of this approach is the assumption that the plastic strain ε_p is functionally proportional to the elastic state of stress (or strain) and number of load repetitions. This constitutive deformation law is considered applicable for any material type and at any point within the pavement system. The response of any material must be experimentally determined from laboratory tests for conditions (times, temperature, stress state, moisture, density, etc.) expected to occur in-situ.

Provided the plastic deformation response is known, elastic theory (either linear or non-linear) is then used to determine the expected stress state within the pavement. By subdividing each layer into convenient thicknesses (Δz_j) and determining the average stress state at each layer increment, the permanent deformation within the i^{th} layer, δ_i^p may be found by summing the $(\varepsilon_i^p) \times (\Delta z_i)$ products. This process is done for each layer present in the pavement so that it is termed “layer strain” rutting model. The total permanent deformation of the pavement

is found from:

$$\delta_t^p = \sum_{i=1}^n \delta_i^p \quad (3-1)$$

where δ_t^p is total permanent deformation of the pavement; δ_i^p is permanent deformation within the i^{th} layer; and n is number of layers.

Obviously, such a summation process is done along a vertical axis (constant horizontal plane coordinates). While different permanent deformation models have been proposed, only the three most promising layer strain rutting models, MEPDG rutting model (NCHRP 1-37A 2004), NCHRP 1-40B rutting model (Schwartz 2006), and VESYS rutting model (Kenis 1978; Kenis and Wang 1997), are discussed below.

3.2.1.1 MEPDG Rutting Model

The final MEPDG HMA rutting model is presented below:

$$\frac{\varepsilon_p}{\varepsilon_r} = k_1 \times 10^{-3.4488} T^{1.5606} N^{0.479244} \quad (3-2)$$

where ε_p is permanent strain; ε_r is resilient strain; T is temperature (°F); N is number of load repetitions; and k_1 is depth adjustment coefficient and is defined as follows:

$$k_1 = (C_1 + C_2 \times D) \times 0.328196^D \quad (3-3)$$

$$C_1 = -0.1039h_{ac}^2 + 2.4868h_{ac} - 17.342 \quad (3-4)$$

$$C_2 = 0.0172h_{ac}^2 - 1.7331h_{ac} + 27.428 \quad (3-5)$$

where h_{ac} is total HMA thickness (inch); and D is depth below the surface (inch).

3.2.1.2 NCHRP 1-40B Rutting Model

NCHRP 1-40B rutting model has the same format as the MEPDG rutting model. The enhancement is to adjust permanent deformation constants based on HMA volumetric properties.

$$\frac{\varepsilon_p}{\varepsilon_r} = k_1 \left(10^{k_{r1}} T^{k_{r2}} N^{k_{r3}} \right) \quad (3-6)$$

where k_1 is depth adjustment function defined in the MEPDG rutting model. The parameters k_{r1} , k_{r2} , and k_{r3} are material properties defined below.

Constant k_{r1} is defined as follows:

$$k_{r1} = \log \left[1.5093 \times 10^{-3} \times K_{r1} \times V_a^{0.5213} \times V_{beff}^{1.0057} \right] - 3.4488 \quad (3-7)$$

where V_{beff} is effective asphalt content in volume (%); and K_{r1} is the intercept coefficient shown in Figure 3-3.

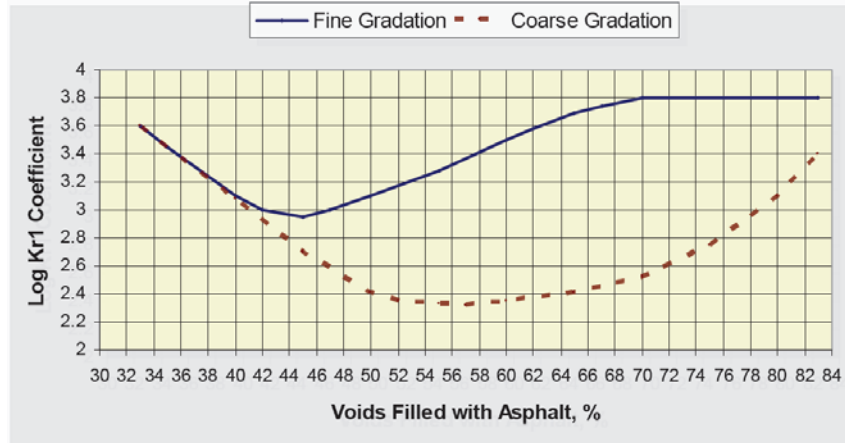


Figure 3-3. Log K_{r1} Coefficient vs. Voids Filled with Asphalt (%) (Schwartz 2006).

Constant k_{r2} is defined below:

$$k_{r2} = 1.5606 \left(\frac{V_a}{V_{a(design)}} \right)^{0.25} \left(\frac{P_b}{P_{b(opt)}} \right)^{1.25} F_{index} C_{index} \quad (3-8)$$

where $V_{a(design)}$ is design air voids; P_b is asphalt content by weight; $P_{b(opt)}$ is design asphalt content by weight; F_{index} is fine aggregate angularity index (Table 3-1); and C_{index} is coarse aggregate angularity index (Table 3-2).

Table 3-1. Fine Aggregate Angularity Index Used to Adjust F_{index} .

Gradation – External to Restricted Zone	Fine Aggregate Angularity	
	<45	>45
Dense Grading – External to Restricted Zone	1.00	0.90
Dense Grading – through Restricted Zone	1.05	1.00

Table 3-2. Coarse Aggregate Angularity Index Used to Adjust C_{index} .

Type of Gradation	Percent Crushed Material with Two Faces				
	0	25	50	75	100
Well Graded	1.1	1.05	1.0	1.0	0.9
Gap Graded	1.2	1.1	1.05	1.0	0.9

Constant k_{r3} is presented below:

$$k_{r3} = 0.4791 \times K_{r3} \times \frac{P_b}{P_{b(opt)}} \quad (3-9)$$

where K_{r3} is the slope coefficient; for fine-graded mixes with $GI < 20$, K_{r3} is 0.40; for coarse-graded mixes with $20 < GI < 40$, K_{r3} is 0.70; for coarse-graded mixes with $GI > 40$, K_{r3} is 0.80; and GI is gradation index and defined below:

$$GI = \sum_{i=3/8}^{#50} |P_i - P_{i(0.45)}| \quad (3-10)$$

3.2.1.3 VESYS Rutting Model

The VESYS rutting model is based on the assumption (or laboratory permanent deformation law) that the permanent strain per loading pulse occurring in a material specimen can be expressed by:

$$\frac{\Delta \varepsilon_p(N)}{\varepsilon} = \mu N^{-\alpha} \quad (3-11)$$

where $\Delta \varepsilon_p(N)$ is vertical permanent strain at load repetition, N ; ε is peak haversine load strain for a load pulse of duration of 0.1 sec measured on the 200th repetition; and μ and α are material properties depending on stress state, temperature, etc.

The above equation assumes that ε remains relatively constant throughout the test, and thus, the permanent strain increment, $\Delta \varepsilon_p(N)$, at any load cycle is:

$$\Delta \varepsilon_p(N) = \varepsilon - \varepsilon_r(N) \quad (3-12)$$

where $\varepsilon_r(N)$ is the resilient or rebound strain taking place at cycle N . Then, the rut depth for any single layer after N load cycles can be written as:

$$R_D = H \times \varepsilon_p = H \times \varepsilon \frac{\mu}{1-\alpha} N^{1-\alpha} \quad (3-13)$$

where H is layer thickness.

The VESYS layer rutting model estimates the permanent deformation in each finite layer as the product of the elastic compression in that layer and the layer material permanent deformation law associated with that layer. The layer rutting model is expressed by:

$$R_D = \int_{N_i}^{N_j} U_s^+ \frac{e_t}{e_s} \mu_{sub} N^{-\alpha_{sub}} + \sum_{i=1}^{n-1} \int_{N_i}^{N_j} (U_i^+ - U_i^-) \mu_i N^{-\alpha_i} \quad (3-14)$$

where U_s^+ is the deflection at the top of the subgrade due to single axle load; U_i^+ and U_i^- are deflections at the top and bottom of finite layer i due to axle group; e_t is strain at top of subgrade due to the axle group; e_s is strain at top of subgrade due to a single axle; μ_{sub} and α_{sub} are permanent deformation parameters of the subgrade; and μ_i and α_i are permanent deformation parameters of layer i .

The major feature of the VESYS rutting model is to characterize layer properties rather than global parameters used by the MEPDG. For each layer, the VESYS rutting model requires permanent deformation parameters: μ and α_i .

3.2.2 Category 2: WesTrack Shearing Strain Rutting Model

An alternative to the layer strain approach has been recently proposed to model the rutting behavior of the WesTrack test sections (Epps et al. 2002). In this approach, the pavement is modeled as a multi-layered elastic system with the asphalt concrete modulus determined from the repeated simple shear test at constant height (RSST-CH) tests. Rutting in AC is assumed to be controlled by shear deformations. Computed elastic shear stress and strain (τ , γ^e) at a depth of 50 mm beneath the edge of the tire are used for rutting estimates. Densification of the asphalt concrete is excluded in the rutting estimates since it has a comparatively small influence on surface rutting.

In simple loading, permanent shear strain in the AC is assumed to accumulate according to the following expression:

$$\gamma^i = a \times \exp(b \tau) \times \gamma^e \times n^c \quad (3-15)$$

where τ is shear stress determined at this depth using elastic analysis; γ^e is the corresponding elastic shear strain; n is the number of axle load repetitions; and a , b , c are regression coefficients obtained from field data, RSST-CH laboratory test data, and the elastic simulations, respectively.

Rutting in an HMA layer due to the shear deformation is determined from the following:

$$RD_{AC} = K * \gamma_j^i \quad (3-16)$$

For a 6-inch layer, the value of K is 5.5 where the rut depth (RD) is expressed in inches.

3.2.3 Proposed HMA Rutting Model

As noted previously, the WesTrack shearing rutting model requires the RSST-CH to characterize permanent deformation properties of HMA mixes and predict pavement rutting using empirical shift factors. The feature of the WesTrack shearing rutting model is that only the

HMA layer located at 2 inches below the pavement surface, regardless of how many HMA layers exist in the pavement structure, is required to be evaluated under the RSST-CH. The disadvantages of the WesTrack shearing rutting model are 1) high variability of RSST-CH and 2) very limited uses and validation.

Regarding the layer strain models, both MEPDG and NCHRP 1-40B rutting models have specific parameters and do not need to run laboratory testing. While the NCHRP 1-40B rutting model is an enhanced MEPDG model and considers many more factors (e.g., asphalt binder content, angularity, gradation) influencing rutting, asphalt binder PG grade (a parameter that most affects rutting of HMA pavement based on accelerated load testing) is not directly considered in the NCHRP 1-40B rutting model. It is worth noting that not requiring laboratory testing is both advantageous and disadvantageous for these two models, because while it makes the models simple to implement, not using laboratory characterization of HMA mixes may lead to inaccurate rutting prediction. However, HMA mixes are very complex, and laboratory characterization of permanent deformation properties is critical to adequately predict field rutting performance.

Different from both the MEPDG and NCHRP 1-40B rutting models, the major feature of the VESYS layer rutting model is to characterize layer properties rather than global parameters used by the MEPDG. For each layer, the VESYS rutting model requires permanent deformation parameters: α_i and μ_i . Its disadvantage also is acquiring these layer properties and running repeated load tests for each layer. However, recognizing the complexity of HMA mixes, it is necessary to characterize each HMA layer's permanent deformation properties in order to make a more accurate prediction. Therefore, the VESYS layer rutting model was ultimately selected for modeling HMA layer rutting. The detailed HMA layer rutting model is presented below.

$$R_D = \sum_{i=1}^N k_{RD} \int (U_i^+ - U_i^-) \mu_i N^{-\alpha_i} \quad (3-17)$$

where k_{RD} is calibration factor; U_i^+ and U_i^- are deflection at top and bottom of finite layer i due to axle group; N is number of HMA layers; and μ_i and α_i are permanent deformation parameters of HMA layer i .

It is clear that the two key issues of the recommended rutting model are to 1) calculate the deflection of each HMA layer and 2) determine permanent deformation parameters for each HMA layer: μ_i and α_i in the lab. Additionally, the rutting accumulation principle under different traffic loads and environmental conditions should also be addressed. All these three issues will be discussed in the next section.

3.3 DEVELOPMENT OF HMA RUTTING MODEL

As noted above, the VESYS layer rutting model has been recommended for predicting HMA rutting. However, there are three issues that need to be further addressed. The following text will further discuss each one.

3.3.1 Calculation of HMA Deflection

Currently, different multi-layer linear elastic programs are available for calculating pavement deflection. To be consistent with the current TxDOT pavement design program, FPS19W (which uses the well-known Weslea multi-layer elastic program), the Weslea program was chosen to calculate the HMA deflections for rutting prediction.

3.3.2 Laboratory Determination of HMA Rutting Properties: μ and α

The most often used laboratory test for determining the permanent deformation properties of HMA materials is the repeated load test. Generally, the repeated load test is run without confining pressure with 0.1 second loading and 0.9 second rest period. After reviewing historical references about the repeated load test in the literature (Kenis 1978; Witeczak et al. 2000), Zhou et al. have standardized a repeated load test protocol for HMA mixes and documented it in Report 0-5798-P1: Laboratory and Field Procedures Used to Characterize Materials. But, it was found later that it is ideal to conduct the repeated load test at three temperatures for Texas climate: 77/25 °F/°C, 104/40 °F/°C, and 122/50 °F/°C. For each temperature, the applied load is listed in Table 3-3. In case of preferring only one test temperature, the recommended test temperature is 104 °F/40 °C. The specimen size is 4-inch (100 mm) diameter by 6-inch (150 mm) high and its preparation is the same as that for the dynamic modulus test, to be discussed later. The detailed test protocol can be found in Report 0-5798-P1 (Zhou et al. 2009a).

Table 3-3. Repeated Load Test Temperatures and Load Levels.

Test temperature (°F)	77	104	122
Applied deviator stress (psi)	30	20	10

To determine the rutting parameters from the repeated load test, the accumulative permanent deformation (or strain) versus the number of load repetitions (N), as shown in Figure 3-4, is generally plotted on a log-log scale and is often expressed by the classical power law model:

$$\varepsilon_p = aN^b \quad (3-18)$$

where parameters a and b are regression constants depending on the mix itself, test temperature, and load level. The intercept a represents the permanent strain at $N=1$, whereas the slope b represents the rate of change in permanent strain as a function of the change in load repetitions ($\log N$). Note that the parameters a and b , are determined from the linear portion of the permanent strain curve only.

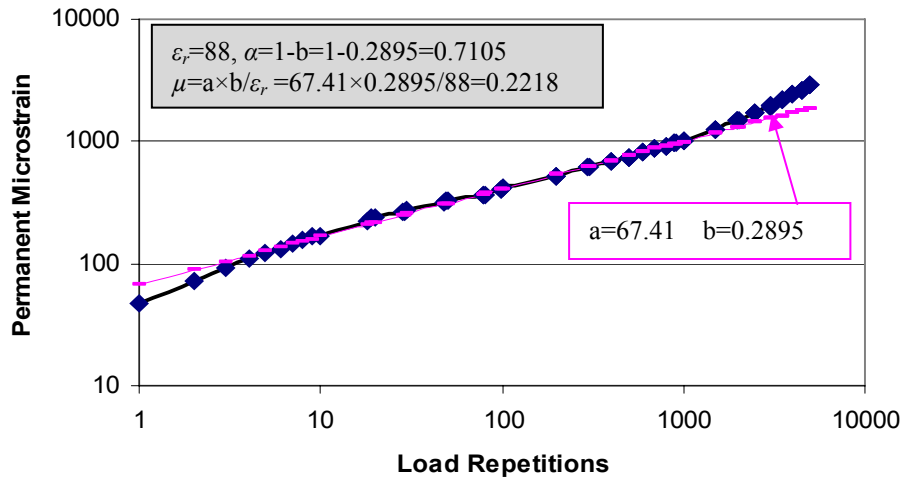


Figure 3-4. Plot of Regression Constants “a” and “b” from Log Permanent Strain – Log Number of Loading Cycles.

From Equation 3-18, the permanent strain per load repetition $\Delta\epsilon_p(N)$ can be deduced and expressed by:

$$\Delta\epsilon_p(N) = abN^{b-1} \quad (3-19)$$

Meanwhile, the resilient strain (ϵ_r) is generally assumed to be independent of the load repetitions (N) and is calculated based on the measurement on the 200th repetition. As a consequence, the ratio of permanent strain to resilient strain of the HMA mix can be expressed by:

$$\frac{\Delta\epsilon_p(N)}{\epsilon_r} = \left(\frac{ab}{\epsilon_r}\right)N^{b-1} \quad (3-20)$$

Rutting parameters μ and α , are defined by:

$$\mu = \frac{ab}{\epsilon_r} \quad (3-21)$$

$$\alpha = 1 - b \quad (3-22)$$

For the HMA mix shown in Figure 3-4, known resilient microstrain $\epsilon_r = 88$, intercept $a = 67.41$, and slope $b = 0.2895$, the rutting parameters μ and α can be determined by:

$$\mu = \frac{ab}{\epsilon_r} = \frac{67.41 \times 0.2895}{88} = 0.2218$$

$$\alpha = 1 - b = 1 - 0.2895 = 0.7105$$

3.3.3 Rutting Accumulation Principle

To consider the effects of stresses of different magnitude on the development of rutting, which result from variations in *traffic loads* and *environmental conditions*, an accumulative damage hypothesis is required. A “*time-hardening*” procedure appears to provide a reasonable approach (Lytton et al. 1993; Epps et al. 2002).

For each season i , ε_i^p is computed from:

$$\varepsilon_i^p = \varepsilon_i^{p(N=1)} \left[\left(N_{eqi} + n_i \right)^b - N_{eqi}^b \right] \quad (3-23)$$

where ε_i^p (at $N=1$) is the permanent strain at the first load repetition; n_i is the number of load repetitions during season i ; N_{eqi} is the equivalent total number of load repetitions at beginning of season i ; and b is the slope of the permanent deformation curve (Figure 3-4).

The N_{eq} is obtained for each element k with the time-hardening matching scheme as follows:

$$\begin{aligned} \text{Season 1} \quad N_{eq} &= 0 \\ \varepsilon_1^p &= \varepsilon_1^{p(N=1)} N_1^{b_1} \end{aligned} \quad (3-24)$$

$$\text{Season 2} \quad N_{eq2} = \left[\frac{\varepsilon_1^p}{\varepsilon_2^{p(N=1)}} \right]^{\frac{1}{b_2}} \quad (3-25)$$

$$\varepsilon_2^p = \varepsilon_2^{p(N=1)} \left[\left(N_{eq2} + n_2 \right)^{b_2} - N_{eq2}^{b_2} \right] \quad (3-26)$$

$$\text{Season } i \quad N_{eqi} = \left[\frac{\varepsilon_{i-1}^p}{\varepsilon_i^{p(N=1)}} \right]^{\frac{1}{b_i}} \quad (3-27)$$

$$\varepsilon_i^p = \varepsilon_i^{p(N=1)} \left[\left(N_{eqi} + n_i \right)^{b_i} - N_{eqi}^{b_i} \right] \quad (3-28)$$

With the above developed HMA rutting model, the next step is to calibrate it using field rutting data and then verify it using different field rutting data.

3.4 CALIBRATION OF THE DEVELOPED HMA RUTTING MODEL

The purpose of calibration is to determine the calibration factor k_{RD} in the HMA rutting model. As shown previously, the calibration factor in the MEPDG rutting model is a function of pavement temperature and asphalt layer thickness. Additionally, it has also been recognized that permanent strain (ϵ_p) may not be directly proportional to resilient strain (ϵ_r) but related to both resilient strain and modulus (Brown et al. 2006), so that a modulus (or strain) factor is necessary for the calibration. Therefore, it is anticipated that k_{RD} is also related to pavement temperature (T), HMA modulus, and HMA thickness (h_{AC}), as presented below:

$$k_{RD} = f_1(T) \times f_2(E) \times f_3(h_{AC}) \quad (3-29)$$

Therefore, the calibration process was to determine a pavement temperature correction factor, $f_1(T)$, modulus correction factor, $f_2(E)$, and HMA thickness correction factor, $f_3(h_{AC})$, using field rutting data.

3.4.1 Determination of Calibration Correction Factors: $f_1(T)$ and $f_2(E)$

In this research project, the field rutting data from the NCAT (National Center for Asphalt Technology) pavement test track were used to determine both $f_1(T)$ and $f_2(E)$. As noted below, the sections of the NCAT test track selected for the model calibration are thin sections and most of them are less than 3 inches total HMA thickness. Based on the national rutting trench studies conducted by NCAT (Brown and Cross 1992) and the trench studies in Texas (Figures 3-1 and 3-2), most of the rutting occurred only in the top 4 inches of HMA material. Therefore, the thickness factor for the sections of the NCAT test track was assumed to be 1.0 when determining the calibration factors $f_1(T)$ and $f_2(E)$.

Figure 3-5 shows the 2006 experimental sections of the test track, which were constructed in October 2006 and trafficked in November 2006. The ESALs were applied with four fully loaded trucks at 45 mph with 3 trailers per tractor. Each tractor pulled a total load of approximately 152,000 lb, including approximately 12,000 lb for the front steer axle and the rest spreading over the other 7 axles. The cumulative ESALs for the NCAT Test Track are plotted in Figure 3-6.

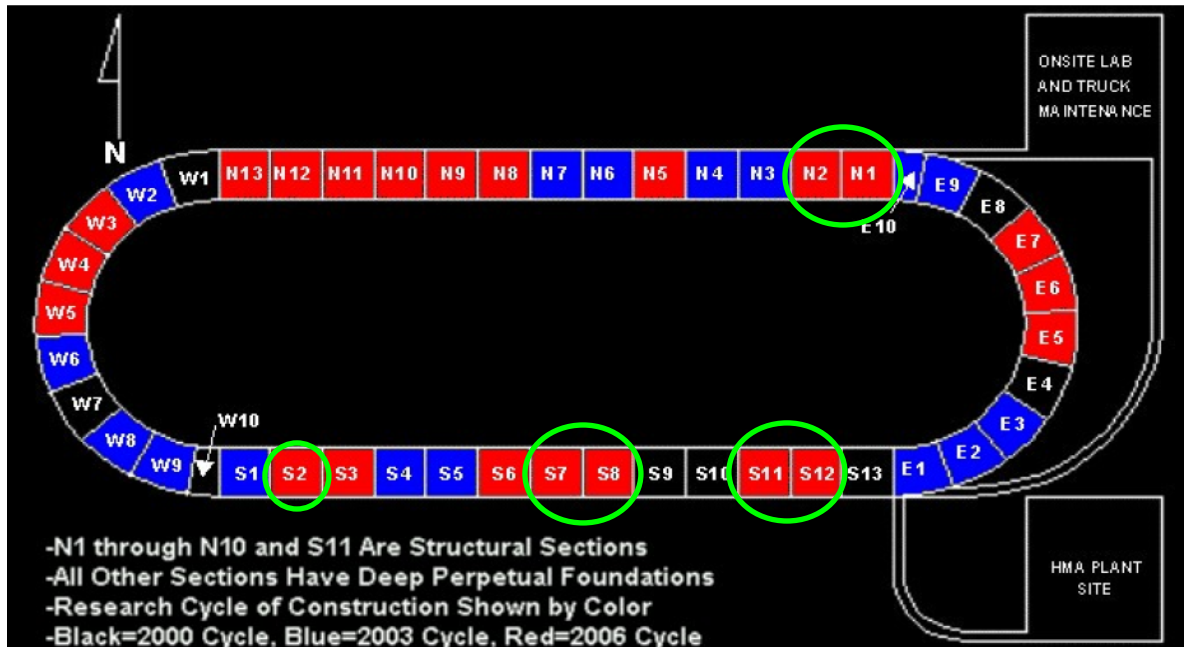


Figure 3-5. 2006 Experimental Sections of the NCAT Test Track.

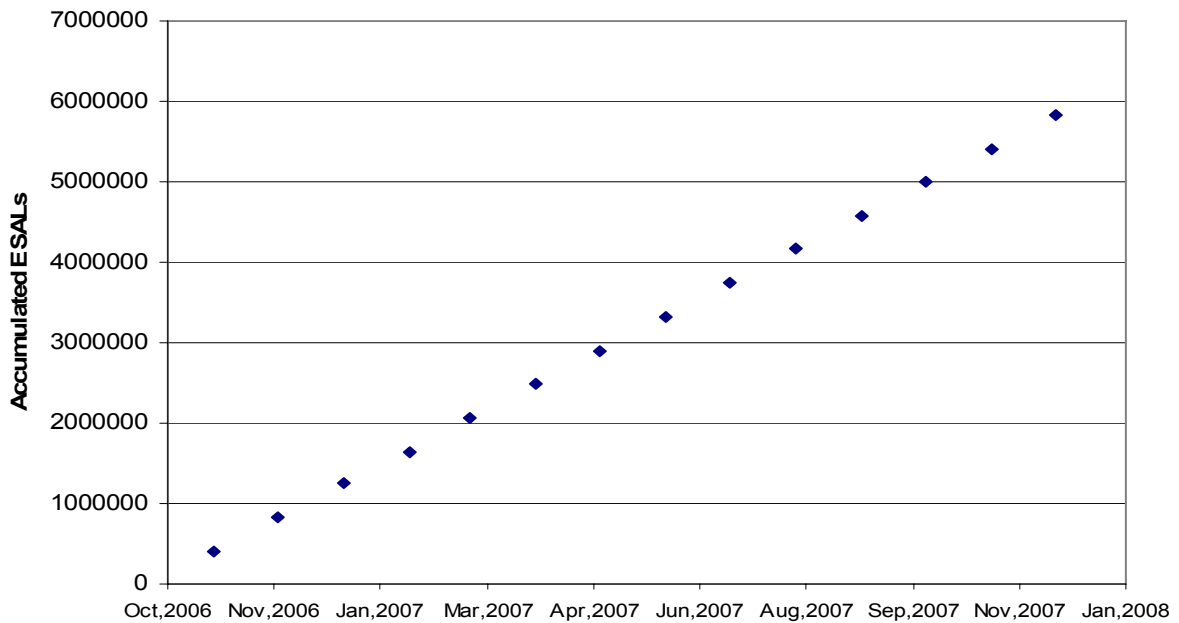


Figure 3-6. Accumulated Traffic Loads in ESALs at the NCAT Test Track.

A total of 8 sections, N1, N2, S2, S7A, S7B, S8A, S8B, and S12 were selected for determining the calibration factors $f_1(T)$ and $f_2(E)$. As shown in Figure 3-7, rut depths of these 8 sections after around 6 million ESALs loading ranged from small (Sections N1, 1.4 mm; N2, 1.5 mm; and S2, 0.7 mm), intermediate (Section S12, 13.8 mm), and very deep rutting (Sections 7A, 33.4 mm; 7B, 21.3 mm; 8A, 23 mm; and 8B, 24.6 mm). With the exception of Sections N1 and N2, all other sections were either mill/inlay or thin asphalt overlay over a very thick existing asphalt layer and all overlays were less than 4 inches. Sections N1 and N2 were full-depth new construction and had a very small amount of rutting which in this analysis was assumed to be from the top asphalt layer. Plant mixes from these 8 test sections were compacted using the Superpave Gyratory Compactor (SGC) to mold samples for both the dynamic modulus test and the repeated load test. Figure 3-8 shows an example of prepared samples (4-inch diameter by 6-inch height) for both tests. The dynamic modulus test was conducted over five different temperatures of 14, 40, 70, 100, and 130 °F and six loading frequencies of 25, 10, 5, 1, 0.5, and 0.1 Hz for each test temperature. Figure 3-9 shows the dynamic modulus master curves for the selected HMA mixes. Additionally, the repeated load test was run at three temperatures: 77, 104, and 122 °F. The permanent deformation properties (μ , α) for each selected section determined from the repeated load test are tabulated in Table 3-4.

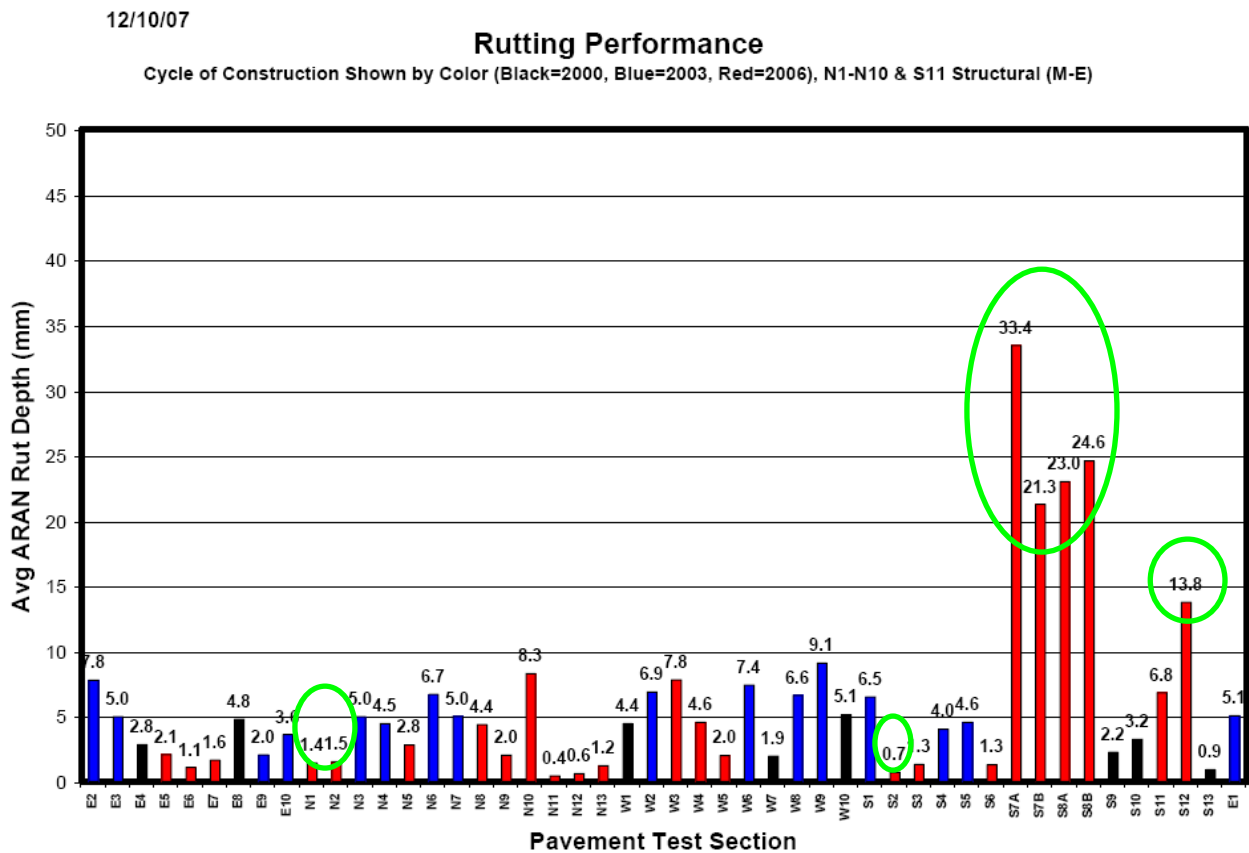


Figure 3-7. Measured Rut Depths of Test Track Sections.



Figure 3-8. Examples of Prepared Specimens for Dynamic Modulus Test and Repeated Load Test.

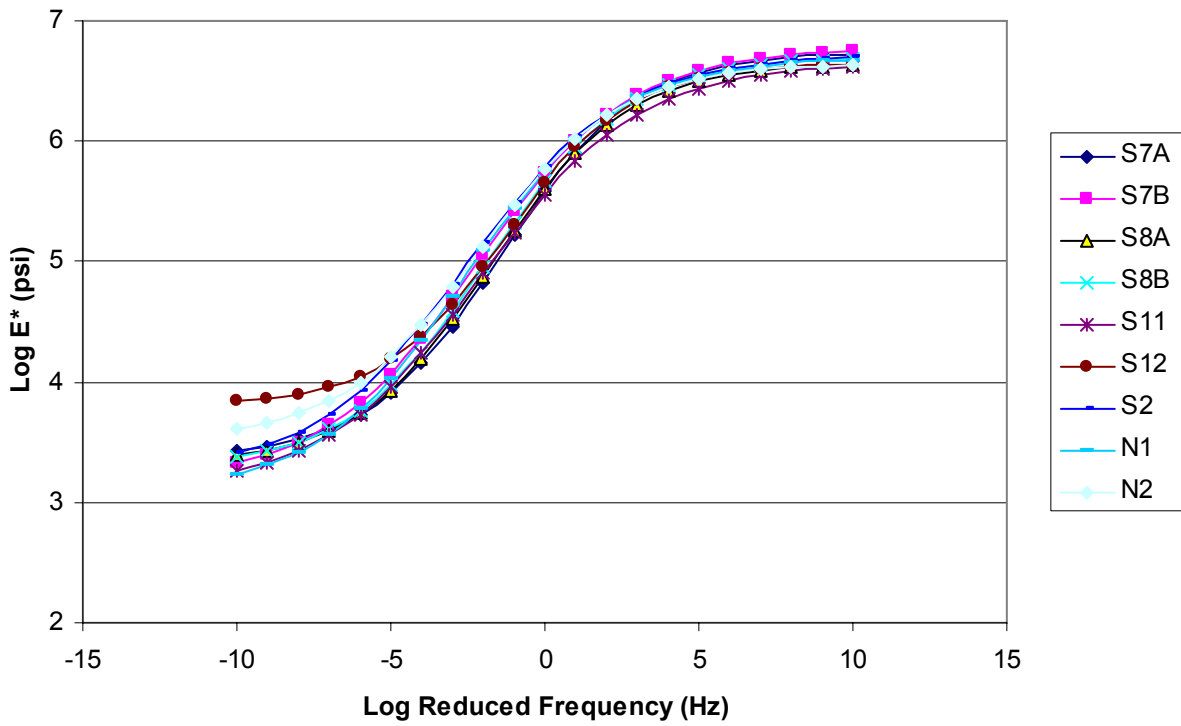


Figure 3-9. Dynamic Modulus Master Curves of the HMA Mixes Used for Calibration.

Table 3-4. μ and α Values of Selected Sections Determined from the Repeated Load Test.

Mixes	77 °F		104 °F		122 °F	
	α	μ	α	μ	α	μ
7A	0.752	0.987	0.744	1.179	0.725	1.139
7B	0.754	1.025	0.766	1.255	0.762	1.040
8A	0.797	0.850	0.786	0.988	0.774	1.000
8B	0.782	0.970	0.789	1.245	0.802	1.195
S11	0.580	0.152	0.761	0.726	0.855	1.167
S12	0.750	0.638	0.838	0.873	0.830	0.820
S2	0.708	0.372	0.781	0.681	0.802	0.958
N1	0.600	0.236	0.821	1.143	0.877	1.377
N2	0.667	0.211	0.832	0.872	0.878	1.126

In the calibration process, the climate data from the weather station at Opelika, Alabama, where the test track is located were used as input to the EICM model to predict HMA layer temperature. Note that the modulus (E value) used for determining $f_2(E)$ during the calibration was chosen at 130 °F and 10 Hz. There are two reasons for choosing such a specific temperature and frequency; one reason is that rutting in most cases occurs at high temperatures (beyond 100 °F), and the other is that the dynamic modulus at 130 °F and 10 Hz had good correlations with field rut depth, as shown in the NCHRP Report 465 (Witczak et al. 2002).

A trial and error approach was used to determine both $f_1(T)$ and $f_2(E)$ while minimizing the difference between the predicted and the measured rut depth, as shown in Figure 3-10. The final temperature factor and modulus factor are presented below. Note that the time-hardening principle is used when considering the rutting development from one temperature to the others.

$$f_1(T) = 0.191112 + \frac{3.643124}{1 + e^{18.3009 - 0.204437T}} \quad (3-25)$$

$$f_2(E) = 0.30787 + \frac{1.27860}{1 + e^{-8.28248 + 0.09239E}} \quad (3-26)$$

where T is HMA overlay temperature, °F; and E (ksi) is the HMA overlay modulus measured at 130 °F and 10 Hz.

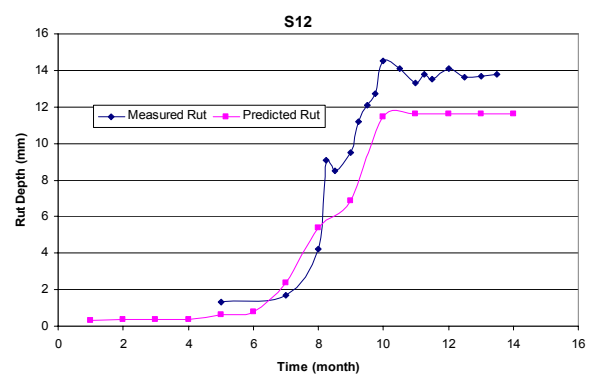
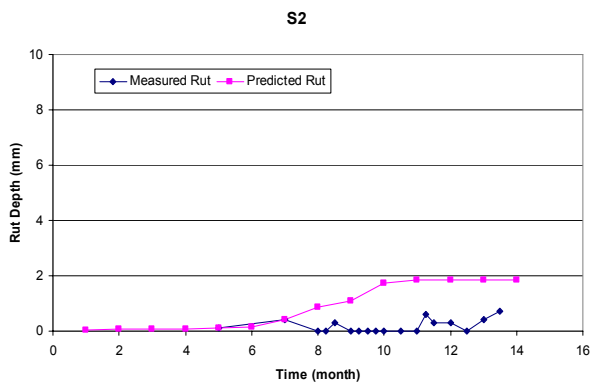
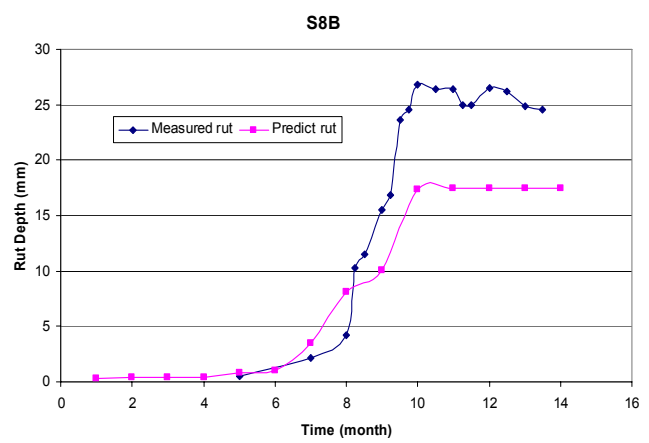
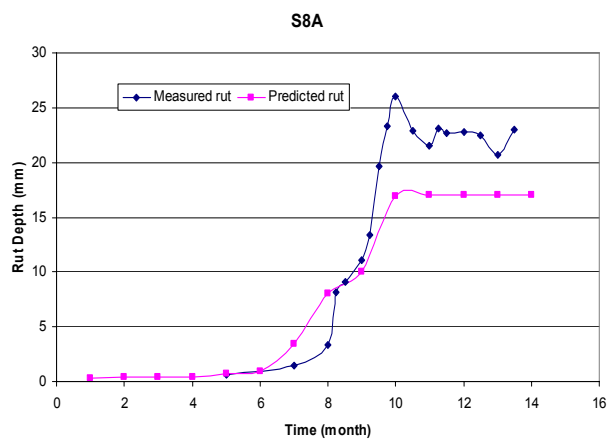
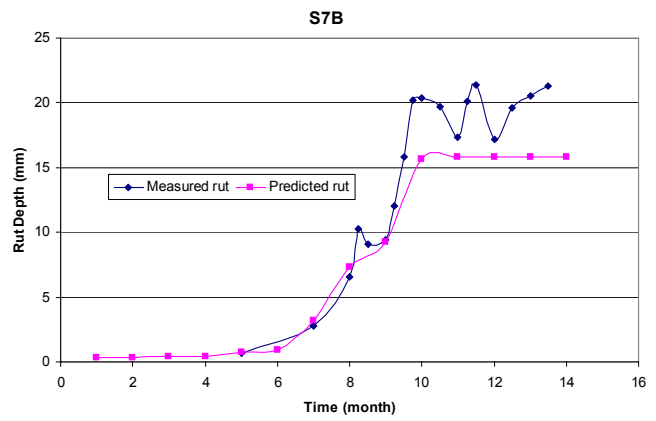
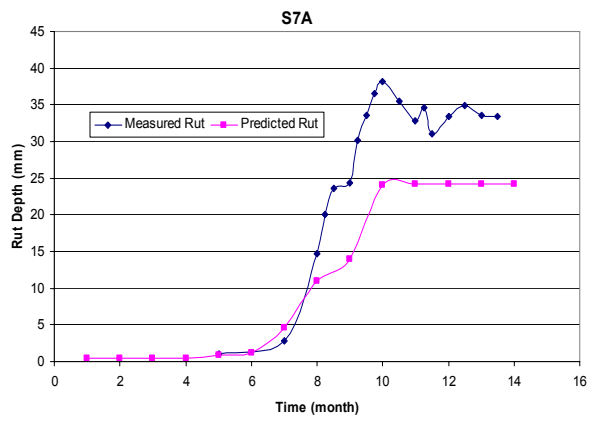


Figure 3-10. Comparisons between the Measured and Predicted Rut Development.

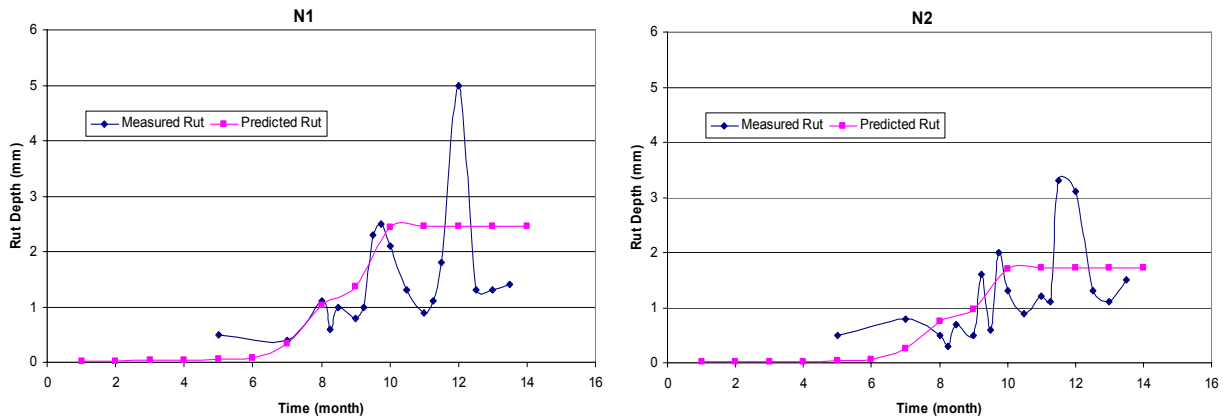


Figure 3-10. Comparisons between the Measured and Predicted Rut Development (Continued).

3.4.2 Determination of HMA Overlay Thickness Correction Factor

Currently, all layer strain-based rutting models, including the proposed model in this chapter, predict deeper rutting within the thicker asphalt overlays. In the field, rutting continually increases with thicker and thicker HMA layers until the HMA layer thickness reaches a certain value (normally around 4–5 inches), beyond which the HMA layer rutting normally does not change much with increasing the HMA thickness. To model the field conditions, an HMA thickness correction factor, $f_3(h_{AC})$ is added to the model and calibrated using the rutting data from eight LTPP-SPS5 asphalt overlay sections on US175 near Dallas, Texas.

As part of the LTPP program, eight asphalt overlay sections were built on US175 in Dallas, Texas, in 1991 (SHRP 1992). These eight test sections representing combinations of the three features (thin vs. thick overlays, virgin vs. recycled, and milled vs. non-milled) were placed adjacent to each other for comparison. Table 3-5 presents the basic information about the SPS5 test sections. US175 is a moderately traveled highway with two lanes per direction. The average daily traffic (ADT) for this roadway in 1990 was 24,000 vehicles with 6 percent trucks. The traffic information (ESALs) of this SPS5 section recorded in the LTPP database is plotted in Figure 3-11. The projected 20-year traffic volume is around 3.6 million ESALs.

Table 3-5. Basic Information of the SPS5 Test Sections.

Section ID	Overlay thickness	Milling	RAP	Virgin binder
48A502	2 inch	No	35% RAP	AC5
48A509	2 inch	2 inch	35% RAP	AC5
48A508	5 inch	2 inch	35% RAP	AC5
48A503	5 inch	No	35% RAP	AC5
48A507	5 inch	No	No	AC10+3% Latex
48A504	5 inch	2 inch	No	AC10+3% Latex
48A506	2 inch	2 inch	No	AC10+3% Latex
48A505	2 inch	No	No	AC10+3% Latex

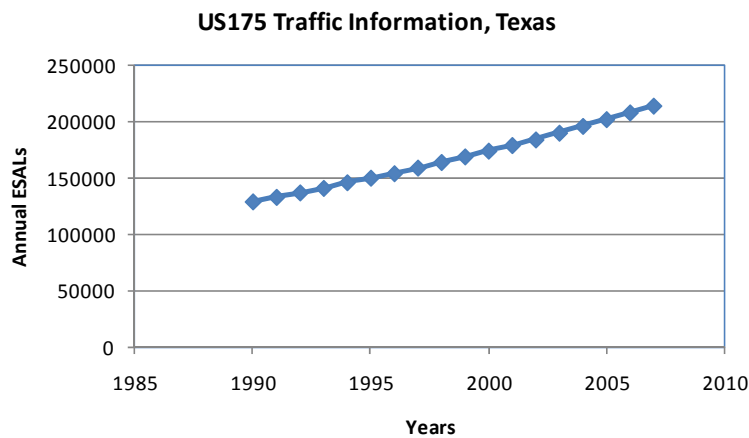


Figure 3-11. Annual Traffic Loading on US175 near Dallas, Texas.

While still performing very well, a forensic study was conducted in September 2008. Field cores from Sections 48A502, 48A503, 48A504, 48A505, 48A507, and 48A508 were taken for lab testing. Both the dynamic modulus test and the repeated load test were conducted on thicker overlay sections including 48A503, 48A504, 48A507, and 48A508. [Figure 3-12](#) shows the dynamic modulus test results, and [Table 3-6](#) lists the α and μ values determined from the repeated load test results.

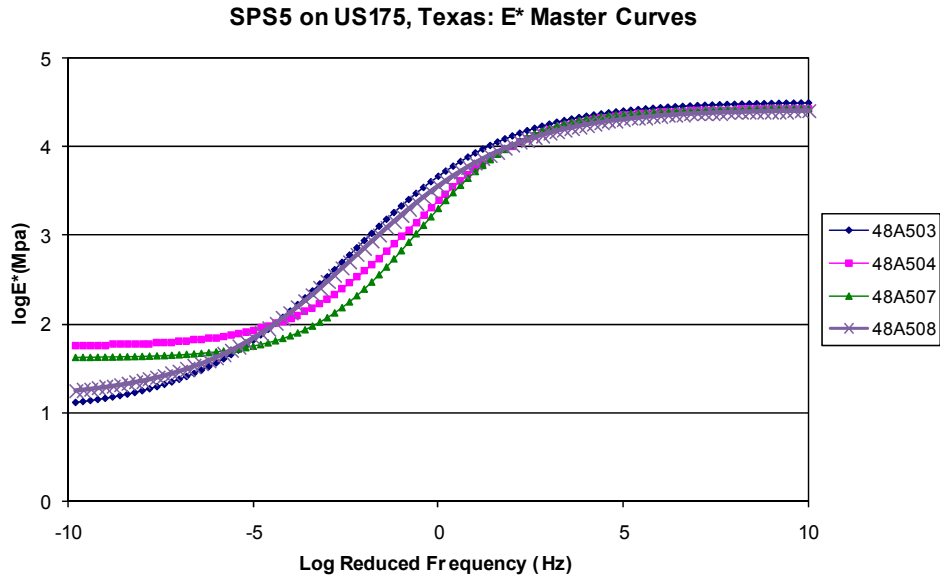


Figure 3-12. Dynamic Modulus and Repeated Load Test Results.

Table 3-6. Rutting Parameters at 40 °C.

Section	α	μ
48A503	0.7708	0.5351
48A504	0.6497	0.7249
48A507	0.7648	0.4029
48A508	0.7793	0.4611

The rutting development on these sections were predicted based the lab test results (Figure 3-12 and Table 3-6), the real traffic data (Figure 3-11), and asphalt overlay pavement temperature data predicted from the EICM program using a weather station at Dallas, Texas. The predicted rutting was then compared with the measured rutting history recorded in the LTPP database (Witzcak 2005). Again, the trial and error approach was adopted to determine $f_3(h_{AC})$, while minimizing the difference between the predicted and the measured rut depth, as shown in Figure 3-13. The final $f_3(h_{AC})$ is presented below:

$$f_3(h_{AC}) = \left(0.01445272 h_1^3 - 0.12471319 h_1^2 + 0.22193794 h_1 + 1.37640722 \right) \times \left(0.00567302 h_2^3 + 0.07104301 h_2^2 - 0.49592553 h_2 + 2.12378879 \right) \times \left(0.00199314 + \frac{0.54035153}{1 + e^{-2.61478586 + 0.58494148 (h_1 + h_2)}} \right) \quad (3-32)$$

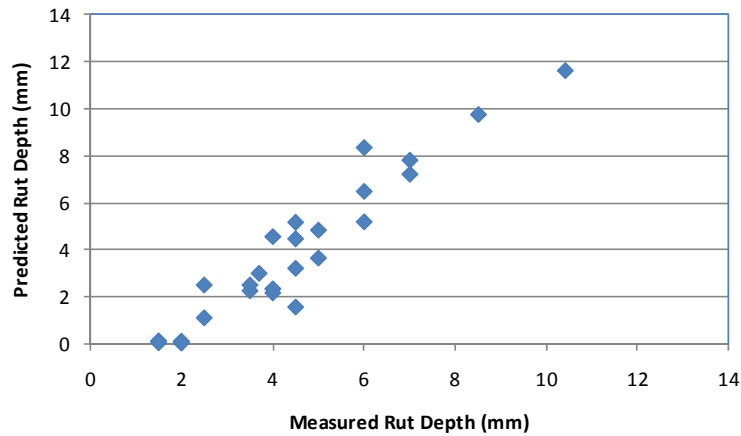


Figure 3-13. Rut Depths Comparison of SPS5 Sections: Measured vs. Predicted.

3.5 VALIDATION OF THE CALIBRATED HMA RUTTING MODEL

It is necessary and important to validate the accuracy and reasonableness of the calibrated HMA layer rutting model using an independent data source. In this study, the NCAT Test Track 2000 rutting data were employed for this validation process. Note that the rutting model was initially calibrated using the NCAT Test Track 2006 rutting data.

Since the NCAT Test Track 2000 had finished before the Research Project 0-5798 started, neither plant mixes nor raw material were available to this study. After carefully reviewing the literature, some useful information about the NCAT Test Track 2000 was found in one of the NCHRP 9-19 reports: Field Validation of the Simple Performance Test in which the measured rutting data, traffic loading conditions, dynamic modulus test and repeated load test results of several test sections were well documented (Witzcak 2005). Three test sections, N02, N12, and N13, were identified for the purpose of validating the rutting model. Figure 3-14 shows the dynamic modulus master curves of the three test sections, and Table 3-7 lists the permanent deformation parameters (μ , α) determined from the repeated load test, at 100 °F. The comparisons between the predicted and the measured rutting development are shown in Figure 3-15. Generally, the predicted rutting matches the measured rutting in the field. Thus, the calibrated HMA overlay rutting model appears valid.

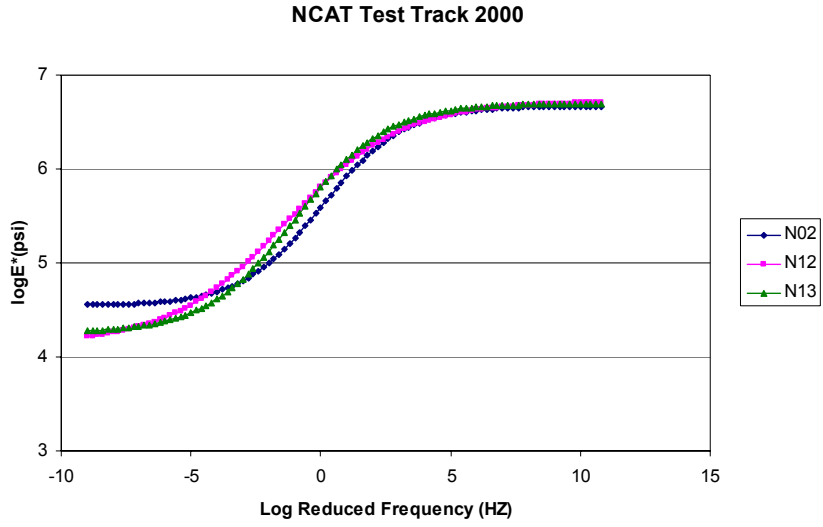


Figure 3-14. Dynamic Modulus Master Curves of Sections N02, N12, and N13.

Table 3-7. Permanent Deformation Properties of Sections N02, N12, and N13 at 100 °F.

Section	N02	N12	N13
μ	0.478	0.182	0.840
α	0.720	0.548	0.780

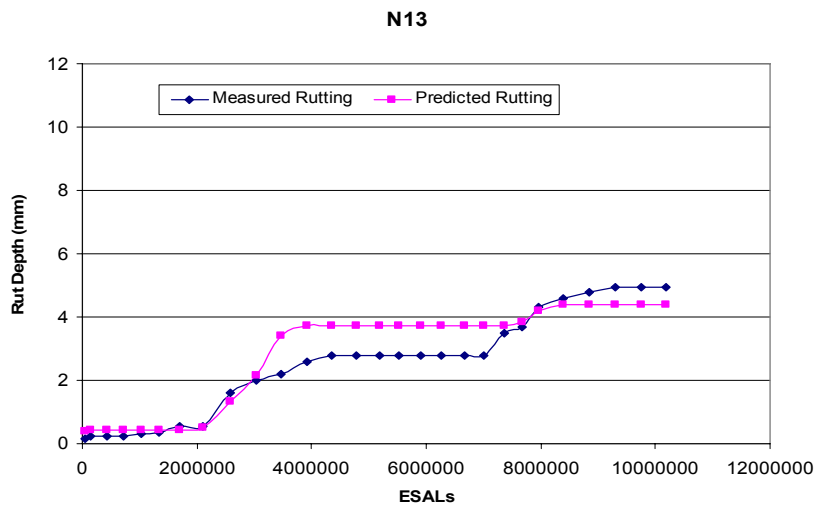
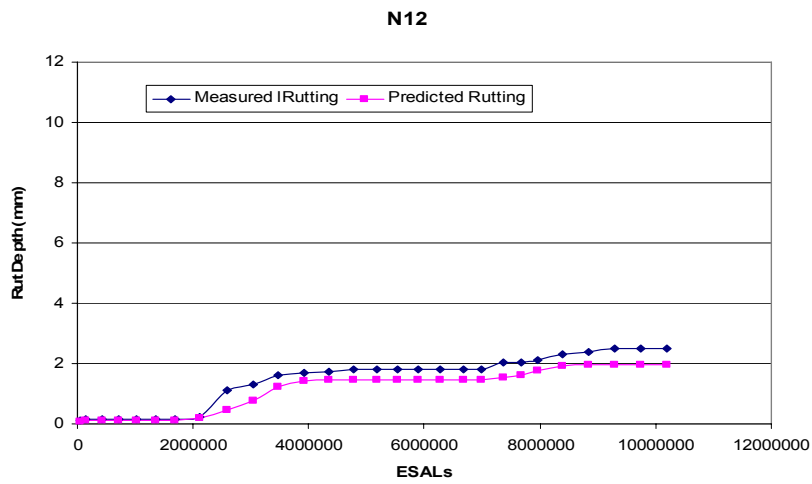
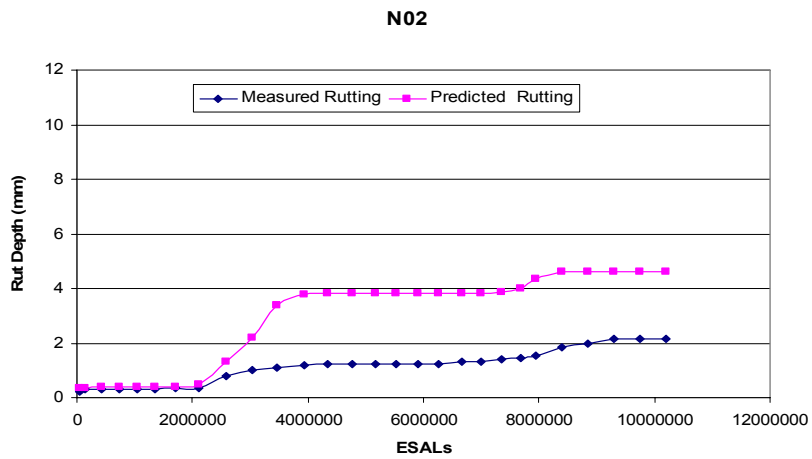


Figure 3-15. Comparisons between the Predicted and Measured Rutting Development of Sections N02, N12, and N13.

3.6 SUMMARY AND CONCLUSIONS

This chapter discussed the M-E rutting models for HMA layers. Based on the work presented in this chapter, the following conclusions and recommendations are made.

- After reviewing existing rutting models in the literature, it was found that the well-known VESYS layer rutting model still is a rational choice to model HMA rutting development. The main feature of the VESYS layer rutting model is to characterize layer properties rather than global parameters used in the MEPDG. For each layer, the VESYS rutting model requires rutting parameters: α_i and μ_i . The HMA rutting parameters (α and μ), which are some of the fundamental input parameters required in the proposed M-E rutting model, can be directly determined from the repeated load test.
- The proposed HMA rutting model was preliminarily calibrated using measured rutting data from 8 test sections of the NCAT Test Track 2006 and another 4 test sections of SPS5 asphalt overlays on US175 near Dallas, Texas. Then the calibrated model was further verified using the rutting data of 3 test sections of the NCAT Test Track 2000. Thus far, satisfactory results have been obtained.

Overall, the M-E rutting model proposed in this chapter offers great potential for rationally modeling and accurately predicting the HMA rutting development. Although comparable results with field measurements were obtained in this study, further model validation and calibration with more field data, varied traffic load spectrums, different environmental conditions, and different materials (HMA mix types) are still required.

CHAPTER 4

DEVELOPMENT, CALIBRATION, AND VALIDATION OF HMA FATIGUE CRACKING MODEL

4.1 INTRODUCTION

Fatigue cracking is one of the major distress modes considered in asphalt pavement designs. Generally, fatigue cracking starts from micro-cracks that grow and coalesce to form macro-cracks that finally penetrate through the asphalt surface layer. Accordingly, the number of traffic load repetitions (N_f) to cause a crack to initiate and propagate through the asphalt surface layer is the sum of the number of load repetitions needed for micro-cracks to coalesce to initiate a macro-crack (crack initiation, N_i), and the number of load repetitions required for the macro-crack to propagate to the surface (crack propagation, N_p). However, crack propagation (N_p) is often not directly considered in various existing mechanistic-empirical (*M-E*) fatigue analysis approaches such as the Asphalt Institute (AI 1982, 1993), Shell (Bonnaure et al. 1980; SHELL 1985), and MEPDG (NCHRP 1-37A 2004). The two main problems with current fatigue cracking initiation approaches are 1) except for the bottom asphalt layer, the contribution of asphalt layers (such as surface layer, intermediate layer), to pavement fatigue life is not fully considered; and 2) the influence of total thickness of asphalt layers on pavement fatigue life is underestimated. Thus, to accurately predict fatigue cracking, it is necessary to include both crack initiation (N_i) and crack propagation (N_p). In an effort to address some of these shortcomings, this chapter focuses on developing a practical approach for directly considering both crack initiation and crack propagation in the fatigue prediction process.

The research approach utilized to achieve the above objective includes four steps:

- 1) Fatigue cracking model review and recommendation;
- 2) Development of the fatigue cracking model;
- 3) Calibration of the developed fatigue model; and
- 4) Validation of the calibrated fatigue cracking model.

The detailed work conducted is presented in the subsequent text.

4.2 FATIGUE CRACKING MODEL REVIEW AND RECOMMENDATION

Fatigue cracking is one of the major distress modes considered in asphalt pavement designs and has been studied for several decades. In 1955, Hveem demonstrated the concept that fatigue cracking has a higher propensity to occur on an asphalt pavement when the pavement experiences a larger deflection and a higher loading frequency (Hveem 1955). Since then, different types of fatigue cracking models have been proposed. Generally speaking, most of existing fatigue cracking models, as shown in Equation 4-1, actually only describe the crack initiation phase of asphalt pavement cracking, which are often named strain-based fatigue models. The most well-known strain-based fatigue models and the most recently developed models are discussed below. The general form of the classic fatigue equation is:

$$N_f = k_1 \left(\frac{1}{\varepsilon_t} \right)^{k_2} \left(\frac{1}{S_{mix}} \right)^{k_3} \quad (4-1)$$

where N_f is the number of repetitions of load to cause fatigue cracking; ε_t is the tensile strain at the critical location; S_{mix} is the stiffness (modulus) of the material; and k_1 , k_2 , and k_3 are constants from laboratory testing and field calibration.

4.2.1 Shell Oil Fatigue Cracking Model

Because of the known impact between stress state and damage mechanism for different thicknesses of asphalt layers, Shell Oil Company developed fatigue damage prediction equations for the two major forms of laboratory fatigue testing (Bonnaure et al. 1980). In practice, the constant stress equation would be recommended for thick asphalt layer design, whereas the constant strain would be for thinner layers, although the transition from thick to thin is somewhat arbitrary. The equations developed are presented as follows:

$$\text{Constant strain: } N_f = A_f \left[0.17PI - 0.0085PI(V_b) + 0.0454V_b - 0.112 \right]^5 \varepsilon_t^{-5} E^{-1.8} \quad (4-2)$$

$$\text{Constant stress: } N_f = A_f \left[0.0252PI - 0.00126PI(V_b) + 0.00673V_b - 0.0167 \right]^5 \varepsilon_t^{-5} E^{-1.4} \quad (4-3)$$

where N_f is the number of repetitions to fatigue cracking; ε_t is the tensile strain at the critical location; E is the stiffness of the material; V_b is the effective asphalt content in volume (%); A_f is the laboratory to field adjustment factor (default = 1.0); and PI is the penetration index.

4.2.2 Asphalt Institute (MS-1) Model

$$N_f = 0.00432 * 10^{4.84 \left(\frac{V_b}{V_b + V_a} - 0.69 \right)} \varepsilon_t^{-3.291} E^{-0.854} \quad (4-4)$$

where N_f is the number of repetitions to fatigue cracking; ε_t is the tensile strain at the critical location; E is the stiffness of the material; V_b is the effective asphalt content in volume (%); and V_a is the air voids content (%).

Note that this MS-1 fatigue equation is based upon modifications to constant stress laboratory fatigue criteria. The Asphalt Institute Ninth Edition of the MS-1 design manual uses a field calibration factor of 18.4 so that predictions from the model can be matched to observed field performance (AI 1981). This correction factor was developed for a 20 percent level of wheelpath cracking; it was recommended by Finn in his classic NCHRP 1-10 study (Finn et al. 1977).

4.2.3 MEPDG Fatigue Cracking Model

The NCHRP 1-37A research team examined the Shell Oil and the MS-1 models for consideration in the recently developed MEPDG. The Shell Oil models possessed more scatter and did not possess any definite trends (El-Basyouny and Witzczak 2005); also, the MS-1 model had much less scatter and resulted in a definite trend. Thus, the MS-1 model was selected and implemented in the MEPDG. In contrast to the models described above, the MEPDG fatigue cracking model actually includes the following three models:

4.2.3.1 Number of the Load Repetitions Fatigue Model

$$N_f = 0.00432 * k_1 * C \left(\frac{1}{\varepsilon_t} \right)^{3.9492} \left(\frac{1}{E} \right)^{1.281} \quad (4-5)$$

where N_f is the number of repetitions to fatigue cracking; ε_t is the tensile strain at the critical location; E is the stiffness of the material; h_{ac} is the asphalt layer thickness (inches); and k_1 , and C are correction factors given below:

$$C = 10^{4.84 \left(\frac{V_b}{V_b + V_a} - 0.69 \right)} \quad (4-6)$$

$$k_1 = \frac{1}{0.000398 + \frac{0.003602}{1 + e^{11.02 - 3.49 * h_{ac}}}} \quad (4-7)$$

4.2.3.2 Fatigue Damage Model

Fatigue damage caused by different traffic loads is calculated as the ratio of the applied number of traffic repetitions to the allowable number of load repetitions (to some failure level) as shown in Equation 4-8.

$$D = \sum_{i=1}^T \frac{n_i}{N_i} \quad (4-8)$$

where D is the fatigue damage factor; T is the total number of periods; n_i is the actual traffic for period i ; and N_i is the allowable failure repetitions under conditions prevailing in period i .

4.2.3.3 Fatigue Cracking Amount Model

Finally, another transfer function is used to calculate the fatigue cracking from the fatigue damage, which was developed and calibrated using the LTPP data. The final fatigue damage versus cracking amount model in the MEPDG is as follows:

$$FC = \left(\frac{6000}{1 + e^{C_1 - C_2 * \log D}} \right) * \left(\frac{1}{60} \right) \quad (4-9)$$

where FC is the percentage of fatigue cracking of the total lane area; D is the damage factor (Equation 4-8); C_1 and C_2 are defined by:

$$C_1 = -2 * C_2 \quad (4-10)$$

$$C_2 = -2.40874 - 39.748 * (1 + h_{ac})^{-2.85609} \quad (4-11)$$

where h_{ac} is asphalt layer thickness (inches).

4.2.4 CalME Fatigue Cracking Model

The CalME fatigue cracking model is a damage-based fatigue cracking model in which the fatigue damage caused by repeated loading is evaluated through the stiffness ratio (SR), as proposed by Tsai et al. (2003). In the present version of CalME, the SR is predicted in the following equation (Ullidtz et al. 2006):

$$SR = \exp(-\alpha \times N^\beta) \quad (4-12)$$

where SR is the stiffness ratio, defined as the ratio of the stiffness at repetition n over the initial stiffness (taken at about 50 repetitions); N is the number of load applications; and α and β are assumed on the format:

$$\alpha = \exp(\alpha A + \alpha B \times t + \alpha C \times \ln(w) + \alpha D \times t \times \ln(w)) \quad (4-13)$$

$$\beta = \beta A + \beta B \times t + \beta C \times \ln(w) \quad (4-14)$$

where t is the temperature ($^{\circ}\text{C}$); w is the internal energy density ($\frac{1}{2} \times \varepsilon^2 \times E$); and αA , αB , αC , αD , βA , βB and βC are constants determined from the 4-point bending beam fatigue tests under controlled strain.

The use of the SR damage-based approach has several advantages: 1) stiffness is easy to measure both in the laboratory and in the field, and 2) stiffness is often utilized as an input for linear layered-elastic programs for pavement analysis, thus making it useful for programming fatigue performance prediction. However, no asphalt thickness design program but the CalME program uses this approach. Actually, Monismith and his associates are continuously developing this model. More research is still needed to refine this model (Ullidtz et al. 2005).

4.2.5 OT-Based Fatigue Cracking Model

Most recently, Zhou et al. developed an Overlay Test (OT)-based fatigue cracking prediction approach (Zhou et al. 2007). Detailed information about the OT-based approach is discussed below.

As noted previously, fatigue cracking is the combination of a crack initiation and crack propagation process. The number of traffic load repetitions (N_f) to cause a crack to initiate and propagate through the asphalt surface layer is the sum of the number of load repetitions needed for micro-cracks to coalesce to initiate a macro-crack (crack initiation, N_i) and the number of load repetitions required for the macro-crack to propagate to the surface (crack propagation, N_p).

$$N_f = N_i + N_p \quad (4-15)$$

In the OT-based approach, both N_i and N_p are estimated from the fracture properties (A and n), which are determined from the OT.

4.2.5.1 Estimation of N_i

The traditional fatigue models established based on bending beam fatigue tests mainly address the crack initiation stage. Thus, the traditional fatigue model shown in Equation 4-16 is proposed to estimate N_i .

$$N_i = k_1 \left(\frac{1}{\varepsilon} \right)^{k_2} \quad (4-16)$$

where N_i is the number of load repetitions required for crack initiation; ε is the tensile strain at the bottom of asphalt layer calculated from multi-layer liner elastic programs (such as Weslea); and k_1 and k_2 are material related parameters.

It is apparent that the key issue of estimating N_i is to establish a “bridge” between fracture properties (A and n) and fatigue parameters k_1 and k_2 . Based on fracture mechanics, Lytton et al. found the following relationships between these parameters (Lytton et al. 1993):

$$k_1 = \frac{d^{\left(\frac{1-n}{2}\right)}}{Ar^n(1-nq)E^n} \left[1 - \left(\frac{c_0}{d} \right)^{(1-nq)} \right] \quad (4-17)$$

$$k_2 = n \quad (4-18)$$

Equation 4-17 indicates that parameter k_1 (or $\log k_1$) is a function of $k_2 (= n)$, A , and E :

$$\log k_1 = f(k_2, E, A) \quad (4-19)$$

As reported by Schapery (1984), Molenaar (1983), Jacobs (1995), Lytton et al. (1993), and Erkens et al. (1997), the fracture property A is highly related to parameters n ($= k_2$) and $\log E$. Thus, it is reasonable to simplify Equation 4-17 as follows:

$$\log k_1 = a_1 + a_2 k_2 + a_3 \log E \quad (4-20)$$

where a_1 , a_2 , and a_3 are regression constants. A very similar relationship shown in Equation 4-20 can also be developed based on continuum damage mechanics (Lee et al. 2003). Therefore, Equation 4-20 is theoretically sound. The key to estimating parameter k_1 is to determine regression constants a_1 , a_2 , and a_3 .

In order to do so, the results from historical fatigue test data were reviewed. It was found that the bending beam fatigue test (BBFT) is the most often used method to characterize fatigue behavior of HMA mixes. In this project, several sources of BBFT data were assembled and used to develop the required regression parameters in Equation 4-20. After carefully reviewing the available BBFT data, the following data sets were selected for modeling:

- SHRP A-003A fatigue data (Tayebali et al. 1994): 218 tests,
- Harvey et al. 1996: 211 tests,
- Sousa et al. 1998: 129 tests,
- Tsai 2001-WesTrack fatigue data (Tsai 2001): 150 tests,
- Ghuzlan and Carpenter 2003: 478 tests, and
- Tsai and Monisimth 2005: 162 tests.

The total number of available BBFT data sets was 1348. The test variables covered in these 1348 sets of data include type of asphalt binder (conventional and modified), asphalt contents, type of aggregates, type of HMA mixes (dense-graded, Superpave, and SMA), air void contents, test temperatures, and aging conditions.

Using the “Solver” optimization technique in Microsoft Excel® by minimizing the sum of squared errors between the measured and the predicted k_1 , the regression constants a_1 , a_2 , and a_3 were determined, and the final k_1 equation is presented below. Figure 4-1 shows the predicted and the measured $\log k_1$.

$$k_1 = 10^{6.97001 - 3.20145k_2 - 0.83661 \log E} \quad R^2=0.99 \quad (4-21)$$

With Equations 4-16, 4-18, and 4-21, N_f can be estimated provided that tensile strain at the bottom of asphalt layer and modulus of asphalt layer are known.

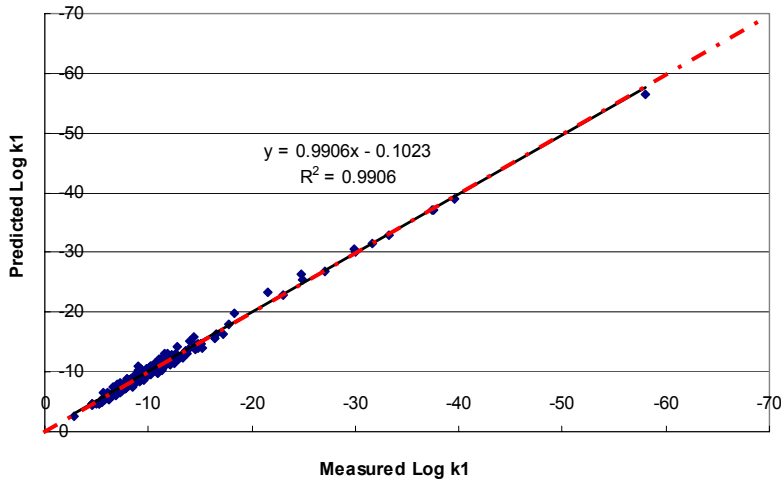


Figure 4-1. Predicted $\log k_I$ vs. Measured $\log k_I$.

4.2.5.2 Estimation of N_p

Theoretically, with known fracture properties A and n (determined from the OT) and Stress Intensity Factor (SIF, computed from the FE program or regression equations), N_p can be estimated from Equation 4-22:

$$N_p = \int_{c_0}^h \frac{1}{A(\Delta K)^n} dc \quad (4-22)$$

where c_0 is the initial crack length and h is asphalt layer thickness. Based on micro-mechanics theory and laboratory test results, Lytton et al. (1993) recommended an initial macro-crack length (c_0) of 7.5 mm, which results from micro-cracks growth.

However, one axle passing over a crack results in three loading sequences: shearing (approaching to a crack), bending (loading on the top of the crack), and shearing (leaving from the crack). These three loading sequences make it difficult to directly estimate N_p from Equation 4-22. In this project, an alternative approach was proposed.

Instead of estimating N_p from Equation 4-22, the authors recommended calculating the crack propagation length induced by one axle pass using the following form of Paris' law.

$$\Delta c = A(\Delta K)^n \times \Delta N \quad (4-23)$$

Note that for one axle pass, a crack should propagate three times: Δc_s for the approaching wheel load, Δc_b for the wheel load at the evaluated location, and Δc_s for the departing wheel load, corresponding to the shearing, bending, and shearing loading sequence, respectively. Thus, the crack propagation length (Δc) induced by one axle pass is the sum of Δc_s , Δc_b , and Δc_s .

$$\Delta c = 2 \times \Delta c_s + \Delta c_b = A \times \left[2 \times (\Delta K_{Shearing})^n + (\Delta K_{Bending})^n \right] \times \Delta N \quad (4-24)$$

Add more axle passes and repeat the above process until the accumulated crack length is equal to asphalt layer thickness (h). Then, N_p is the sum of all the number of passes.

4.2.5.3 Fatigue Damage Model

Fatigue damage caused by a specified number of load repetitions (n_i) is estimated using Miner's law (Equation 4-25).

$$D = \sum \frac{n_i}{N_f} \quad (4-25)$$

4.2.5.4 Fatigue Cracking Area Model

Fatigue cracking area is estimated by:

$$crack\ area(\%) = \frac{100}{1 + \exp(a_1 * \log D)} \quad (4-26)$$

where D is the fatigue damage factor determined from Equation 4-25, and a_1 is a calibration coefficient and equals -7.78 based on field APT fatigue cracking data (Zhou et al. 2007).

Note that Equation 4-26 has a sigmoidal function form, which is bounded with 0 percent cracking as a minimum and 100 percent cracking as a maximum. Specifically, it was assumed that a fatigue cracking value of 50 percent cracking of the total area of the wheel path theoretically occurs at a damage percentage of 100 percent.

In summary, based on theoretical review and the 1348 sets of BBFT data, a “bridge” (equations) between the crack initiation model (traditional fatigue model) and crack propagation model (Paris' law) was developed in this section. An OT-based fatigue cracking prediction approach including both crack initiation and crack propagation was then proposed.

4.2.6 Proposed Fatigue Cracking Model

Table 4-1 presents a comparison among the fatigue cracking models discussed previously, based on several parameters, such as the capability of characterizing the fatigue crack initiation and propagation process, and compatibility of the model to the existing TxDOT flexible pavement system (FPS) framework. As noted in Table 4-1, the strain-based fatigue models consider only crack initiation of fatigue cracking and ignore the crack propagation stage. The CalME considers the fatigue damage, but this approach still focuses on the crack initiation stage. The authors believe that the lack of focus on crack propagation is why the current “crack initiation” approaches require very large field calibration factors, on the order of 15 to 300. Compared with all other models, the OT-based fatigue cracking model is currently thought to be the best option for better modeling fatigue cracking, and it is recommended for inclusion in a future Tex-ME program. Furthermore, this approach has proven to be a practical approach for predicting fatigue cracking under TxDOT 9-1502 pooled-fund study project (Zhou et al. 2007).

Table 4-1. Comparison of Fatigue Cracking Modeling Approaches.

Fatigue Models		Development Status	Fatigue Mechanisms		Compatible with FPS	
			Crack Initiation	Crack Propagation Bending+Shear	Yes	No
Strain-based Model	Shell Oil	Finished	√		√	
	AI	Finished	√		√	
	MEPDG	Finished	√		√	
Damage-based Models	CalME	Under improvement	√		√	
OT-based Fatigue Cracking Model		Finished	√	√	√	

In summary, the proposed fatigue cracking model is composed of three components as listed below:

1) Fatigue life model:

$$N_f = N_i + N_p \quad (4-27)$$

$$N_i = k_1 \left(\frac{1}{\varepsilon} \right)^{k_2} \quad (4-28)$$

$$\log k_1 = 6.97001 - 3.20145 k_2 - 0.83661 \log E \quad (4-29)$$

$$k_2 = n \quad (4-30)$$

$$N_p = \sum \Delta N_{pi} \quad (4-31)$$

$$\sum \Delta N_{pi} = \frac{\sum \Delta c_{pi}}{k_{p1} AK_I^n + k_{p2} AK_{II}^n} \quad (4-32)$$

where Δc_{pi} is crack propagation length caused by ΔN_{pi} (number of load repetitions); k_{p1} and k_{p2} are field calibration factors; and all other factors are the same as previously defined.

- 2) Fatigue damage model:

$$D = \sum \frac{n_i}{N_i} \quad (4-33)$$

- 3) Fatigue cracking area model:

$$\text{cracking area}(\%) = \frac{100}{1 + \exp(-7.78 * \log D)} \quad (4-34)$$

However, several issues of the OT-based fatigue cracking model still need to be addressed and they are:

- 1) Validation of k_1 - k_2 relationship (Equation 4-29) using Texas mixes,
- 2) SIF calculation and associated regression equations, and
- 3) HMA fracture properties (A and n) determination.

All three of these issues will be discussed in the next section.

4.3 FURTHER DEVELOPMENT OF THE PROPOSED FATIGUE CRACKING MODEL

As noted above, the OT-based fatigue cracking model was recommended for predicting fatigue cracking development in asphalt pavements. However, there are three areas needing further enhancement. The following sections will discuss each one.

4.3.1 Validation of k_1 - k_2 Relationship Using Texas Mixes

The relationship between k_1 , and k_2 (Equation 4-29) developed previously was based on bending beam fatigue tests on a variety of HMA mixes, but none of them were from Texas. Therefore, it is necessary to check the accuracy of applying the k_1 - k_2 relationship to Texas mixes.

When reviewing the literature, it was found that the bending beam fatigue tests were conducted on selected Texas mixes under two TxDOT research projects: 0-4468 (Walubita et al. 2005) and 0-5132 (Prozzi et al. 2006). Figure 4-2 presents the measured $\log k_1$ from the bending beam fatigue test and the $\log k_1$ predicted using the k_1 - k_2 relationship (Equation 4-29). It is clear that the accuracy of the k_1 - k_2 relationship is valid for these Texas mixtures.

Texas Mixes
(TTI 0-4468 and CTR 0-5132)

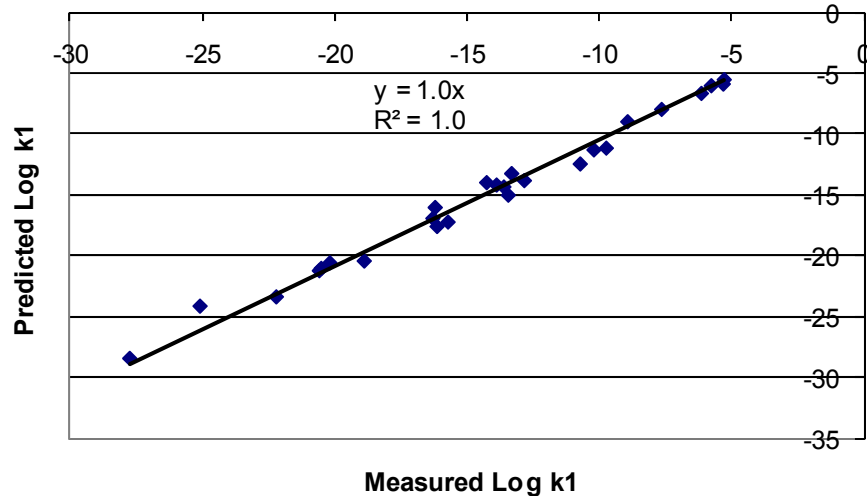


Figure 4-2. Validation of k_1 - k_2 Relationship Using Texas Mixes.

4.3.2 SIF Computation and Associated Regression Equations

As one of the key parameters of Paris' law, the SIF computation becomes a very critical aspect of crack propagation analysis. Currently, two categories of SIF-computation finite element (FE) programs are available. The first category includes commercial FE packages such as ABAQUS, ANSYS, etc., which are general or multi-purpose. However, their complex nature, user-unfriendliness, and user cost makes these packages not readily applicable for routine crack propagation analysis and pavement design. The second category incorporates those FE tools specifically developed for pavement SIF computation. For example, Lytton and his associates (Chang et al. 1976) developed a 2-D *CRACKTIP* program at TTI in 1976. Currently, the most advanced pavement crack propagation program is the *CAPA-3D* (Computer Aided Pavement Analysis) developed at the Delft University of Technology in the 1990s (Scarpas et al. 1997). The *CAPA-3D* program has some special functions for crack propagation, such as special elements for simulating interface conditions and interlayers, automatic re-meshing techniques to simulate crack propagation, etc. All of these functions make the *CAPA-3D* a good option for crack propagation analysis. Unfortunately, due to its 3-D characteristics, the inherent high-end hardware requirements and execution time demands render it suitable primarily for research purposes. To circumvent this scenario, the authors have developed a semi-analytical FE method-based crack propagation program named *SA-CrackPro* for SIF computation. More information about the *SA-CrackPro* program and associated SIF analysis are given in the following paragraphs.

4.3.2.1 SA-CrackPro for SIF Computation

A new FE analysis package, *SA-CrackPro*, was developed at TTI (Hu et al. 2008). The *SA-CrackPro* is essentially a 2-D SIF calculation program that incorporates a Semi-Analytical (SA) method so that the *SA-CrackPro* can provide the same satisfactory computations and results as a 3-D FE program at a much faster speed and with much fewer computer resource requirements.

To simulate the pavement layer interface and load transfer conditions at the joints (or cracks), thin-layer elements were introduced. To sufficiently and accurately model crack propagation, FE auto-meshing and re-meshing techniques were proposed and implemented in the program. The expressions for extracting the SIF values using plane strain assumptions are given in Equations 4-35 and 4-36, and the corresponding finite element meshing around the crack tip is shown in Figure 4-3.

$$K_I = \frac{G\sqrt{2\pi}}{\sqrt{r_{a-b-c}}(4-4\mu)} [4(u_d - u_b) + (u_c - u_e)] \quad (4-35)$$

$$K_{II} = \frac{G\sqrt{2\pi}}{\sqrt{r_{a-b-c}}(4-4\mu)} [4(v_d - v_b) + (v_c - v_e)] \quad (4-36)$$

where r_{a-b-c} is the distance from a crack tip point 'a' to point 'c'; K_I and K_{II} are SIF values for Mode I (opening crack mode) and Mode II (shearing crack mode), respectively; G is the shearing elastic modulus ($= \frac{E}{2(1+\mu)}$ for isotropic elements); μ is Poisson's ratio; and u_i, v_i are the x, y displacements at point i .

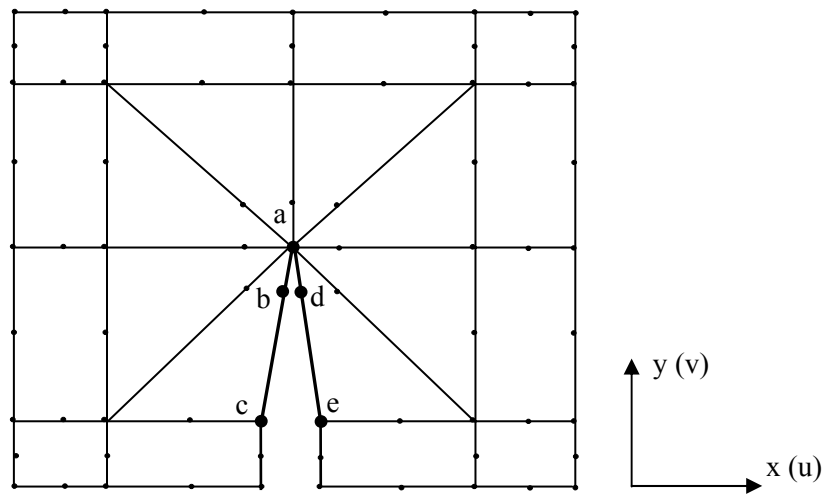


Figure 4-3. Finite Elements Meshing around Crack Tip.

To verify the accuracy of the *SA-CrackPro* program, a side by side comparison was conducted between *ANSYS-3D* (ANSYS 2004) and *SA-CrackPro* under the standard single axle load of 80 kN with a tire pressure of 0.689 MPa. The analyzed pavement structure consists of a 75 mm thick HMA surface layer, a cracked cement treated based layer, a subbase layer, and subgrade. SIF results for bending mode K_I and shearing mode K_{II} from these two programs are presented in Figure 4-4. It is apparent that the *SA-CrackPro* program has comparable accuracy with the *ANSYS-3D*. It is worth noting that the current running speed of the *SA-CrackPro* program is still not fast enough to be incorporated directly into a pavement design procedure for crack propagation analysis. However, with this verified *SA-CrackPro* program, it becomes possible to conduct extensive SIF computations and then develop SIF regression equations.

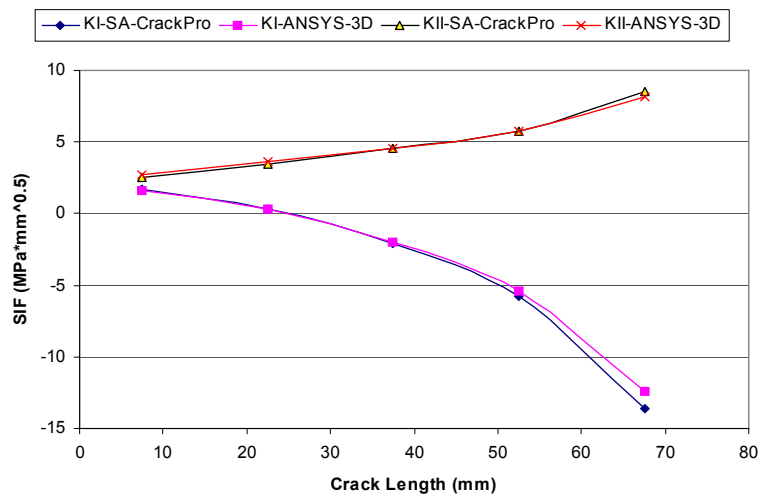


Figure 4-4. SIF Comparison between *SA-CrackPro* and *ANSYS-3D*.

4.3.2.2 SIF Analyses

With this verified *SA-CrackPro* program, four factors including structural and material parameters (i.e., layer modulus and thickness), multi-layer base and/or subbase (equivalent layer thickness), multi-HMA layers, and load spectrum were investigated before extensive SIF computations on various pavement structures under different traffic loads were conducted. The findings from the SIF analyses are presented below.

4.3.2.2.1 Effect of Structural and Material Parameters on SIF

A 3-layer pavement structure consisting of an HMA layer, base, and subgrade was used to identify the significant influential parameters on bending and shearing SIF modes. Table 4-2 provides pavement structural thickness and material properties used for computing SIF values and the associated statistical analysis. The total factorial combinations analyzed for each mode of SIF (K_I or K_{II}) were 2916 ($=3*3*3*4*3*9$). The purpose of the statistical analysis was to determine the parameters that have significant influence on K_I or K_{II} . The SPSS software (SPSS Inc. 2003) was used for statistical analysis, and the Pearson correlation results are listed in Table 4-3.

Table 4-2. Structural and Material Properties Used in the Analysis.

Parameters	Range	Selected values	Count number
H1: HMA layer thickness (mm)	50–200	50, 100, 200	3
E1: HMA layer modulus (MPa)	2000–15000	2000, 6000, 15000	3
H2: base layer thickness (mm)	150–450	150, 300, 450	3
E2: base layer modulus (MPa)	100–3500	100, 400, 1000, 3500	4
E3: subgrade modulus (MPa)	30–120	30, 60, 120	3
c/H1 (c-crack length)	0.1–0.9	0.1, 0.2, 0.3, 0.4, 0.5, 0.6, 0.7, 0.8, 0.9	9

Note: total runs for each mode (K_I, K_{II}) = $3*3*3*3*4*3*9=2916$.

Table 4-3. Statistic Analysis Results.

Parameters	Pearson Correlation		
	SIF	K_I	K_{II}
H1	Pearson Correlation	.135(*)	-.183(*)
	Significance	.000	.000
E1	Pearson Correlation	.328(*)	.217(*)
	Significance	.000	.000
H2	Pearson Correlation	-.056(*)	-.062(*)
	Significance	.033	.001
E2	Pearson Correlation	-.397(*)	-.330(*)
	Significance	.000	.000
E3	Pearson Correlation	-.014	-.014
	Significance	.593	.444
c	Pearson Correlation	-.258(*)	.369(*)
	Sig. (2-tailed)	.000	.000

Note: * Correlation is significant at the 0.01 level (2-tailed).

It can be seen that all the variables except the subgrade modulus have significant influences on both K_I and K_{II} and accordingly should be incorporated into SIF regression equations being developed. This finding about the subgrade does not mean that the subgrade has no influence on pavement responses. As reported by Huang (1993), the main influence of the subgrade is on pavement surface deflections, vertical compressive stress in the layer lying directly above the subgrade, and compressive strain of the subgrade itself. According to Table 4-3, the subgrade modulus did not significantly influence both the K_I and K_{II} and associated crack propagation, and so a fixed 50 MPa subgrade modulus was utilized for the rest of the SIF analyses in this study.

4.3.2.2.2 Consideration of a Multi-Layered Base and/or Subbase

Pavement structures often include more than one base or subbase layers with different moduli. If this is the case, it is desirable to transfer the multi-layer base and/subbase into an equivalent single layer with only one composite modulus value using Odemark's method of equivalent layer thickness (MET) (Odemark 1949). Note that the application of MET and use of a single composite modulus value was necessary in order to reduce the amount of SIF computations. This approach has been widely used for pavement response analyses (Ullidtz 1987) and FWD backcalculation (Ullidtz et al. 2006). However, whether or not this layer thickness equivalent concept works for SIF has not been fully explored in the literature. To verify this concept, one pavement structure consisting of an HMA layer, a base layer, two subbase layers, and the subgrade was analyzed, as shown in Figure 4-5. More than 10,000 SIF computations (K_I and K_{II}) were run using the *SA-CrackPro* program. Figure 4-6 shows the SIF comparisons between un-transformed and transformed pavement structures. It is obvious from the results shown in Figure 4-6 that the Odemark's equivalent thickness concept is still applicable to SIF computations. With this verification, the pavement structures being used for developing SIF regression equations can be simplified to consist of only HMA layer(s), a base layer, and the subgrade.

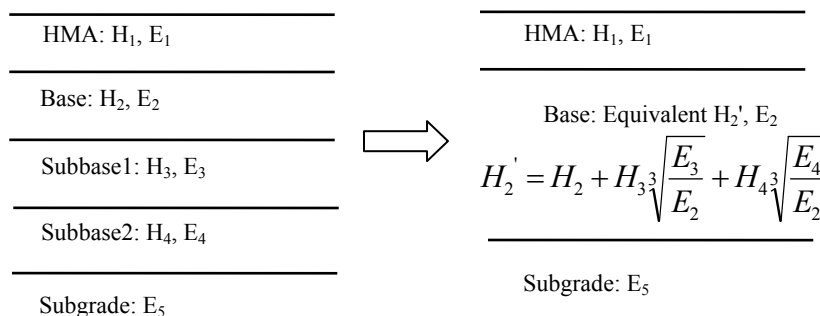
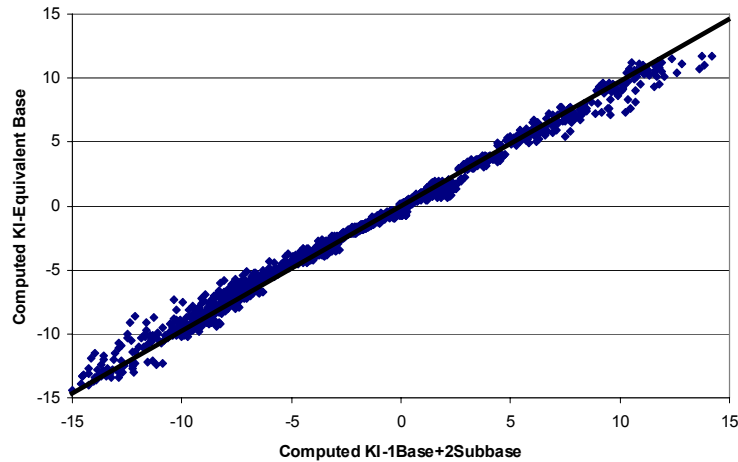
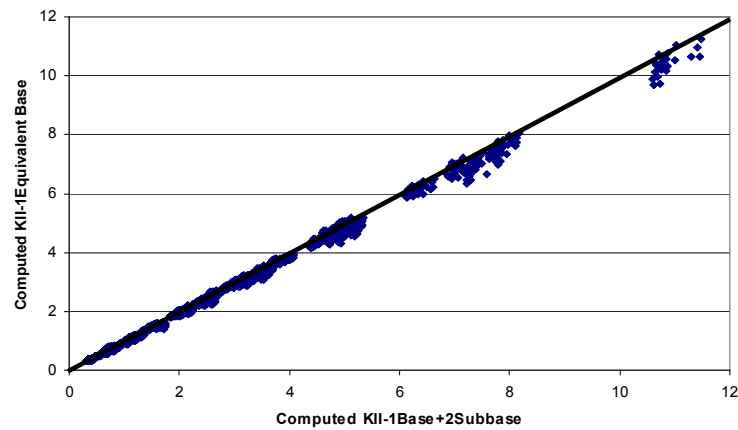


Figure 4-5. Pavement Structures and Associated Odemark's Transformation.



(a) K_I verification



(b) K_{II} verification

Figure 4-6. Verification of the MET Approach for Multi-Base Pavement Structures.

4.3.2.2.3 Consideration of a Multi-Layered HMA

Similarly, it is expected that the MET approach may be applicable to HMA layers. To check the validity of the MET approach for HMA layers, pavement structures with two-layer HMA and associated equivalent structures, as shown in [Figure 4-7](#), were analyzed. The results are presented in [Figure 4-8](#). It is clear that the MET approach is also applicable for HMA layers. Therefore, multi-layered HMA can also be treated as one HMA layer using the MET approach, which significantly simplifies the SIF computations and regression equation development.

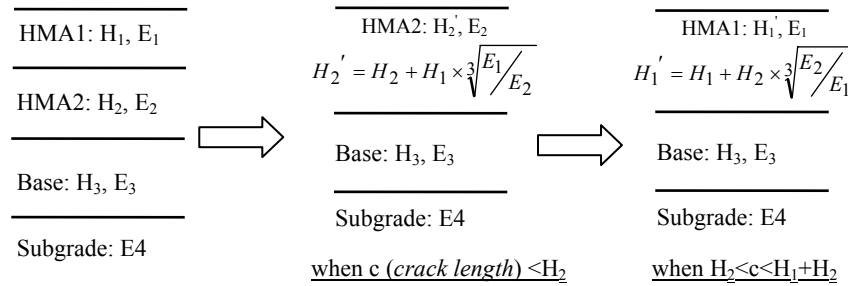
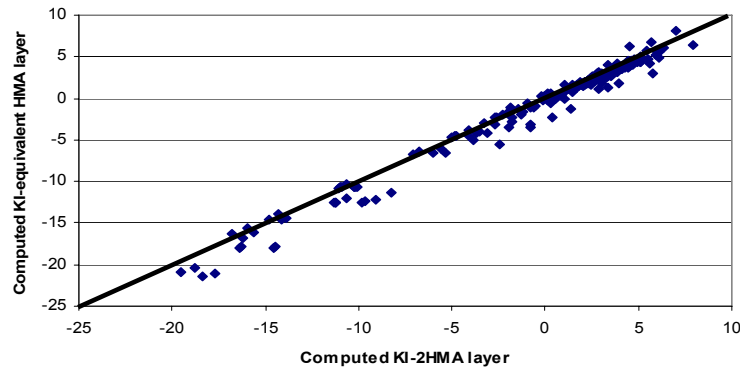
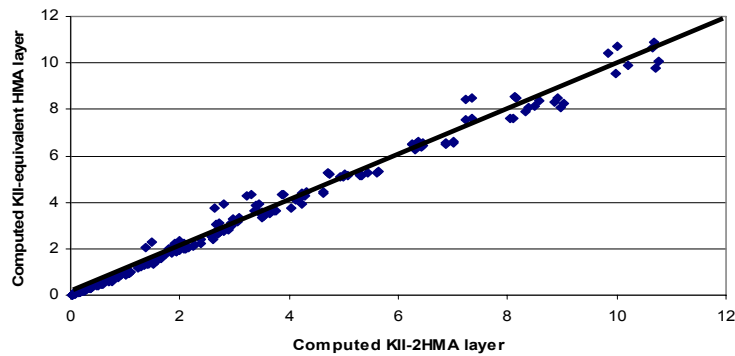


Figure 4-7. Two-HMA Pavement Structure and Associated Odemark's Transformation.



(a) K_I verification



(b) K_{II} verification

Figure 4-8. Verification of the MET Approach for Multi-HMA Pavement Structures.

4.3.2.2.4 Consideration of the Traffic Load Spectrum

For simplicity purposes, the multi-axle and multi-level traffic loading is often handled through the equivalent single axle load concept in different pavement design procedures around the world. However, this is not the case any more in the MEPDG (NCHRP 1-37A 2004). The impact of a full load spectrum on pavement response and associated performance is directly considered in the MEPDG (NCHRP 1-37A 2004). Therefore, it is also desirable to fully consider the influence of a varied traffic load spectrum when analyzing crack propagation. In particular, the influence of multi-axle and multi-level traffic loading on both the bending and shearing SIFs needs to be investigated. Detailed information is presented below.

4.3.2.2.4.1 Multi-Axle Traffic Loading Analysis

As stated by Huang (1993), “if one passage of each set of multiple axles is assumed to be one repetition, the damage caused by an 80 kN (18 kips) single axle is nearly the same as that caused by 160 kN (36 kips) tandem axles or 240 kN (54 kips) tridem axles; if one passage of tandem axles is assumed to be two repetitions and that the tridem axles to be three repetitions, the damage caused by 160 kN (36 kips) tandem and 240 kN (54 kips) tridem axles are two and three times greater than that by an 80 kN (18 kips) single axle. Both assumptions are apparently incorrect.” One approach Huang proposed is demonstrated in Figure 4-9. Figure 4-9 shows a tandem-axle load and associated tensile strain responses at different locations. The effect of this tandem-axle load on fatigue damage and associated crack initiation is often taken into account by considering both ϵ_a and $\epsilon_a - \epsilon_b$ (the difference between the strain computed at the 2nd (or 1st) axle load and the strain between axle load); see Figure 4-9. This is considered a reasonable approach because the damage caused by the horizontal tensile strains in both traffic direction and perpendicular to the traffic direction contribute to fatigue damage including the associated crack initiation process. Note that a similar approach has been used in VESYS (Jordahal and Rauhut 1983), KENLAYER (Huang 1993), and even in the MEPDG (NCHRP 1-37A 2004). Apparently, more research is needed in this area.

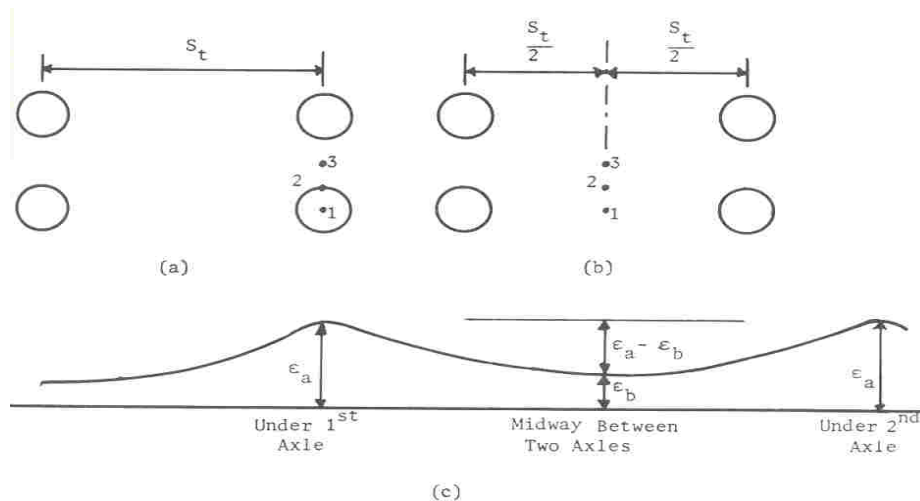
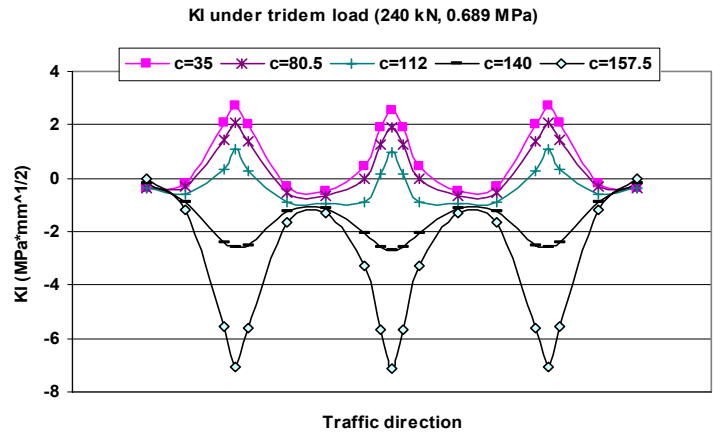


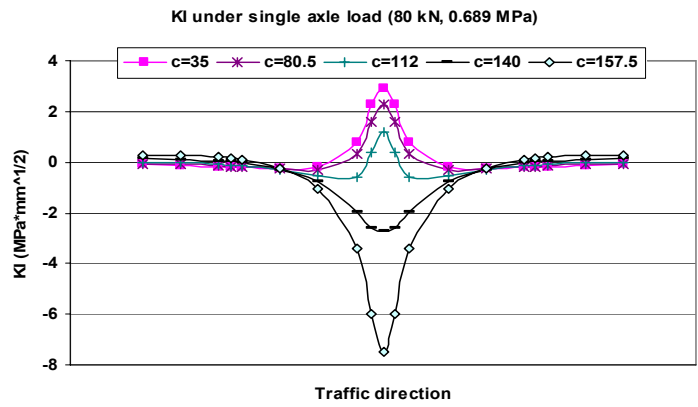
Figure 4-9. Tandem Traffic Loading (Huang 1993).

However, this approach may not be applicable to crack propagation because of the existence of a macro-crack. In the stage of crack propagation, a macro-crack in the direction perpendicular to traffic exists and ideally propagates in the vertical direction toward the pavement surface. The main contributions to the crack propagation are from K_I and K_{II} in traffic direction. As an example, a pavement structure consisting of the two HMA layers, a base layer, and the subgrade was used for investigating the K_I and K_{II} values corresponding to different crack lengths under a moving tridem-axle load passing over a crack. Figure 4-10 shows the K_I and K_{II} development at different crack lengths under a 240 kN tridem-axle load with a tire pressure of 0.689 MPa. For comparison purposes, the K_I and K_{II} development at different crack lengths under an 80 kN single axle load with a pressure of 0.689 MPa is also presented in Figure 4-10. The maximum K_I and K_{II} values under the tridem-axle load are almost the same as those under the single axle load. Extensive analysis results show that this observation is also true for other pavement structures under different types of multi-axle loads. Therefore, multi-axle loads,

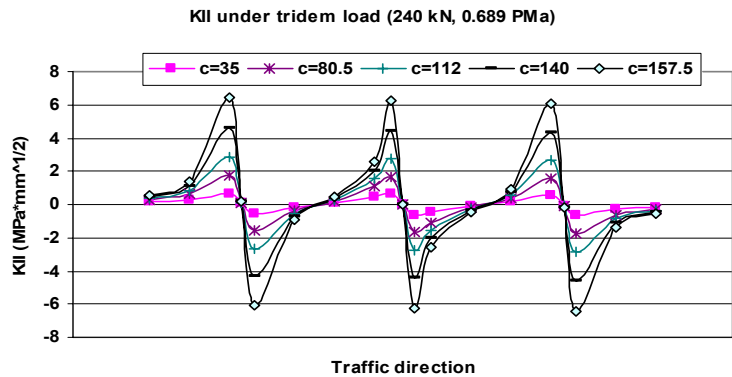
for simplicity, can be handled through multiple applications of the single axle load. Thus, the varied traffic loading spectrum can be easily analyzed as a multi-level single axle load issue, which is discussed in the subsequent section.



(a) K_I under tridem-axle load

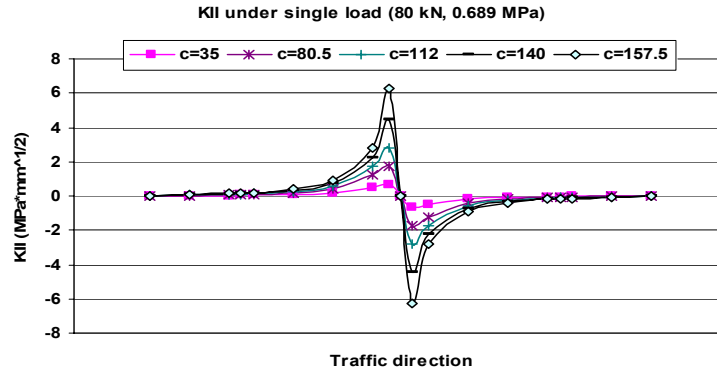


(b) K_I under single axle load



(c) K_{II} under tridem-axle load

Figure 4-10. K_I and K_{II} Comparison: Tridem vs. Single Axle Load.



(d) K_{II} under single axle load

Figure 4-10. K_I and K_{II} Comparison: Tridem vs. Single Axle Load (Continued).

4.3.2.2.4.2 Multi-Level Single Axle Load Configuration

For a single axle traffic load, its load level varies in a very wide range, which may result from varying tire pressure, contact area, and/or both. It is well known that both K_I and K_{II} are linearly proportional to the tire pressure for the same contact area. Thus, only one tire pressure of 0.689 MPa was used in this analysis. K_I and K_{II} under the other tire pressures can be readily determined.

In the case of varying contact area but keeping constant tire pressure, K_I and K_{II} must be specifically calculated for each contact area (= effective tire width \times tire length). The tire length and associated contact area increases with an increase in load level while keeping constant tire pressure, but the effective tire width hardly varies with load level (Fernando et al. 2006). Therefore, the increasing contact area is actually equal to an increase in the tire length, since the effective tire width does not vary with the load level.

After reviewing the default load spectrum in the MEPDG (NCHRP 1-37A 2004), four levels of single axle loads were recommended for developing SIF regression equations, as listed in Table 4-4. Note that a constant effective tire width of 158 mm was chosen based on the text book of "Pavement Analysis and Design" by Huang (1993). The SIF values corresponding to the other load level (or contact area/tire length) can be interpolated or extrapolated based on these SIF values.

Table 4-4. Four Single Axle Loads Recommended for SIF Analysis.

Axle load (kN)	Tire pressure (MPa)	Effective tire width (mm)	Tire length (mm)
17.8	0.689	158	41
49.0	0.689	158	112
80.1	0.689	158	184
111.3	0.689	158	255

Note: a standard single axle consists of two sets of dual tires.

Built on the above discussions, SIF regression equations are developed and presented in the next section.

4.3.2.3 SIF Regression Equations

Since the MET approach is validated for SIF, only pavement structures with an HMA layer, a base layer, and the subgrade ($E=50$ MPa), as shown in Figure 4-11, were analyzed to develop SIF regression equations. For each pavement structure, the SIF in both bending and shearing modes under four load levels (see Table 4-4) were calculated. Note that the bending mode refers to the loading centered just at the top of the crack; the shearing mode refers to the loading edge at the top of the crack. Therefore, a total of 8 SIF regression equations have been developed based on more than 20,000 computations. Only the SIF (K_I and K_{II}) regression equations under 80.1 kN single axle load are presented below. The goodness of fit is shown in Figure 4-12 in which all SIF data computations are plotted. All the other regression equations are listed in Appendix A. Note that the K_I and K_{II} equations have the same polynomial expression format (Equation 4-37):

$$K_I \text{ (or } K_{II}) = K_a \times [K_b \times (c/H_1)^3 + K_c \times (c/H_1)^2 + K_d \times (c/H_1) + K_e] \quad (4-37)$$

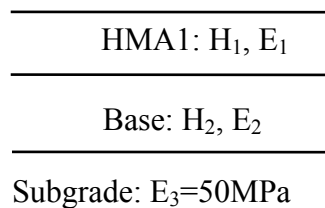


Figure 4-11. Three-Layered Pavement Structures Used for Developing SIF Equations.

4.3.2.3.1 K_I Regression Equation for Single Axle Load of 80.1 kN

$$K_a = -28.2351 \times \log H_2 - 0.03445 \times (\log E_2)^{5.03578} - 92.5705 \times (\log H_1)^2 + 384.5243 \times \log H_1 + 13.57506 \times (\log E_1)^2 - 57.1769 \times \log E_1 - 242.6717 \quad (4-38)$$

$$K_b = -13.9384 \times [3.91207 \times (\log E_1)^{-0.00829} \times (\log E_2)^{0.01342} - 3.95065] \times (-14.2644 \times c^{-0.33181} + 2.11619) \quad (4-39)$$

$$K_c = -1.06934 \times [-2.6973 \times 10^{-5} \times (\log E_1)^{8.89101} \times (\log E_2)^{-6.14968} - 0.18365] \times (-1.50466 \times c^{0.22368} + 4.65218) \quad (4-40)$$

$$K_d = -1.29624 \times [16.16007 \times (\log E_1)^{0.21666} \times (\log E_2)^{-0.22422} - 17.0456] \times (-3.18193 \times c^{-0.66665} - 0.00990) \quad (4-41)$$

$$K_e = 0.73249 \times (\log E_1)^{-0.16697} \times (\log E_2)^{0.19116} - 0.67707 \quad (4-42)$$

4.3.2.3.2 K_{II} Regression Equation for Single Axle Load of 80.1 kN

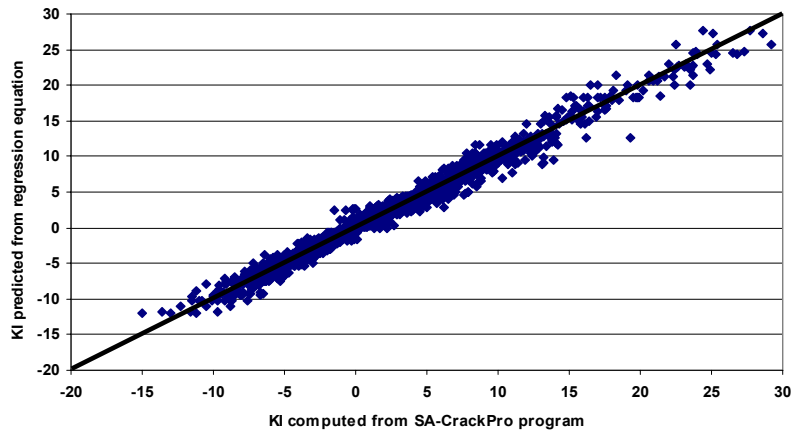
$$K_a = -4.1658 \times \log H_2 + 4.9293 \times (\log E_2)^{0.8297} - 6.0112 \times (\log H_1)^2 - 33.0880 \times \log H_1 - 0.2581 \times (\log E_1)^2 - 0.8718 \times \log E_1 + 128.3965 \quad (4-43)$$

$$K_b = 0.5743 \times (E_1/E_2)^{0.3055} \times (1.1128 \times c^{-0.2289} - 0.2218) \quad (4-44)$$

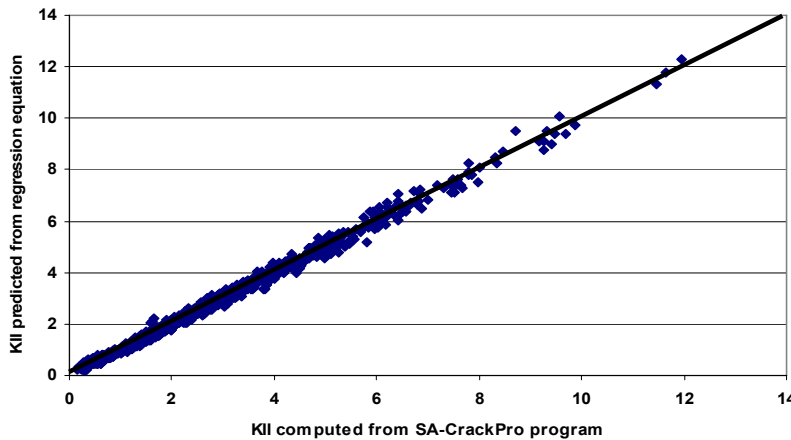
$$K_c = 0.1762 \times (E_1/E_2)^{0.2076} \times (0.0008 \times c^{1.4041} - 1.7494) \quad (4-45)$$

$$K_d = 0.5394 \times (E_1/E_2)^{0.2268} \times (0.4059 \times c^{0.1237} - 0.3068) \quad (4-46)$$

$$K_e = -9.5338 \times 10^{-6} \times (E_1/E_2)^{1.6938} - 0.0027 \quad (4-47)$$



(a) K_I plot



(b) K_{II} plot

Figure 4-12. SIF Values Predicted by Regression Equation vs. SIF Calculated by *SA-CrackPro* Program.

4.3.3 Overlay Tester for HMA Fracture Properties: A and n

As discussed previously, the other two key parameters of the proposed fatigue cracking model are fracture properties: A and n . These two parameters are directly related to both crack initiation and crack propagation stages so that it is critical to accurately measure these two parameters in the laboratory.

Different laboratory tests for characterizing the HMA fracture properties (A and n) have been conducted for a long time (Majidzadeh et al. 1970; Salam 1971; Salam and Monismith 1972; Majidzadeh et al. 1976; Germann and Lytton 1979; Elmitiny 1980; Pickett and Lytton 1983; Button and Lytton 1987; Molenaar 1983; Jacobs 1995; Jacobs et al. 1996; Erkens et al. 1997; Roque et al. 1999). Among these tests, the most systematic laboratory studies on fracture properties (A and n) were conducted by Molenaar and his associates (Molenaar 1983; Jacobs 1995; Erkens et al. 1997). The most often used test is the repeated direct tension test. However, this test method is relatively difficult to conduct and accordingly has not been widely used in the

field of asphalt pavement. Recently, Zhou et al. (2007) developed a very simple, quick test procedure to determine fracture properties of HMA mixtures (A and n) using the OT. All the above test procedures, including the OT, address only Mode I fracture (opening and/or bending mode loading). Regarding the Mode II fracture (shearing mode loading), there is to date no simple performance test available to adequately characterize this fracture mode. In most cases, it is assumed that Modes I and II share the same fracture properties (A and n).

The key parts of the OT are shown in Figure 4-13; it consists of two steel plates, one fixed and the other that moves horizontally to simulate the opening and closing of joints or cracks in the old pavements beneath HMA overlays. The OT specimen is glued to the two steel plates, with half of its length resting on each plate. Generally, the OT is run in an opening displacement-controlled cyclic mode at a predefined loading rate. The key components and features of this procedure are described below.

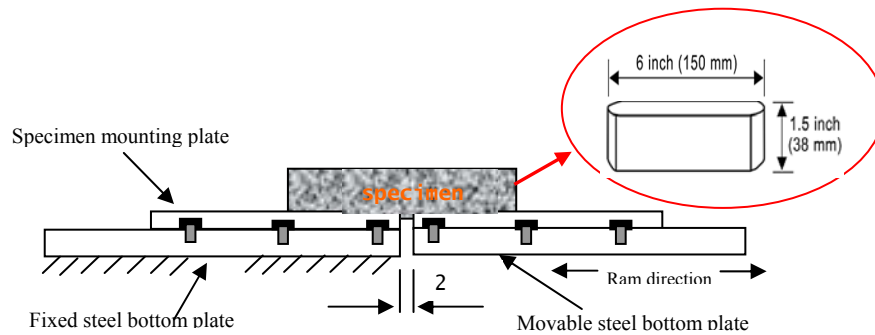


Figure 4-13. OT Concept.

4.3.3.1 OT Specimen

One important feature of the OT for fracture properties (A and n) is the specimen size: 6-inch (150 mm) long by 3-inch (75 mm) wide by 1.5-inch (38 mm) high. This size of specimen can be easily cut from a sample prepared by the SGC or from a field core. Figure 4-14 shows the OT specimen preparation sequence for a SGC molded specimen.

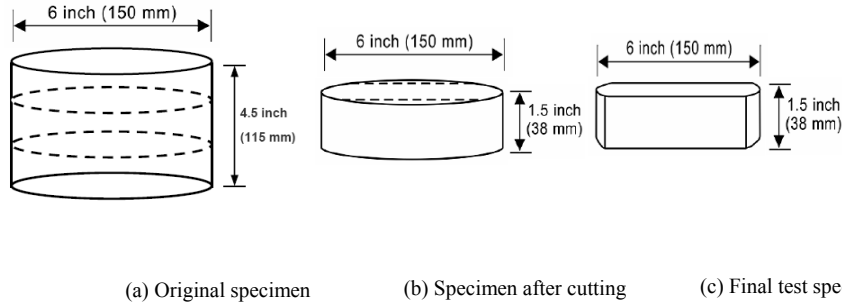


Figure 4-14. OT Specimen Preparation from SGC Molded Sample.

4.3.3.2 Enhanced OT Test Procedure for Fracture Properties (A and n)

Over the past several years, the regular OT test (Tex-248-F) was used for determining HMA fracture properties. Two problems have been identified with the regular OT test for HMA fracture properties. One is the unknown specimen modulus that is critical to determine the fracture parameter A value; the other is that the opening displacement of 0.025 inch (0.64 mm) under regular OT test is too big for many Texas limestone mixes resulting in a very low number of cycles to failure for the regular OT test that are not enough for fracture properties determination. After recognizing these two problems, an enhanced, two-step OT test procedure was proposed and is presented next. It is worth noting that the previously published 0-5798-P1: Laboratory and Field Procedures Used to Characterize Materials does not contain the latest development on determining fracture properties (A and n). The following steps should be followed instead of the previous ones documented in the 0-5798-P1.

- Step 1, OT-E test:

First, to perform the OT-E test using the OT machine, the regular OT machine needs to be enhanced with three additional apparatus: 1) sample end plates and glue gig, 2) connecting plates, and 3) external LVDTs. Figure 4-15 shows the sample end plates, glue gig, and glued specimen within the glue gig. Figure 4-16 illustrates the connecting plates and associated assembling steps. Figure 4-17 displays the external LVDTs and overview of the specimen with mounted LVDTs. Note that the gauge length of the LVDTs is 3.5 inches (88 mm).

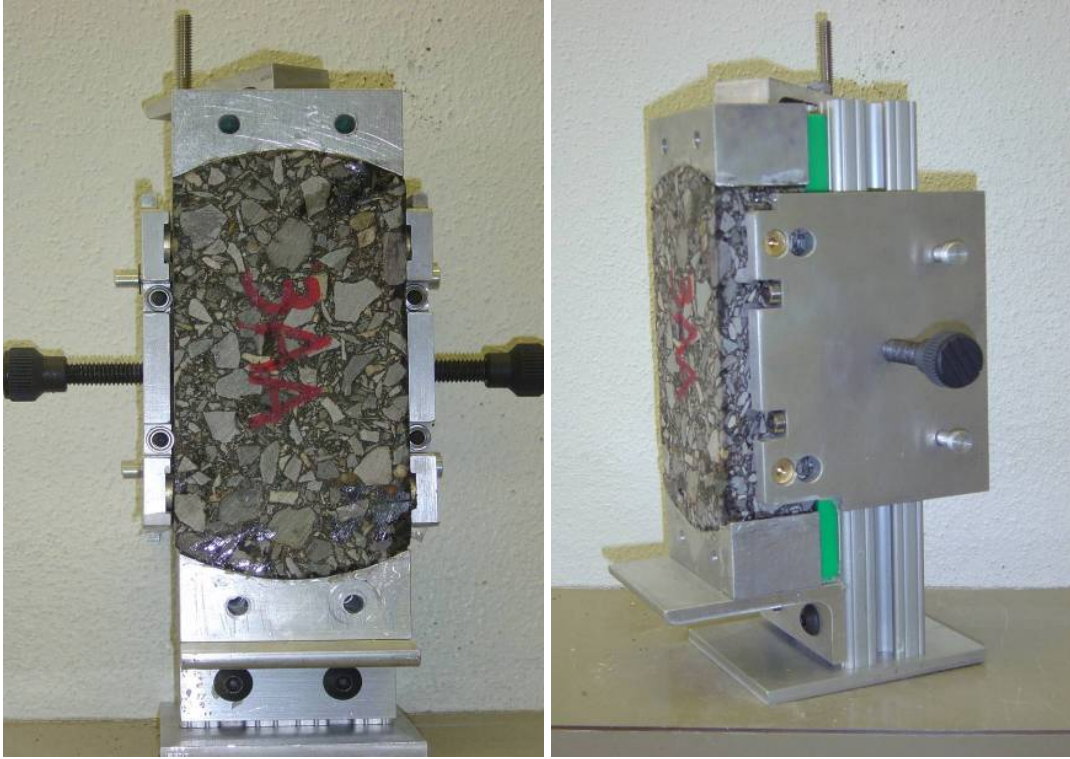


Figure 4-15. Sample End Plates and Glue Gig.

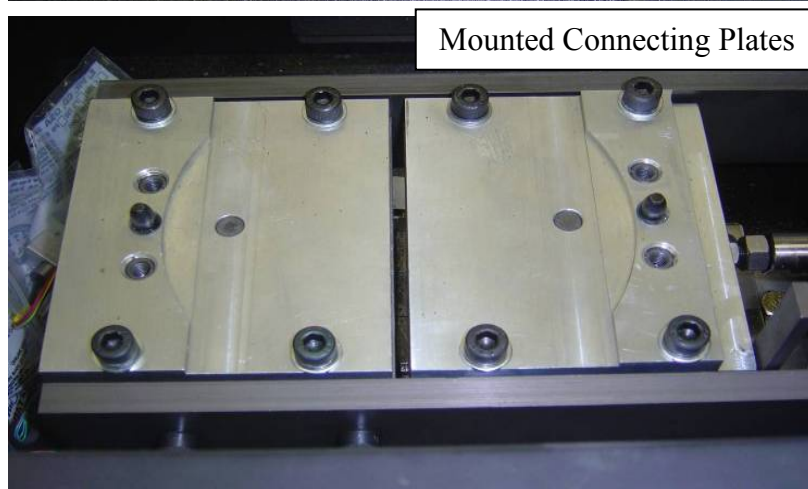


Figure 4-16. Connecting Plates.

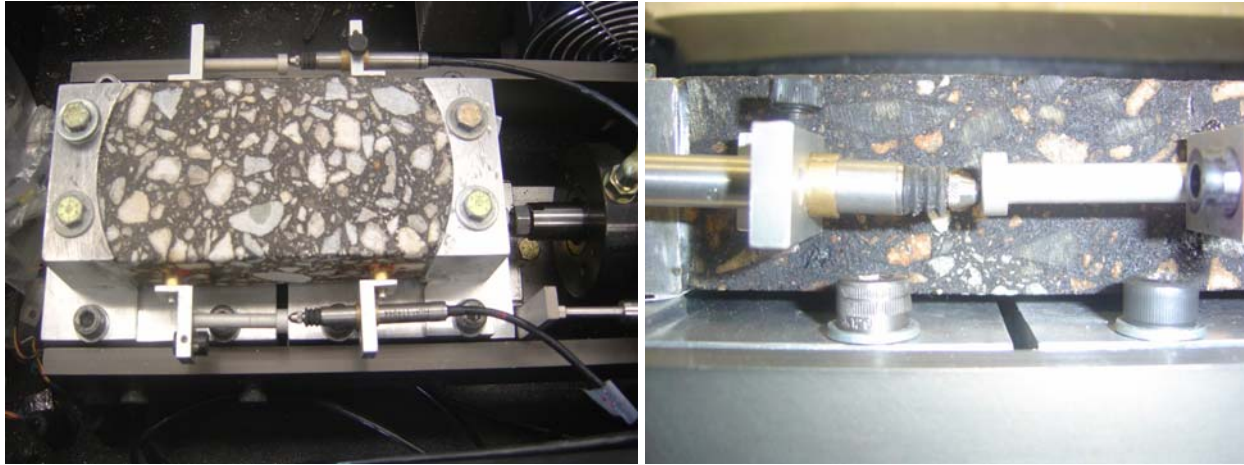


Figure 4-17. External LVDTs and Overview of LVDT Mounted Specimen.

Second, the main purpose of the OT-E test here is not to develop the E master curve but rather to determine the E value for later SIF calculation. Thus, the proposed OT-E test is to be conducted at the same test temperature and frequency in a displacement controlled tension mode as those used for the standard OT test. For example, if the OT is run at 77 °F (25 °C) and 0.1 Hz (10 sec per cycle), then the corresponding OT-E test should be performed at 77 °F (25 °C) and 0.1 Hz as well, but its opening displacement should be much smaller so that no damage will occur to the specimen. The recommended opening displacement is 0.0009 inch (0.023 mm) and the corresponding strain level within the specimen is about 75 microstrain, which is consistent with the MEPDG dynamic modulus test (AASHTO TP62-03).

Third, the proposed loading waveform for OT-E test is haversine-shaped. There are two reasons to choose the haversine loading waveform. One is that most modulus test procedures, including the MEPDG dynamic modulus test, use this type of loading waveform. The other reason is that it is easy to analyze and model the stress-strain curves (Equations 4-48 and 4-49) and then determine the modulus value using Equation 4-50:

$$\text{stress:} \quad \sigma = \sigma_0 \sin(\omega t) \quad (4-48)$$

$$\text{strain:} \quad \varepsilon = \varepsilon_0 \sin(\omega t - \theta) \quad (4-49)$$

$$\text{dynamic modulus:} \quad E = \frac{\sigma_0}{\varepsilon_0} \quad (4-50)$$

where σ_0 is peak stress; ε_0 is peak strain; E is dynamic modulus; θ is phase angle; ω is angular velocity; and t is time.

- Step 2, OT test:

A modified version of TxDOT test method Tex-248-F should be followed when running the OT for fracture properties (A and n). As noted previously, the minor required changes are:

- 1) Reduce the opening displacement to 0.017 inch (0.43 mm) from the regular 0.025 inch (0.63 mm).
- 2) Run the OT until it reaches 100 cycles. If the OT stopped within less than 50 cycles, reduce the opening displacement to 0.015 inch or less, run it again until it reaches a minimum of 50 cycles.

After performing these two OT tests, fracture properties, A and n can be determined based on the collected test data. Detailed information is given in next section.

4.3.3.3 Determination of Fracture Properties: A and n

HMA mixtures are complex materials. However, for simplicity and practical applications, HMA mixtures are often assumed to be quasi-elastic materials represented by dynamic modulus and Poisson's ratio. With this assumption, the well-known Paris' law (Paris and Erdogan 1963) shown in Equation 4-51 can be used to describe crack propagation of HMA mixtures.

$$\frac{dc}{dN} = A(\Delta K)^n \quad (4-51)$$

where c is crack length; N is number of load repetitions; dc/dN is crack speed or rate of crack growth; ΔK is change of stress intensity factor (SIF); and A and n are fracture properties of material.

In view of Equation 4-51, it can be seen that the information required for determining fracture properties (A and n) includes 1) crack length (c) corresponding to a specific number of load repetitions (N) and 2) the SIF corresponding to any specific crack length (c). The proposed approach for determining the SIF and crack length (c) is discussed as follows.

4.3.3.3.1 Crack Length Estimation

To monitor crack length growth, researchers have used several different techniques such as crack foil (Jacobs 1995) or the Digital Image Correlation (DIC) techniques (Seo et al. 2004). Recently, TTI purchased a DIC system with *two cameras* to monitor crack growth on both sides of the specimen. It was found that crack propagation is a very complicated phenomenon. Even for such a small OT specimen, a crack grows in a 3-D field rather than a 2-D cross-sectional field. Furthermore, the crack growth rate on one side of the specimen, in most cases, is different from that on the other side. HMA mix heterogeneity, non-uniform air void distribution, and residual stresses are considered as some of the contributing factors for the observed differences in the crack growth rate on either side of the OT specimen during testing. Recognizing the complexity of crack growth, some simplification and assumptions were made in this project in order to practically estimate crack length. These assumptions are:

- 1) an equivalent (or ideal) crack starts from the bottom at the center of the OT specimen and propagates vertically (in a 2-D field) to the top surface of the specimen;
- 2) the reduction of the maximum load from the first cycle is attributed to crack development/growth; and
- 3) as assumed previously, HMA mixtures are quasi-elastic and represented by dynamic modulus and Poisson's ratio ($\mu=0.35$). Note that the visco-elastic properties of HMA mixtures are indirectly considered through using dynamic modulus, which is time-temperature dependent.

With these assumptions, a backcalculation approach can be used for crack length estimation. Actually, this approach has been successfully used by [Jacobs \(1995\)](#) and later [Roque et al. \(1999\)](#) to estimate the crack length from the recorded load and/or strain. In particular for the OT, the maximum load required to reach a specific maximum opening displacement (MOD-gap opening between the plates) is proportional to the dynamic modulus of the OT specimen, and decreases with crack length growth, provided that the MOD is constant. To exclude the influence of the dynamic modulus and the MOD, the maximum load corresponding to any crack length was normalized to the maximum load corresponding to “zero” crack length, which is determined through extrapolation. [Figure 4-18](#) shows the relationship between the normalized maximum load (y) and crack length (x) developed through FE calculations. A corresponding regression equation is also presented in [Figure 4-18](#).

Since the maximum load at each cycle is automatically recorded during the OT testing, it is easy to estimate the equivalent crack length (c) for each specific cycle (N) from [Figure 4-18](#), and then develop the relationship between the c and N , and accordingly dc/dN vs. N .

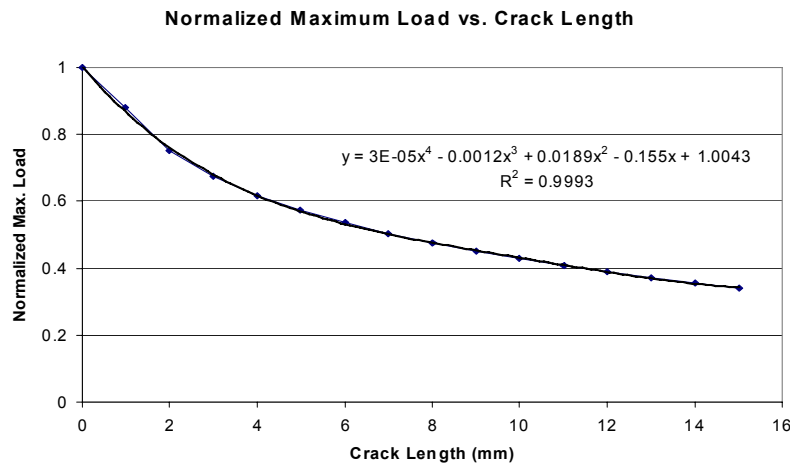


Figure 4-18. Normalized Maximum Load vs. Crack Length.

4.3.3.3.2 SIF Determination

Based on the previous assumptions (see 4.3.3.3.1 Crack Length Estimation), the SIF was specifically analyzed for OT specimens using a 2-D *CrackPro* FE program (a modified *SA-CrackPro* program). The SIF is linearly proportional to the dynamic modulus (E) of the OT specimen and the MOD. Therefore, the SIFs corresponding to variable crack lengths (c) were calculated only for $E = 1$ MPa (0.145 ksi) and MOD = 1 mm. These results are presented in

Figure 4-19. To facilitate implementation, a regression equation shown in Figure 4-19 was developed for the SIF vs. crack length at the condition of $E=1$ MPa (0.145 ksi) and $MOD = 1$ mm. For any other E and MOD combinations, the corresponding SIF can be determined by Equation 4-52:

$$SIF = 0.2911 * E * MOD * c^{0.4590} \quad (4-52)$$

where E is the dynamic modulus; MOD is the maximum opening displacement; and c is the crack length.

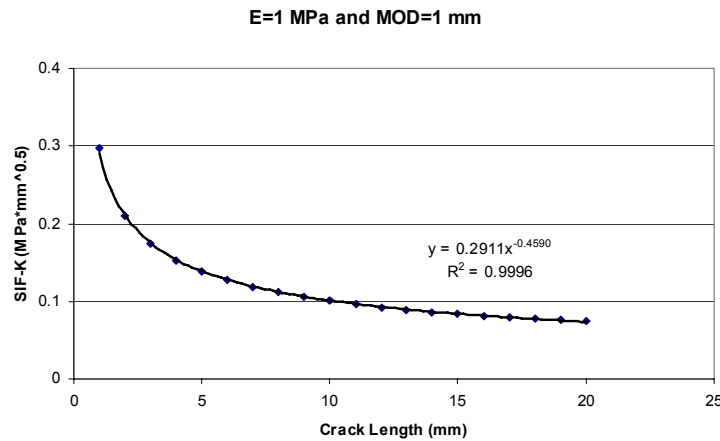


Figure 4-19. Calculated SIF vs. Crack Length.

Additionally, it can be seen that the SIF shown in Figure 4-19 decreases rapidly at the beginning and its decreasing rate becomes smaller and smaller with crack length growth. This observation indicates that the initial crack propagation stage is very important to determine reasonable fracture properties of HMA mixtures for the OT, which means that the required fracture properties should be determined from the initial stage of the OT testing (perhaps within 20 minutes). This feature separates the displacement-controlled OT from all other load-controlled fracture tests, such as direct tension test (Majidzadeh et al. 1970; Salam 1971; Molenaar 1983; Jacobs 1995) and indirect tension test (Roque et al. 1999), because these load-controlled tests are often focused on the late crack propagation stage where the SIF increases rapidly so that these tests generally take a very long time (i.e., hours.)

4.3.3.3 Determination of Fracture Properties: A and n

With known SIF (K) and crack growth rate (dc/dN), the fracture properties (A and n) can be readily determined. Figure 4-20 shows the five steps of determining the HMA fracture properties (A and n). Currently, a Microsoft© Excel macro named *TTI-OT* has been developed to automatically analyze the OT test results and determine the HMA fracture properties (A and n).

4.3.3.4 Features of the OT for Determining HMA Fracture Properties: A and n

Different from other test methods for determining the HMA fracture properties, the OT method has the following three features:

- 1) Specimen size (6-inch [150 mm] long by 3-inch [75 mm] wide by 1.5-inch [38 mm] high): This size of specimen can be easily cut from samples compacted by the SGC or from field cores;
- 2) Specimen preparation (Figure 4-14): neither a hole in the center nor a notch at the bottom of the specimen is required, since a crack is always initiated in the first cycle;
- 3) Testing time: In contrast to other fracture test types (i.e., IDT or repeated direct tension test), which generally have lengthy testing times, the OT for fracture properties (A and n) can generally be done within 20 minutes.

With the above developed fatigue cracking model, the next step is to calibrate it using field fatigue cracking data and then validate it using different field fatigue cracking data.

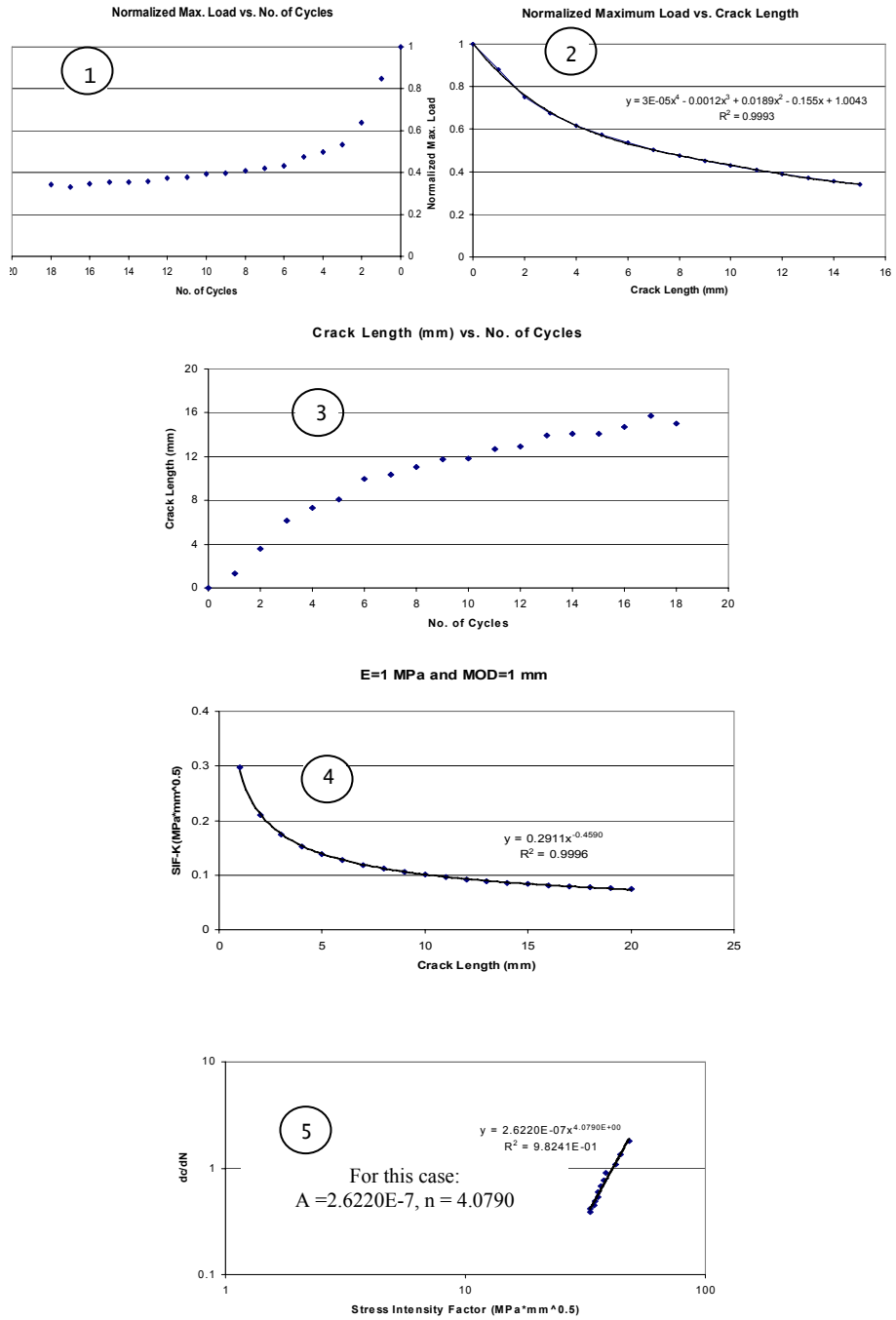


Figure 4-20. Determination of Fracture Properties: A and n .

4.4 CALIBRATION OF THE DEVELOPED FATIGUE CRACKING MODEL

The purpose of calibrating the developed fatigue cracking model is to determine the calibration factors k_{p1} and k_{p2} in Equation 4-32. In this research project, the field fatigue cracking data measured from the NCAT pavement test track 2006 were used to determine parameters k_{p1} and k_{p2} . Figure 4-21 shows the 2006 experimental sections of the test track. The ESALs were applied with four fully loaded trucks at 45 mph with 3 trailers per tractor. Each tractor pulled a load of approximately 152,000 lb, including approximately 12,000 lb for the front steer axle and the rest spreading over the other 7 axles. At the end of December 2008, around 10 million ESALs had been applied to the test track. Note that some test sections (such as N3, N4, N6, and N7) marked in blue color in Figure 4-21 are test sections built in 2003, and those sections had been trafficked 10 million ESALs before starting the 2006 traffic.

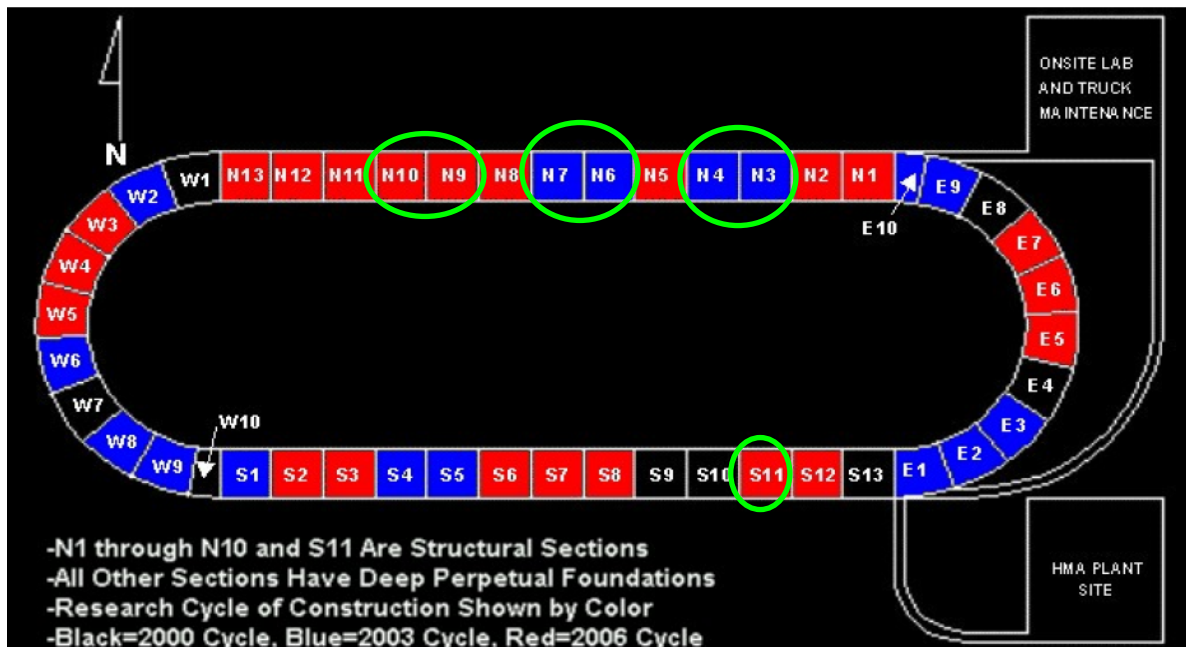


Figure 4-21. 2006 Experimental Sections of the NCAT Test Track.

A total of 7 sections, N3, N4, N6, N7, N9, N10, and S11 were selected for determining the calibration factors k_{p1} and k_{p2} . Among these seven sections, fatigue cracking occurred at three sections N6, N7, and S11, as shown in Figure 4-22. But there is no sign of any fatigue cracking at sections N3, N4, and N9, as indicated in Figure 4-23. Section N10 is a very interesting one, because it showed fatigue cracking in the surface, but it was found later that the surface cracking was not traditional fatigue cracking. Instead, it was due to layer delamination, as evidenced in Figure 4-23. Therefore, Section N10 was evaluated as having no traditional fatigue cracking. In summary, three sections (N6, N7, and S11) with fatigue cracking and four sections (N3, N4, N9, and N10) without fatigue cracking were used for the fatigue cracking model calibration.

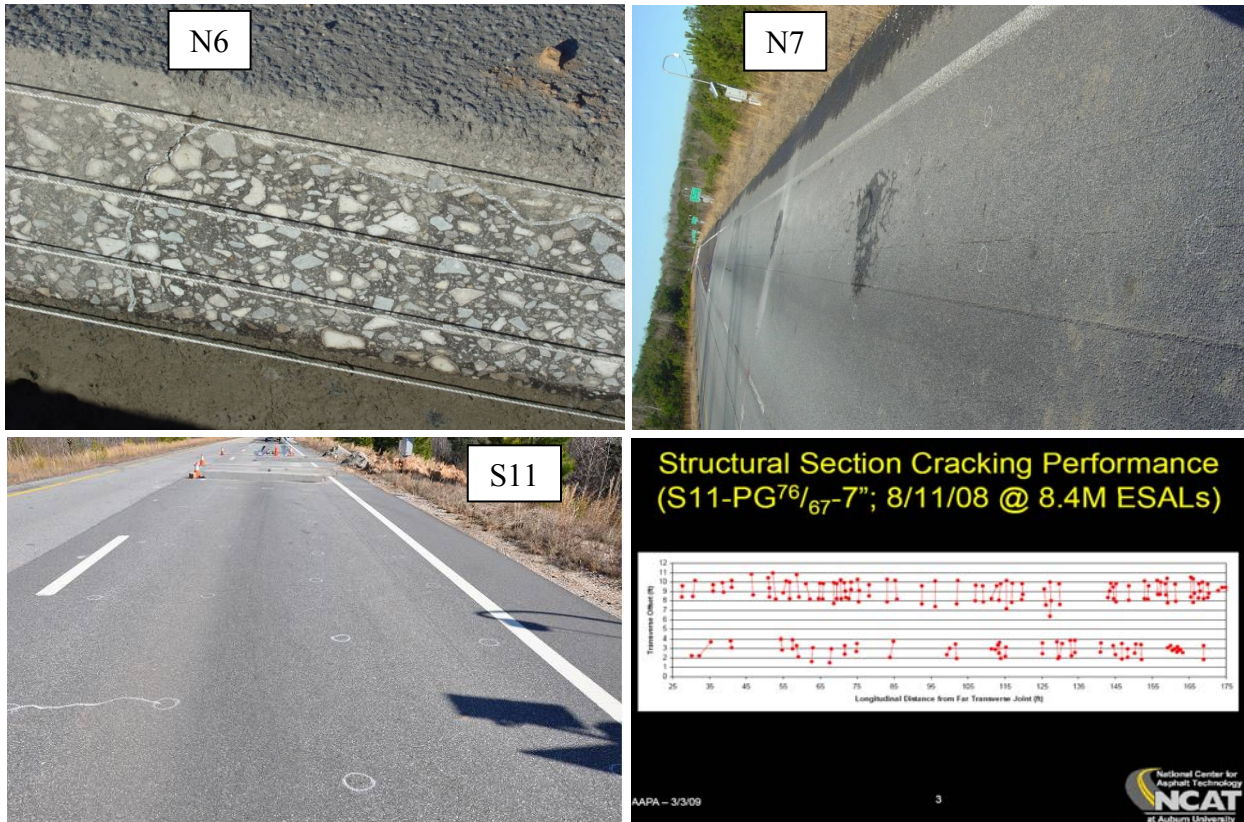


Figure 4-22. Sections with Fatigue Cracking: N6, N7, and S11.



Figure 4-23. Sections without Fatigue Cracking: N3, N4, N9, and N10.

The structural information of the selected seven test sections is displayed in [Figure 4-24](#). Plant mixes sampled from these seven test sections during construction were compacted using SGC to mold samples for the dynamic modulus test. The dynamic modulus test was conducted over five different temperatures of 14, 40, 70, 100, and 130 °F and six loading frequencies of 25, 10, 5, 1, 0.5, and 0.1 Hz for each test temperature. [Figure 4-25](#) shows the dynamic modulus master curves for the mixes of the selected seven test sections. Note that the dynamic modulus test data for Sections N3, N4, N6, and N7 were from the NCAT research report 06-01: Material Properties of the 2003 NCAT Test Track Structural Study ([Timm and Priest 2006](#)), because these sections were built in 2003 and no plant mixes were available to TTI.

N3	N4	N6	N7
9' HMA with PG 67-22	9' HMA with PG 76-22	7' HMA with PG 67-22	7' HMA with PG 67-22
6' Granular base	6' Granular base	6' Granular base	6' Granular base
Subgrade	Subgrade	Subgrade	Subgrade

N9	N10	S11
14' HMA	7' HMA	7' HMA
6' Granular base	6' Granular base	6' Granular base
Subgrade	Subgrade	Subgrade

Figure 4-24. Pavement Structural Information of NCAT Sections Used for Fatigue Cracking Model Calibration.

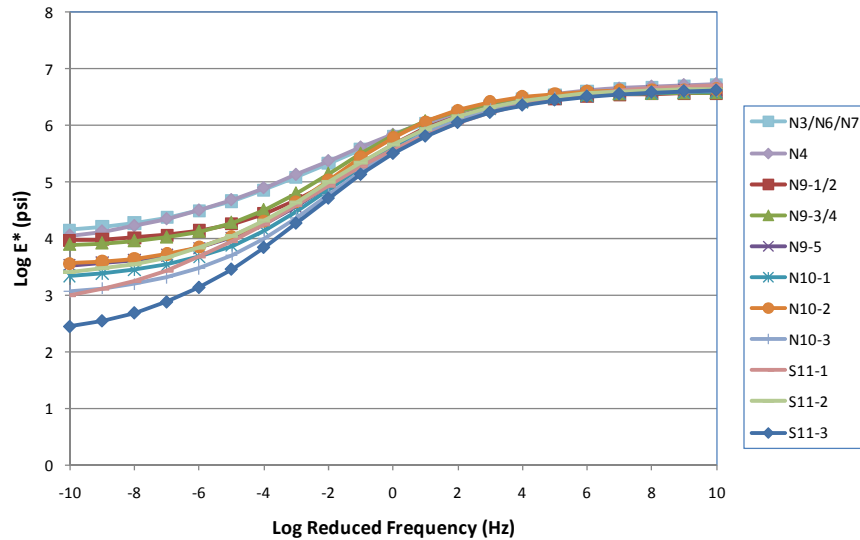


Figure 4-25. Dynamic Modulus Master Curves of the HMA Mixes Used for Fatigue Cracking Calibration.

Furthermore, field cores were taken from the selected seven test sections for the enhanced OT test to determine HMA layer fracture properties. The previously proposed two-step OT tests (Figure 4-26) were followed and the measured HMA layer fracture properties of the test sections are listed in Table 4-5.

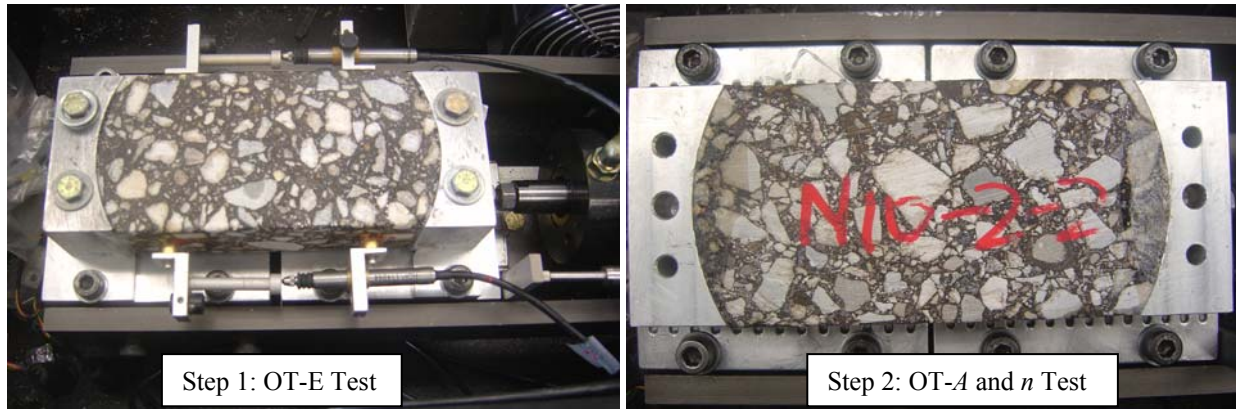


Figure 4-26. Two-Step OT Test for HMA Fracture Properties: A and n .

Table 4-5. Measured HMA Fracture Properties.

Section	A	n
N3	4.0293E-08	4.3323
N4	6.2989E-09	3.8249
N6	2.8479E-08	4.3440
N7	2.8479E-08	4.3440
N9-1/2	2.1539E-08	4.2272
N9-3/4	3.8255E-08	4.6643
N9-5	1.0327E-08	4.3160
N10-1	8.2174E-09	4.3261
N10-2	2.0208E-08	4.2860
N10-3	3.3391E-08	4.8566
S11-1	1.0106E-07	4.4456
S11-2	1.0106E-07	4.4456
S11-3	3.4440E-07	4.3028

A trial and error approach was to determine both k_{p1} and k_{p2} while minimizing the difference between the predicted and the measured fatigue cracking, as shown in [Figure 4-27](#). The final values of the calibration factors k_{p1} and k_{p2} are: $k_{p1}=2$ and $k_{p2}=4$. Note that the measured surface cracking at Section N10 was due to delamination, as discussed previously.

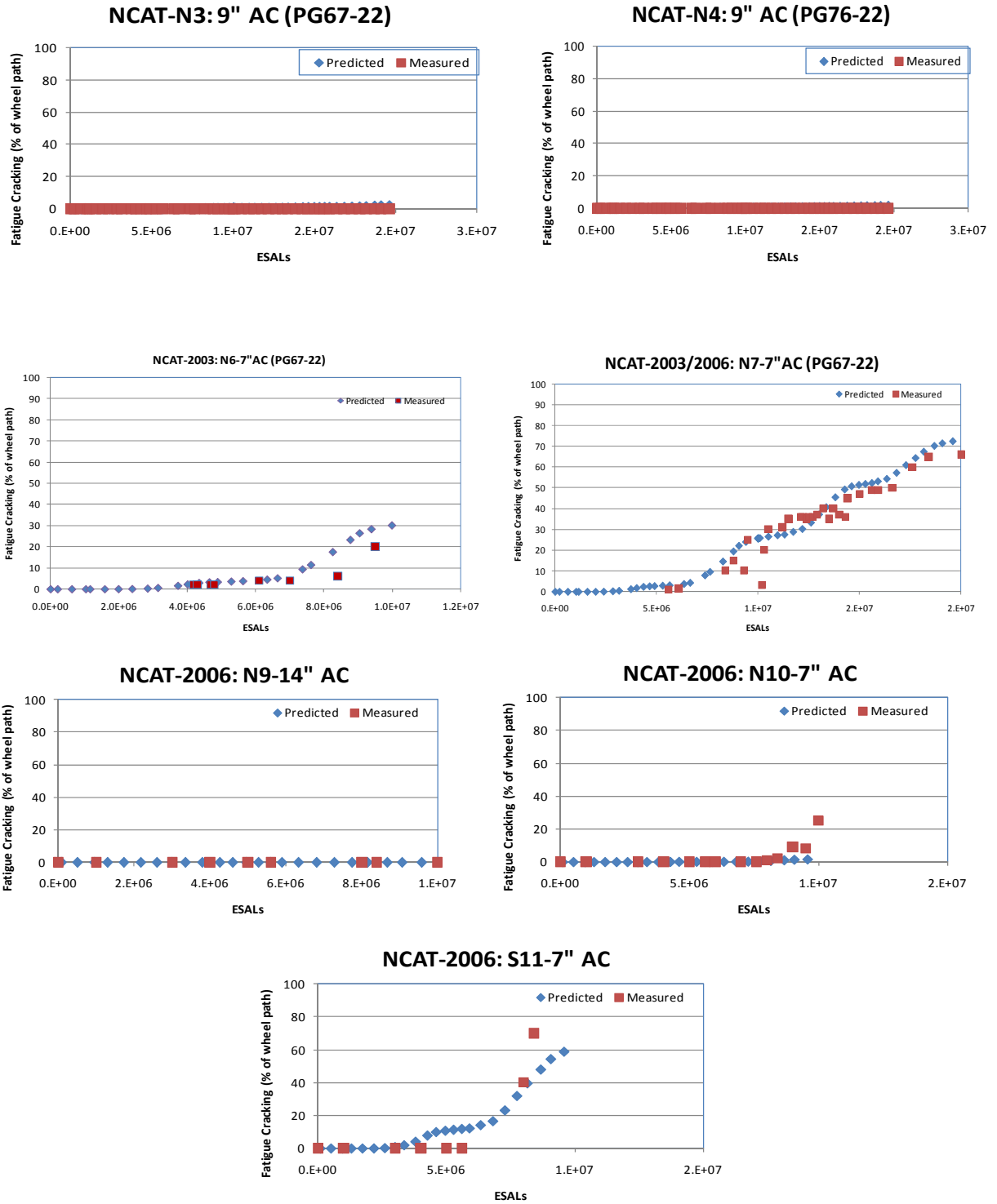


Figure 4-27. Comparisons of the Measured and Predicted Fatigue Cracking Development.

4.5 VALIDATION OF THE CALIBRATED FATIGUE CRACKING MODEL

Similar to the rutting model validation, an independent data source was used to validate the accuracy and reasonableness of the calibrated fatigue cracking model. In this study, the fatigue cracking data of two structural test sections (N1 and N2) collected from the NCAT Test Track 2003 were employed for this validation. [Figure 4-28](#) shows fatigue cracking observed in Section N1, and [Figure 4-29](#) further evidences that the cracking observed in the surface was traditional bottom-up fatigue cracking.

[Figure 4-30](#) shows the structural layer information of the two sections (N1 and N2) used for model validation. Again, the dynamic modulus test data for Sections N1 and N2, as shown in [Figure 4-31](#), were from the NCAT research report 06-01: Material Properties of the 2003 NCAT Test Track Structural Study, because these sections were built in 2003 and no plant mixes were available to TTI. Fortunately, several field cores from these two test sections saved for record were provided to TTI for fracture properties measurement. Again, the two-step enhanced OT test was performed on the cores and the determined fracture properties (A and n) for Sections N1 and N2 are listed in [Table 4-6](#). Finally, the comparisons between the predicted and the measured fatigue cracking development are shown in [Figure 4-32](#). Generally, the predicted fatigue cracking matches the measured fatigue cracking in the field. Thus, the calibrated fatigue cracking model is valid for pavement sections evaluated in this study. Further testing should be performed to determine more global validity.



Figure 4-28. Observed Fatigue Cracking at Section N1 (NCAT 2005).



Figure 4-29. Evidence of Bottom-Up Fatigue Cracking.

N1	N2
5' HMA with PG 76-22	5' HMA with PG 67-22
6' Granular base	6' Granular base
Subgrade	Subgrade

Figure 4-30. Pavement Structural Information of NCAT 2003 Sections N1 and N2.

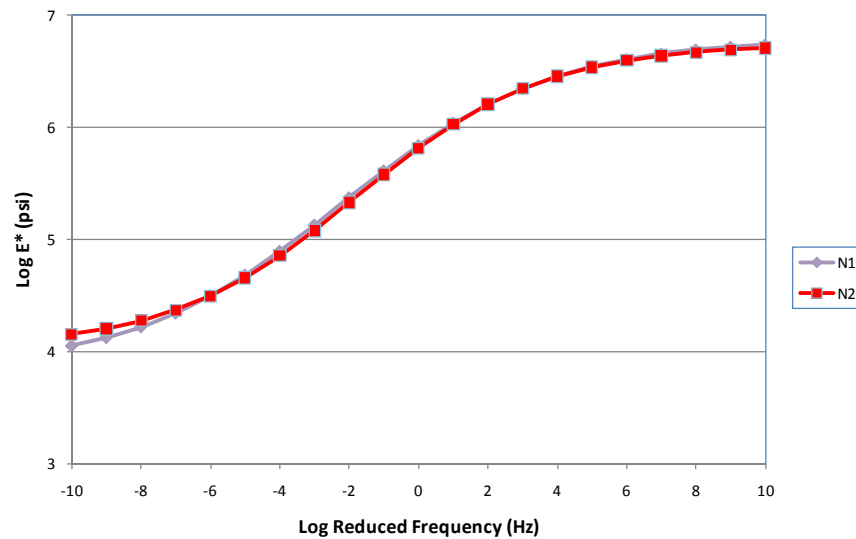


Figure 4-31. Dynamic Modulus Master Curves of HMA Mixes Used for Sections N1 and N2.

Table 4-6. Measured HMA Fracture Properties.

Section	A	n
N1-2003	6.2989E-09	3.8249
N2-2003	3.4429E-08	5.1337

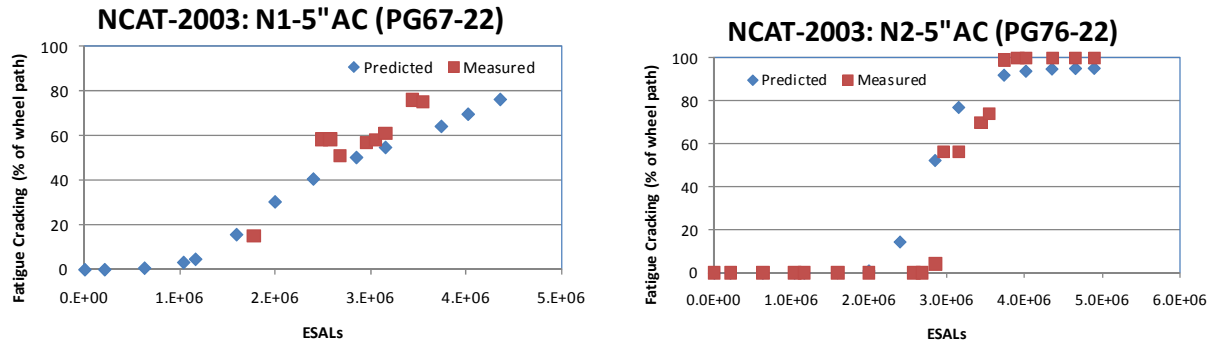


Figure 4-32. Comparisons of the Measured and Predicted Fatigue Cracking Development.

4.6 SUMMARY AND CONCLUSIONS

This chapter discussed the M-E based fatigue cracking models. Based on the work presented in this chapter, the following conclusions and recommendations are made.

- After reviewing existing fatigue cracking models in the literature, it was found that the OT-based fatigue cracking prediction approach is a rational choice to model fatigue cracking development. The main features of the OT-based fatigue cracking model include 1) consideration of both crack initiation and crack propagation, 2) full consideration of the contribution of other asphalt layers (such as surface layer, intermediate layer), in addition to the bottom asphalt layer, to pavement fatigue life, and 3) simple OT test for determining the material properties required for predicting both crack propagation and cracking initiation. A two-step enhanced OT test was proposed for determining the HMA fracture properties (A and n).
- Based on extensive SIF computations and statistical analysis, eight SIF regression equations have been developed, and these equations make it possible and practical to directly consider the crack propagation caused by a variable traffic load spectrum when predicting fatigue cracking. It was also found that the MET approach is valid for both multi-layered HMA and bases (and/or subbases).
- The proposed fatigue cracking model was preliminarily calibrated using measured fatigue cracking data from seven test sections of the NCAT Test Track 2006. Then the calibrated model was further validated using the fatigue cracking data of two test sections of the NCAT Test Track 2003. Thus far, satisfactory results have been obtained.

Overall, the M-E fatigue cracking model proposed in this chapter offers great potential for rationally modeling and accurately predicting the fatigue cracking development. Although comparable results with field measurements were obtained in this study, further model validation and calibration with more field data, varied traffic load spectrums, different environmental conditions, and different materials (HMA mix types) are still required.

CHAPTER 5

DEVELOPMENT, CALIBRATION, AND VALIDATION OF CTB FATIGUE CRACKING MODEL

This chapter reviews fatigue cracking models for predicting cracking of chemically stabilized layers in flexible pavement systems. The engineering properties of stabilized materials are defined first before discussing two models, including the recently developed MEPDG and the model used in the PCA thickness design software, for predicting load associated cracking of cement treated bases. Finally, the model input requirements and associated laboratory tests are discussed.

5.1 DEFINITION OF CHEMICALLY STABILIZED MATERIALS

In both the MEPDG and the PCA programs, chemically stabilized layers are high quality base materials that are treated with cement. These programs are intended for use with “engineered” bases or sub-bases. An engineered base requires a formal laboratory design procedure where both strength and durability criteria are achieved. Where a small amount of stabilizer is added to granular base materials to improve their strength, lower the plasticity index, or decrease moisture susceptibility, this will not be considered an engineered material unless a strength/durability test is performed. Without the use of strength and durability criteria in the design process, the resulting bases should be considered unbound materials.

On the other hand, if these layers are engineered to provide structural support, then they can be treated as stabilized structural layers. To ensure durability and long-term adequate performance of stabilized materials, the MEPDG recommends the 7-day unconfined compressive strength (UCS) criteria shown in [Table 5-1](#).

Table 5-1. Minimum Values of 7 Days Unconfined Compressive Strength for Chemically Stabilized Materials in the MEPDG.

	Rigid pavements	Flexible pavements
Base	500 psi	750 psi
Subbase, select material, and subgrade	200 psi	250 psi

The numbers proposed in [Table 5-1](#) are thought to be high, many DOTs have recently moved to designing stabilized bases with lower strength requirements. A common 7-day strength requirement is 300 psi. In some DOTs, 7-day strengths of between 150 and 250 psi have been used with success. The models discussed in these following sections are thought appropriate for all bases designed for a minimum strength of 220 psi, provided they meet some moisture sensitivity requirement. This is often evaluated through strength testing following sample moisture conditioning, where 80 percent retained strength is frequently recommended (minimum 175 psi wet strength).

5.2 FATIGUE CRACKING MODELS FOR CHEMICALLY STABILIZED MATERIALS

Both the MEPDG and PCA models are presented as follows.

5.2.1 MEPDG Fatigue Cracking Models for Chemically Stabilized Materials

The fatigue relationship used in the MEPDG is a function of the stress ratio:

$$\log N_f = \frac{(0.972\beta_{c1} - (\frac{\sigma_t}{M_r}))}{0.0825 * \beta_{c2}} \quad (5-1)$$

where N_f is number of repetitions to fatigue cracking of the stabilized layer; σ_t is maximum traffic induced tensile stress at the bottom of the stabilized layer (psi); M_r is 28-day modulus of rupture (Flexural Strength) (psi); and β_{c1} , β_{c2} is field calibration factors.

5.2.2 PCA Fatigue Cracking Models for Chemically Stabilized Materials

The PCA already have a fatigue relationship that they have used for many years to design pavements containing cement treated bases. This relationship is also a function of the stress ratio but in an exponential form and is shown below:

$$N_f = \left(\frac{\beta_{c4}}{\sigma_t/M_r} \right)^{\beta_{c3} \cdot 20} \quad (5-2)$$

where β_{c3} , β_{c4} are field calibration factors.

Currently little attention has been given to the calibration of these models within the MEPDG research effort. However in a recently completed research study, Dr. Jacob Uzan calibrated these two models using the accelerated pavement test data from an earlier PCA study (Scullion et al. 2006). He developed factors for two materials types: cement treated base and fine graded soil cement subbase type material. The calibration curves for both are shown in Figures 5-1 and 5-2. The fine graded soil cement would be equivalent to a stabilized sub-base layer.

The final calibration factors for these two types of cement treated materials are presented below:

- For cement treated base:
 $\beta_{c1}=1.0645$, $\beta_{c2}=0.9003$, $\beta_{c3}=1.0259$, and $\beta_{c4}=1.1368$
- For fine-grained soil cement:
 $\beta_{c1}=1.8985$, $\beta_{c2}=2.5580$, $\beta_{c3}=0.6052$, and $\beta_{c4}=2.1154$

Granular Soil Cement

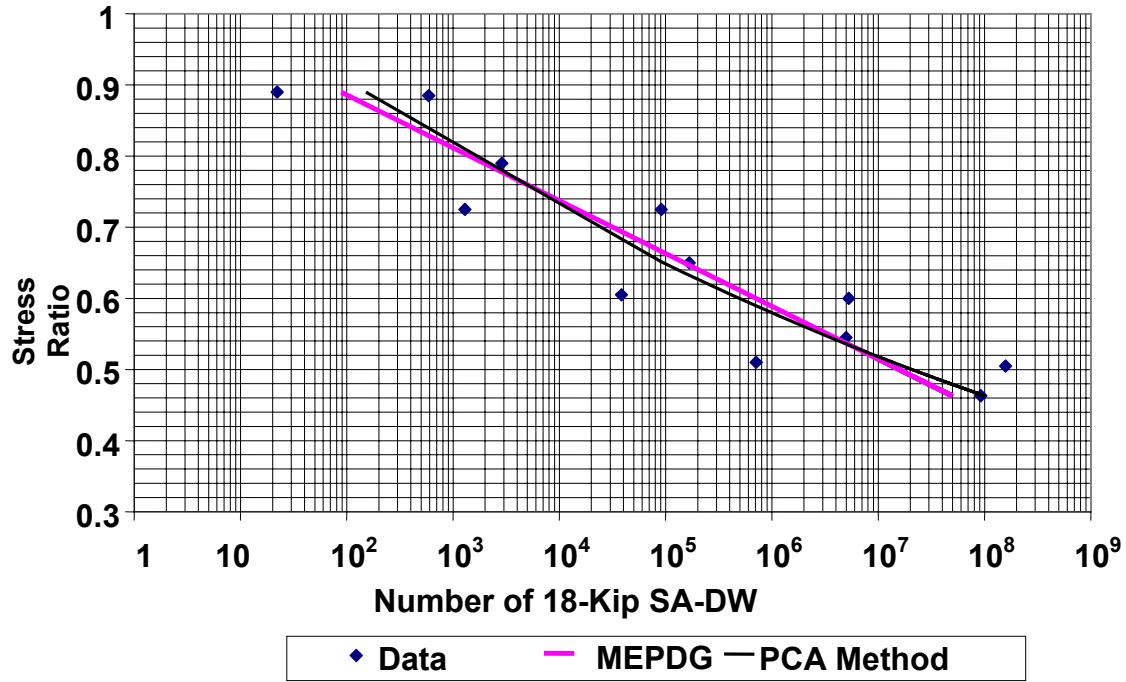


Figure 5-1. Calibration for Cement Treated Base.

Fine Grained Soil Cement

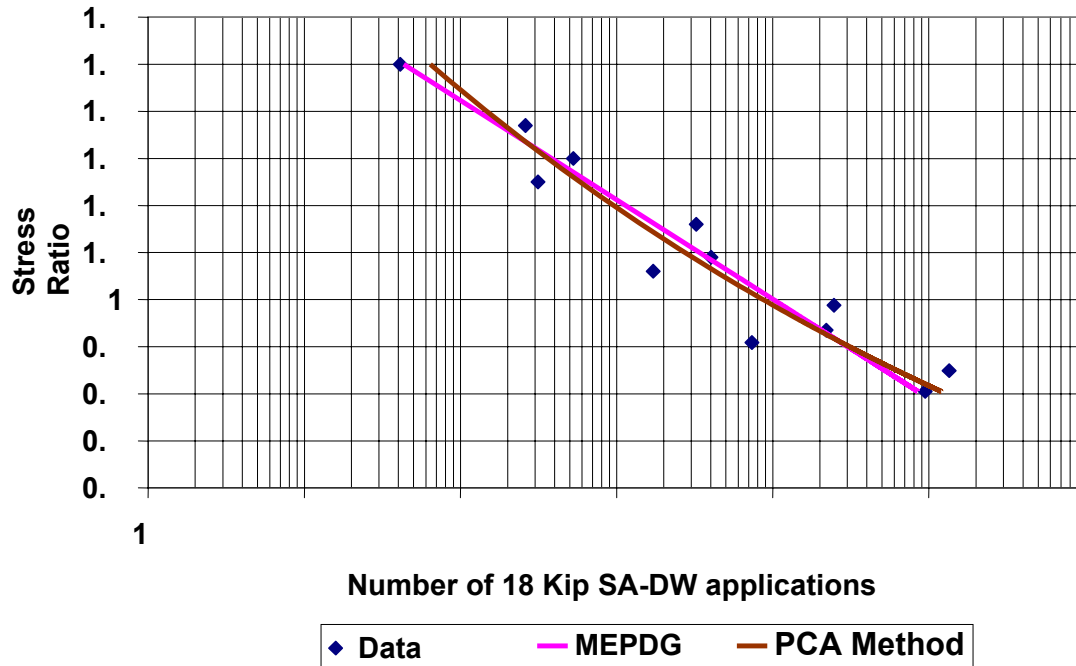


Figure 5-2. Calibration for Fine-Grained Soil Cement.

The PCA has evaluated these models and compared them with their existing design procedures. The current plan is to incorporate both of these design models into a new PCA pavement design software package (currently called PCA-PAVE) scheduled to be released in early 2010. This software is under final review by PCA and some details of the design package's capabilities are presented in [Appendix B](#) of this report. This software has several innovative approaches for calculating the damage from multiple axles. The proposed performance models and transfer functions (calibration factors) should be considered for inclusion into a future TxDOT implementation effort.

5.3 MODEL INPUT REQUIREMENTS AND ASSOCIATED LABORATORY TESTING

The two major material inputs required by the proposed models are resilient modulus and modulus of rupture of the stabilized materials. Significant efforts have been made to evaluate how to generate these two input parameters. As with other design efforts, three levels of input are proposed, with Level 1 being the research level where lab testing is required and Level 3 being standard default values. Based on a review of recent literature the recommendation for determining these values is presented as follows:

- Level 1 resilient modulus input: The standard resilient modulus test proposed by MEPDG is not recommended for routine use. The test is very difficult to run on cement treated materials. The strain levels are very low, requiring accurate instrumentation. The biggest problem is that even with careful sample preparation, problems are still encountered with the end conditions – unlike unbound materials where a few seating loads will ensure good contact. Seating loads do not ensure uniform contact with cement treated materials, where even small unevenness of the surface causes major differences in strains measured on either side of the test sample.

For the limited test program conducted it appears that the seismic modulus device is a better, more repeatable test for estimating the resilient modulus of stabilized materials. The seismic modulus equipment is widely available within TxDOT; the resilient modulus can be estimated to be 75 percent of the measured seismic modulus ([Scullion et al. 2006](#)).

Measuring Modulus of Rupture in the laboratory was performed; however, this is also difficult particularly if the treated base has a relatively low stabilizer content. An example of data collected running the Level 1 test is described later in this chapter.

- Level 2 resilient modulus input: The most attractive level for most users will be Level 2 where the design values are related to the standard 7-day UCS value. The recommended relationships ([Scullion et al. 2006](#)) are given below.

For cement treated bases

$$28 \text{ day Modulus of Rupture (ksi)} = 7.30 * \sqrt{UCS} \quad (5-3)$$

$$\text{Resilient Modulus (ksi)} = 36.5 * \sqrt{UCS} \quad (5-4)$$

For fine-grained soil cement

$$28 \text{ day Modulus of Rupture (ksi)} = 6.32 * \sqrt{UCS} \quad (5-5)$$

$$\text{Resilient Modulus (ksi)} = 31.6 * \sqrt{UCS} \quad (5-6)$$

- Level 3 resilient modulus input: The default values are given below.

For cement treated bases

Resilient Modulus 600 ksi, Modulus of Rupture 125 psi, Poisson's Ratio 0.20

For fine-grained soil cement

Resilient Modulus 300 ksi, Modulus of Rupture 60 psi, Poisson's Ratio 0.20

The Level 2 approach seems reasonable. An example of how to perform the tests for Level 1 evaluations is described in the next section.

5.4 METHODS OF DETERMINING INPUT VALUES FOR TYPICAL MATERIALS

The Level 1 input option always permits designers to develop their own input values for new materials that have not previously been characterized. For soil cement stabilized bases the procedures described below can be used for this characterization. In this study a standard Texas limestone base material is treated with different levels of cement and UCS; seismic modulus and modulus of rupture values were determined.

In any laboratory strength determinations the first step is to generate a optimum moisture content and max density curve using standard TxDOT protocols. For this demonstration the OMC that was obtained for the samples containing 3 percent cement was used to determine the moisture content to be used when fabricating the samples. This was achieved by adjusting the moisture content by 0.25 percent moisture per 1 percent cement for the samples containing 2 percent and 4 percent cement. Samples were molded in triplicate using the Texas drop-hammer, were wrapped in plastic wrap, and moist cured for a period of 7 days before determining the UCS in accordance with TEX-120E. The results of this testing are shown in [Table 5-2](#).

Table 5-2. TEX-117-E UCS Results.

Sample ID	UCS (psi)
2% Cement - A	316.7
2% Cement - B	329.4
2% Cement - C	306.1
3% Cement - A	429.9
3% Cement - B	440.6
3% Cement - C	457.2
4% Cement - A	586.0
4% Cement - B	582.1
4% Cement - C	606.5

The seismic modulus was also obtained on the UCS samples using the Free-Free Resonant Column Test. This test is conducted by measuring the velocity that an elastic wave propagates through a cylindrical specimen by tapping one end of the sample with a hammer instrumented with a load cell, which measures the energy input and triggers a timing circuit. An accelerometer mounted at the other end of the sample records the time of arrival of the longitudinal and transverse waves in order for the software to perform its calculations. This is shown in [Figure 5-3](#).



Figure 5-3. Seismic Modulus Test Being Conducted.

For this demonstration this test was conducted on the samples at 3 days and at 7 days prior to breaking the samples in the UCS test. The results of this testing are shown in [Table 5-3](#).

Table 5-3. Seismic Modulus Results.

Sample ID	Seismic Modulus (ksi)	
	3 Day	7 Day
2% Cement -A	939.3	1011.3
2% Cement - B	964.8	1008.9
2% Cement - C	927.8	1089.4
3% Cement -A	982.7	1151.5
3% Cement - B	928.6	1095.6
3% Cement - C	942.7	1235.1
4% Cement -A	987.6	1239.2
4% Cement - B	963.2	1245.6
4% Cement - C	1012.5	1401.1

5.4.1 Modulus of Rupture

Samples for the modulus of rupture test were fabricated in triplicate using a 6-inch x 6-inch x 20-inch beam mold and were compacted in two lifts at 72 blows per lift with a 10 lb tamper. These samples were then moist cured for a period of 28 days before determining the modulus of rupture in accordance with TEX-448-A: Flexural Strength of Concrete Using Simple Beam Third-Point Loading. The results of this testing are shown in [Table 5-4](#).

[Figure 5-4](#) shows this test being conducted. A summary of all test results is provided in [Table 5-5](#).

Table 5- 4. Modulus of Rupture Results.

Sample ID	Modulus of Rupture
2% Cement -A	67.5
2% Cement - B	74.2
2% Cement - C	75.8
3% Cement -A	90.0
3% Cement - B	93.3
3% Cement - C	94.2
4% Cement -A	117.5
4% Cement - B	118.3
4% Cement - C	116.7



Figure 5-4. Modulus of Rupture Test Set-Up.

Table 5- 5. Summary of All Results.

Cement Content (%)	Seismic Modulus (ksi)		7-day UCS (psi)	28-day MR (psi)
	Day 3	Day 7		
2% Cement - A	939.3	1011.3	316.7	67.5
2% Cement - B	964.8	1008.9	329.4	74.2
2% Cement - C	927.8	1089.4	306.1	75.8
3% Cement - A	982.7	1151.5	429.9	90.0
3% Cement - B	928.6	1095.6	440.6	93.3
3% Cement - C	942.7	1235.1	457.2	94.2
4% Cement - A	987.6	1239.2	586.0	117.5
4% Cement - B	963.2	1245.6	582.1	118.3
4% Cement - C	1012.5	1401.1	606.5	116.7

In this study the base material reacted very well with cement. Under normal TxDOT criteria the design cement content is selected as the content that achieves the 300 psi strength in 7 days. In this case the 2 percent cement level would be specified. Based on the values presented in [Table 5-5](#) the following engineering properties would be used in the structural design program:

Resilient Modulus = 780 ksi (75% of average seismic modulus)
 28 day Modulus of Rupture = 72 psi

5.5 SUMMARY AND CONCLUSIONS

This chapter discussed the CTB fatigue cracking model. Based on the work presented in this chapter, the following conclusions and recommendations are made.

- 1) The recommended mechanistic empirical performance model for pavements with stabilized bases is the fatigue model based on comparing the computed traffic induced tensile stress at the bottom of the stabilized layers with the modulus of rupture of that layer.
- 2) Two models have been proposed and both provide similar predictions of pavement life.
- 3) The MEPDG research effort has made little progress at providing calibration factors for both of these models.
- 4) The calibration work performed by Dr. Jacob Uzan is thought to be the best available, and the calibration factors presented in this chapter should be incorporated into future design software until better data are available.
- 5) The software package PCA-Pave should be reviewed by TxDOT engineers to determine its suitability for modification and integration into the future TxDOT M-E system.

CHAPTER 6

VALIDATION OF LOADGAGE PROGRAM FOR LOW-VOLUME ROADS

6.1 INTRODUCTION

On many low-volume Farm-to-Market (FM) roads where the expected number of cumulative 18-kip ESALs is low, it is not uncommon to find trucks with wheel loads that exceed those corresponding to the standard 18-kip single axle configuration used in pavement design. These occasional overloads could give rise to subgrade shear failure, particularly under conditions where the base or subgrade is wet. Thus, pavement engineers check the results from the FPS program against the Texas modified triaxial design procedure to ensure that the design thickness provides adequate cover to protect the subgrade against occasional overstressing that could lead to shear failure. In cases where the thickness requirement from the triaxial method is greater than the pavement thickness determined from FPS, current practice recommends using the pavement thickness based on the modified triaxial design method unless the engineer can justify using the FPS results.

In TxDOT Project 0-4519, TTI researchers verified the method used by [McDowell \(1955\)](#) to develop the existing triaxial design curves. The procedure McDowell developed uses a stress analysis to establish the depth of cover required to keep the load induced stresses in the subgrade within the material's failure envelope (as defined by its Texas triaxial class). In Project 0-4519, researchers demonstrated the methodology by re-creating the existing load-thickness design curves and conducting field and laboratory tests to verify these curves. This verification compared the allowable wheel loads determined from the design curves with the corresponding wheel loads established from test data. Considering that the modified triaxial design method is based on a theoretical analysis of allowable wheel loads using layered elastic theory, researchers in Project 0-4519 conducted plate bearing tests on full-scale field sections, given that the load configuration for this test most closely approximates the loading assumptions used in developing the existing design curves. A total of 30 full-scale pavement sections consisting of untreated and stabilized materials placed on two different subgrades were constructed within the Riverside Campus of Texas A&M University for the purpose of conducting plate bearing tests to verify the triaxial design curves.

The research and development efforts conducted in Project 0-4519 are documented in two companion reports by [Fernando et al. \(2008a\)](#) and by [Fernando et al. \(2008b\)](#). The reader is referred to these reports for details on the work conducted during the project. This work led to the development of the *LoadGage* computer program for checking flexible pavement designs that incorporates improvements to the modified triaxial design method currently implemented by TxDOT. Among the enhancements implemented in *LoadGage* are:

- a stress-based analysis procedure that provides users with greater versatility in modeling flexible pavement systems compared to the limited range of approximate layered elastic solutions represented in the existing modified triaxial thickness design curves;

- more realistic modeling of tandem axle loads, in lieu of the current practice of using a correction factor of 1.3, which was found to be overly conservative from the verification efforts conducted in Project 0-4519;
- an extensive database of soil properties covering each of the 254 Texas counties for evaluating the effects of moisture changes on soil strength properties; and
- a moisture correction procedure (to account for differences between wet and dry regions of the state) that provides users the option of adjusting strength properties determined from laboratory triaxial tests (such as TxDOT Test Method Tex-117E) to the expected in-service moisture conditions.

This chapter documents additional efforts made in Project 0-5798 to verify the *LoadGage* program for checking flexible pavement designs of low-volume roads. For this work, researchers constructed flexible pavement sections at the Texas A&M Riverside Campus, at the same clay site on which test sections in Project 0-4519 were built to verify the modified triaxial load-thickness design curves. In this follow-up investigation, researchers used a loaded truck to apply repetitive loads and monitored the development of rutting on the sections tested. Researchers then compared the measured rut depths on these sections against the allowable wheel loads predicted from *LoadGage* and the existing Tex-117E triaxial design curves to check how these methods ranked the sections relative to the rut depths measured from the tests.

6.2 DESCRIPTION OF TEST SECTIONS

Figure 6-1 shows a schematic layout of the test sections built on this project to verify the *LoadGage* program. There are six sections altogether, as identified in the test matrix given in Table 6-1. The three southern sections are underlain by 6 inches of lime-treated clay while the three northern sections are directly placed on top of the native clay subgrade. All sections are 24-ft wide.

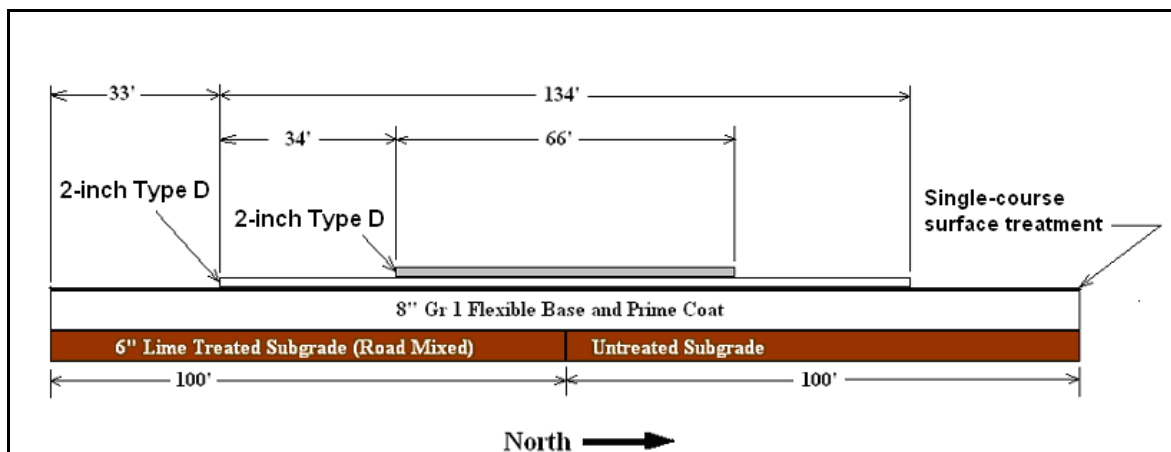


Figure 6-1. Schematic Layout of Test Sections Placed at the Riverside Campus.

Table 6-1. Matrix of Test Sections.

Surface Material	Subgrade Treatment	
	6-inch lime-treated clay	No lime treatment
Single-course surface treatment	X	X
2-inch Type D mix	X	X
4-inch Type D mix	X	X

Figure 6-2 shows the sequence of construction of the test sections. The contractor first had to remove the existing sections from Project 0-4519 to expose the native clay subgrade. As illustrated in Figure 6-2, these sections were placed on two 12-ft wide lanes. Sections on the west lane were built with 12-inch base while those on the east lane had 6-inch base. Thus, to level the existing subgrade, the second step required the contractor to cut 3 inches of the existing clay on the east lane and to use the excavated material as fill on the west lane. The contractor then treated the clay material with lime over the first 100 ft of the test track as shown in Figure 6-1. After mixing and compaction of the lime-treated clay, the contractor then placed the 8-inch flexible base over the width and length of the test track. He then primed the base and subsequently placed the one-course surface treatment. The 2-inch Type D mix was then placed in two lifts over the intervals shown in Figure 6-1. During placement of the hot-mix, the contractor built transitions between the sections identified in this figure and in Table 6-1.

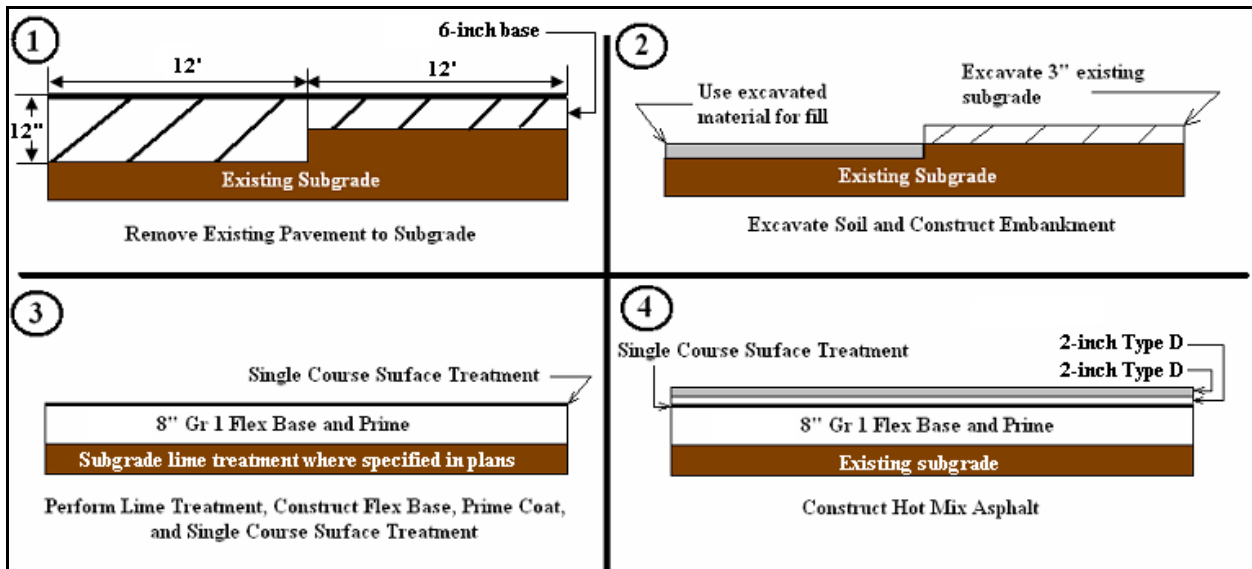


Figure 6-2. Sequence of Test Track Construction (Elevation View Looking North).

Figure 6-3 shows a picture of the test track after construction. In setting up the sections for testing, the research supervisor selected a test area that straddled the two 12-ft lanes placed during construction. The boundaries of this test area are delineated by the red paint dots shown in Figure 6-3. This area is 12-ft wide, covers the length of the track, and has a 6-ft shoulder on each side. Researchers conducted nondestructive tests on the sections included within this area to characterize pavement layer moduli and thickness profiles using the falling weight deflectometer and ground penetrating radar (GPR). The next section presents the data and findings from these tests.



Figure 6-3. Picture of Test Track after Construction.

6.3 NONDESTRUCTIVE TESTING OF AS-BUILT SECTIONS

6.3.1 GPR Data Collection

Researchers collected GPR data with the air-coupled system shown in [Figure 6-4](#). GPR data were collected on both wheel paths of the 12-ft wide test lane, the boundaries of which are delineated by the painted dots in [Figure 6-3](#). Researchers used the PAVECHECK program by [Liu and Scullion \(2007\)](#) to determine the thickness profiles from the GPR data. [Figure 6-5](#) illustrates GPR data collected on the west (left) wheel path of the lane surveyed. The chart on the left is a color representation of the GPR traces collected on the test lane while the chart on the right shows an example GPR trace where the reflected energies from the pavement layer interfaces are plotted versus arrival times. The amplitudes of the reflections and the arrival times of the reflections determined from each trace are used to compute the layer dielectrics and thicknesses at the given station. By processing all the traces collected from the survey, the thickness profiles over the path tested can be determined. The principles behind using the GPR to determine layer thickness profiles are presented in the report by [Scullion and Chen \(1999\)](#) and will not be repeated here. These same principles are used in the PAVECHECK program to determine layer thicknesses from the GPR data.



Figure 6-4. Air-Coupled GPR System Mounted on TTI Van.

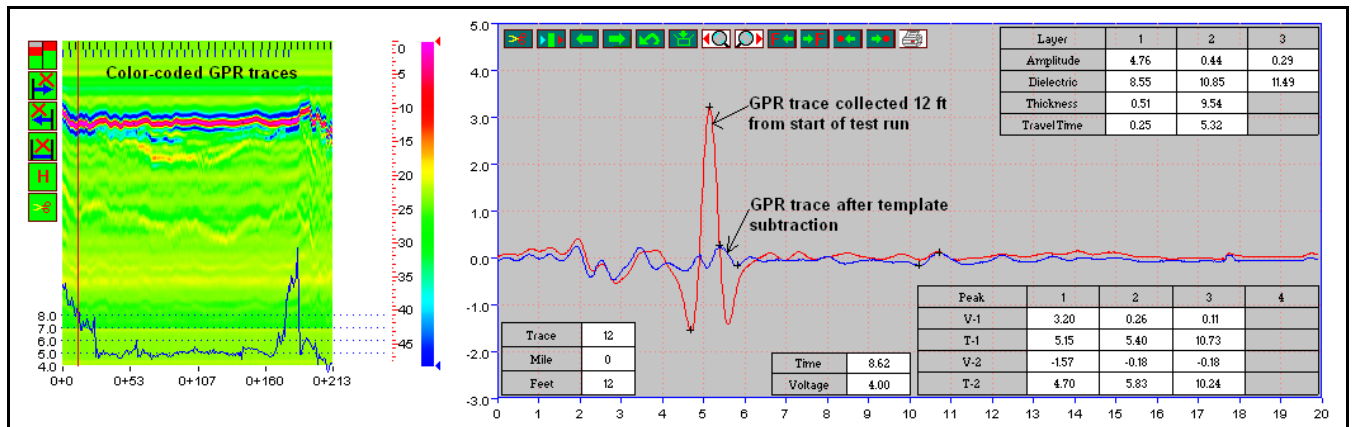


Figure 6-5. Illustration of GPR Data Collected on Annex Sections.

Figures 6-6 and 6-7 show the layer thickness profiles obtained from the GPR data processing. The thickness profiles shown for layers 1, 2 and 3 correspond, respectively, to the surface, base, and lime-stabilized clay layers. The correspondence between the surface thickness profiles and the test sections is illustrated in Figure 6-8. Researchers note that the reflections from the bottom of the lime-stabilized subgrade were generally not visible from the GPR traces. Thus, it was not possible to determine the thickness of this layer using GPR over the entire range where the plans called for lime treatment of the clay subgrade.

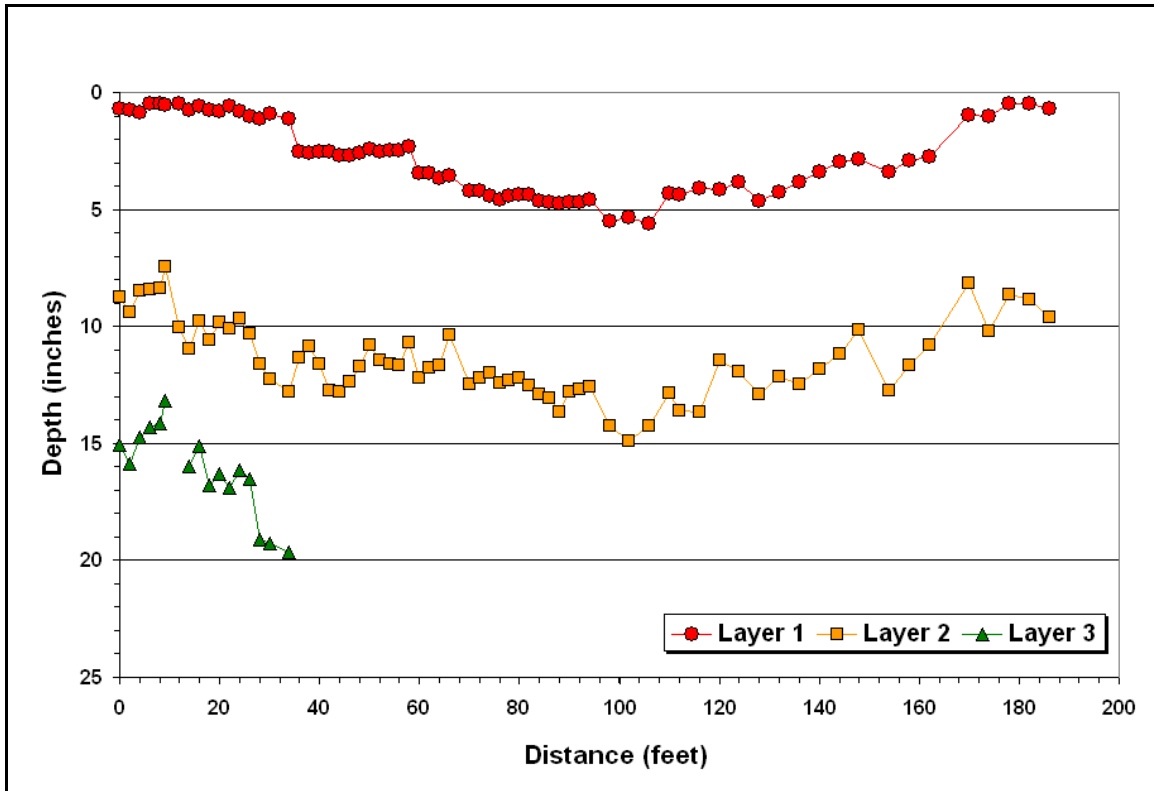


Figure 6-6. Thickness Profiles Determined from GPR Data on West Wheel Path.

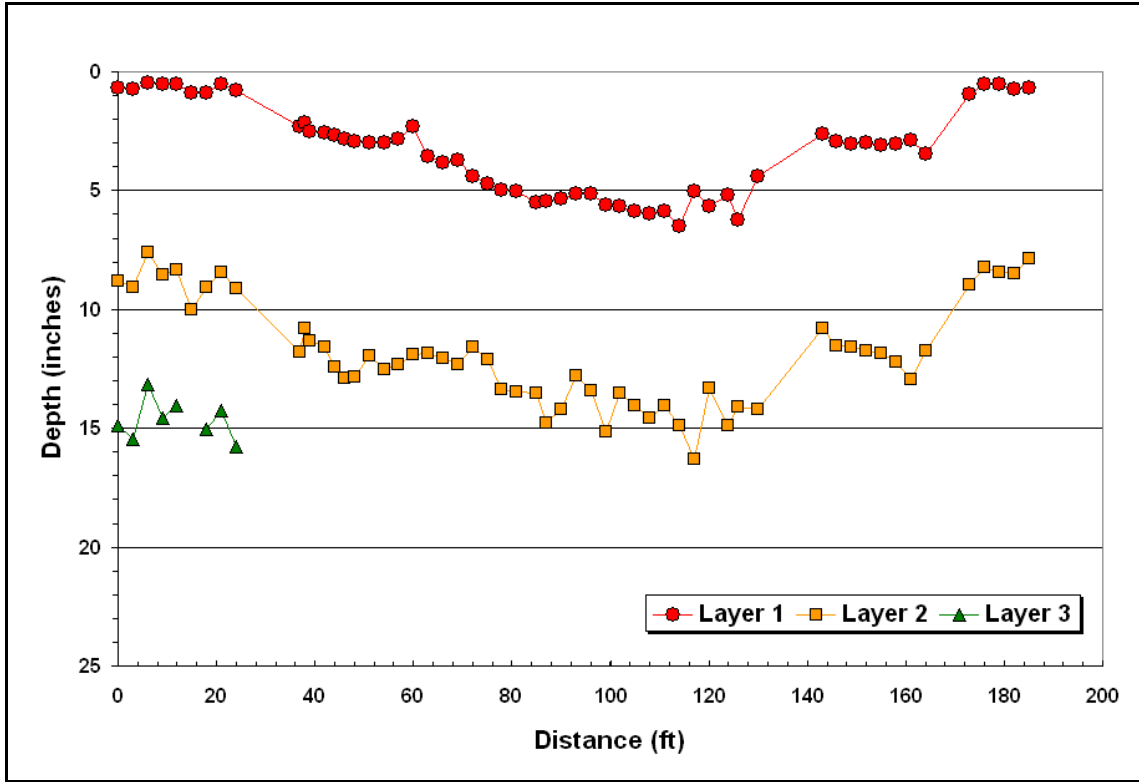


Figure 6-7. Thickness Profiles Determined from GPR Data on East Wheel Path.

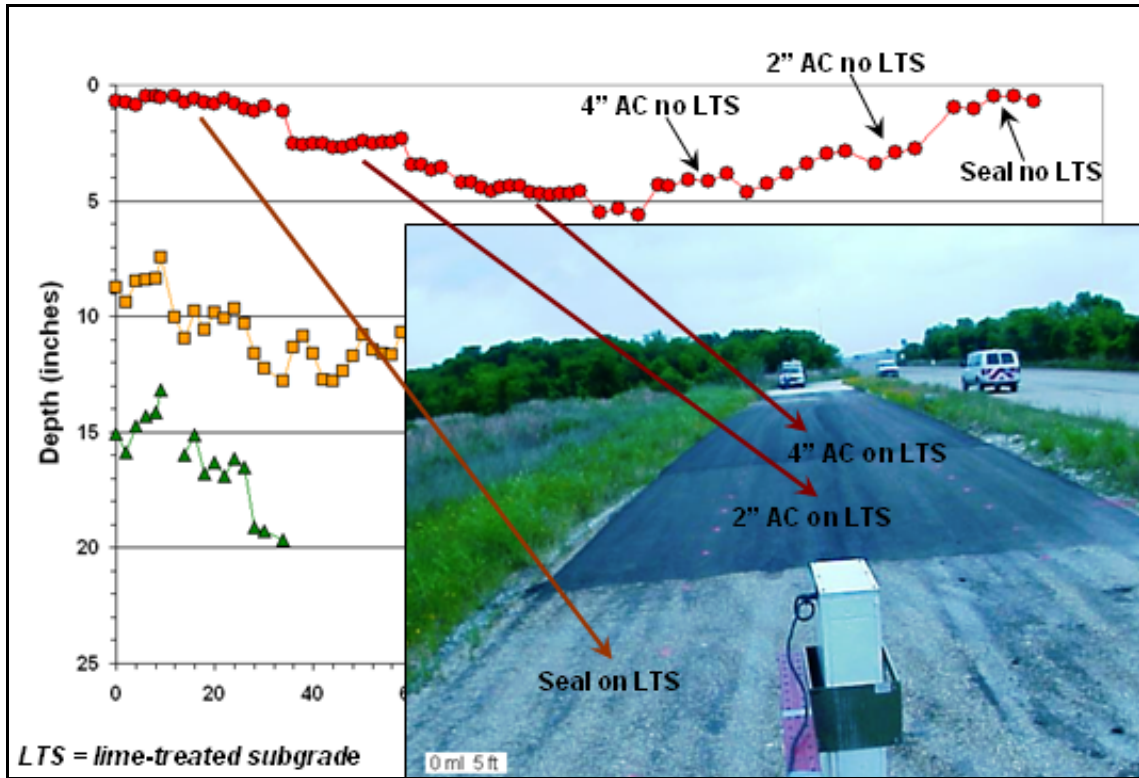


Figure 6.8. Correspondence between Surface Thickness Profile and Annex Test Sections.

6.3.2 FWD and Dynamic Cone Penetrometer (DCP) Tests

Researchers also conducted falling weight deflectometer tests on the Annex sections to characterize pavement layer stiffness for the purpose of evaluating the load bearing capacity on each test section using the *LoadGage* program. These tests were conducted on each wheel path at drop height two. Given the layer thickness estimates from the GPR, researchers used the MODULUS program (Scullion and Liu 2001) to backcalculate the stiffness of each material from the measured FWD deflections.

Figure 6-9 compares the FWD sensor 1 deflections (R1) taken on the west wheel path with the deflections taken at corresponding stations on the east wheel path. This figure shows that the west wheel path deflections are noticeably higher than the measured deflections on the other wheel path. Since the test lane straddled the two 12-ft lanes placed during construction, the differences in the sensor 1 deflections appear to reflect differences in the construction of the two 12-ft lanes. Note that the west wheel path is located on a fill area while the east wheel path is on a cut based on the construction sequence illustrated in Figure 6-2. This observed difference between the measured wheel path deflections essentially doubled the number of available sections for verifying the *LoadGage* program in this project. While this doubling came about at the expense of replication, researchers are of the opinion that this circumstance turned out to be favorable given the limited number of test sections. Further verifications on additional test sections are recommended in a follow-up project.

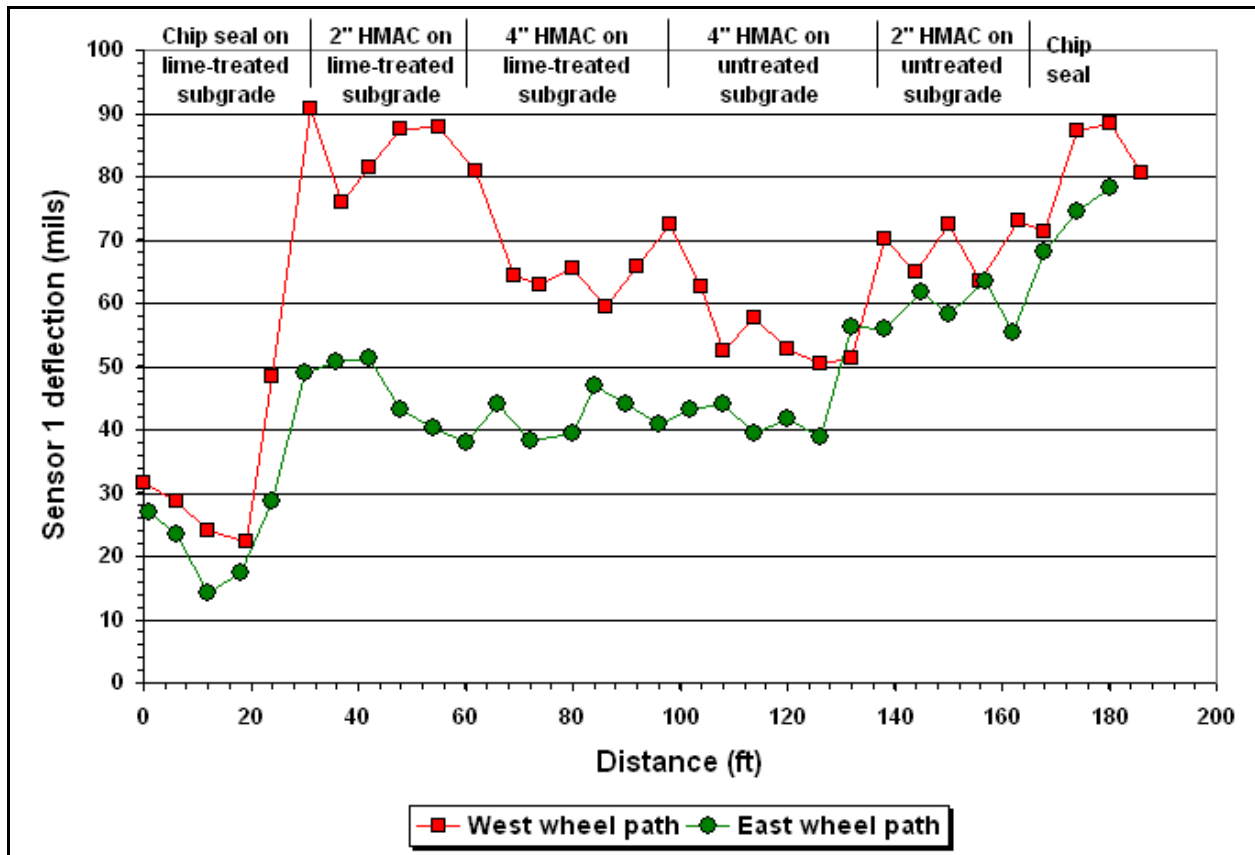


Figure 6-9. Comparison of FWD Sensor 1 Deflections on Both Wheel Paths.

Figure 6-9 also shows higher sensor 1 deflections on the hot-mix asphalt concrete (HMAC) sections compared to the measured deflections on the chip seal section over lime-treated subgrade (LTS). Since the test site was used in an earlier research project to build sections of varying base materials to verify TxDOT's modified triaxial design procedure, there was concern on whether all materials from the previous project were removed. In this regard, the researcher in charge of construction at the site confirmed that all materials from the earlier project were removed prior to placement of the new sections as specified in the plans. To further verify the observation noted in the FWD data, researchers ran DCP tests at various locations along the west wheel path. Table 6-2 shows the DCP test locations along with estimates of the layer stiffness for each material as determined from the penetration rates. The estimates of base and subgrade stiffness on the chip seal LTS section are noticeably higher than the DCP estimates of layer stiffness on the hot-mix sections. These results are consistent with the lower FWD deflections measured on this chip seal section. Further, researchers examined plots of the DCP data shown in Figures 6-10 to 6-15 and found no indications of additional layers that could be attributed to leftover materials from the previous project. Thus, it appears that the observed trends in the FWD data are simply showing as-built differences between the test sections.

Table 6-2. DCP Layer Stiffness Estimates.

Section	Station (ft)	Layer stiffness (ksi)		
		Base	LTS	Native clay subgrade
Chip seal on LTS	24	79.0	18.9	13.0
2" HMAC on LTS	48	53.9	18.7	5.6
4" HMAC on LTS	84	39.7	14.5	9.0
4" HMAC	120	58.5	N/A	11.2
2" HMAC	144	52.0	N/A	5.8
Chip seal	178	40.1	N/A	8.1

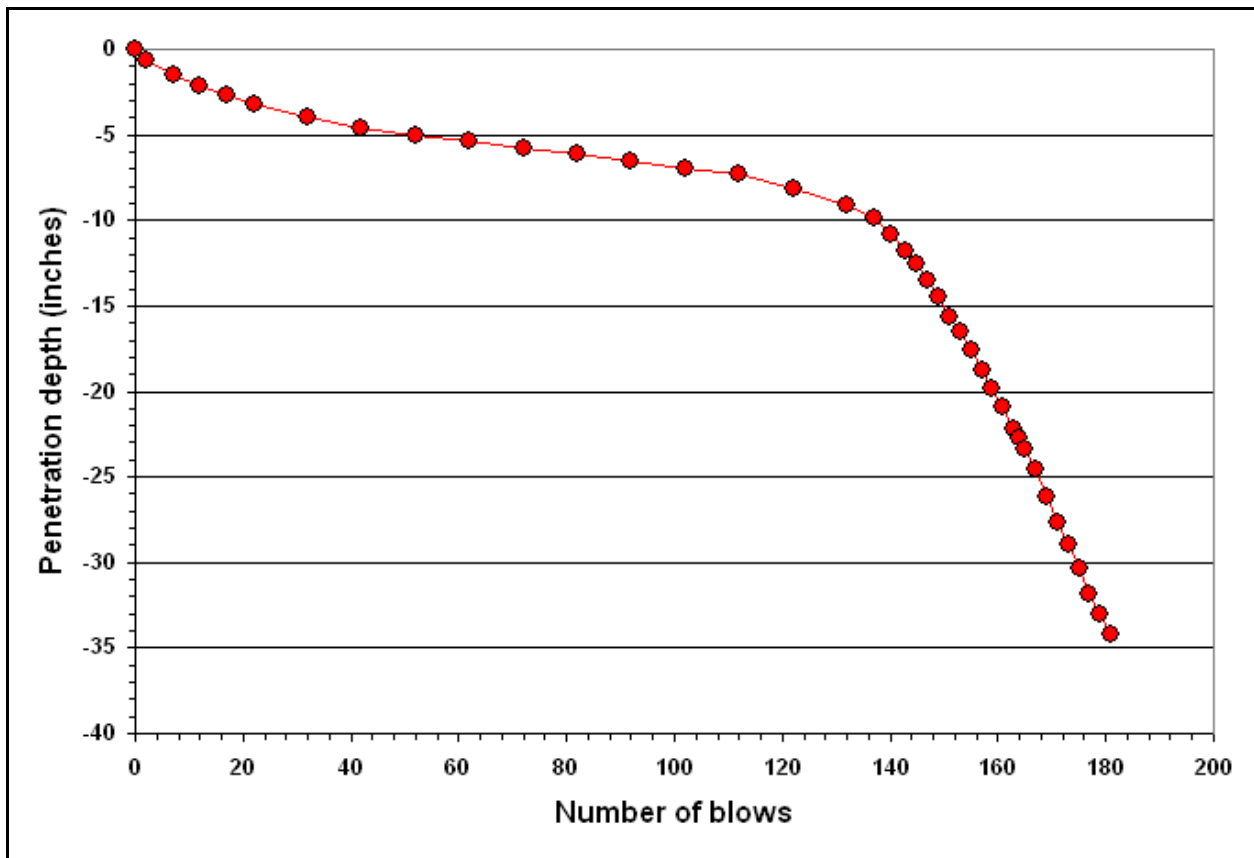


Figure 6-10. DCP Test Data on Chip Seal LTS Section.

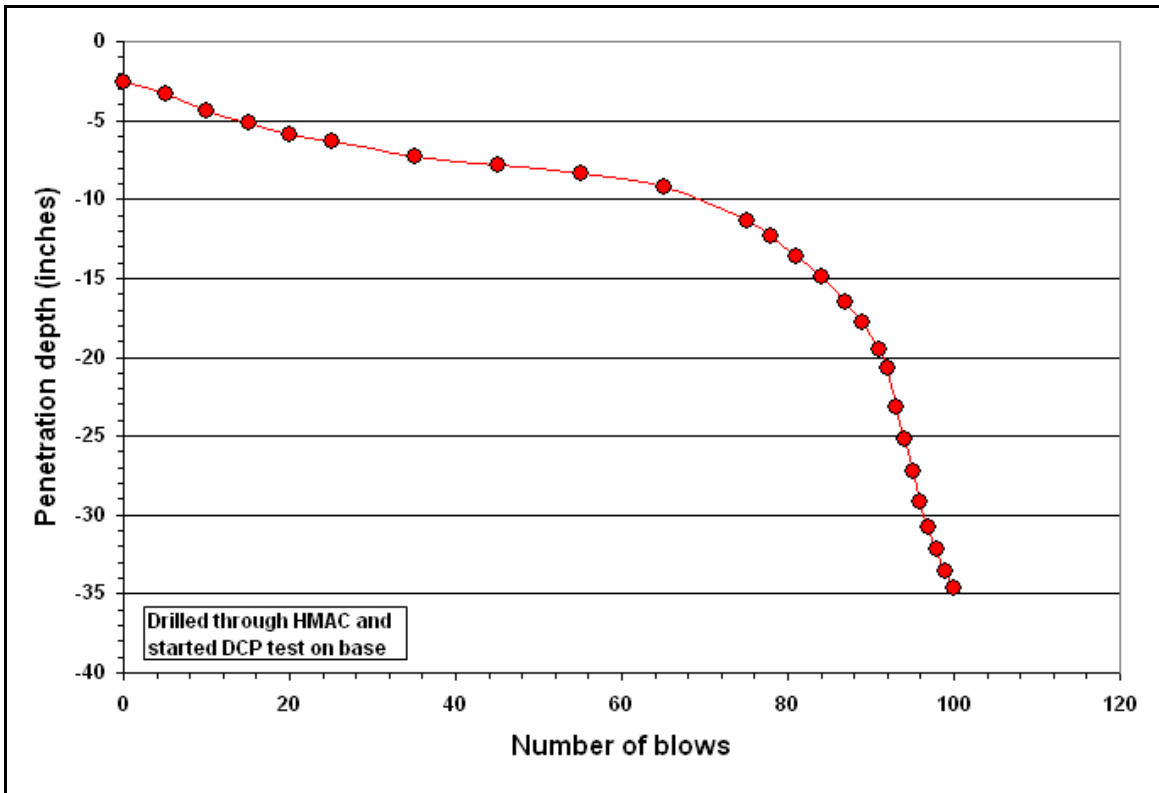


Figure 6-11. DCP Test Data on 2-inch HMAC LTS Section.

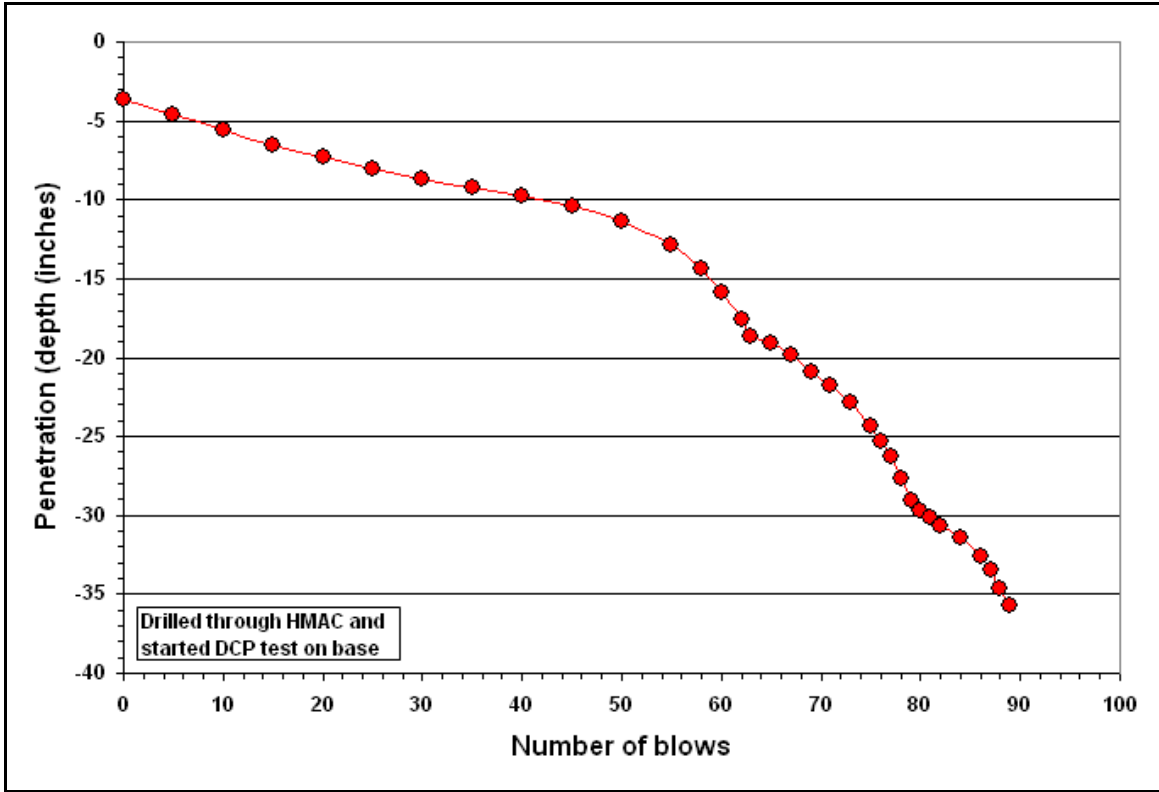


Figure 6-12. DCP Test Data on 4-inch HMAC LTS Section.

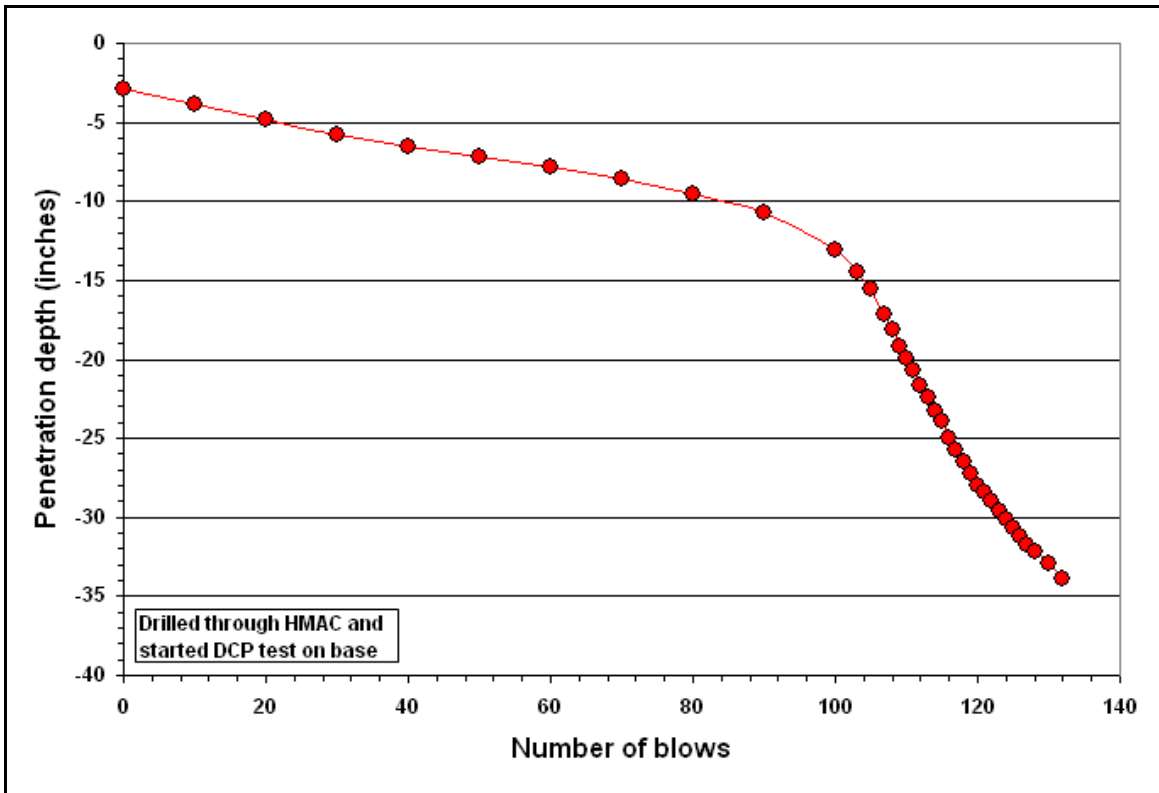


Figure 6-13. DCP Test Data on 4-inch HMAC Section without LTS.

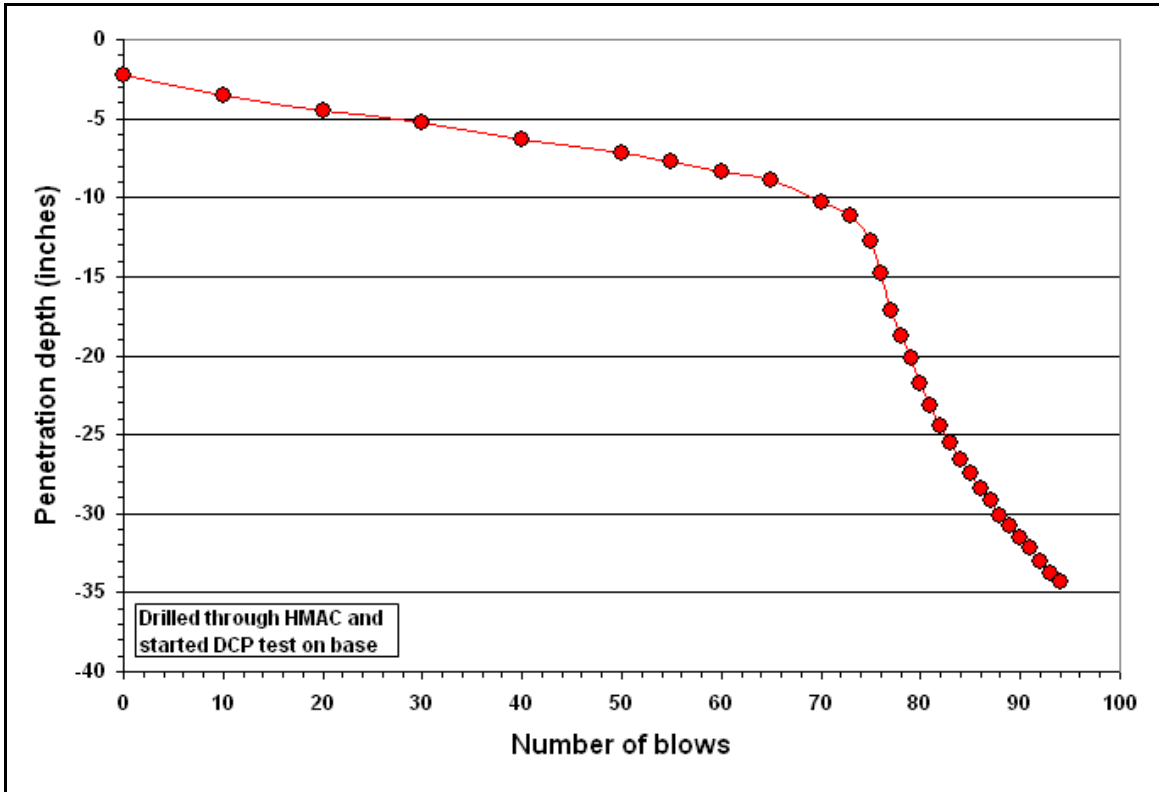


Figure 6-14. DCP Test Data on 2-inch HMAC Section without LTS.

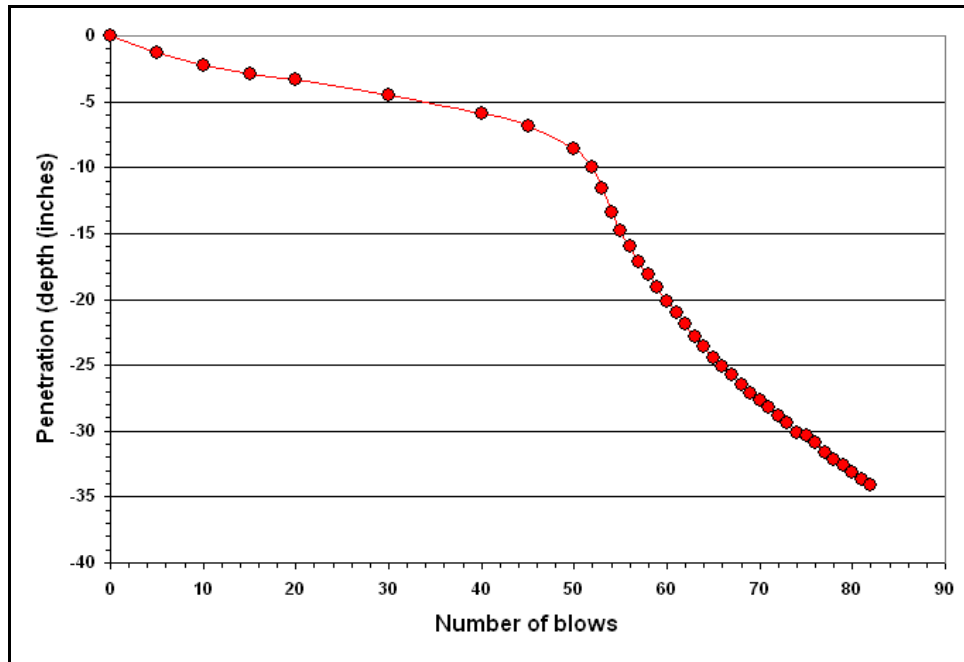


Figure 6-15. DCP Test Data on Chip Seal Section without LTS.

Researchers also used the MODULUS program to backcalculate the stiffness of each layer from the measured FWD deflections. In general, researchers encountered difficulty in fitting the measured deflection basins on the HMAC sections, particularly the sensor 1 deflections, which were observed to be about a factor of three higher than the sensor 2 deflections. Figure 6-16 illustrates this observation with data collected along the west wheel path of the 2-inch HMAC LTS section. Researchers found that the MODULUS program generally converged to unrealistically low values of HMAC stiffness (< 100 ksi) in order to achieve a reasonable match between the predicted and measured sensor 1 deflections.

The difference between the sensor 1 and sensor 2 deflections is generally referred to as the surface curvature index (SCI). Figures 6-17 and 6-18 show the SCIs computed from the FWD deflections taken along the west and east wheel paths, respectively. Based on these SCIs and the given HMAC thicknesses, the hot-mix sections classify as “Very Poor” in terms of upper pavement strength according to the MODULUS layer strength classification scheme. Since a high surface curvature index might result from the presence of a shallow, thin weak lift, researchers also conducted FWD backcalculations where the chip seal placed between the hot-mix and the flexible base was modeled as a weak thin lift. Researchers found that this approach led to more reasonable agreement between the predicted and measured deflections as illustrated in Figures 6-19 to 6-23. In addition, more realistic estimates of the HMAC modulus were obtained. Thus, researchers used this approach to backcalculate pavement layer moduli for the purpose of predicting allowable wheel loads using the *LoadGage* program. Researchers note that the presence of a weak thin lift is in accordance with observations made by technicians who commented that the seal coat appeared spongy at locations where they took cores along the west shoulder of the test lane.

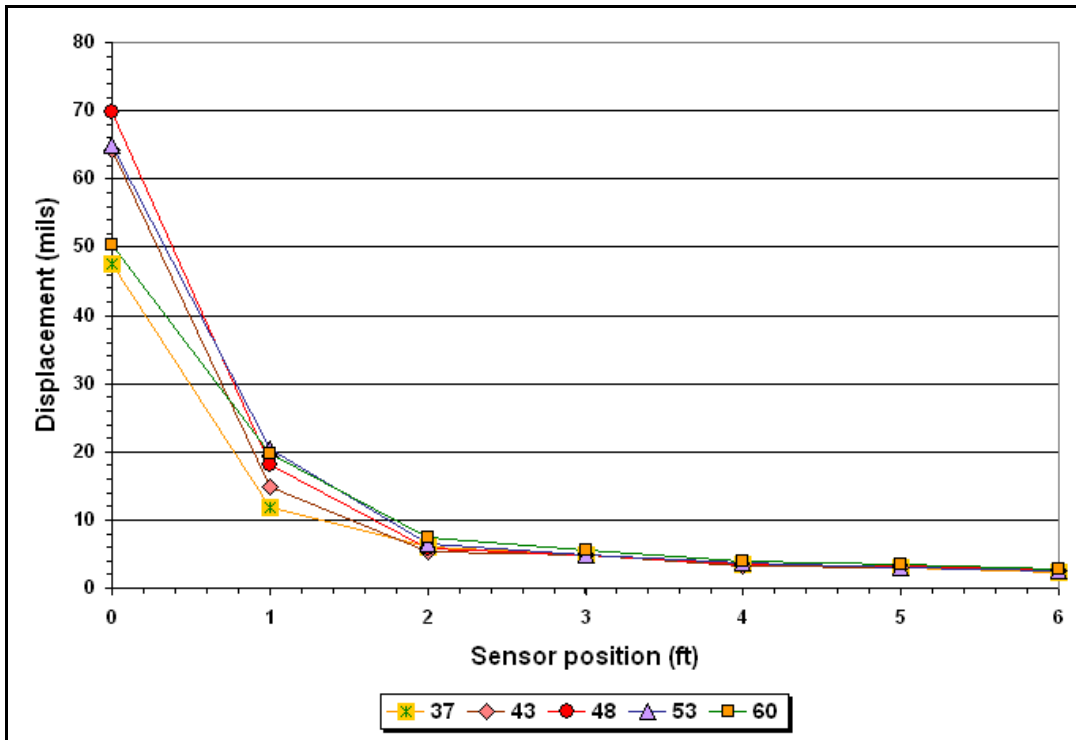


Figure 6-16. FWD Deflection Basins Measured at Five Stations along West Wheel Path of 2-inch HMAC LTS Section.

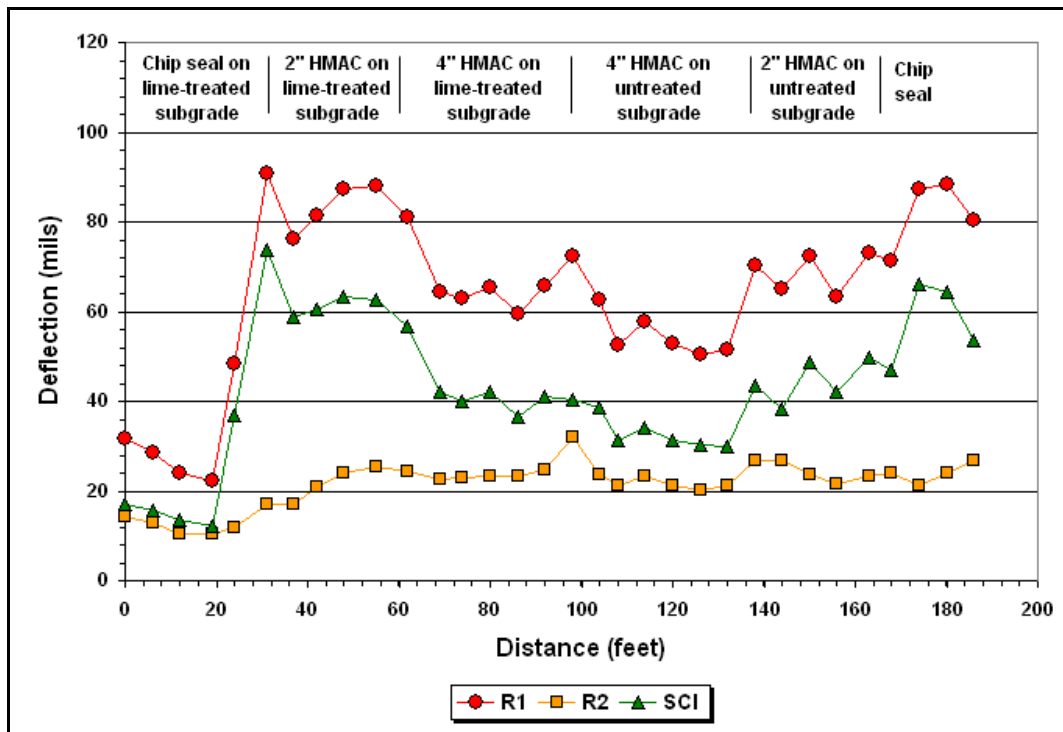


Figure 6-17. SCIs Computed from Sensors 1 and 2 Deflections along West Wheel Path.

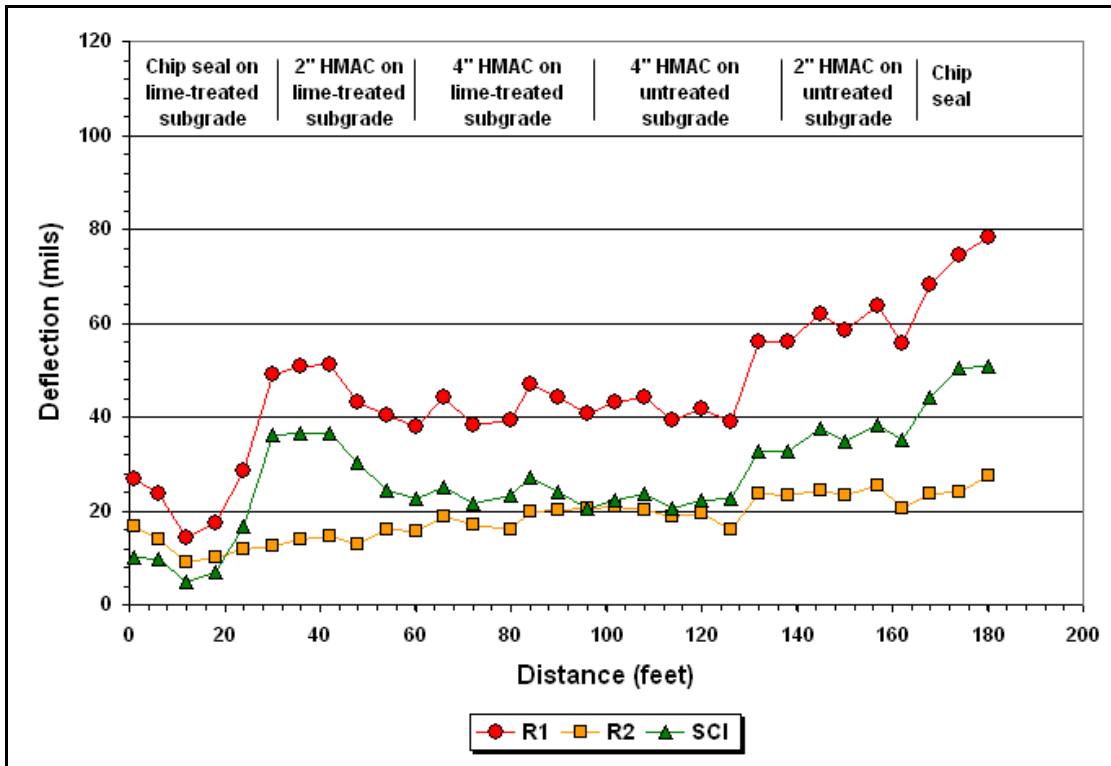


Figure 6-18. SCIs Computed from Sensors 1 and 2 Deflections along East Wheel Path.

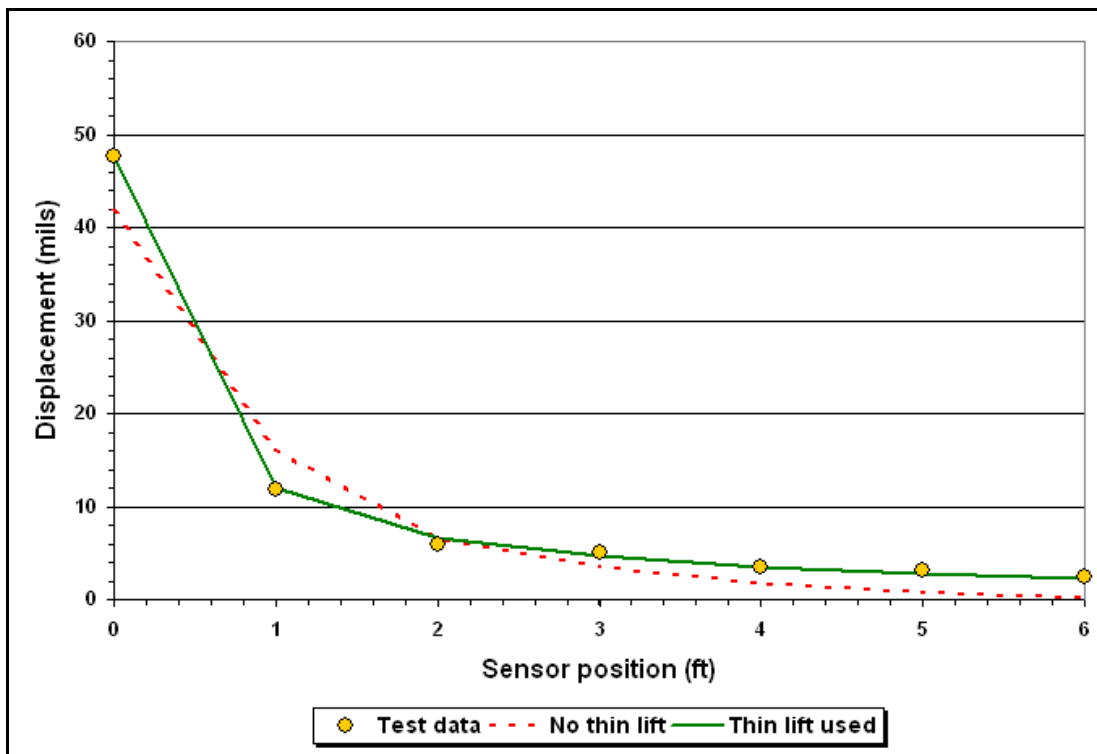


Figure 6-19. Comparison of Fitted Deflection Basins to Measured Deflections at Station 37 on West Wheel Path of 2-inch HMAC LTS Section.

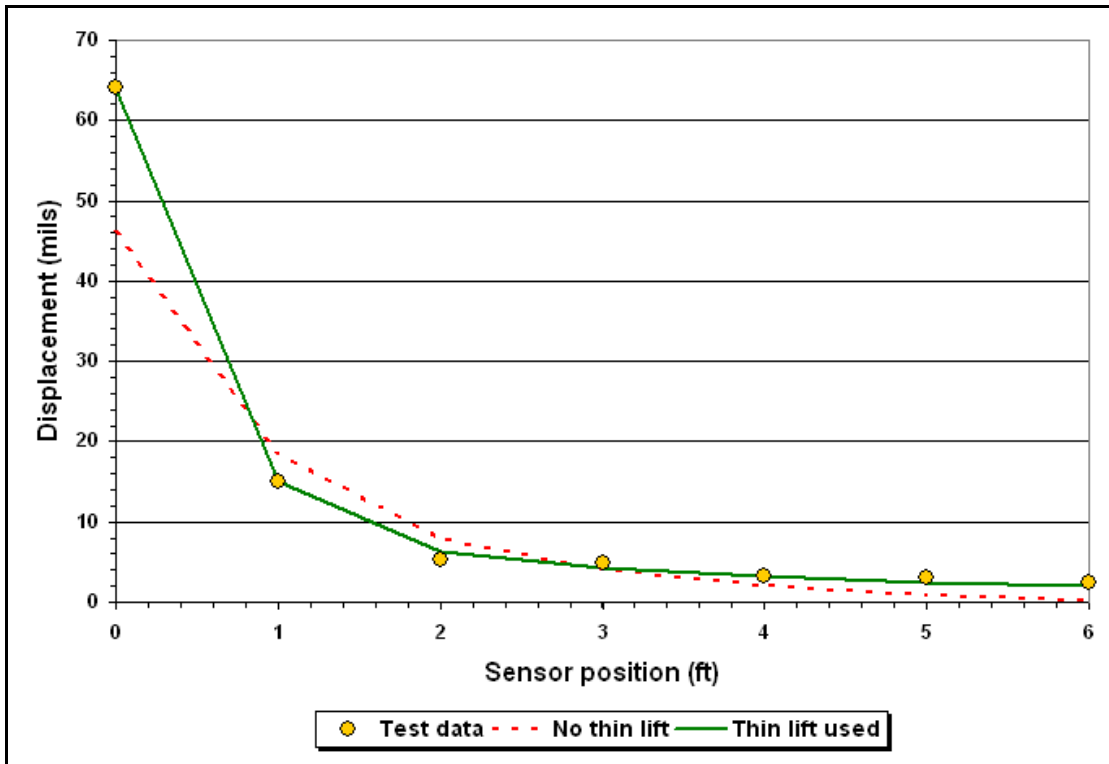


Figure 6-20. Comparison of Fitted Deflection Basins to Measured Deflections at Station 43 on West Wheel Path of 2-inch HMAC LTS Section.

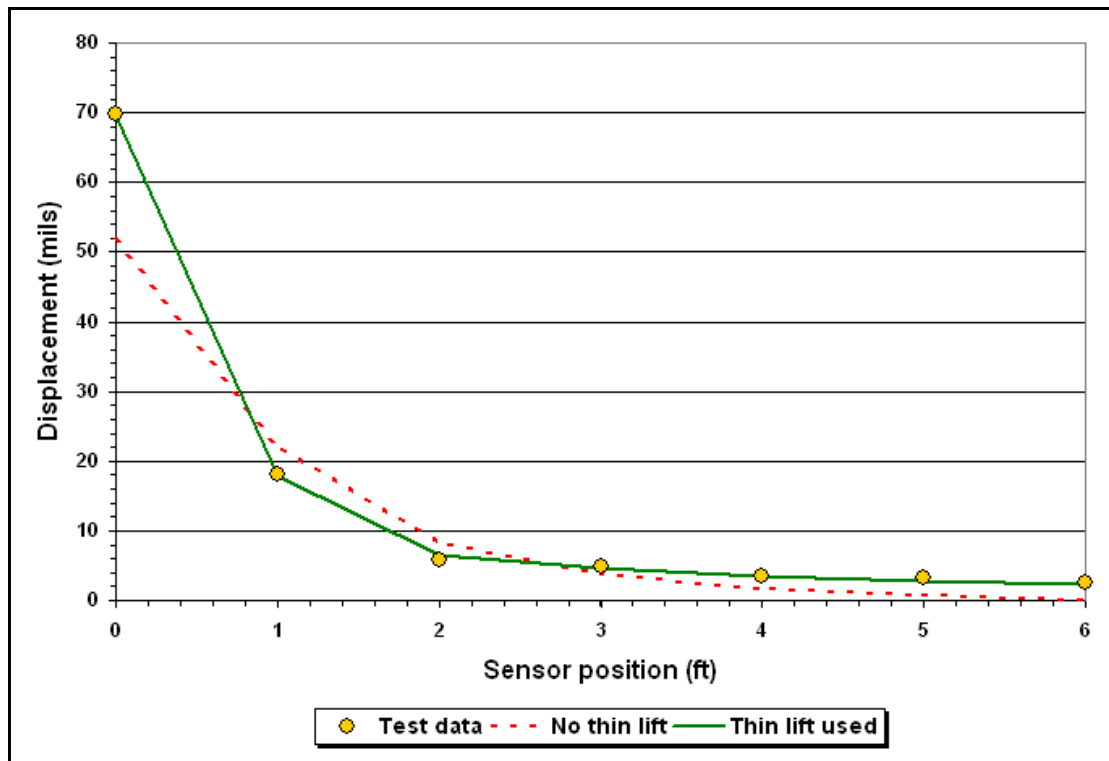


Figure 6-21. Comparison of Fitted Deflection Basins to Measured Deflections at Station 48 on West Wheel Path of 2-inch HMAC LTS Section.

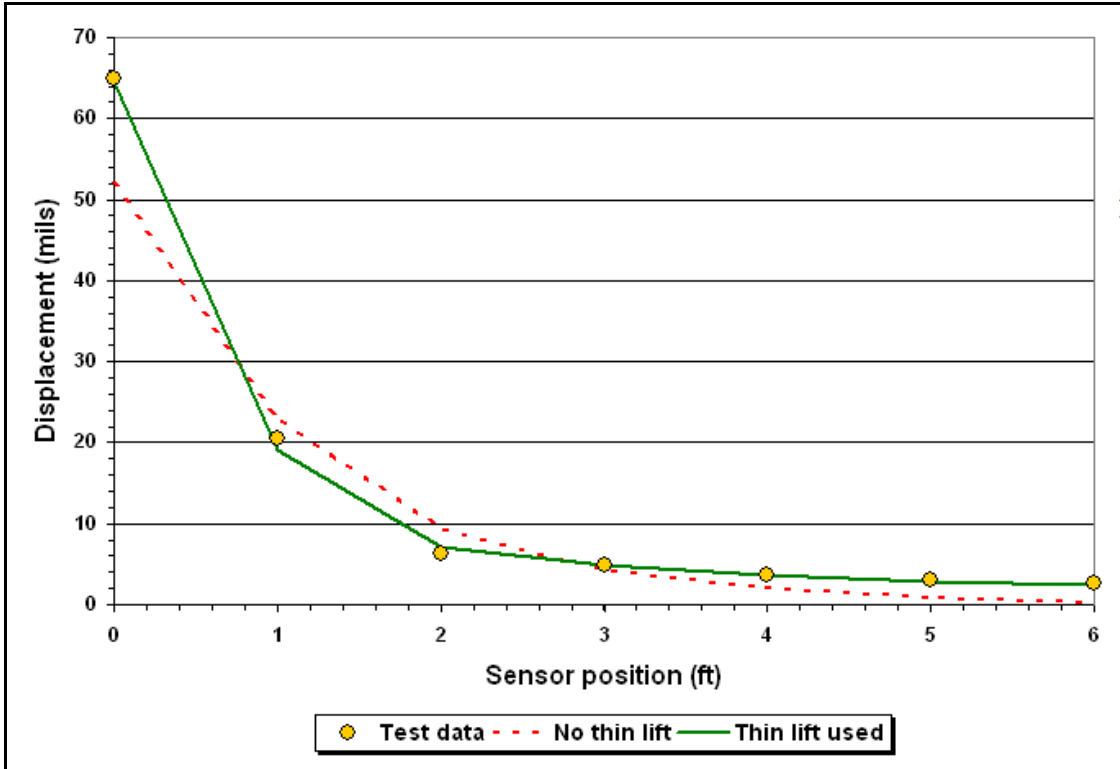


Figure 6-22. Comparison of Fitted Deflection Basins to Measured Deflections at Station 53 on West Wheel Path of 2-inch HMAC LTS Section.

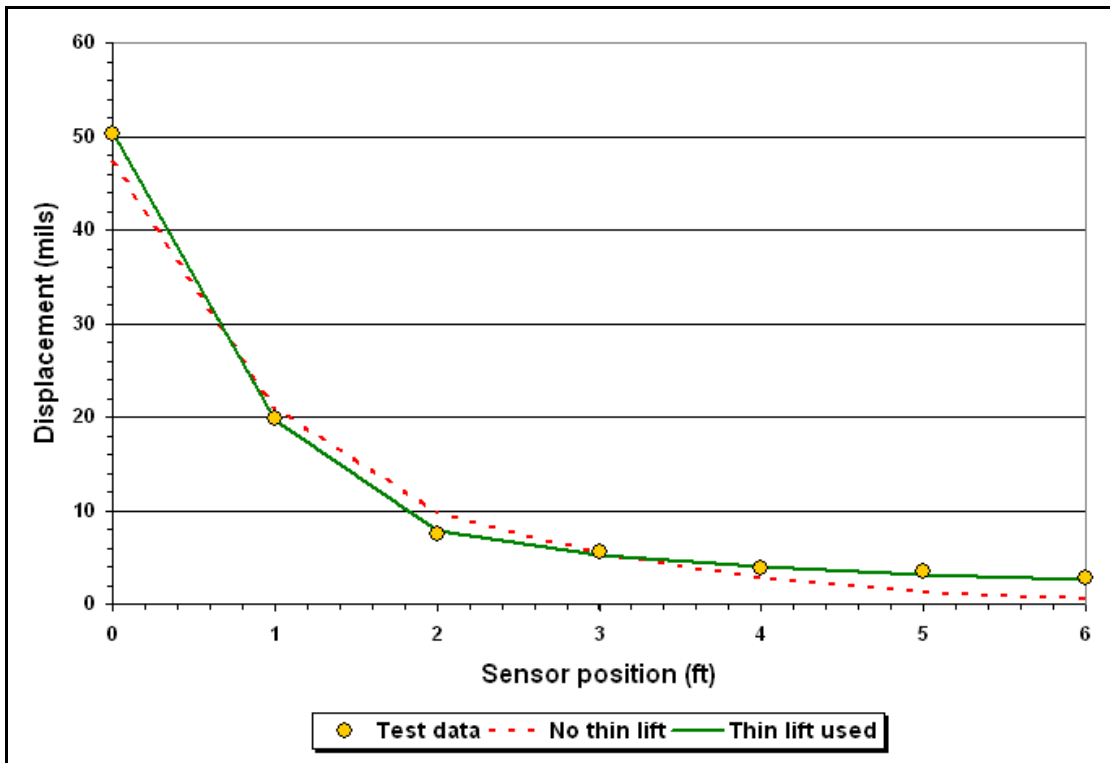


Figure 6-23. Comparison of Fitted Deflection Basins to Measured Deflections at Station 60 on West Wheel Path of 2-inch HMAC LTS Section.

6.4 LOADGAGE VERIFICATION

6.4.1 Determination of Allowable Wheel Loads

Prior to running repetitive load tests on the Annex sections, researchers conducted another round of FWD testing to characterize in-situ layer moduli close to the time of the repetitive load tests. In addition, researchers collected clay samples along the west shoulder to determine in-situ moisture contents. Tables 6-3 and 6-4 show the results from backcalculations made using the MODULUS program with the FWD data collected on the test sections just prior to repetitive load testing. Based on the experience documented previously with analyzing FWD data from earlier tests, researchers modeled a weak thin lift between the Type D mix and flexible base to backcalculate pavement layer stiffness using the MODULUS program. This approach was used for the FWD backcalculations on the HMAC sections.

Table 6-3. Summary of FWD Backcalculations along West Wheel Path.

Section	Material	Backcalculated modulus (ksi)	Poisson's ratio	Thickness (inches)
Chip seal on LTS	Seal + flexible base	149.3	0.40	9.7
	LTS	43.9	0.35	6.0
	Native clay subgrade	10.8	0.45	
2-inch HMAC on LTS	Type D	200.0	0.30	2.0
	Weak thin lift	5.0	0.30	1.7
	Flexible base	33.5	0.40	8.0
	LTS + native subgrade	8.6	0.45	
4-inch HMAC on LTS	Type D	100.0	0.30	4.0
	Weak thin lift	2.0	0.30	0.9
	Flexible base	15.0	0.40	8.0
	LTS + native subgrade	6.5	0.45	
4-inch HMAC no LTS	Type D	106.6	0.30	4.0
	Weak thin lift	2.0	0.30	0.9
	Flexible base	15.1	0.40	8.0
	Native clay subgrade	7.2	0.45	
2-inch HMAC no LTS	Type D	282.9	0.30	2.0
	Weak thin lift	2.0	0.30	1.4
	Flexible base	25.0	0.35	7.0
	Native clay subgrade	7.5	0.45	
Chip seal no LTS	Seal + flexible base	20.0	0.30	8.7
	Native clay subgrade	7.0	0.45	

Table 6-4. Summary of FWD Backcalculations along East Wheel Path.

Section	Material	Backcalculated modulus (ksi)	Poisson's ratio	Thickness (inches)
Chip seal on LTS	Seal + flexible base	81.4	0.35	9.1
	LTS	64.4	0.30	6.0
	Native clay subgrade	9.4	0.45	
2-inch HMAC on LTS	Type D	386.8	0.30	2.0
	Weak thin lift	4.3	0.30	1.7
	Flexible base	137.7	0.35	9.0
	LTS + native subgrade	9.9	0.45	
4-inch HMAC on LTS	Type D	200.0	0.30	4.0
	Weak thin lift	2.3	0.30	2.0
	Flexible base	72.2	0.40	9.0
	LTS + native subgrade	13.7	0.45	
4-inch HMAC no LTS	Type D	178.3	0.30	4.0
	Weak thin lift	2.1	0.30	2.0
	Flexible base	32.9	0.40	9.0
	Native clay subgrade	10.2	0.45	
2-inch HMAC no LTS	Type D	309.4	0.30	2.0
	Weak thin lift	2.0	0.30	1.2
	Flexible base	30.0	0.40	8.0
	Native clay subgrade	8.0	0.45	
Chip seal no LTS	Seal + flexible base	20.0	0.35	8.5
	Native clay subgrade	7.6	0.45	

Given the results from the FWD backcalculations, researchers used the *LoadGage* program to predict the allowable wheel loads on the test sections for each wheel path. [Table 6-5](#) shows the results from this analysis. For comparison, the table also shows the allowable wheel loads based on the modified triaxial pavement design method as determined using TxDOT's FPS-19 flexible pavement design program.

To predict the allowable wheel loads based on *LoadGage*, researchers used the in-situ moisture contents determined from the clay samples taken at the test site to perform moisture corrections of the strength properties determined from triaxial tests done in accordance with TxDOT Test Method Tex-117E. The moisture correction procedure in the *LoadGage* program uses relationships between the cohesion and friction angle, and soil suction, which varies with moisture content as given by the material's soil-water characteristic curve (SWCC). [Figure 6-24](#) shows this curve for the clay material found at the Annex site along with the coefficients of [Gardner's equation \(1958\)](#) that defines the SWCC.

Table 6-5. Predicted Allowable Loads.¹

Section	<i>LoadGage</i>		Modified Triaxial Design Method (Tex-117E) ²	
	West wheel path	East wheel path	West wheel path	East wheel path
Chip seal on LTS	7650	7300	5975	5550
2-inch HMAC on LTS	3580	7890	8230	9140
4-inch HMAC on LTS	6080	9690	9340	11,480
4-inch HMAC no LTS	12,110	17,030	4420	6010
2-inch HMAC no LTS	10,650	11,460	2720	3225
Chip seal no LTS	4765	4340	1420	1355

¹ For a dual wheel configuration

² Based on Texas triaxial class of 6.1 for the clay subgrade

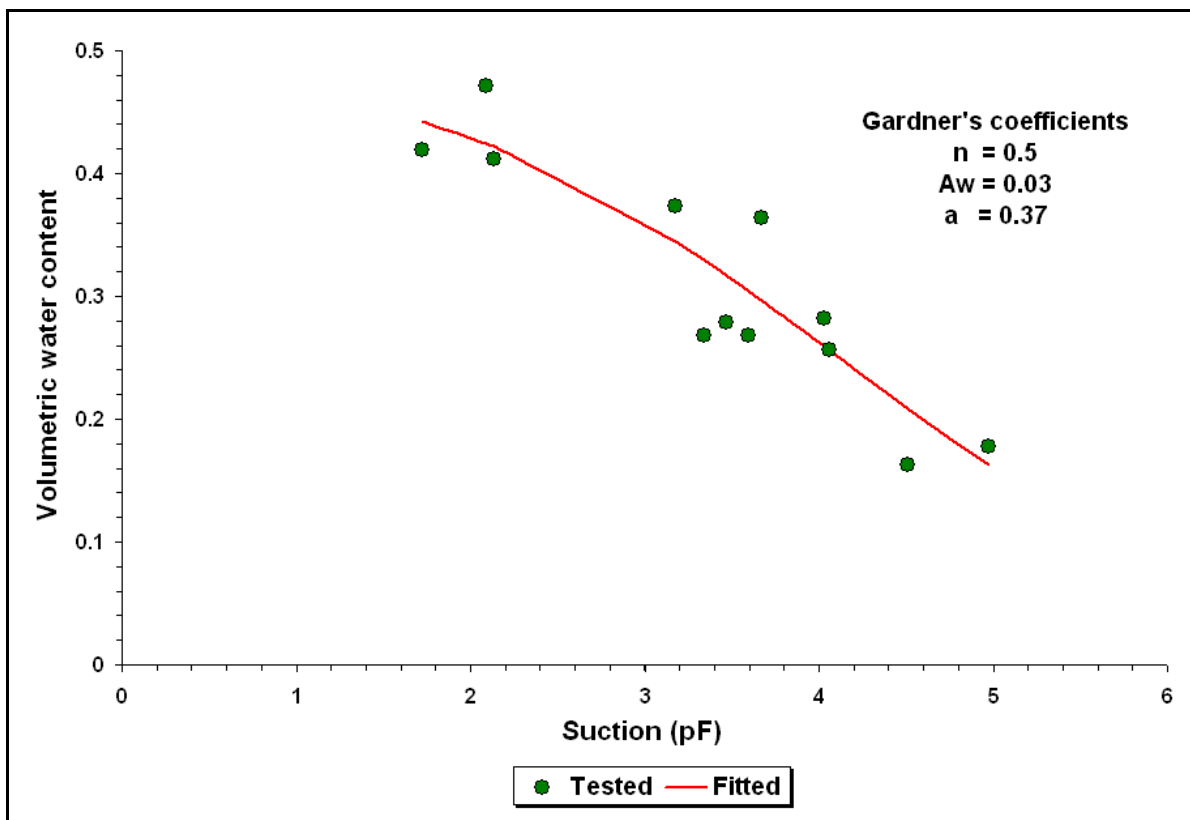


Figure 6-24. Soil-Water Characteristic Curve for Clay Material at Test Site.

This equation is given by:

$$\theta = \frac{n}{1 + A_w |h_p|^a} \quad (6.1)$$

where θ is the volumetric moisture content; h_p is the soil suction or negative pore pressure in cm of water head; n is the porosity; and A_w and a are model coefficients.

Table 6-6 shows the in-situ moisture contents for each section along with the moisture-corrected strength properties that were used in determining the allowable dual wheel loads using the Mohr-Coulomb failure criterion. For reference, the cohesion and friction angle determined based on TxDOT Test Method Tex-117E are 1.70 psi and 10.25°, respectively, at a capillary-saturated moisture content of 25 percent. The interested reader is referred to the report by Fernando et al. (2008b) for a description of the moisture correction procedure used in the *LoadGage* program.

Table 6-6. Moisture-Corrected Strength Properties of Clay Subgrade.

Section	Gravimetric moisture content (percent)	Cohesion (psi)	Friction angle (°)
Chip seal on LTS	26.9	1.46	12.84
2-inch HMAC on LTS	26.9	1.46	12.84
4-inch HMAC on LTS	22.9	2.42	8.16
4-inch HMAC no LTS	20.1	5.06	5.94
2-inch HMAC no LTS	20.0	5.21	5.87
Chip seal no LTS	20.9	4.00	6.54
Test Method Tex-117E	25.0	1.70	10.25

6.4.2 Repetitive Loading of Test Sections

Researchers used a single-unit truck with concrete blocks loaded on its flat bed to apply repetitive loads on the test sections. With the number of concrete blocks available, the single drive axle was loaded to 29,150 lb (14,500 lb on the left set of dual tires and 14,650 lb on the right). The test sections received a total of 112 load cycles and developed rutting on the wheel paths that varied with the test sections as summarized in Table 6-7.

Table 6-7. Measured Rut Depths after Repetitive Loading of Test Sections.

Section	Measured rut depth (inches)	
	West wheel path	East wheel path
Chip seal on LTS	0.35	0.42
2-inch HMAC on LTS	0.61	0.22
4-inch HMAC on LTS	0.60	0.16
4-inch HMAC no LTS	0.31	0.06
2-inch HMAC no LTS	0.38	0.28
Chip seal no LTS	0.90	1.05

To verify the *LoadGage* program based on results from the repetitive load tests, researchers examined the correlation between the predicted allowable loads and the measured rut depths at the end of tests. Researchers note that this prediction of allowable loading is based on a stress analysis wherein a check is made to verify whether the shear stresses induced under load are within the Mohr-Coulomb failure envelope of the subgrade as defined by the material's cohesion and friction angle. [Chester McDowell \(1955\)](#) used this same approach in developing the Texas triaxial design method. While the allowable load predictions are not based on repetitive load criteria, researchers decided to compare the *LoadGage* predictions against the observed performance of the sections from the repetitive load tests with the objective of determining whether the predictions exhibit a significant relationship with the measured rut depths at the end of tests. Specifically, does a higher allowable load based on the Mohr-Coulomb failure envelope translate to better performance, i.e., less rutting for a given number of load applications?

[Figure 6-25](#) plots the measured rut depths with the predicted allowable loads on the test sections. The bars in the figure correspond to the measured rut depths while the symbols connected by lines correspond to the allowable loads that are read off the secondary vertical axis. [Figure 6-25](#) shows that sections with shallower rut depths are associated with higher predicted allowable loads from *LoadGage*. This correlation is more readily observed in [Figure 6-26](#), which plots the predicted allowable loads with the measured rut depths at the end of tests. There is clearly an inverse relationship between these variables, which is quantified by the fitted curve to the data. The power law relationship shown in the figure is statistically significant and demonstrates the *LoadGage* predictions to be reasonable and in accordance with the observed performance of the test sections.

For comparison, [Figure 6-27](#) plots the allowable loads based on the modified Texas triaxial design method in Tex-117E with the measured rut depths at the end of tests. Researchers fitted the same power law model to the data, which is shown as the solid line in [Figure 6-27](#). While an inverse relationship is indicated in the figure, the relationship is weak compared to the correlation between the *LoadGage* predictions and the measured rut depths shown previously in [Figure 6-26](#).

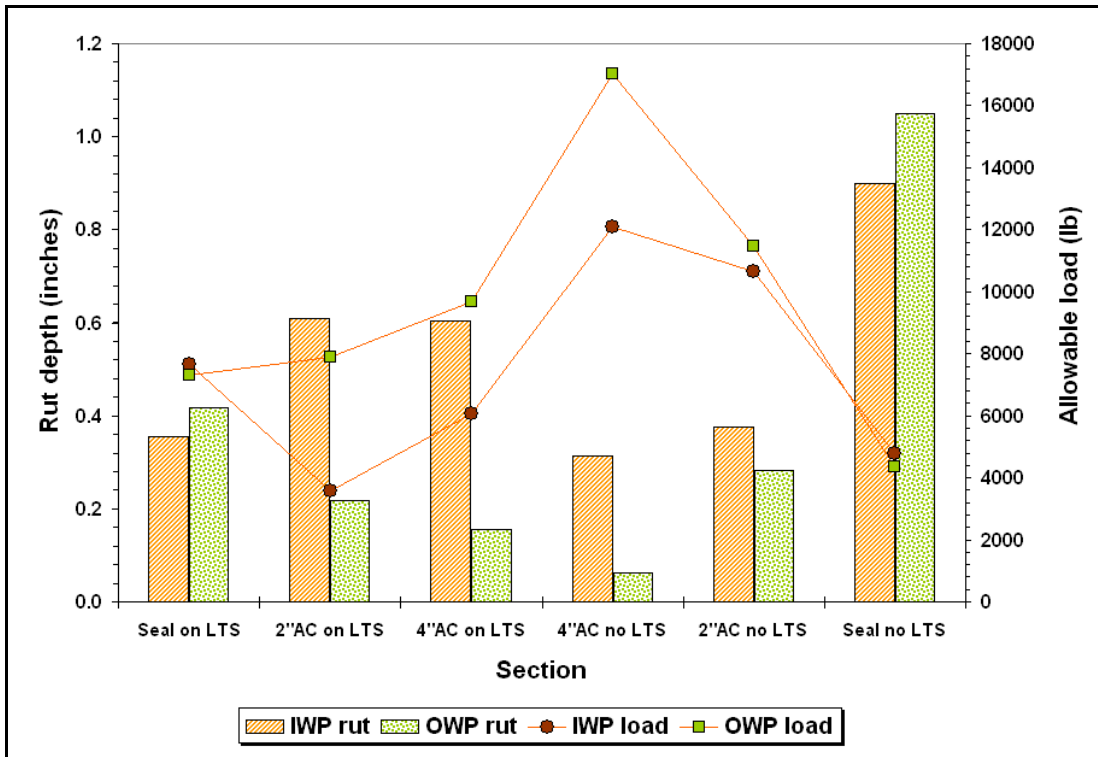


Figure 6-25. Comparison of Measured Rut Depths with *LoadGage* Predicted Allowable Loads on Sections Tested.

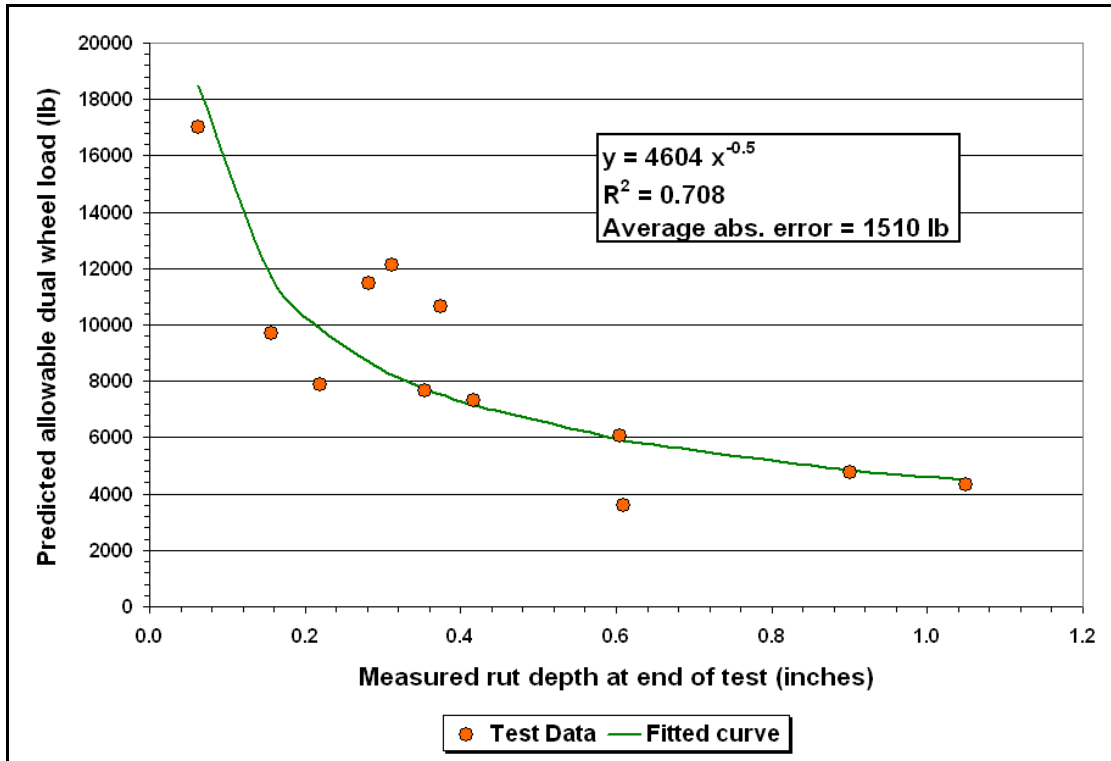


Figure 6-26. Relationship between Measured Rut Depths and *LoadGage* Predicted Allowable Loads.

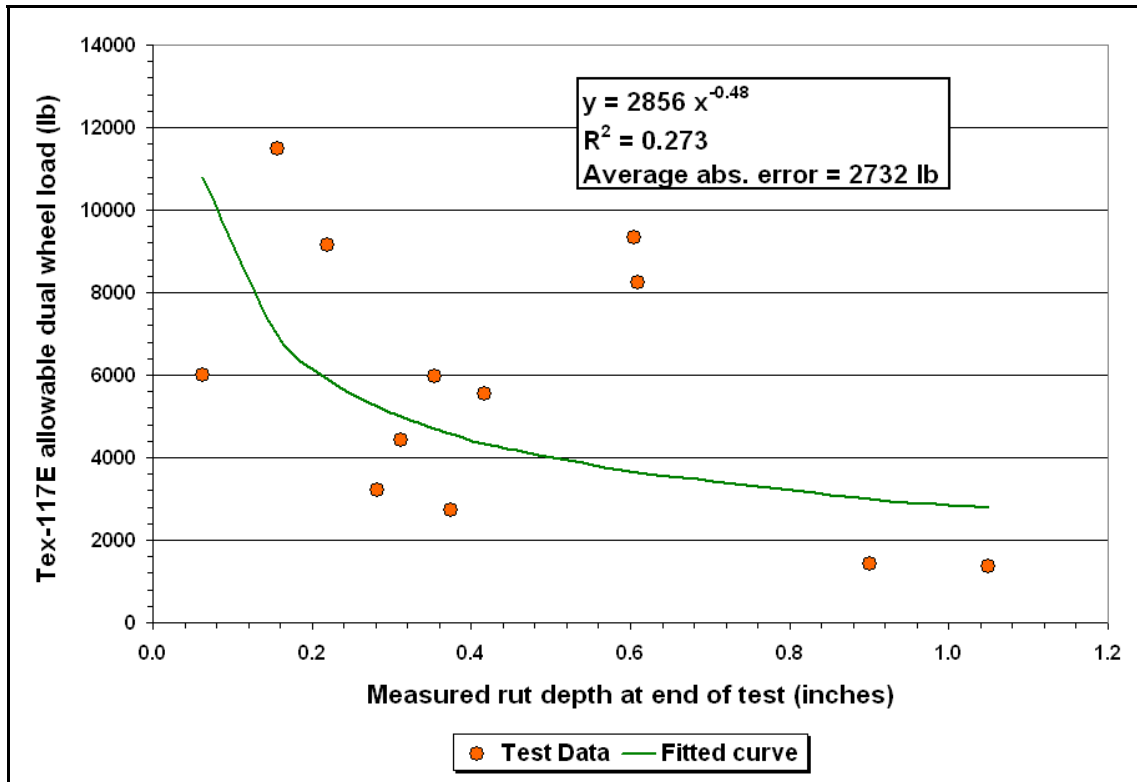


Figure 6-27. Relationship between Measured Rut Depths and Tex-117E Predicted Allowable Loads.

6.5 SUMMARY AND CONCLUSIONS

This chapter discussed the field tests conducted by researchers to verify the *LoadGage* program based on repetitive loading of full-scale field sections constructed during this project. This work follows-up on earlier tests conducted in Project 0-4519, which compared the predicted allowable wheel loads from *LoadGage* with corresponding wheel loads determined from plate bearing tests. For the verification presented herein, researchers compared the *LoadGage* predictions against the observed performance of the sections tested, with the objective of determining whether the predictions exhibit a significant relationship with the measured rut depths at the end of tests. Researchers found a statistically significant inverse relationship between the predicted, moisture-corrected allowable loads and the measured rut depths, with a power law model giving a reasonable fit to the test data, as indicated by an R^2 of about 71 percent and an average absolute error of about 1500 lb. In comparison, researchers found the correlation between the measured rut depths and the predicted Tex-117E allowable loads to be weak. In this instance, fitting the same power law model to the test data gave an R^2 of about 27 percent and an average absolute error of about 2700 lb.

The test results demonstrated the importance of considering moisture effects to determine allowable wheel loads based on the Mohr-Coulomb failure criterion used in the existing triaxial design check. Based on the results obtained, researchers found that *LoadGage* yields reasonable predictions of allowable wheel loads and recommend its use for triaxial design checks in the TexME pavement design framework. Beyond the practice of performing triaxial design checks,

additional development work should focus on rutting predictions for thin pavements. This work will require design, construction, materials and performance data on in-service or accelerated pavement test sections to verify and calibrate existing permanent deformation models, particularly for thin pavements on which available data are lacking. In the near term, this development work will benefit from use of an accelerated pavement test facility, which provides the opportunity to build and test a representative range of thin pavements expeditiously. In the long-term, TxDOT pavement databases should include monitoring data on in-service thin pavements to provide for future verification and calibration of the TexME rutting model for these pavements.

CHAPTER 7

CONCLUSIONS AND RECOMMENDATIONS

7.1 CONCLUSIONS

Based on the work presented previously, the following conclusions and recommendations are made:

- After reviewing all existing pavement performance models the VESYS model was recommended for predicting flexible pavement layer rutting, and an Overlay Tester-based fatigue cracking model was proposed, which includes both crack initiation and propagation models.
- A complete literature review was conducted to identify test procedures for characterizing material properties needed to predict pavement response and distresses. In particular, the test procedures for measuring HMA dynamic modulus, fracture, and permanent deformation properties, resilient modulus, and permanent deformation properties of base/subbase and subgrade materials were evaluated and then revised for TexME in this study.
- The repeated load test was proposed for characterizing HMA materials and modeling HMA rutting. This test was validated with field measured rutting data from both NCAT test track and Texas highways. Also the use of the Overlay Test for fatigue cracking was verified using the accelerated pavement test results (ALF and HVS).
- The multi-layer linear elastic system was evaluated to compute asphalt pavement response. Its validity was verified through comparing the measured tensile strains under accelerated pavement ALF loading with the computed ones.
- Existing pavement performance models (or transfer functions) were also evaluated and reasonable models for predicting pavement distresses (such as rutting, fatigue cracking) were recommended for TexME. The recommended pavement performance models (or transfer functions) were further developed and then calibrated using real field performance data. Specifically, the HMA rutting model was calibrated using the rutting data from the NCAT test track and the LTPP-SPS 5 test sections on US175 near Dallas. During the model calibration, either lab molded plant mix samples or field cores were characterized using HMA dynamic modulus tests and repeated load tests to develop material properties. Calibration factors for the HMA rutting model were developed through minimizing the difference between the measured field rut depths and the ones predicted from the model. A similar approach was used to calibrate the fatigue cracking model.
- Additionally, the calibrated pavement performance models (or transfer functions) were further validated using separate data sets from the original performance data used for model calibration.

- Default material properties, including dynamic modulus, permanent deformation parameters, fracture properties, were established for a range of the most commonly used surface HMA mixes in Texas (Zhou et al. 2009a). Mixtures evaluated were: performance mixes (SMAs) as well as Type C and D dense-graded mixes. The influence of the different grades of binder on these mixes was also established. These values can be incorporated into future model validation studies. Future work should measure similar properties for the Type A and B dense-graded base mixes.
- For granular bases, the resilient modulus and repeated load permanent deformation tests were found to classify base materials in the same rank order as the observed District performance. The moduli values (at 5 psi confining and 15 psi deviator stress) for the different classes of base were found to be in the range of 35 to 70 ksi, which is very similar to the values obtained from FWD testing.
- It was determined that the optimum moisture content with the same compaction energy per unit volume is influenced by sample size. Therefore to use the nationally recommended sample height of 6-inch diameter by 12-inch height will require the use of this size of sample when running the OMC curves.
- More work is recommended to improve the repeatability of the granular base tests. More work will also be required to incorporate the effect of base moisture content on predicted performance.
- For cement and other stabilized bases, very little recent work was found in the current literature on model development or calibration. Recent work funded by the Portland Cement Association has proposed calibration factors for the models proposed in the MEPDG, these factors should be considered for incorporation in a future TexME design system until further evaluation of stabilized materials proves otherwise.
- Several experimental test sections were constructed at Texas A&M's Riverside Campus and later trafficked to validate the *LoadGage* program that was developed for thin pavement design. Very reasonable maximum allowable load limits were found when moisture correction factors were applied to the laboratory measured engineering properties.

7.2 RECOMMENDATIONS

The FPS19 design system was implemented in the mid 1990s and has served TxDOT well in providing consistent designs statewide. The existing FPS19 program presents a recommended pavement structure based on predictions of pavement roughness. This proposed structure is then checked using either a simple ME model (which uses well established fatigue cracking and subgrade rutting models) or, for thin pavement structures, the Texas Triaxial check system is run to predict whether the maximum anticipated load for the highway will cause the subgrade to fail in shear. However, the current FPS19 system has many limitations in that it does not use any results from lab testing, so it is difficult to quantify benefits from improved base materials or superior asphalt mixes. No checking of asphalt rutting is performed which

has been demonstrated to be the source of most rutting found on Texas highways with 3 inches or thicker HMA layer. Furthermore the Texas Triaxial check system is well known to be too conservative for many regions, particularly those in north and west Texas.

Project 0-5798 has demonstrated that calibrated models are now available to make reasonable predictions of the most common distresses found on Texas highways. The Tex ME system described in this report is highly suited for replacing the existing simple ME check inside of FPS and the *LoadGage* system could replace the Texas Triaxial check. Simple performance related tests are now available to characterize soils, base, and asphalt materials in the lab, and these properties can be incorporated into a new thickness analysis and design system.

Researchers strongly recommend that TxDOT consider incorporating all of the calibrated models from this study, and those recommended herein from other national studies, into a user-friendly design software package, together with a database of default material properties. The proposed system will be used to run in parallel with the existing FPS system so that the proposed performance models can be further evaluated, validated and refined. The models developed in study 0-5123-3 (Zhou et al. 2009b) for predicting reflection cracking should eventually be included in the final design system. The framework for the proposed system is shown below in Figure 7-1.

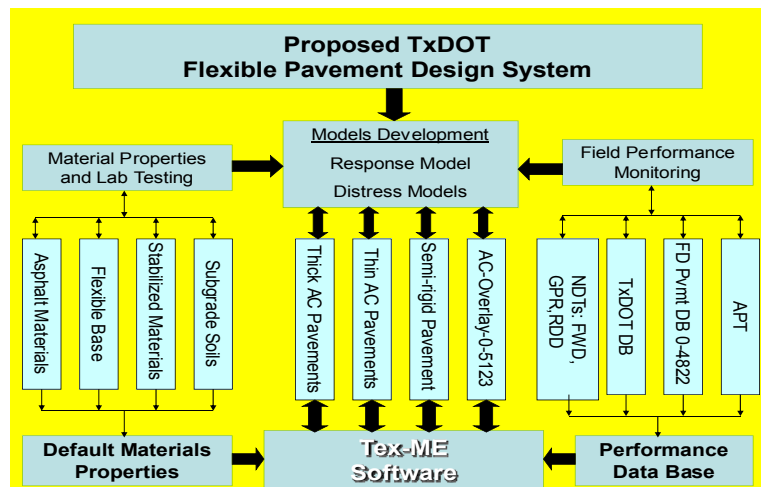


Figure 7-1. Outline for the Proposed TexME Design System.

All of the models recommended in this report should be incorporated into this design package. In the proposed system, TxDOT’s existing databases (such as the data base established for the perpetual pavements) will be available to supply additional information on properties from a range of different materials. A very important component, also included in Figure 7-1, is an Accelerated Pavement Test system that could be used for a whole range of model development and model verification activities. In addition to validating or updating mechanistic cracking and rutting models it could be used to further validate *LoadGage* where a range of thin pavements could rapidly be

tested to failure. The 0-5798 researchers made extensive use of available APT data when performing calibration of the recommended models. Similar programs should be considered for the future, either in-house or in cooperation with agencies actively operating APT systems.

To support the TexME system, the material properties shown below in Figure 7-2 will be required. Procedures for running all of these tests were published in an earlier report of this study. The development of all of the material properties from the lab tests is now automated with macros available at TTI.

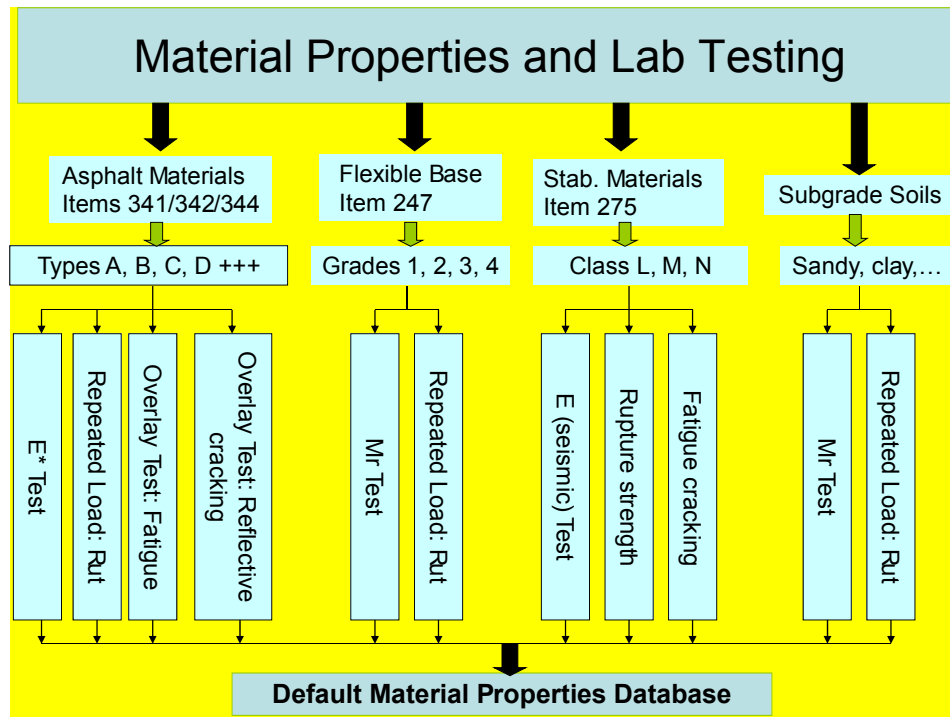


Figure 7-2. Material Testing to Support TexME.

One major limitation of the proposed system is that the only laboratory in Texas that can run the required tests is the laboratory at the Texas Transportation Institute. TxDOT labs cannot, at the moment, run any of the repeated load tests for either the rutting or cracking properties of all pavement materials. Long-term implementation of the proposed system should eventually include the establishment of an advanced design materials laboratory within the Construction Division's materials lab at Cedar Park.

Additionally a significant new development has been announced in the HMA mix test area. Figure 7-3 shows new commercially available simple performance equipment that was recently developed (Fall 2009). This equipment can measure all of the required modulus and repeated load permanent deformation properties for HMA materials. The real innovation in this equipment is the use of new sensors that are automatically mounted around the sample. This eliminates many of the problems and much of the time required to set up and run this test. The total cost of this system is \$75,000.



Figure 7-3. New Generation of HMA Test Equipment with Automated Sensors.

Summarizing these recommendations, the following action plan is proposed.

- Incorporate all of the proposed models into a user-friendly prototype design package, similar in format to the package developed for the overlay design system in study 0-5123. The package should also incorporate a linear elastic stress prediction module and the Enhanced Integrated Climatic models.
- Assemble all of the default materials properties for the commonly used asphalt, base, and subgrade materials. Many of these are available, but additional testing will be required (for example Type A and B mixes, a wider range of base materials).
- Establish a test plan to validate the proposed system on a range of TxDOT design projects.
- Establish an advanced material testing Lab at Cedar Park, which should include:
 - Purchase of new generation HMA test equipment as shown in [Figure 7-3](#) (Cost \$75,000).
 - Upgrade of TxDOT's existing base and soils dynamic testing equipment to match the capabilities of the TTI equipment (Cost \$50,000 estimate).
 - Upgrade of TxDOT's overlay test equipment to permit the measurement of fracture parameters (Cost \$10,000 estimate).
- Provide training to TxDOT personnel responsible for material testing.
- Provide training to TxDOT personnel in running the new performance models and interpreting the results.

REFERENCES

- AASHTO 1993, *Guide for Design of Pavement Structures*. American Association of State Highway and Transportation Officials, Washington, D.C., 1993.
- AASHTO TP31-94: *Standard Test Method for Determination of the Resilient Modulus of Bituminous Mixtures by Indirect Tension*, American Association of State Highway and Transportation Officials, Washington, D.C., 1994.
- AASHTO TP62-03, *Standard Test Method for Determining the Dynamic Modulus of Hot-Mix Asphalt Concrete Mixtures*, American Association of State Highway and Transportation Officials, Washington, D.C., 2003.
- AASHTO T320-03, *Method for Determining the Permanent Shear Strain and Stiffness of Asphalt Mixtures Using the Superpave Shear Tester (SST)*, American Association of State Highway and Transportation Officials, Washington, D.C., 2003.
- AI, *Thickness Design Manual (MS-1)*, 9th ed. The Asphalt Institute, College Park, MD, 1981.
- AI, *Research and Development of the Asphalt Institute's Thickness Design Manual (MS-1)*, Technical Report Research Report 82-2, Asphalt Institute, 1982.
- AI, *Mix Design Methods for Asphalt Concrete and Other Hot-Mix Types (MS-2)*, Asphalt Institute, Lexington, Kentucky, 6th Edition, 1993.
- Al-Khateeb, G., A. Shenoy, N. H. Gibson, and T. Harman, A New Simplistic Model for Dynamic Modulus Predictions of Asphalt Paving Mixtures, *Journal of the Association of Asphalt Paving Technologists*, Vol. 75 CD-ROM, 2006.
- Al-Qadi, I. L, Loulizi, A., Elseifi, M. and S. Lahouar, The Virginia Smart Road: The Impact of Pavement Instrumentation on Understanding Pavement Performance. *Journal of the Association of Asphalt Pavement Technologists*, AAPT, Vol. 73, 2004.
- Al-Qadi, I. L, Yoo, P. J. and Elseifi, M.A., Effects of Tire Configurations on Pavement Damage. *Journal of the Association of Asphalt Pavement Technologists*, AAPT, Vol. 74, 2005.
- Al-Qadi, I., W. Xie, and M. A. Elseifi, Frequency Determination from Vehicular Loading Time Pulse to Predict Appropriate Complex Modulus in MEPDG, *Journal of The Association of Asphalt Paving Technologists*, AAPT, Vol. 77, pp. 739-772, 2008.
- Andrei, D., M. W. Witczak, and M. W. Mirza, *Development of Revised Predictive Model for the Dynamic (Complex) Modulus of Asphalt Mixtures. Development of the 2002 Guide for the Design of New and Rehabilitated Pavement Structures, NCHRP I-37A*, Interim Team Technical Report, Department of Civil Engineering, University of Maryland of College Park, MD, 1999.
- ANSYS 9.0. User Manual, Ansys Inc., Canonsburg, PA, 2004.

- ASTM D 4123-82: *Standard Test Method for Indirect Tension Test for Resilient Modulus of Bituminous Mixtures*, 1982.
- Barksdale, R. D., Compressive Stress Pulse Times in Flexible Pavements for Use in Dynamic Testing, In *Highway Research Record 345*, HRB, National Research Council, Washington, D.C., pp. 32–44, 1971.
- Barksdale, R. D., Laboratory Evaluation of Rutting in Base Course Materials, *Proceedings of the 3rd International Conference on the Structural Design of Asphalt Pavements*, Vol. I, London, England, 1972.
- Barksdale, R. D., NCHRP 1-28: *Proposed Test Protocol for Determination of the Resilient Modulus of Bituminous Mixtures by Indirect Tension*, October 1996.
- Bonnaure, F. A. Gravois, and J. Udron. A new method for predicting the fatigue life of bituminous mixes. *Proceedings of the Association of Asphalt Paving Technologists*, Vol. 49, pp. 499-529, 1980.
- Brown, S. F., Determination of Young's Modulus for Bituminous Materials in Pavement Design, In *Highway Research Record*. No.431, Highway Research Board, pp. 38-49, 1973.
- Brown, E. R., and S. Cross, A National Study of Rutting in Asphalt Pavement, *Proceedings of AAPT*, Vol. 61, pp. 535-582, 1992.
- Brown, S. F., M. M. Darter, G. Larson, M. Witczak, and M. El-Basyouny, *Independent Review of the Mechanistic-Empirical Pavement Design Guide and Software*, NCHRP Research Results Digest 307, September 2006.
- Buttlar, W. G., M. P. Wagoner, Z. You, and S. T. Brovold, Simplifying the Hollow Cylinder Tensile Test Procedure Through Volume-Based Strain, *Journal of the Association of Asphalt Paving Technologists*, Vol. 73, pp. 370-396, 2004.
- Button, J. W. and Lytton, R. L., Evaluation of Fabrics, Fibers, and Grids in Overlays, *Proceedings of the Sixth International Conference on Structural Design of Asphalt Pavements*, The University of Michigan, Vol. 1, pp. 925-934, 1987.
- Chang H. S., Lytton R. L., Carpenter S. H., *Prediction of Thermal Reflection Cracking in West Texas*, Texas Transportation Institute, Research Report 18-3, Study 2-8-73-18, March, 1976.
- Chehab, G. R., E. N. O Quinn, and Y. R. Kim, Specimen Geometry Study for Direct Tension Test Based on Mechanical Tests and Air Void Variation in Asphalt Concrete Specimens Compacted by the Superpave Gyrotory Compactor, *Transportation Research Record 1723*, Transportation Research Board, Washington, D. C., 2000.

- Christensen, D. W., T. Pellinen, and R. F. Bonaquist, Hirsch Model for Estimating the Modulus of Asphalt Concrete, *Journal of Association of Asphalt Paving Technologists*, Vol. 72, 2003.
- Deacon, J. A., *Fatigue of Asphalt Concrete, Doctoral dissertation*, University of California, Berkeley, California, 1965.
- Dongré, R., L. Myers, J. D'Angelo, C. Paugh, and J. Gudimettla, Field Evaluation of Witczak and Hirsh Models for Predicting Dynamic Modulus of Hot-Mix Asphalt, *Journal of The Association of Asphalt Paving Technologists*, AAPT, Vol. 74, 2005.
- El-Basyouny, M. and M. W. Witczak, Calibration of Alligator Fatigue Cracking Model for 2002 Design Guide. *Journal of Transportation Research Board* 1919, Washington D.C., pp. 77-86, 2005.
- Elmitiny, M. R. N., *Material Characterization for Studying Flexible Pavement Behavior in Fatigue and Permanent Deformation*, Ph. D. Dissertation, The Ohio State University, 1980.
- Epps, J. A., A. Hand, S. Seeds, T. Scholz, S. Alavi, C. Ashmore, C. L. Monismith, J. A. Deacon, J. T. Harvey, and R. B. Leahy, Recommended Performance-Related Specifications for Hot-Mix Asphalt Construction. *NCHRP Report 455*, National Cooperative Highway Research Program, Transportation Research Board, National Research Council, Washington, D.C., pp. 496, 2002.
- Erkens, S., Moraal, J., Molenaar, A. A. A., Groenendijk, J., and M. Jacobs, Using Paris' Law to Determine Fatigue Characteristics – A Discussion, *Proceedings of the 8th International Conference on Asphalt Pavements*, Seattle, WA, pp. 1123-1142, August 10-14, 1997.
- Fernando, E. G., Musani, D., Park, D-W., Liu, W., *Evaluation of Effects of Tire Size and Inflation Pressure on Tire Contact Stresses and Pavement Response*, FHWA/TX-06/0-4361-1, Texas Transportation Institute, College Station, Texas, August 2006.
- Fernando, E. G., J. Oh, C. Estakhri and S. Nazarian. *Verification of the Load-Thickness Design Curves in the Modified Triaxial Design Method*. Research Report 0-4519-1, Texas Transportation Institute, Texas A&M University, College Station, TX, 2008a.
- Fernando, E. G., J. Oh, D. Ryu and S. Nazarian. *Consideration of Regional Variations in Climatic and Soil Conditions in the Modified Triaxial Design Method*. Research Report 0-4519-2, Texas Transportation Institute, Texas A&M University, College Station, TX, 2008b.
- Finn, F.N., Sraf, C., Kulkarni, R., Nair, K., Smith, W., and A. Abdullad, The Use of Prediction Subsystems for the Design of Pavement Structures, *Proceedings of Fourth International Conference on Structural Design of Asphalt Pavements*, University of Michigan, Ann Arbor, MI, pp. 3-38, 1977.

- Gardner, W. R. *Some Steady State Solutions of the Unsaturated Moisture Flow Equation with Application of Evaporation from a Water Table*. Soil Science, Vol. 85, pp. 223-232, 1958.
- Germann, F. P. and R. L. Lytton, *Methodology for Predicting the Reflection Cracking Life of Asphalt Concrete Overlays*, Research report FHWA/TX-79/09+207-5, College Station, Texas, March 1979.
- Ghuzlan, K. A., and S. H. Carpenter, *Traditional Fatigue Analysis of Asphalt Concrete Mixtures*, Transportation Research Board, CD-ROM, Washington, D.C., 2003.
- Gokhale, S., Choubane, B., Byron, T., and M. Tia, *Rut Initiation Mechanisms in Asphalt Mixtures as Generated Under Accelerated Pavement Testing*, *Journal of Transportation Research Record* 1940, pp. 136-145, 2005.
- Harvey, J. T., Deacon, J., Tsai, B., and C. L. Monismith, *Fatigue Performance of Asphalt Concrete Mixes and Its Relationship to Asphalt Concrete Pavement Performance in California*. RTA-65W485-2, Asphalt Research Program, CAL/APT Program, Institute of Transportation Studies, University of California at Berkeley, Berkeley, CA, 1996.
- Harvey, J. T., and L. Popescu, *Rutting of Caltrans Asphalt Concrete and Asphalt-Rubber Hot Mix Under Different Wheels, Tires, and Temperatures—Accelerated Pavement Testing Evaluation*, Draft report prepared for California Department of Transportation Pavement Research Center, CAL/APT Program, Institute of Transportation Studies, University of California, Berkeley, CA. UCPRC-RR-2000-0, January 2000.
- Hu, S., Hu, X., Zhou, F., and L. Walubita, *SA-CrackPro: A New Finite Element Analysis Tool for Pavement Crack Propagation*, *Journal of Transportation Research Record* 2068, pp. 10-19, 2008.
- Huekelom, W., and A. J. G. Klomp, *Consideration of Calculated Strains at Various Depths in Connection with the Stability of Asphalt Pavements*, *Proceedings of the 2nd International Conference on the Structural Design of Asphalt Pavements*, Vol. I, Ann Arbor, Michigan, 1967.
- Huang, Y. H., *Pavement Analysis Design*, Prentice Hall, Englewood Cliffs, NJ 07632, 1993.
- Hveem, F. N., "Pavement Deflections and Fatigue Failures." *Bulletin 114 HRB*, National Research Council, Washington, D.C, pp. 43-87, 1955.
- Jacobs, M. M. J., *Crack Growth in Asphaltic Mixes*, Ph.D. Dissertation, Delft University of Technology, the Netherlands, 1995.
- Jacobs, M. M. J., P. C. Hopman, and A. A. A. Molenaar, *Application of Fracture Mechanics in Principles to Analyze Cracking in Asphalt Concrete*, *Journal of the Association of Asphalt Paving Technologists*, Vol. 65, pp. 1-39, 1996.

- Jordahl, P. R., and Rauhut, J. B., *Flexible Pavement Model VESYS IV-B*, Report prepared for Federal Highway Administration under Contract DTFH61-C-00175, 1983.
- Kenis, W. J., *Predictive Design Procedure, VESYS User's Manual: An Interim Design Method for Flexible Pavement Using the VESYS Structural Subsystem*. Final Report No. FHWA-RD-77-154, FHWA, Washington D.C., 1978.
- Kenis, W. J., and W. Wang, "Calibrating Mechanistic Flexible Pavement Rutting Models From Full Scale Accelerated Tests, *Proceedings of the Eighth International Conference on Asphalt Pavements*, Vol. I, pp. 663-672, Seattle, Washington, 1997.
- Kim, Y. R., Y. Seo, M. King, and M. Momen, Dynamic Modulus Testing of Asphalt Concrete in Indirect Tension Mode, Transportation Research Board 83rd Annual Meeting Compendium papers, Transportation Research Board, Washington, D. C., 2003.
- Lee, H.J., Kim, Y. R., and S. W. Lee, Prediction of Asphalt Mix Fatigue Life with Viscoelastic Material Properties, *Journal of the Transportation Research Board*, No. 1832, pp.139-147, 2003.
- Liu, W. and T. Scullion. *PAVECHECK: Updated User's Manual*. Research Report 0-5495-1, Texas Transportation Institute, Texas A&M University, College Station, Tex., 2007.
- Loulizi, A., I. Al-Qadi, S. Lahouar, and T. E. Freeman, Measurement of Vertical Compressive Stress Pulse in Flexible Pavements: Representation for Dynamic Loading Tests. *In Transportation Research Record*. No. 1816, TRB, National Research Council, Washington, D.C., pp. 125-136, 2002.
- Lytton, R. L., J. Uzan, E. G. Fernando, R. Roque, D. Hiltunen, and S. M. Stoffels, *Development and Validation of Performance Prediction Models and Specifications for Asphalt Binders and Paving Mixes*, SHRP A-357, National Research Council, Washington, D. C., 1993.
- Majidzadeh, K., Kaufmann, E. M., and D. V. Ramsamooj, Application of Fracture Mechanics in the Analysis of Pavement Fatigue, *Proceedings of Association of Asphalt Pavement Technologists*, Vol. 40, pp. 227-246, 1970.
- Majidzadeh, K., M. Dat, and F. Makdisi-Ilyas, *Application of Fracture Mechanics for Improved Design of Bituminous Concrete, Vol. 2 Evaluation of Improved Mixture Formulations, and the Effect of Temperature Conditions on Fatigue Models*, Report No. FHWA-RD-76-92, Final Report, June 1976.
- McDowell, C. *Wheel-Load-Stress Computations Related to Flexible Pavement Design*. Bulletin 114, Highway Research Board, Washington, D.C., pp. 1-20, 1955.
- McLean, D. B., *Permanent Deformation Characteristics of Asphalt Concrete*, Ph.D. dissertation, University of California, Berkeley, 1974.

- Molenaar, A. A. A., *Structural Performance and Design of Flexible Road Constructions and Asphalt Concrete Overlays*, Ph.D. Dissertation, Delft University of Technology, The Netherlands, 1983.
- Monismith, C. L., Resilient Modulus Testing: Interpretation of Laboratory Results for Design Purposes, *Proceedings of the Workshop on Resilient Modulus Testing*, Oregon State University, Corvallis, Oregon, 1989.
- Morris, J., and R. C. G. Haas, Designing for Rutting in Asphalt Pavements, Canadian Technical Asphalt Association Annual Meeting, 1972.
- Odemark, N.: *Undersökning av elasticitetsegenskaperna hos olika jordartersamt teori för beräkning av beläggningar enligt elasticitetsteorin*. StatensVäginstitut, Meddelande 77, Sweden, 1949.
- NCAT, Asphalt Technology News, Vol. 17, No. 1, National Center for Asphalt Technology, Spring 2005.
- NCHRP Project 1-37A. *Guide for Mechanistic-Empirical Design of New and Rehabilitated Pavement Structures*. Final Report, TRB, National Research Council, Washington, D.C., March 2004. <http://trb.org/mepdg/guide.htm>.
- Paris, P.C. and F. Erdogan “A Critical Analysis of Crack Propagation Laws”, *Transactions of the ASME, Journal of Basic Engineering*, Series D, 85, No. 3, 1963.
- Park, S. W. and R. A. Schapery, Methods of Interconversion between Linear Visco-elastic Material Functions, Part I: A Numerical Method Based on Prony Series, *International Journal of Solid and Structure*, Vol. 36, No. 11, pp. 1653-1675, 1999.
- Pickett, D. L. and Lytton, R. L., Laboratory Evaluation of Selected Fabrics for Reinforcement of Asphaltic Concrete Overlays, Research Report 261-1, Texas Transportation Institute, The Texas A&M University System, College Station, Texas, August 1983.
- Press, W. H., B. P. Flannery, S. A. Teukolsky, and W. T. Vetterling, *Numerical Recipes in C: The Art of Scientific Computing*, Cambridge University Press; 2 edition, October 30, 1992.
- Prozzi, J. A., J. P. Aguiar-Moya, A. F. Smit, M. Tahmoressi, and K. Fults, *Recommendations for Reducing Superpave Compaction Effort to Improve Mixture Durability and Fatigue Performance*, FHWA/TX-07/0-5132-1, Center for Transportation Research, 3208 Red River, Suite 200, Austin, TX 78705-2650, 2006.
- Romain, J. E., Rut Depth Prediction in Asphalt Pavements, Research Report No. 150, Centre de Recherches Routieres, Brasseks, Belgium, 1969.

- Roque, R., Zhang, Z., Sankar, B., Detaremination of Crack Growth Rate Parameters of Asphalt Mixtures Using the Superpave IDT, *Journal of the Association of Asphalt Paving Technologists*, Vol. 68, pp. 404-433, 1999.
- Qi, X., T. Mitchell, K. Stuart, J. Youtcheff, K. Petros, T. Harman, and G. Al-Khateeb, Strain Responses in ALF Modified-Binder Pavement Study, *the CD Proceedings of 2nd International Conference on Accelerated Pavement Testing*, Minneapolis, MN, Sept. 2004.
- Salam, Y. M., *Characterization of deformation and fracture of asphalt concrete*, PhD. Dissertation, University of California, Berkeley, 1971.
- Salam, Y. M. and C. L. Monismith, Fracture Characteristics of Asphalt Concrete, *Proceedings of Association of Asphalt Paving Technologists*, Vol. 41, pp. 215-256, 1972.
- Scarpas A., Al-Khoury R., Gulp C.A.P.M. and Erkens S.M.J.G., Finite Element Simulation of Damage Development in Asphalt Concrete Pavements, *8th Int. Conf. on Asphalt Pavements, Volume 1 Proceeding*, University of Washington, Seattle, Washington, pp. 673-692, 1997.
- Schapery, R.A., "Correspondence Principles and a Generalized J-Integral for Large Deformation and Fracture Analysis of Viscoelastic Media." *International Journal of Fracture*, Vol. 25, pp. 195-223, 1984.
- Schwartz, C., Improving Mechanistic-Empirical Models for Predicting HMA Rutting, Presented at 2006 Symposium on Models Used to Predict Pavement Performance, Laramie, Wyoming.
<http://www.petersenasphaltconference.org/download/Schwartz%20Improving%20Mechanistic-Empirical%20Models%20for%20Predicting%20HMA%20Rutting.pdf>.
- Scullion, T. and Y. Chen. *COLORMAP Version 2, User's Manual with Help Menus*. Research Report 0-1702-5, Texas Transportation Institute, College Station, Tx., 1999.
- Scullion, T. and W. Liu. *MODULUS 6.0 for Windows: User's Manual*. Research Report 0-1869-2, Texas Transportation Institute, College Station, Texas, 2001.
- Scullion, T., J. Uzan, S. Hilbrich, and P. Chen, *Thickness Design System for Pavements Containing Soil Cement bases*, Research Report 400381-1, Texas Transportation Institute, Texas A&M University, College Station, Texas, July 2006.
- Seo, Y., Y. R. Kim, R. A. Schapery, M. W. Witzczak, R. Bonaquist, A Study of Crack-Tip Deformation and Crack Growth in Asphalt Concrete Using Fracture Mechanics, *Journal of Association of Asphalt Paving Technologists*, Vol. 74, pp. 200-228, 2004.
- SHELL. *Shell pavement design manual and addendum*. SHELL International Petroleum Company Limited, Shell Ltd., London, 1985.

- SHRP Southern Region Coordination Office, Asphalt Rehabilitation Study on US175 IN Kaufman County, Texas, Final Report-SPS5 Project, July 1992.
- Simo, J. C. and T. J. R. Hughes, *Computational Inelasticity*, Springer-Verlag, New York, 2000.
- Sousa, J.B., J. C. Pais, M. Prates, R. Barros, P. Langlois, and A- M. Leclerc, Effect of Aggregate Gradation on Fatigue Life of Asphalt Concrete Mixes, *Transportation Research Record*, No. 1630, pp. 62-68, 1998.
- SPSS Inc., 2003
- Tayebali, A. A., J. A. Deacon, J. S. Coplantz, J. T. Harvey, and C. L. Monismith, *Fatigue Response of Asphalt Aggregate Mixes*. SHRP-A-404, Strategic Highway Research Program, National Research Council, Washington, D.C., 1994.
- Timm, D. H. and A. L. Priest, *Material Properties of the 2003 NCAT Test Track Structural Study*, National Center for Asphalt Technology, 2006.
- Tsai, B. W., *High Temperature Fatigue and Fatigue Damage Process of Aggregate-Asphalt Mixes*, Ph.D. Dissertation, University of California at Berkeley, June 2001.
- Tsai, B. W., J. T. Harvey, and C. L. Monismith, "Application of Weibull Theory in Prediction of Asphalt Concrete Fatigue Performance." *Transportation Research Record No. 1832*. Transportation Research Board, National Research Council, Washington, D.C., pp. 121-130, 2003.
- Tsai, B.W. and C.L. Monismith, Influence of Asphalt Binder Properties on the Fatigue Performance of Asphalt Concrete Pavements, *Journal of the Association of Asphalt Paving Technologists*, Vol. 74, 2005.
- Ullidtz, P., *Pavement Analysis*, 1987.
- Ullidtz, P., *Modelling Flexible Pavement Response and Performance*, 1998.
- Ullidtz, P., J. T. Harvey, B. W. Tsai, and C. L. Monismith, *Calibration of Incremental-Recursive Flexible Damage Models in CalME Using HVS Experiments*. Report prepared for the California Department of Transportation (Caltrans) Division of Research and Innovation by the University of California Pavement Research Center, Davis and Berkeley. UCPRC-RR-2005-06, April 2005.
- Van der Poel, C., A General System Describing the Visco-Elastic Properties of Bitumens and Its Relation to Routine Test Data, *Journal of Applied Chemistry*, Vol. 4, pp. 221-236, 1954.
- Walubita, L. F., A. E. Martin, S. H. Jung, C. J. Glover, A. Chowdhury, E. S. Park, and R. L. Lytton, *Preliminary Fatigue Analysis of A Common TxDOT Hot Mix Asphalt Concrete Mixture*, FHWA/TX-05/0-4468-1, Texas Transportation Institute, College Station, Texas 77843-3135, 2005.

- Witczak, M. W., R. F. Bonaquist, H. Von Quintus, and K. Kaloush, Specimen Geometry and Aggregate Size Effects in Uniaxial Compression and Constant Height Shear Tests, *Journal of the Association of Asphalt Paving Technologists*, Vol. 69, pp. 457-496, 2000.
- Witczak, M. W., K. Kaloush, T. Pellinen, M. El-Basyouny, and H. Von Quintus, Simple Performance Test for Superpave Mix Design, NCHRP Report 465, Washington D.C., 2002.
- Witczak, M. W., NCHRP 1-28A: *Recommended Standard Test Method for Determination of the Resilient Modulus of Bituminous Mixtures by Indirect Tension*, May 2003.
- Witczak, M. W., *Simple Performance Tests: Summary of Recommended Methods and Database*, NCHRP Report 547, Washington D.C., 2005.
- Zhou, F., S. Hu, and T. Scullion, *Development and Verification of the Overlay Tester Based Fatigue Cracking Prediction Approach*, FHWA/TX-07/9-1502-01-8, Texas Transportation Institute, College Station, Texas, 2007.
- Zhou, F., E. Fernando, and T. Scullion, *Laboratory and Field Procedures Used to Characterize Materials*, FHWA/TX-09/0-5798-P1, Texas Transportation Institute, College Station, Texas 77843-3135, 2009a.
- Zhou, F., S. Hu, X. Hu, and T. Scullion, *Mechanistic-Empirical Asphalt Overlay Thickness Design and Analysis System*, FHWA/TX-09/0-5123-3, Texas Transportation Institute, College Station, Texas, 77843-3135, 2009b.

APPENDIX A

SIF REGRESSION EQUATIONS

The general format of K_I and K_{II} regression equations is given below:

$$K_I \text{ (or } K_{II}) = K_a \times [K_b \times (c/H_1)^3 + K_c \times (c/H_1)^2 + K_d \times (c/H_1) + K_e]$$

K_I and K_{II} regressions for single axle load of 4 kips

The parameters for K_I regression equation:

$$K_a = -0.18218 \times \log H_2 - 76.6342 \times (\log E_2)^{-7.76842} + 0.46034 \times (\log H_1)^2 - 2.47132 \times \log H_1 - 0.04043 \times (\log E_1)^2 + 0.30400 \times \log E_1 + 3.46256$$

$$K_b = -2.65578 \times [5.6994 \times (\log E_1)^{0.31854} \times (\log E_2)^{-0.17774} - 6.24599] \times (14.04501 \times c^{-0.20634} - 1.09771)$$

$$K_c = -1.90054 \times [2.81813 \times (\log E_1)^{4.94048} \times (\log E_2)^{-3.82827} - 32.3366] \times (-15.6942 \times c^{-21.94474} + 0.14638)$$

$$K_d = -0.81463 \times [-2.19443 \times (\log E_1)^{5.96810} \times (\log E_2)^{-3.98238} + 58.62403] \times (-4.44818 \times c^{-20.981146} + 0.10260)$$

$$K_e = 2.11642 \times (\log E_1)^{2.72857} \times (\log E_2)^{-3.16871} - 1.0145$$

The parameters for K_{II} regression equation:

$$K_a = -0.75806 \times \log H_2 + 2.37697 \times (\log E_2)^{1.19094} + 28.16321 \times (\log H_1)^2 - 122.9592 \times \log H_1 + 0.51546 \times (\log E_1)^2 - 7.46728 \times \log E_1 + 155.77582$$

$$K_b = 5.71917 \times (E_1/E_2)^{0.33474} \times (-2.73464 \times c^{-0.62681} + 0.25414)$$

$$K_c = (12.59706 \times (E_1/E_2)^{0.32415} \times (1.06004 \times c^{-0.05536} - 0.84405))$$

$$K_d = 5.24602 \times 10^{-6} \times (E_1/E_2)^{-0.11786} \times (1.27811 \times c^{1.80059} + 19.49862)$$

$$K_e = -0.61680 \times (E_1/E_2)^{0.00492} + 0.6120$$

K_I and K_{II} regressions for single axle load of 11 kips

The parameters for K_I regression equation:

$$K_a = -55.67674 \times \log H_2 - 403.7929 \times (\log E_2)^{-5.62357} - 25.13843 \times (\log H_1)^2 + 58.02565 \times \log H_1 + 4.65904 \times (\log E_1)^2 + 5.63208 \times \log E_1 + 110.7729$$

$$K_b = -91.8802 \times [-5.86879 \times (\log E_1)^{-0.07699} \times (\log E_2)^{0.07931} + 5.9111] \times (-13.44963 \times c^{-61.88208} + 0.023167)$$

$$K_c = [1.90929 \times (\log E_1)^{0.62552} \times (\log E_2)^{-0.53622} - 2.2319] \times (1.70463 \times c^{-0.10304} - 1.18472) \times (-4.61968)$$

$$K_d = -0.73073 \times [-1.25431 \times (\log E_1)^{2.40458} \times (\log E_2)^{-1.94865} + 3.17707] \times (3.03247 \times c^{-0.03314} - 2.59174)$$

$$K_e = 5.71091 \times (\log E_1)^{-0.00602} \times (\log E_2)^{-0.00158} - 5.63897$$

The parameters for K_{II} regression equation:

$$K_a = -2.29909 \times \log H_2 - 22.01323 \times (\log E_2)^{0.104464} - 67.67709 \times (\log H_1)^2 + 248.28895 \times \log H_1 + 0.93097 \times (\log E_1)^2 - 6.08781 \times \log E_1 - 163.2535$$

$$K_b = 0.67666 \times (E_1/E_2)^{0.49410} \times (17.43199 \times c^{-1.46062} + 0.09356)$$

$$K_c = 0.000696 \times (E_1/E_2)^{0.97842} \times (0.56376 \times c^{0.28703} - 7.74257)$$

$$K_d = 0.000434 \times (E_1/E_2)^{-0.02355} \times (0.000429 \times c^{2.77105} + 96.4334)$$

$$K_e = 0.10513 \times (E_1/E_2)^{0.05399} - 0.08550$$

K_I and K_{II} regressions for single axle load of 25 kips

The parameters for K_I regression equation:

$$K_a = -29.25892 \times \log H_2 - 677.62617 \times (\log E_2)^{-6.64638} - 50.29321 \times (\log H_1)^2 + 200.65951 \times \log H_1 + 2.41642 \times (\log E_1)^2 - 0.63143 \times \log E_1 - 121.81383$$

$$K_b = -48.74833 \times [-6.03271 \times (\log E_1)^{-0.133857} \times (\log E_2)^{0.119975} + 5.93306] \times (-13.44963 \times c^{-61.88208} + 0.12300)$$

$$K_c = -26.2217 \times [2.1730 \times (\log E_1)^{0.15902} \times (\log E_2)^{-0.12699} - 2.29581] \times (5.94321 \times c^{-0.67207} - 0.60759)$$

$$K_d = -0.48795 \times [-0.50384 \times (\log E_1)^{3.23225} \times (\log E_2)^{-2.41452} + 2.73964] \times (4.95550 \times c^{-0.38375} - 0.67581)$$

$$K_e = 13.00533 \times (\log E_1)^{-0.00807} \times (\log E_2)^{-0.00266} - 12.7512$$

The parameters for K_{II} regression equation:

$$K_a = -0.79194 \times \log H_2 + 95.24042 \times (\log E_2)^{-0.02653} - 1.26461 \times (\log H_1)^2 + 7.16705 \times \log H_1 - 0.07389 \times (\log E_1)^2 + 1.45307 \times \log E_1 - 101.3351$$

$$K_b = 5.66101 \times (E_1/E_2)^{0.3389} \times (0.02638 \times c^{-0.58242} + 0.47267)$$

$$K_c = 2.15233 \times (E_1/E_2)^{0.36244} \times (3.83153 \times c^{-0.5590} - 1.50951)$$

$$K_d = 1.57137 \times (E_1/E_2)^{0.24254} \times (5.99529 \times c^{-0.009695} - 4.42581)$$

$$K_e = 7.54762 \times (E_1/E_2)^{-0.01462} - 7.64456$$

APPENDIX B

GRANULAR BASE TESTING

INTRODUCTION

Development of a Texas mechanistic-empirical (TexME) pavement design method requires models for predicting pavement performance to determine the optimum pavement design for the given materials, traffic, and environmental conditions. Toward this goal, this project evaluated (among other things) test methods for characterizing the resilient modulus and permanent deformation behavior of granular base materials that are known predictors of pavement performance. Specific issues examined in this project covered specimen compaction, sample instrumentation, and specimen size. To address these issues, researchers conducted laboratory tests on granular base materials to come up with recommendations for characterizing resilient modulus and permanent deformation properties to support pavement design applications. This appendix presents the findings from these laboratory tests.

SAMPLE COMPACTION AND INSTRUMENTATION

Background

Researchers conducted a laboratory test program to establish requirements for characterizing the permanent deformation behavior of granular materials used for base courses. Repeated load permanent deformation tests were conducted following the test matrix given in [Table B1](#). Based on findings from tests reported by [Andrei \(2003\)](#), researchers decided to evaluate the use of studs for mounting the displacement sensors on the test specimens. [Andrei \(2003\)](#) reported errors in strain measurements from resilient modulus tests where clamps are used to hold the displacement sensors on the test specimens. He identified rotation of the clamps and deformation in the membrane between the clamp and the specimen as two possible causes of measurement errors. This latter factor (deformation in the membrane due to shear) can prevent some of the deformation occurring in the soil to be transmitted to the clamp, resulting in unrealistically high modulus values. Based on the findings from his investigations of measurement errors in resilient modulus tests, [Andrei \(2003\)](#) decided to use studs placed inside the specimen during compaction to support the displacement sensors for resilient modulus testing of fine-grained soils. [Andrei \(2003\)](#) also tried to use studs for coarse-grained materials with larger-sized aggregates. However, he found that the use of studs for these materials did not work well, noting that the internal stud could not find enough support to achieve the required rigidity. After several unsuccessful trials with studs, [Andrei \(2003\)](#) decided to use a clamp setup with an enlarged contact area and flexible connections to test base materials. Notwithstanding these results, TTI researchers decided to include the use of studs in the test matrix given in [Table B1](#) to verify Andrei's findings and for the sake of completeness.

Table B1. Test Matrix for Evaluating Sample Compaction and Instrumentation Options.

Base material	Compaction method	Method for mounting displacement sensor	
		Rubber bands	Studs
Base material placed on Annex test sections	Impact hammer	X	X
	Vibratory	X	X
Base material from SH6 project north of Calvert	Impact hammer	X	X
	Vibratory	X	X

In another project, [Sebesta et al. \(2008\)](#) compared material properties of specimens compacted using TxDOT Test Method Tex-113E (impact hammer) with properties determined from tests on specimens prepared using vibratory compaction. They found that test results on vibratory compacted specimens showed improved triaxial strength properties, reduced moisture susceptibility, and improved rutting resistance as compared with test data on specimens prepared using the traditional impact hammer compaction. However, they cautioned that their tests covered only two Texas base materials and recommended that additional tests be conducted on other materials to verify their findings. In view of this recommendation, researchers in this project included compaction method as a variable in the test matrix given in [Table B1](#).

Sample Preparation

[Figures B1](#) and [B2](#) show the moisture-density curves for the two base materials tested in this investigation. In each figure, researchers determined the moisture-density relationship labeled *Impact Hammer* following TxDOT Test Method Tex-113E. The curve corresponding to vibratory compaction was determined with the same setup and procedure used by [Sebesta et al. \(2008\)](#) in their investigations of compaction methods for roadway base materials. Researchers molded 6-inch diameter × 8-inch high specimens to determine the moisture-density relationships shown in [Figures B1](#) and [B2](#).

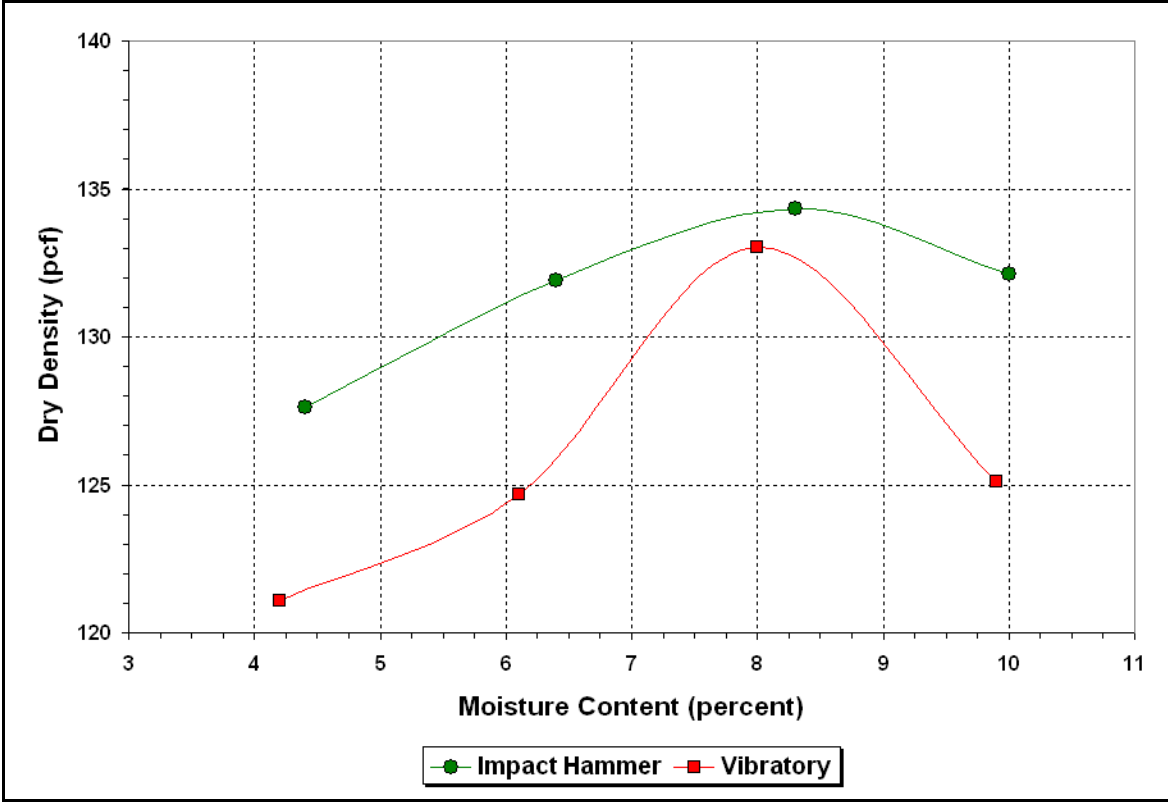


Figure B1. Moisture-Density Curves for Base Material Placed on Annex Test Sections.

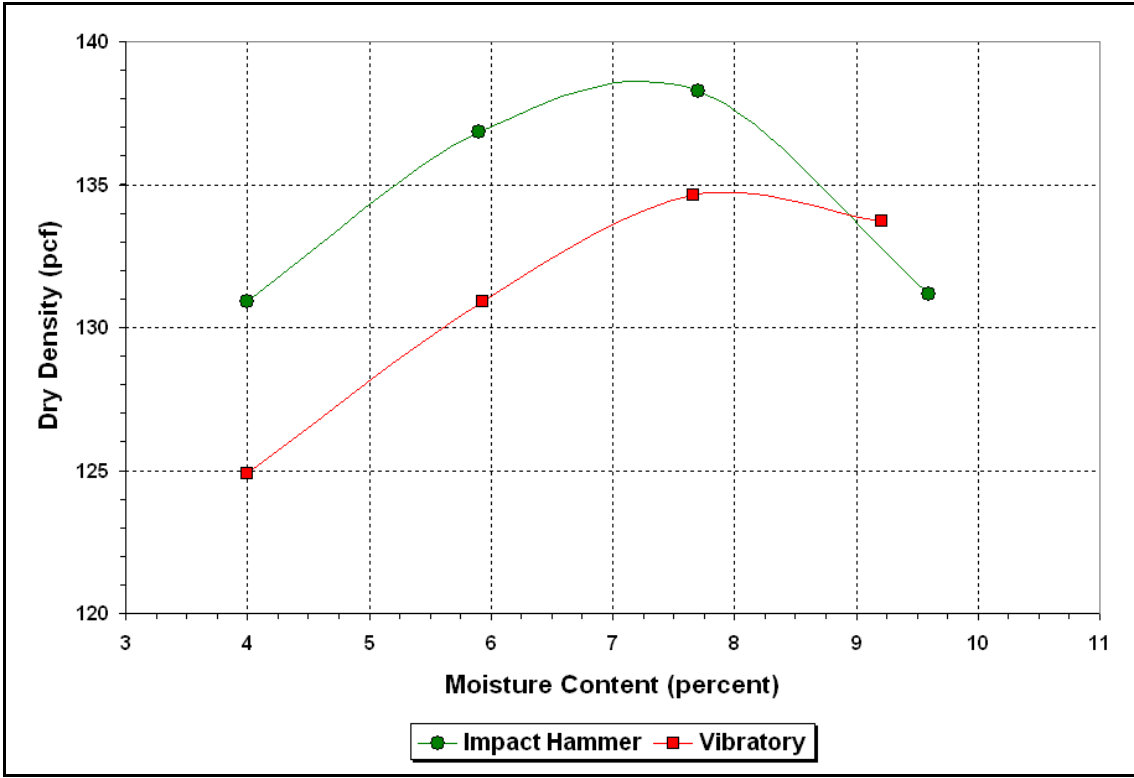


Figure B2. Moisture-Density Curves for Base Material Placed on SH6 Project.

Figure B3 shows the internal piece of the stud placed inside the specimen during compaction. The end facing the side of the mold is curved and has a threaded hole in the middle to where the outer piece that holds the displacement sensor or its platform is attached using an Allen screw (see Figure B4). Four studs are placed on the specimen as shown in Figure B5 to hold two linear variable differential transducers (LVDTs) and their corresponding platforms for measuring strains during testing. The two LVDTs are spaced 180° apart along the circumference of the specimen. Figure B6 illustrates the alternate test setup using rubber bands to secure the LVDT mounts in place during testing. The four mounts are glued to the membrane encasing the specimen prior to placement of the rubber bands. No glue is used with the studs.

Test Results

Table B2 summarizes the permanent deformation properties and resilient moduli determined from the repeated load permanent deformation data on samples prepared using impact hammer compaction. The permanent deformation parameters α and μ shown in this table are based on the VESYS power law permanent deformation model given by the equation:

$$\varepsilon_p = a N^b \quad (B1)$$

where

ε_p	=	permanent strain,
N	=	cumulative load repetitions, and
a, b	=	model parameters.



Figure B3. Inner Stud Piece Placed inside the Specimen during Compaction.



Figure B4. Outer Stud Piece Attached to Inner Piece with Allen Screw.



Figure B5. Molded Specimen with Stud-Mounted LVDT Holders.



Figure B6. Test Setup using Rubber Bands to Hold LVDTs.

Table B2. Material Properties Determined from Permanent Deformation Data on Samples Prepared Using Impact Hammer Compaction.

Base material	Test run	LVDT mounting method	α	μ	M_r (ksi)	Base rutting (inches) ¹
SH6 project north of Calvert	1	rubber bands	0.961	0.416	218.34	0.000
	2	rubber bands	0.950	0.394	55.01	0.154
	3	rubber bands	0.965	0.378	55.89	0.162
	1	studs	0.838	0.915	43.38	0.904
	2	studs	0.763	1.284	42.79	3.245
	3	studs	0.985	0.194	39.95	0.000
Annex test sections	1	rubber bands	0.962	0.304	28.76	0.235
	2	rubber bands	0.958	0.414	31.35	0.285
	3	rubber bands	0.968	0.473	38.82	0.299
	1	studs	0.937	0.295	55.54	0.112
	2	studs	0.951	0.231	71.04	0.071
	3	studs	0.943	0.316	40.60	0.161

¹ VESYS-predicted base rut depth for 26.4 million 18-kip single axle load repetitions over assumed designed period.

To determine the parameters α and μ , equation (B1) is fitted to the permanent deformation data from a given test to determine the power law model coefficients a and b . The permanent deformation parameters α and μ are then determined from these coefficients and the resilient strain ε_r at the 500th load repetition using the following equations:

$$\alpha = 1 - b \quad (\text{B2})$$

$$\mu = \frac{ab}{\varepsilon_r} \quad (\text{B3})$$

Also shown in [Table B2](#) are the resilient modulus (M_r) values based on ε_r and predictions of base layer rutting using the given permanent deformation properties and resilient moduli with the VESYS5W computer program ([Zhou and Scullion 2002](#)). These predictions are based on an assumed pavement structure consisting of a 2-inch hot-mix asphalt concrete mix over a 12-inch flexible base over a sandy soil subgrade. In these simulations, only the properties of the base material were varied according to the properties determined from tests. The properties of the other layers were kept the same in all simulations. In this way, the effects of differences in base properties on the predicted rutting of the base material can be illustrated. Researchers note the following observations from the results given in [Table B2](#).

- The permanent deformation parameters exhibit more variability for SH6 specimens with stud-mounted LVDTs. As a consequence, there is greater variability in the predicted base rutting for these specimens.
- The μ parameter for these same specimens show two unusually high values of 0.915 and 1.284 with corresponding high predictions of base rut depths of 0.9 and 3.2 inches, respectively.
- There is an apparent outlier in the M_r values determined from the test data on SH6 specimens where the conventional method of mounting LVDTs using rubber bands were employed. Specifically, the M_r value of 218 ksi from run 1 is very much different from the resilient moduli determined from runs 2 and 3, which give very comparable values of 55 and 56 ksi, respectively.
- The resilient moduli determined from test data on Annex base specimens exhibit relatively greater variability for the case of stud-mounted LVDTs, where values of 41, 56, and 71 ksi were determined.

Overall, the results exhibit less variability on tests conducted using rubber bands than with studs. In view of this finding, the researchers see no reason to switch from the traditional method of using rubber bands to mount LVDTs for repeated load triaxial tests of granular base materials. [Andrei \(2003\)](#) reached a similar conclusion as discussed earlier. Researchers note that, during specimen preparation, technicians commented on the difficulty of keeping the studs in place during compaction. If the inner stud is not firmly anchored in the specimen, measurement errors due to movement of the studs during testing are possible, as illustrated in [Figure B7](#), which show jitter in the strain data collected from a test done with studs.

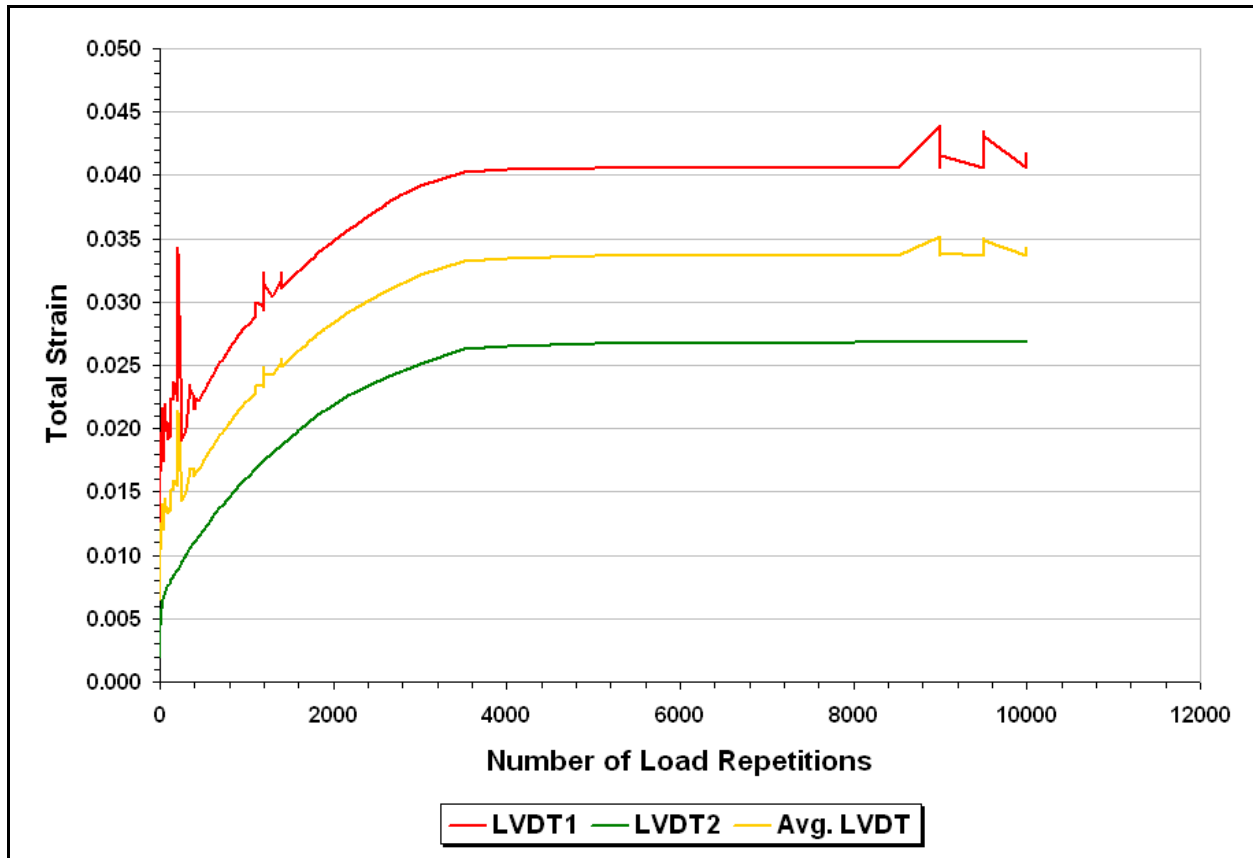


Figure B7. Jitter in Strain Displacements Measured Using Stud-Mounted LVDTs.

With respect to the effect of compaction method, [Table B3](#) shows material properties determined from tests on Annex base specimens where researchers used the traditional method of mounting LVDTs with rubber bands. The results generally show less variability in the material properties determined from repeat runs with the rubber bands, particularly in the μ and M_r values. The results also indicate greater rut resistance and higher stiffness for vibratory compacted specimens, which are in accordance with the findings presented earlier from tests conducted by [Sebesta et al. \(2008\)](#). However, researchers saw a reversal in this trend when stud-mounted LVDTs are used, as evident in the results presented in [Table B4](#). Thus, the main conclusions from this investigation are:

- The traditional method of mounting LVDTs using rubber bands is recommended over the use of studs for repeated load permanent deformation tests of granular base materials. Based on the limited data collected from laboratory tests reported herein, test properties determined using the traditional method exhibited less variability compared to properties determined using studs.
- Based on the limited test data collected in the laboratory, the traditional method of compacting specimens following Test Method Tex-113E should be used until more test data are collected to support a change to vibratory compaction and provide a basis for development of a standard test method.

Table B3. Material Properties Determined from Permanent Deformation Data on Annex Base Samples Tested with Rubber Band Mounted LVDTs.

Test run	Compaction method	α	μ	M_r (ksi)	Base rutting (inches) ¹
1	Impact hammer	0.962	0.304	28.76	0.235
2	Impact hammer	0.958	0.414	31.35	0.285
3	Impact hammer	0.968	0.473	38.82	0.299
1	Vibratory	0.939	0.094	87.15	0.000
2	Vibratory	0.934	0.209	67.69	0.066
3	Vibratory	0.911	0.322	69.52	0.108

¹ VESYS-predicted base rut depth for 26.4 million 18-kip single axle load repetitions over assumed designed period.

Table B4. Material Properties Determined from Permanent Deformation Data on Annex Base Samples Tested with Stud-Mounted LVDTs.

Test run	Compaction method	α	μ	M_r (ksi)	Base rutting (inches) ¹
1	Impact hammer	0.937	0.295	55.54	0.112
2	Impact hammer	0.951	0.231	71.04	0.071
3	Impact hammer	0.943	0.316	40.60	0.161
1	Vibratory	0.920	0.379	33.90	0.237
2	Vibratory	0.885	1.024	36.54	0.748
3	Vibratory	0.950	0.315	32.22	0.202

¹ VESYS-predicted base rut depth for 26.4 million 18-kip single axle load repetitions over assumed designed period.

COMPARISON OF LAB PROPERTIES TO TEXAS TRIAXIAL CLASS VALUES

All of the flexible bases used in Texas have to meet a Texas Triaxial Test requirement as described in Tex Method 117-E. The strength parameters generated in that test include the unconfined compressive strength at both zero and 15 psi confining pressure. In an attempt to relate the engineering properties to Texas Triaxial results, five different bases from the Austin District were tested in the TTI laboratory. Several of these bases were known to be good performers and others were judged by district staff to be marginal. All bases were subject to the complete Tex Method 117-E test and also subject to resilient modulus testing as described above. For these tests the standard impact hammer was used with no studs, all samples were the traditional TxDOT size of 6 by 8 inches high and all tests were run at optimum moisture content. One typical set of data from this test program is shown in [Table B5](#). In this Table, TC is the Texas Triaxial Class of the material, wbm is the Wet Ball Mill value, pi is the plasticity index and M_r is the resilient modulus at 5 psi confining and 15 psi deviator stress. From [Table B5](#) it is apparent that the better material as judged by the Texas Triaxial classification have higher resilient modulus. A graph showing the relationship between the compressive strength at a confining pressure of 15 psi and the measured resilient modulus is shown in [Figure B8](#). There is a strong relationship between all of the Texas Triaxial quality indicators and Resilient Modulus.

Table B5. Results from Texas Triaxial and Resilient Modulus Testing.

base	Lab #	0 psi	3 psi	15 psi	TC	mdd	omc	w/bm	pi	Mr	k1	k2	k3
cap Ag Wool	82052	28	88	203	2.6	130.3	9.5	35	3	43.8	1538.1	0.81	-0.34
vul spice wd	82050	29	108	199	2.5	146.5	6	26	2	46	1243.31	0.49	-0.85
Cap MF	82055	54	111	236	1	150.2	5.2	26	4	60.7	2600	0.82	-0.31
cap MF 2	82054	58	127	233	1	150.4	5.2	26	5	58.4	2499	0.81	-0.28
centex ruby	82051	30	82	180	2.6	136.2	7.2	40	6	32.3	1177	0.85	-0.04

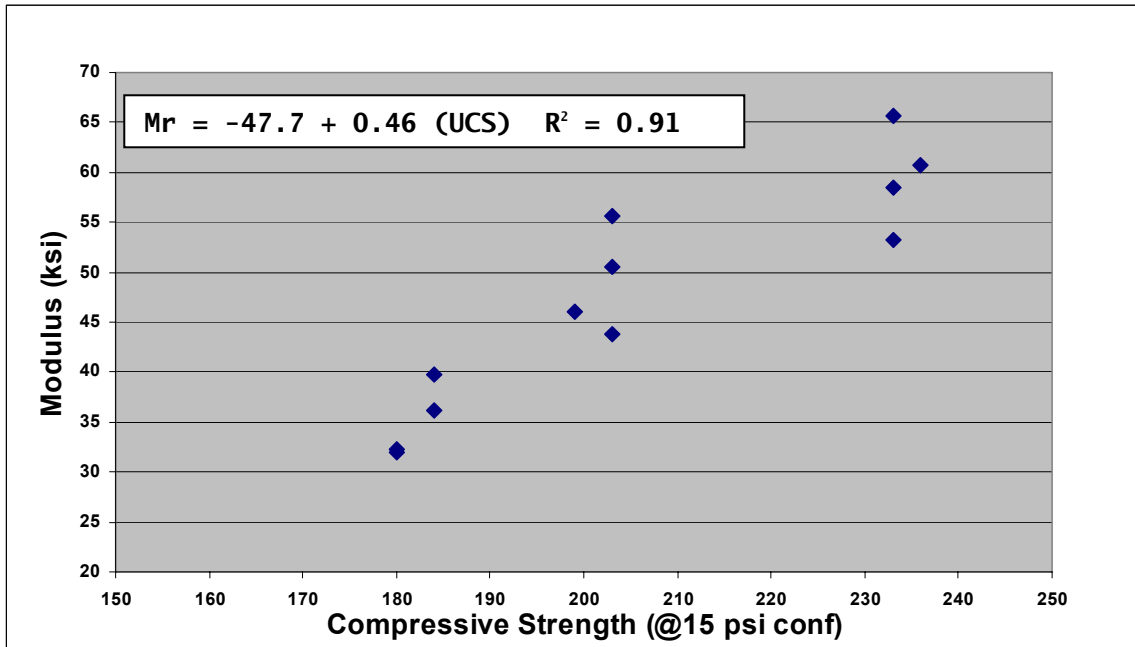


Figure B8. Comparison of 15-psi Compressive Strength to Resilient Modulus.

INFLUENCE OF MOISTURE ON ENGINEERING PROPERTIES OF BASES

Traditionally all of the strength testing on base materials is performed at optimum moisture content. But it is well known that:

- moisture content has a major impact on all engineering properties,
- under normal operating conditions the flexible bases in Texas pavements are typically 2 to 3 percent below optimum (the current construction specifications require that the base be 2 percent below OMC prior to sealing), and
- what distinguishes the good from the poor bases is their moisture susceptibility.

In study 0-5798, only preliminary data were collected on the impact of moisture on granular base materials. One base with known moisture susceptibility problems was subjected to resilient modulus and permanent deformation testing at OMC and OMC plus and minus 1 percent. The results of the permanent deformation testing are shown in [Figure B9](#).

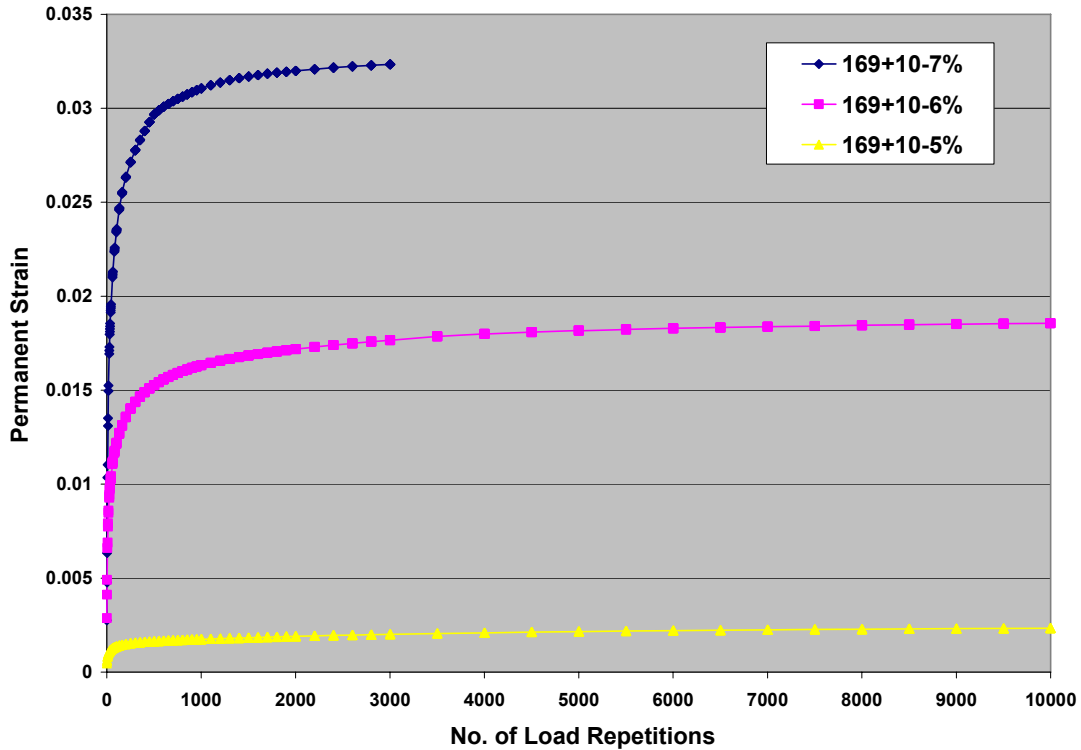


Figure B9. Permanent Deformation Results at Different Moisture Contents.

The resulting engineering properties from this limited study are shown in [Table B6](#).

Table B6. Influence of Moisture on Engineering Properties.

Moisture content	Resilient Modulus M_r (ksi)	α	μ
7%	28.9	0.90	5.89
6%	38.9	0.93	1.52
5%	51.7	0.87	0.39

For this base the influence of moisture content was very dramatic. At 1 percent below optimum the modulus was relatively high and no appreciable permanent deformation was found in the lab tests. However at 1 percent above optimum the modulus dropped by almost 50 percent and the sample failed dramatically in less than 3000 load repetitions. The implication here is that for moisture susceptible bases, their performance will be fine providing they are maintained at a moisture content below OMC; however if moisture is allowed to enter into the system (from surface cracking for example) then complete failure will be rapid and severe.

COMPARISON OF 6×8 VS. 6×12 SPECIMENS

Background

Conventional geotechnical triaxial tests are commonly conducted on cylindrical specimens having a 2:1 ratio between the specimen height and its diameter. However, current TxDOT test methods, such as Tex-113E and Tex-117E, use 6-inch diameter by 8-inch high specimens for testing. As TxDOT transitions to a mechanistic-empirical pavement design procedure, test methods to characterize material properties for pavement design will need to be developed and implemented. As this development takes place, TxDOT will need to revisit existing protocols to determine whether and how current TxDOT standards should be modified to be more in tune with current national standards and engineering practice. As an initial step in this direction, researchers in this project conducted a comparative evaluation of material properties determined from tests on 6×8 and 6×12 specimens. The objective was to collect data to determine which test methods should be used to characterize resilient modulus and permanent deformation properties of granular base materials. This section presents the findings from this comparative evaluation.

Specimens Tested

[Table B7](#) identifies the flexible base materials researchers tested in this comparative evaluation of 6×8 versus 6×12 specimens. The materials were provided by Mike Arellano, Austin District laboratory engineer, who classified the Centex, Wood Pit, and Marble Falls aggregates as poor, marginal and good, respectively, based on the district's experience with the field performance of these materials as shown in [Table B8](#). This table also presents compressive strength data from Tex-117E tests conducted by the Austin District.

Researchers prepared 6×8 and 6×12 specimens based on the optimum moisture contents presented in [Table B9](#). The data shown were determined from Tex-113E tests conducted by the district. Researchers compacted test specimens in 2-inch lifts with the impact hammer following Tex-113E. The same compactive energy per unit volume (compactive effort) was applied to all specimens. [Figure B10](#) shows a picture of the apparatus used to run repetitive load tests for characterizing the permanent deformation properties and resilient moduli of the test specimens. Researchers used the loading sequence that [Zhou et al. \(2009\)](#) recommended for granular base materials to perform these tests. To measure deformations during testing, researchers mounted two LVDTs spaced 180° apart on each specimen. Rubber bands were used to hold the sensors on the specimen based on findings reported earlier from tests conducted with studs. Researchers positioned the LVDTs to measure deformations within the middle 6 inches of the specimen height. Thus, on 6×8 samples the gage points were located 1 inch from the specimen ends while on 6×12 samples, the gage points were located 3 inches from the ends.

Table B7. Base Materials Tested in Evaluating Specimen Size.

Material	Specimen size (inches)	
	6×8	6×12
Marble Falls	X	X
Wood Pit	X	X
Centex	X	X

Table B8. Performance Ranking of Base Materials Tested.

Material	Ranking based on Austin District Experience	Compressive strength at 15 psi confinement (psi)
Marble Falls	1	233
Wood Pit	2	203
Centex	3	183

Table B9. Optimum Moisture Contents and Maximum Dry Densities of Materials Tested.

Material	Maximum dry density (pcf)	Optimum moisture content (%)
Marble Falls	150.4	5.2
Wood Pit	130.3	9.5
Centex	136.8	7.0

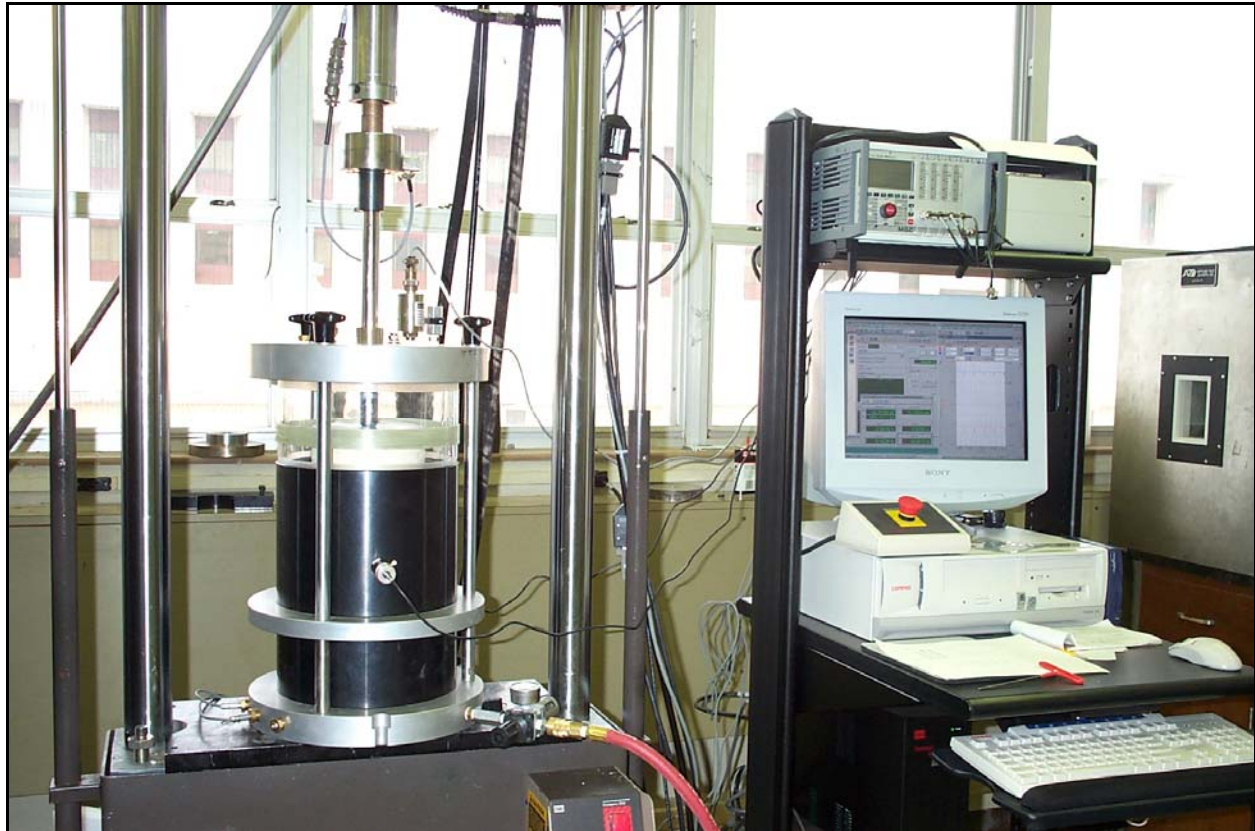


Figure B10. Triaxial Test Apparatus Used for Permanent Deformation and Resilient Modulus Testing.

Permanent Deformation Test Results

Tables B10 to B12 summarize the permanent deformation properties determined from testing, while Figures B11 to B13 illustrate the permanent deformation curves. Researchers note the following observations from these results:

- The 6×12 specimens tend to exhibit higher permanent deformations, particularly for the Wood Pit specimens. For this material, the permanent deformation curves are markedly higher than the corresponding 6×8 specimens, as evident from Figure B12, where the curves for the two groups of specimens show little overlap unlike the curves for the other two materials. Table B11 also shows markedly higher plastic strains ϵ_p at the 5000th load repetition for 6×12 Wood Pit specimens.
- The test repeatability leaves room for improvement based on comparing the permanent deformation curves from repeat runs in Figures B11 to B13. To get a measure of the test variability, researchers determined the coefficients of variation (CV) of the plastic strains ϵ_p at the 5000th load cycle. The CVs ranged from about 5 to 94 percent as shown in Table B13. These statistics are based on using all of the test data. If the apparent outliers indicated in Figures B11 and B12 are excluded, the maximum coefficient of variation drops from about 94 to 44 percent.

Table B10. Permanent Deformation Properties from Tests of Marble Falls Specimens.

Sample size	ϵ_r ($\mu\epsilon$) ¹	ϵ_p ($\mu\epsilon$) ²	a	b	α	μ
6×8	259	1230	0.0006	0.0810	0.919	0.194
6×8	295	2507	0.0012	0.0865	0.913	0.351
6×8	328	2477	0.0008	0.1310	0.869	0.321
6×12	508	11,754	0.0013	0.2550	0.745	0.666
6×12	490	3448	0.0005	0.2200	0.780	0.235
6×12	424	1821	0.0001	0.3052	0.695	0.096

¹ Resilient strain at 500th load repetition in microstrain units

² Plastic strain at 5000th load repetition in microstrain units

Table B11. Permanent Deformation Properties from Tests of Wood Pit Specimens.

Sample size	ϵ_r ($\mu\epsilon$) ¹	ϵ_p ($\mu\epsilon$) ²	a	b	α	μ
6×8	363	2277	0.0003	0.2433	0.757	0.192
6×8	399	3006	0.0005	0.2106	0.789	0.265
6×8	453	6584	0.00004	0.608	0.392	0.047
6×12	786	12,098	0.0002	0.4742	0.526	0.126
6×12	687	11,963	0.0002	0.4842	0.516	0.132
6×12	671	11,080	0.00005	0.6399	0.360	0.044

¹ Resilient strain at 500th load repetition in microstrain units

² Plastic strain at 5000th load repetition in microstrain units

Table B12. Permanent Deformation Properties from Tests of Centex Specimens.

Sample size	ε_r ($\mu\varepsilon$) ¹	ε_p ($\mu\varepsilon$) ²	a	b	α	μ
6×8	404	6058	0.0029	0.0881	0.912	0.626
6×8	460	8187	0.0042	0.0781	0.922	0.713
6×8	655	8764	0.0028	0.1315	0.868	0.571
6×8	372	6660	0.0041	0.0568	0.943	0.624
6×8	341	4431	0.0027	0.0566	0.943	0.454
6×12	631	8694	0.0025	0.1471	0.853	0.582
6×12	459	6865	0.0024	0.1225	0.877	0.643
6×12	576	11,091	0.0025	0.1730	0.827	0.759

¹ Resilient strain at 500th load repetition in microstrain units

² Plastic strain at 5000th load repetition in microstrain units

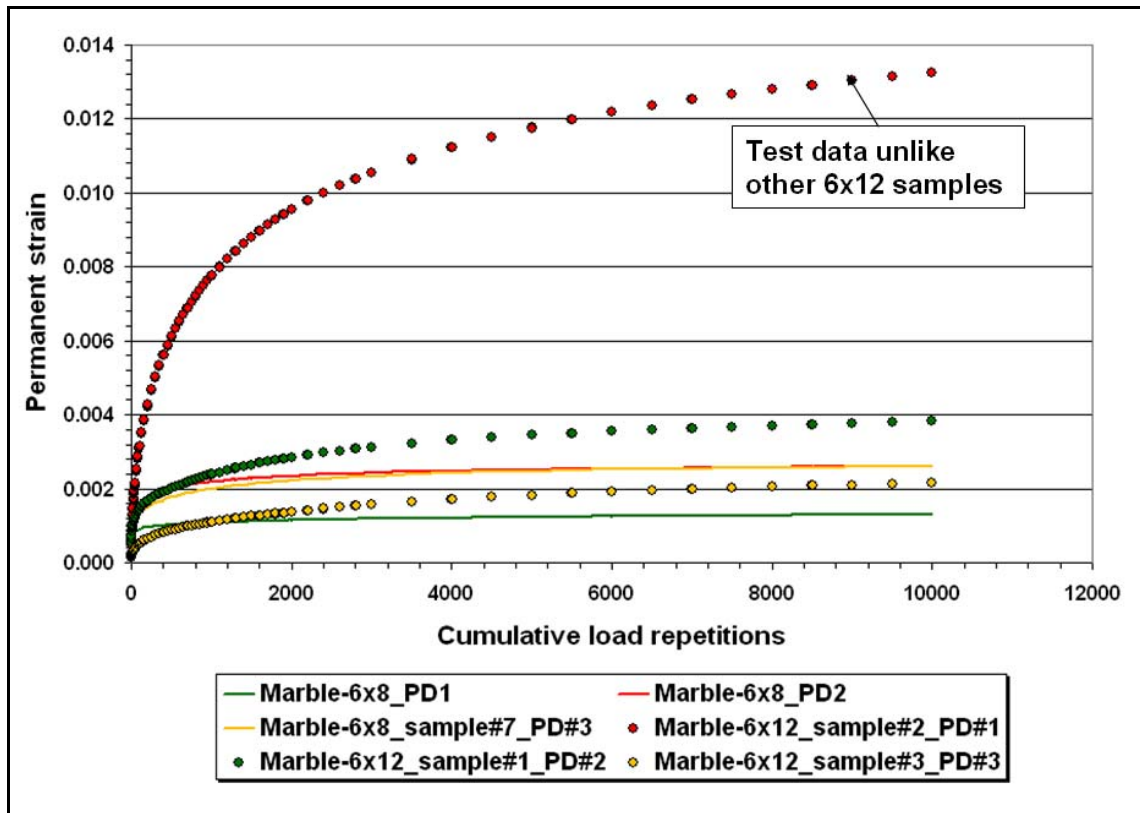


Figure B11. Permanent Deformation Curves from Tests of Marble Falls Specimens.

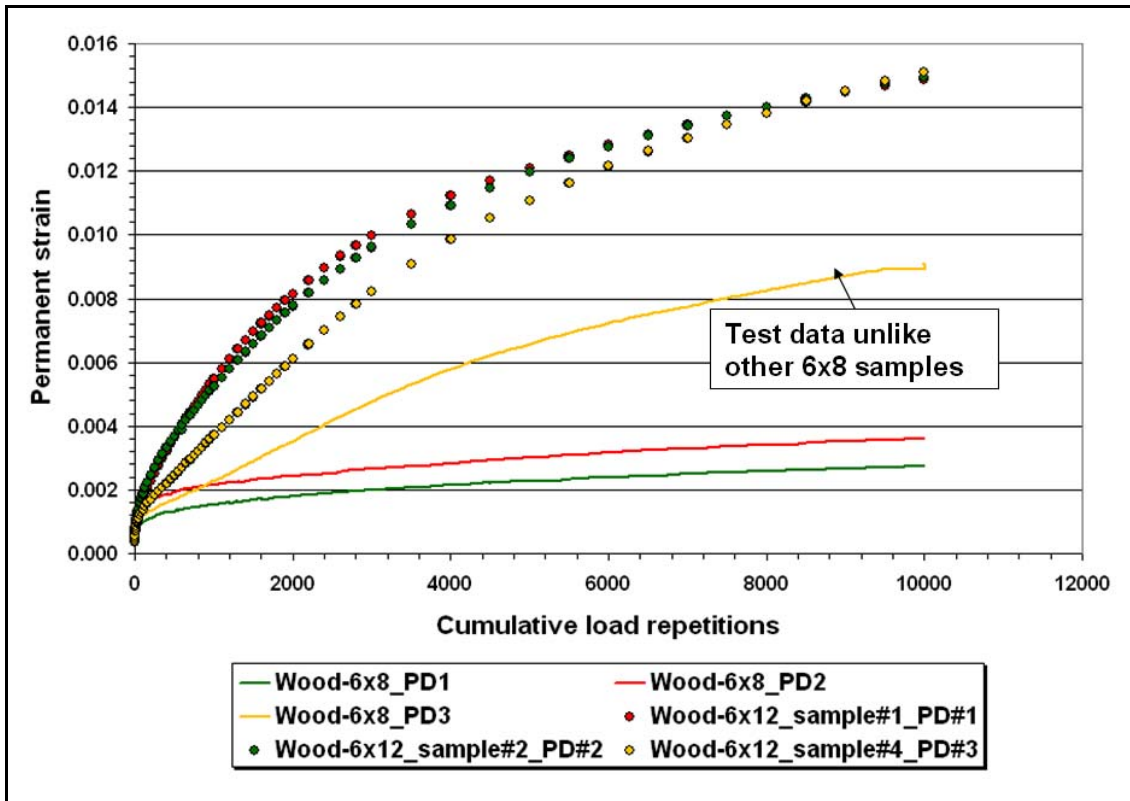


Figure B12. Permanent Deformation Curves from Tests of Wood Pit Specimens.

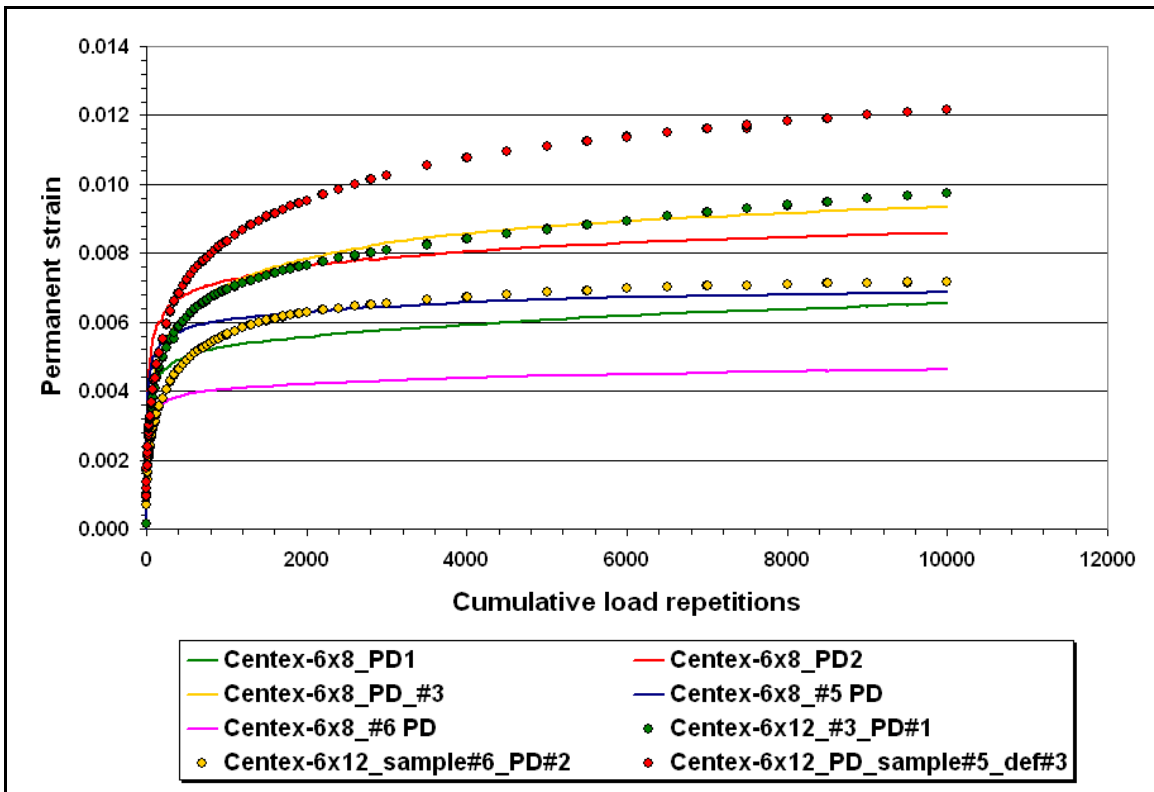


Figure B13. Permanent Deformation Curves from Tests of Centex Specimens.

Table B13. Variability in Measured Plastic Strains at 5000th Load Repetition.

Material	Sample size	Average ε_p ($\mu\varepsilon$)	Std. dev. ε_p ($\mu\varepsilon$)	CV%
Marble Falls	6×8	2071	729	35.18
Marble Falls	6×12	5674	5328	93.89
Wood Pit	6×8	3956	2305	58.29
Wood Pit	6×12	11,714	553	4.72
Centex	6×8	6820	1729	25.36
Centex	6×12	8883	2119	23.86

Using the average of the plastic strains ε_p shown in [Table B13](#), researchers ranked the different materials by sample size. [Table B14](#) shows the rankings obtained. It is observed that the ranking based on 6×8 specimens is in accordance with the district’s ranking of the materials ([Table B8](#)). For the 6×12 specimens, the Marble Falls material still ranks as No. 1. However, the ranks for the other two materials (Wood Pit and Centex) show a reversal.

Researchers also performed statistical tests of significance of the differences between means of the plastic strains ε_p for the sample sizes tested. At a 95 percent confidence level, researchers found that the differences between the mean plastic strains are not significant between corresponding 6×8 and 6×12 Centex and Marble Falls specimens. However, the opposite result was found for the Wood Pit specimens. These findings appear to be consistent with the variability of the permanent deformation data shown in [Figures B11 to B13](#).

Table B14. Material Rankings Based on Mean Plastic Strain at 5000th Load Cycle.

Specimen size	Rank	Material	Average ε_p ($\mu\varepsilon$)
6×8	1	Marble Falls	2071
6×8	2	Wood Pit	3956
6×8	3	Centex	6820
6×12	1	Marble Falls	5674
6×12	2	Centex	8883
6×12	3	Wood Pit	11714

Resilient Modulus Test Results

[Tables B15 to B17](#) present the parameters determined from resilient modulus tests of 6×8 and 6×12 specimens. These tables show the model coefficients K_1 , K_2 and K_3 that define the stress-dependency of the resilient modulus M_r according to the following relationship:

$$M_r = K_1 p_a \left(\frac{\theta}{p_a} \right)^{K_2} \left(\frac{\tau_{oct}}{p_a} + 1 \right)^{K_3} \quad (\text{B4})$$

where

- p_a = atmospheric pressure (14.5 psi),
- θ = bulk stress, and
- τ_{oct} = octahedral shear stress.

The resilient modulus corresponding to a 5 psi confining pressure and 15 psi deviatoric stress is also given in the tables for each specimen tested. Researchers determined the means and standard deviations of the M_r values at this stress state to assess the variability of the test results from repeat runs. Table B18 shows these statistics and the corresponding coefficients of variation. For 6×8 specimens, the coefficients of variation range from about 12 to 31 percent, while for 6×12 specimens, the range is from about 9 to 23 percent.

Researchers also performed statistical tests of significance of the differences between means of the M_r values for the sample sizes tested. At a 95 percent confidence level, researchers found that the differences between 6×8 and 6×12 specimens are not statistically significant for all three base materials. This result is attributed to the variability of the resilient modulus values from repeat runs, suggesting once more that test repeatability is an issue that needs further evaluation.

Using the average M_r values given in Table B18, researchers ranked the different materials by sample size. Table B19 shows the rankings obtained. Once more, the ranking based on 6×8 specimens is observed to be in accord with the district’s ranking of the materials. For the 6×12 specimens, the Centex and Marble Falls materials both show an average M_r of about 43 ksi, while the Wood Pit material shows the lowest value for this specimen size.

Table B15. Resilient Modulus Properties from Tests of Marble Falls Specimens.

Sample size	K_1	K_2	K_3	M_r (ksi) ¹
6×8	2146	0.904	-0.363	53.30
6×8	2912	0.823	-0.447	65.72
6×8	1870	0.657	-0.029	44.33
6×12	2414	0.914	-0.990	46.58
6×12	1699	1.171	-1.023	39.17
6×12	2284	0.895	-1.027	42.79

¹ Calculated resilient modulus at 5 psi confining pressure and 15 psi deviatoric stress

Table B16. Resilient Modulus Properties from Tests of Wood Pit Specimens.

Sample size	K_1	K_2	K_3	M_r (ksi) ¹
6×8	2485	0.980	-0.744	55.77
6×8	2260	0.745	-0.331	50.51
6×8	1032	0.801	0.149	29.33
6×12	926	1.201	-0.803	23.91
6×12	1664	0.895	-0.885	33.07
6×12	1932	0.746	-0.642	38.01

¹ Calculated resilient modulus at 5 psi confining pressure and 15 psi deviatoric stress

Table B17. Resilient Modulus Properties from Tests of Centex Specimens.

Sample size	K_1	K_2	K_3	M_r (ksi) ¹
6×8	1305	0.897	-0.077	36.29
6×8	1498	0.853	-0.113	39.71
6×8	1190	0.891	-0.141	32.08
6×8	1901	1.010	-0.791	42.78
6×12	1411	0.762	0.080	37.87
6×12	2703	0.993	-1.227	50.15
6×12	2009	0.915	-0.781	42.29

¹ Calculated resilient modulus at 5 psi confining pressure and 15 psi deviatoric stress

Table B18. Means and Standard Deviations of M_r Values.

Material	Sample size	Average M_r (ksi) ¹	M_r standard deviation (ksi)	CV (%)
Marble Falls	6×8	54.45	10.74	19.72
Marble Falls	6×12	42.84	3.71	8.65
Wood Pit	6×8	45.20	14.00	30.97
Wood Pit	6×12	31.66	7.16	22.60
Centex	6×8	37.71	4.60	12.18
Centex	6×12	43.44	6.22	14.32

¹ Calculated resilient modulus at 5 psi confining pressure and 15 psi deviatoric stress

Table B19. Material Rankings Based on Average M_r .

Specimen size	Rank	Material	Average M_r (ksi) ¹
6×8	1	Marble Falls	54.45
6×8	2	Wood Pit	45.20
6×8	3	Centex	37.71
6×12	1	Centex	43.44
6×12	2	Marble Falls	42.84
6×12	3	Wood Pit	31.66

¹ Calculated resilient modulus at 5 psi confining pressure and 15 psi deviatoric stress

Concluding Remarks

One notable observation from the comparative evaluation of 6×8 and 6×12 specimens is the observed tendency of 6×12 specimens to show higher permanent strains, particularly for the Wood Pit samples. This observation appears to be contrary to what would be expected given that the gage points for the 6×12 specimens are farther from the specimen ends compared to the locations of the gage points on the 6×8 specimens. One question that came up in efforts to find an explanation for this behavior is whether the Tex-113E moisture-density curve is applicable for preparing 6×12 specimens for permanent deformation and resilient modulus testing. The

moisture-density curve from Tex-113E is based on testing 6×8 specimens. If the moisture-density curve is determined using 6×12 specimens, would it show the same optimum values as those determined from Tex-113E? To investigate this question further, researchers prepared 6×8 and 6×12 samples of the Annex base material, and determined the moisture-density curves for these two sample sizes. Researchers used the Annex base material for these tests since there were not enough of the Austin base materials to prepare specimens after the permanent deformation and resilient modulus tests on these materials were completed.

[Figure B14](#) compares the moisture-density curves between 6×8 and 6×12 specimens. It is observed that the optimum moisture content for the 6×8 specimens is 0.7 percent higher than the corresponding optimum for the 6×12 specimens. This result suggests that if a 6×12 specimen is prepared according to the optimum moisture content based on Tex-113E, the specimen would actually be prepared wet of its optimum and thus show higher permanent strains during testing. To explore this issue further, researchers performed another round of permanent deformation tests on 6×8 and 6×12 Annex base specimens prepared according to the moisture-density curves shown in [Figure B14](#). [Figures B15](#) and [B16](#) show the results from these tests. This time around, it is observed that the 6×8 specimens exhibit higher permanent strains than the 6×12 specimens, unlike the trends noted from the earlier tests. This new set of results suggest the need for additional testing to answer more definitively whether moisture-density curves for sample preparation should be tied to the specimen size.

One final observation to make from the results presented in [Figures B15](#) and [B16](#) concerns the variability of the data from repeat runs. Similar to the earlier results, test repeatability leaves much to be desired and needs further evaluation, in the researchers' opinion, to develop an improved test method that offers better repeatability and to establish how material variability should be addressed in future TexME development work.

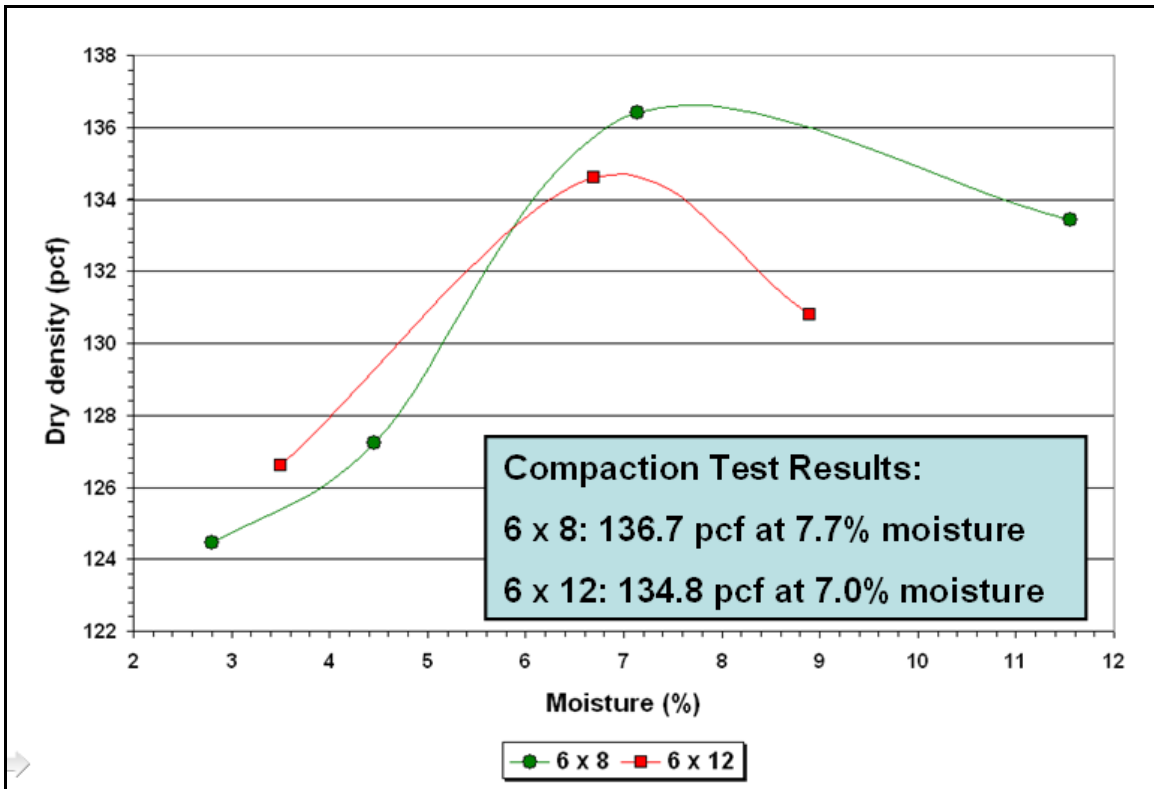


Figure B14. Moisture-Density Curves for 6x8 and 6x12 Specimens.

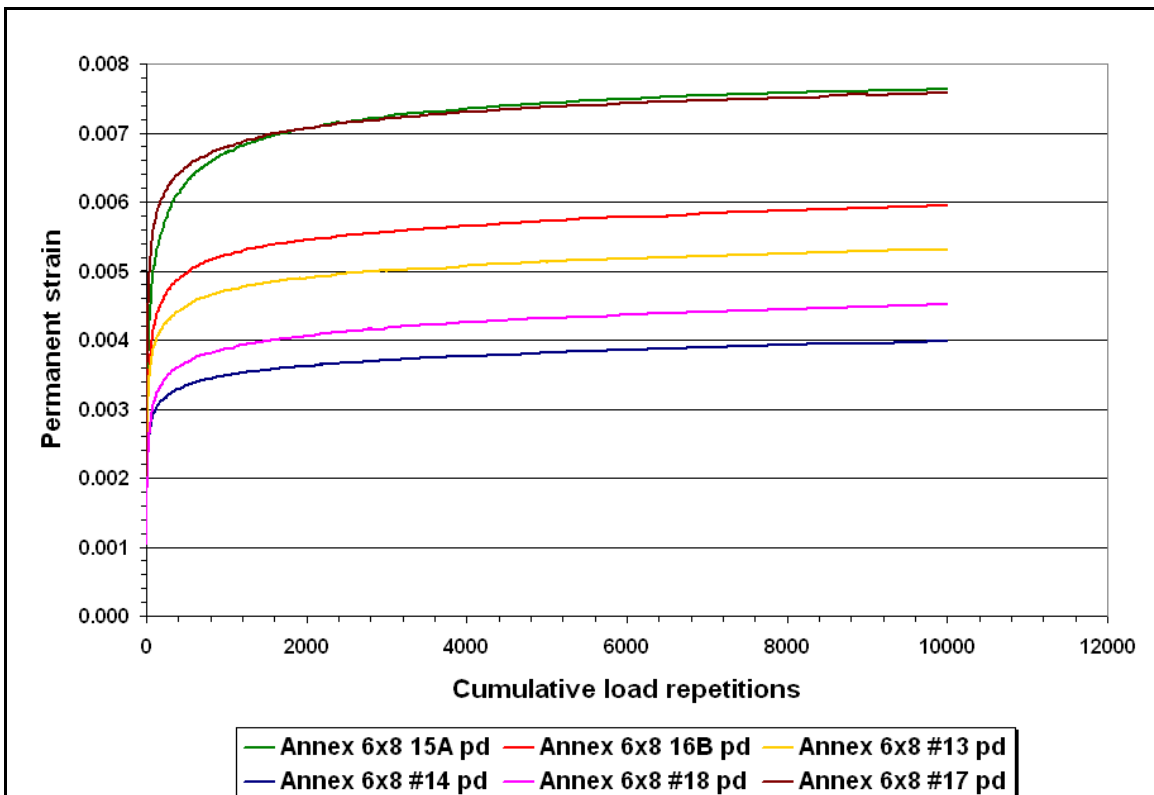


Figure B15. Permanent Deformation Curves from Tests on 6x8 Specimens.

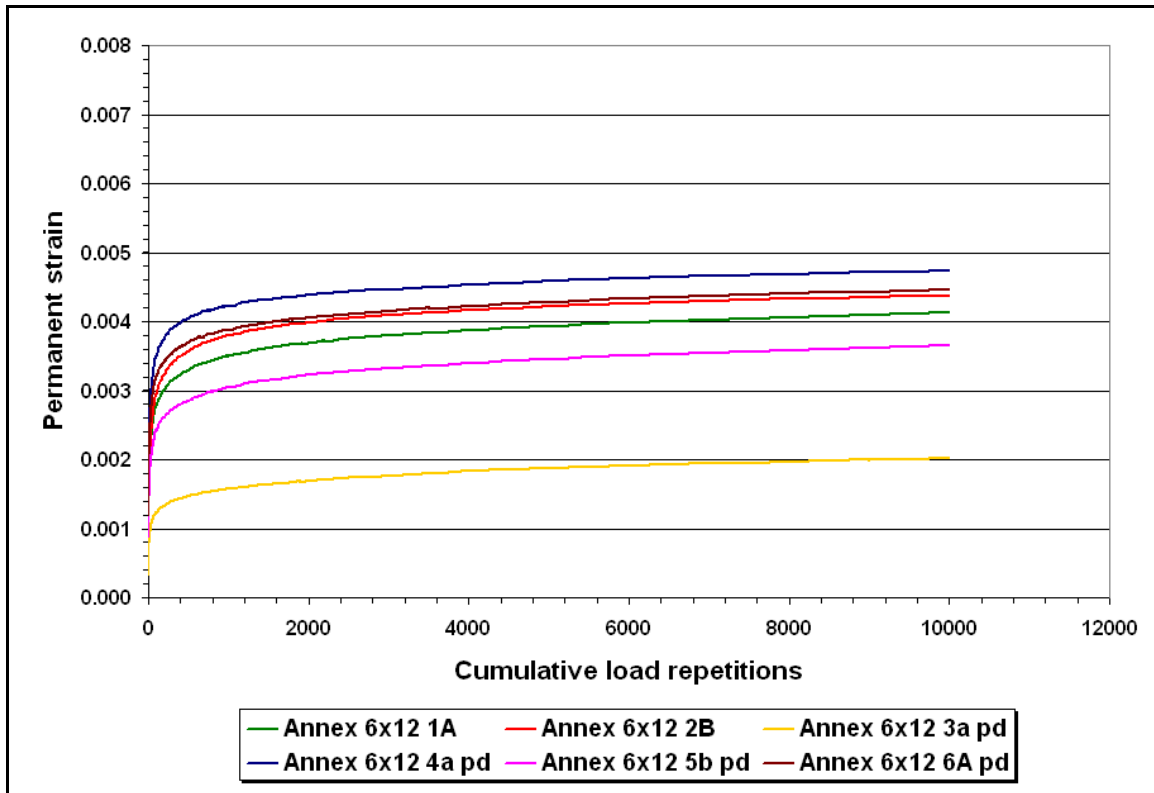


Figure B16. Permanent Deformation Curves from Tests on 6×12 Specimens.

References

- Andrei, D. *Development of a Predictive Model for the Resilient Modulus of Unbound Materials*. PhD. Dissertation, Arizona State University, Tempe, Ariz., 2003.
- Sebesta, S., P. Harris, and W. Liu. *Improving Lab Compaction Methods for Roadway Base Materials*. Research Report 0-5135-2, Texas Transportation Institute, Texas A&M University, College Station, Tex., 2008.
- Zhou, F. and T. Scullion. *VESYS5 Rutting Model Calibrations with Local Accelerated Pavement Test Data and Associated Implementation*. Research Report 9-1502-01-2, Texas Transportation Institute, Texas A&M University, College Station, Tex., 2002.
- Zhou, F., E. Fernando, and T. Scullion. *Laboratory and Field Procedures Used to Characterize Materials*. Product 0-5798-P1, Texas Transportation Institute, Texas A&M University, College Station, Tex., 2009.

APPENDIX C

OVERVIEW OF THE PAVEMENT DESIGN SOFTWARE (PCA-PAVE) FOR PAVEMENTS CONTAINING STABILIZED LAYERS

This appendix demonstrates some of the capabilities built into the PCA's new mechanistic empirical design system (PCA-PAVE). Several of the features and models of this package should be reviewed by TxDOT designers for consideration for incorporation into TxDOT's future ME pavement design implementation efforts.

The PCA-PAVE package was developed by the Texas Transportation Institute with funding provided by the PCA. This program has the capability of handling multiple axle loads and/or multiple truck types. One important feature of this software is its ability to predict damage for any axle configuration including dual and triple axles. The damage contribution for each wheel in multiple axle configurations is computed and accumulated.

The performance models included are:

- cement treated base fatigue cracking ([Scullion et al. 2006](#)),
- cement modified soil fatigue cracking ([Scullion et al. 2006](#)),
- asphalt fatigue cracking,
- subgrade rutting, and
- roller compacted concrete fatigue cracking (PCA existing model)

At the end of this section several of the important screens from the PCA-PAVE package are presented. These are described below.

Figure C1 Main Menu Screen

This first screen is used to build the pavement structure to be used in the analysis. Drop down menus are used to select from the available material types. The main menu bar icons are at the left of the figure; the function of each of these is described below.



This is used to generate the pavement structure to be evaluated. The User adds and deletes layers, selects materials types and thickness, modifies moduli values, poissons ratio, modulus of rupture, etc.



This is for entering load. Load can be entered by either axle loads or by truck types. The data can be entered by day, month, or year.



This is for selecting which model will be used in the performance evaluation. Default values are provided for each of the constants in the models; these can be updated if new information is available.



Once all inputs are complete this runs the program; once complete the individual damage assessments are displayed.



This provides a screen for each of the models selected and it shows the calculated critical stress or strain and the percentage of the pavement life used for the analysis period.



This provides a graph over the 20-year design period of the damage caused to the pavement.

Figure C2 Input Pavement Load

Two options are provided for load entry either by axle type (this screen) or by truck type (Figure C5). The data can also be entered by day, month, or year.

This screen operates by dragging and dropping. Select the axle type of interest by clicking and holding down the left mouse button, drag it to the main box. Default values are provided for most of the entries these can be modified by clicking on the box and entering new numbers. The user enters the number of applications for each axle configuration for the analysis period (year, month, or day).


For the example shown in Figure C2 only one axle type is input; this is a single axle with dual tires with 18,000 lb load and 100 psi tire pressure. The number of load applications was input at 500,000 per year.

Figure C3 Models to be Checked in Analysis

The input pavement structure is displayed along with the available models. To activate a model the user clicks on the small box to the right of the layer information. The model will be displayed to the right of the structure. For the CTB model the two models generated in the research study are presented. The user can select the NCHRP or PCA model.

Figure C4 Graphical Display of Results



Hitting the  icon will display the results shown in [Figure C4](#). The percentage growth used in the analysis is shown on this screen to be 5 percent per year with a design life 20 years. These can be modified and the computations rerun. The results for the CTB and fatigue cracking are on top of one another. This is because the default values were used of $N_f = 100$ million.

The user defines failure in terms of the percent of the life used up. Low level of failure distress (say 25 percent) will accommodate uncertainty in the design procedures such as deterioration in the soil cement due to shrinkage cracking, uncertainty about traffic, modulus of rupture, etc.

Figure C5 Input Loads by Truck Type

This figure shows the input truck types available for use in the analysis. Select the load type by truck and click and drag the trucks to be used. In this example the 3S3 truck (200,000 applications per year) and 3S2 truck (300,000 applications per year). The axle configuration and loads and pressures are displayed for each axle group. These can be changed by the user. Damage is computed for each wheel in the multiple wheel configuration.

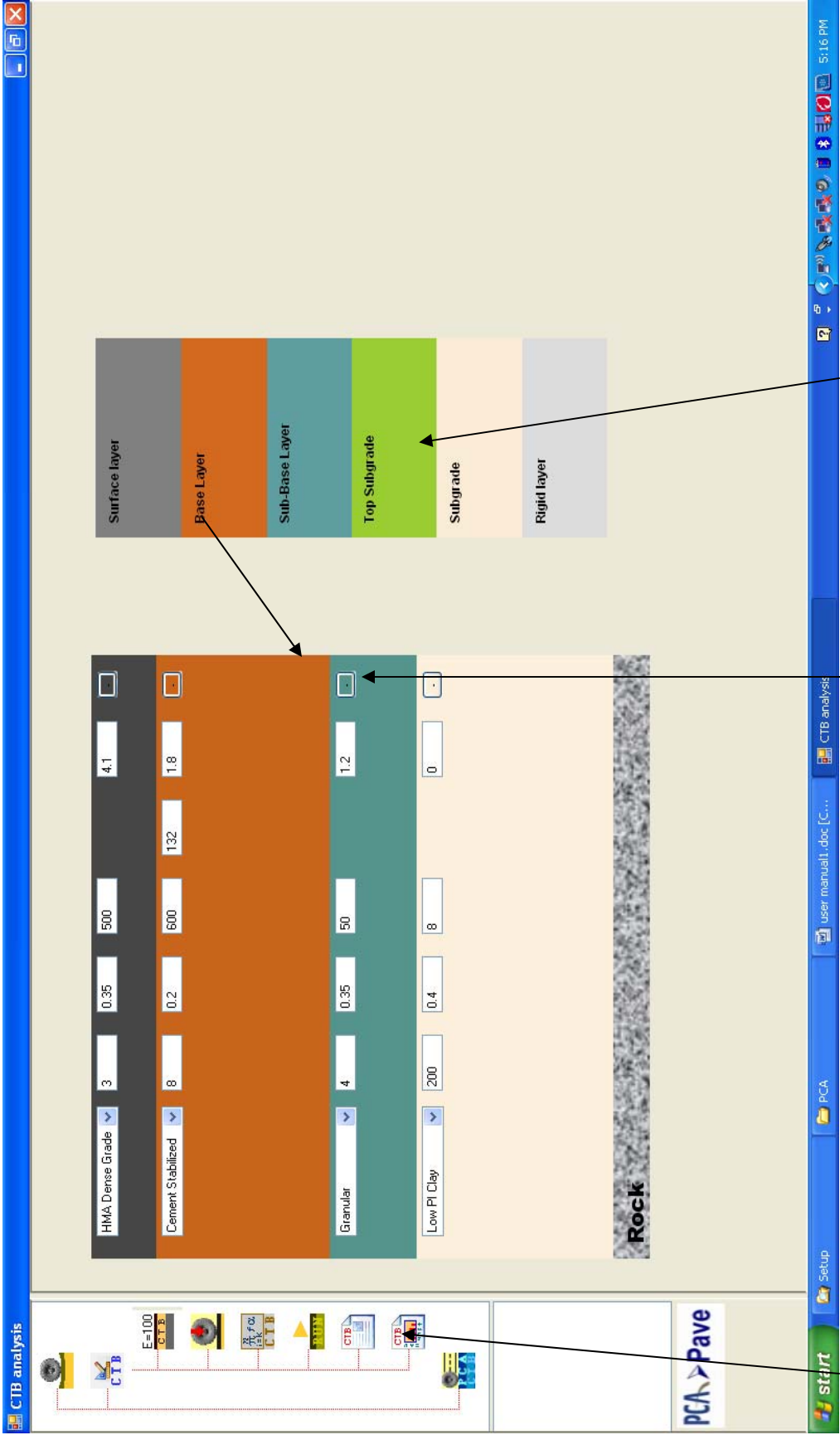


Figure C1. Intro Screen of PCA New Structural Pavement Design Software (PCA Pave).

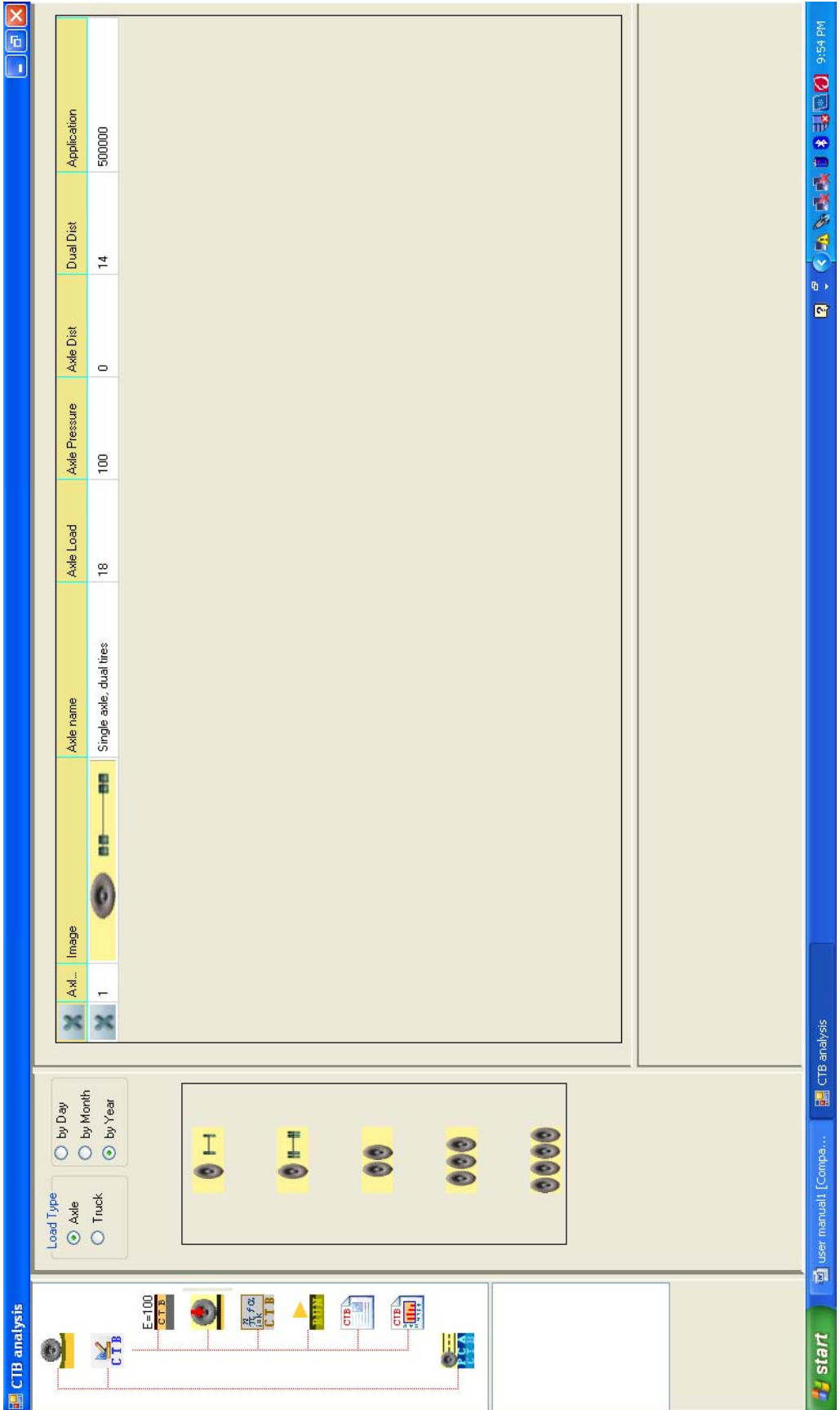


Figure C2. Building Traffic Stream by Axle Type (in This Example 500K 18 kip ESAL's per Year).

The screenshot displays the 'CTB analysis' software interface. On the left, a vertical toolbar contains icons for 'Asphalt Fatigue', 'NCHRP CTB', and 'Rutting Life'. The main workspace shows a cross-section of pavement layers with the following properties:

- HMA Dense Graded:** Th:3, E:500, Asphalt Layer, E1=500. A checkbox for 'Asphalt Fatigue Check' is checked.
- Cement Stabilized:** Th:8, E:632, CTB Layer, MR=132. A checkbox for 'CTB Check' is checked.
- Granular:** Th:4, E:50.
- Low PI Clay:** Th:200, E:8, Sub-Grade Layer. A checkbox for 'SubGrade Rutting Check' is checked.
- Rock:** Represented by a grey textured layer at the bottom.

On the right side, three panels provide equations and parameters:

- Fatigue Life by Asphalt Institute:**

$$N_f = 0.0796 \epsilon_t^{-3.291} E_1^{-0.854}$$

Parameters: ϵ_t (Maximum tensile stress), E_1 (Maximum tensile stress).
- Cement Treated Stabilized Base Layer:**

$$\log(N_f) = \frac{0.972\alpha - \left(\frac{\sigma_t}{MR}\right)^{20p}}{0.0825\beta}$$

$$N_f = \left(\frac{\alpha}{\sigma_t / MR}\right)^{20p}$$

Parameters: α (1.0645), β (0.9003).
- Rutting Life by Asphalt Institute:**

$$N_d = 1.365 \times 10^{-9} \epsilon_p^{-4.47}$$

Parameter: ϵ_p (Maximum tensile stress).

The bottom status bar shows 'CTB analysis', 'Document1 - Microsoft...', and the time '7:05 PM'.

Figure C3. Selecting the Model for Pavement Life Predictions.

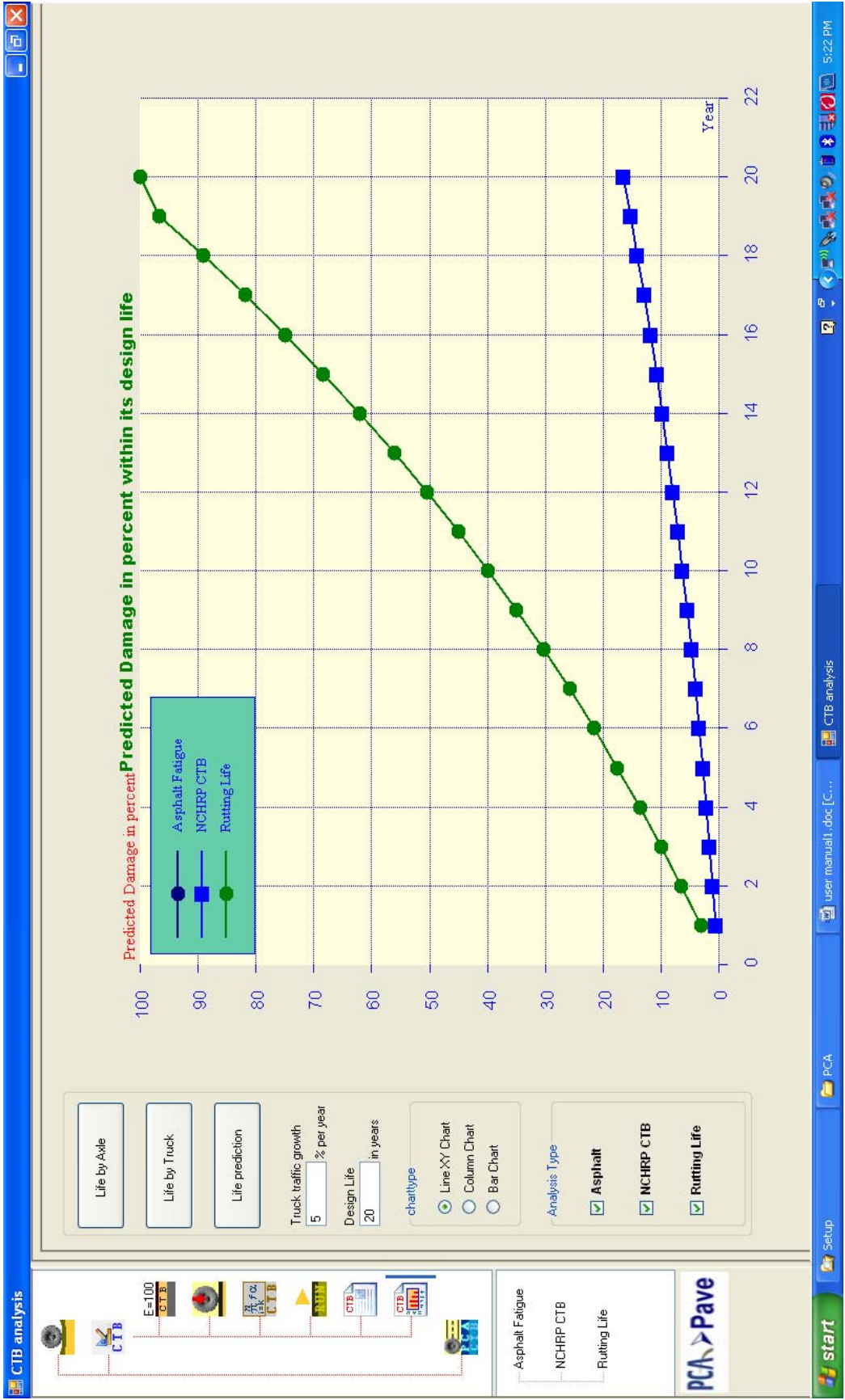


Figure C4. Predicted Growth of Pavement Damage (PCA-PAVE).

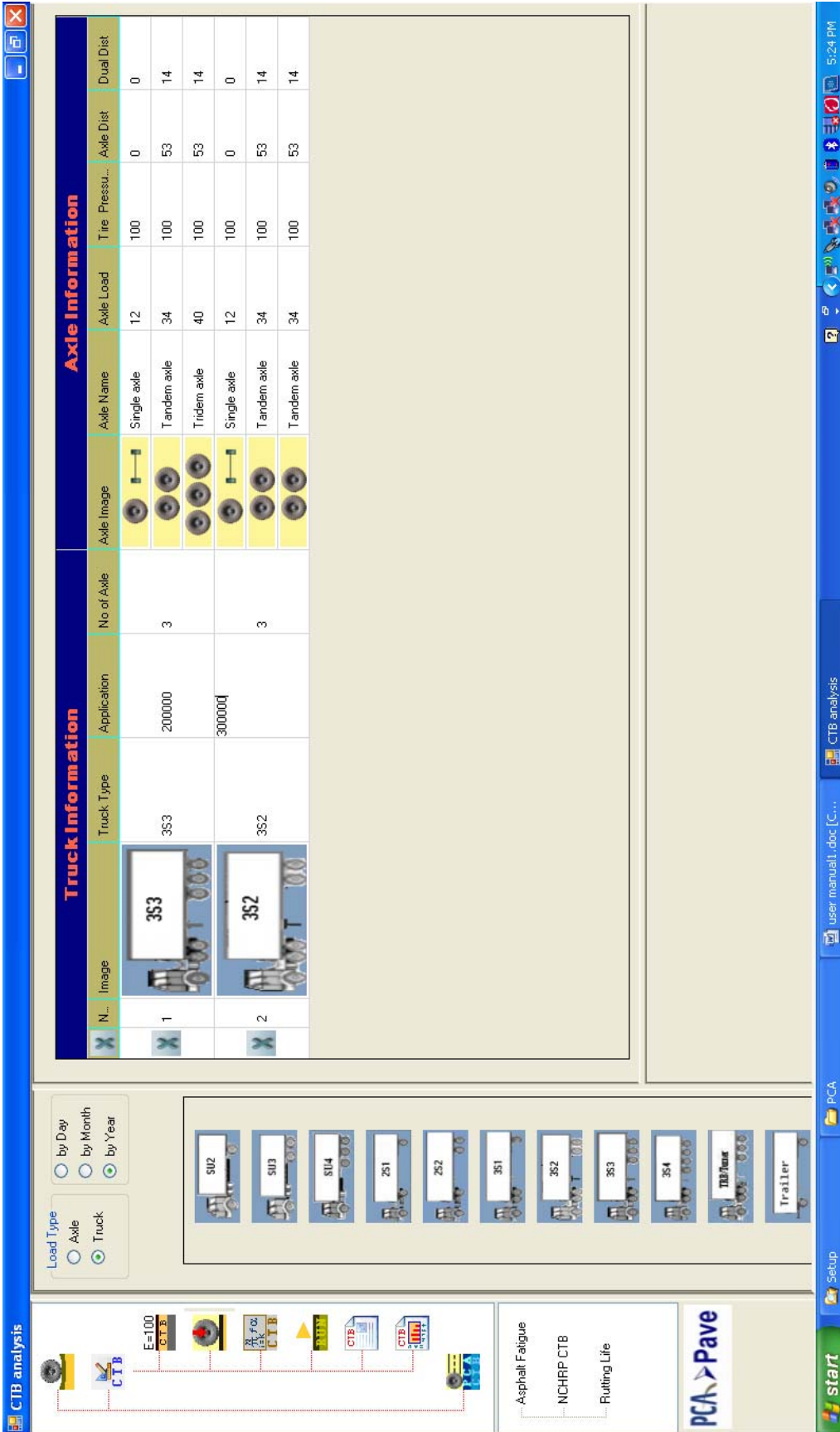


Figure C5. Inputting Traffic Loads by Truck Type rather than Axle Loads.